Spring 2017

Electron impact excitation-ionization of molecules

Esam Abobakr A. Ali

Department: Physics

ELECTRON IMPACT EXCITATION-IONIZATION OF MOLECULES

by

ESAM ABOBAKR A. ALI

A DISSERTATION

Presented to the Faculty of the Graduate School of the

MISSOURI UNIVERSITY OF SCIENCE AND TECHNOLOGY

In Partial Fulfillment of the Requirements for the Degree

DOCTOR OF PHILOSOPHY

in

PHYSICS

2017

Approved

Don H. Madison, Advisor
Jerry L. Peacher
Michael Schulz
Daniel Fischer
Richard Dawes

PUBLICATION DISSERTATION OPTION

This dissertation has been prepared in publication format. The first section gives a brief historical introduction of atomic collisions. The second section gives a review of the few body problem and the approximations which have been applied here. Then there are the collection of published and submitted papers and the last section deals with conclusions followed by the appendices. The papers have been published as follows:

Paper I, Pages 24-39 have been published to *J. Chem. Phys.* **141**, 124307 (2014)

Paper II, Pages 40-54 have been published to *Phys Rev A* **92**, 042711 (2015).

Paper III, Pages 55-76 have been published to *J. Chem. Phys.* **143**, 184310(2015).

Paper IV, Pages 77-91 have been published to *Phys Rev A* **93**, 062705 (2016)

Paper V, Pages 92-108 have been published to *Phys Rev A* **93**, 062707 (2016).

Paper VI, Pages 109-126 have been published to *J. Chem. Phys.* **145**, 164306 (2016).

Paper VII, Pages 127-142 have been published to *Phys Rev A* **95**, 022701 (2017).

Paper VIII, Pages 143-168 have been published to *Phys Rev A* **88**, 062705 (2013).

Paper IX, Pages 169-181 have been published to *Phys Rev A* **89**, 062713 (2014)

Paper X, Pages 182-195 have been published to *J. Phys. B* **48**, 115201 (2015).

ABSTRACT

In the last few decades, the study of atomic collisions by electron-impact has made significant advances. The most difficult case to study is electron impact ionization of molecules for which many approximations have to be made and the validity of these approximations can only be checked by comparing with experiment.

In this thesis, I have examined the Molecular three-body distorted wave (M3DW) or Molecular four-body distorted wave (M4DW) approximations for electron-impact ionization. These models use a fully quantum mechanical approach where all particles are treated quantum mechanically and the post collision interaction (PCI) is treated to all orders of perturbation. These electron impact ionization collisions play central roles in the physics and chemistry of upper atmosphere, biofuel, the operation of discharges and lasers, radiation induced damage in biological material like damage to DNA by secondary electrons, and plasma etching processes.

For the M3DW model, I will present results for electron impact single ionization of small molecules such as Water, Ethane, and Carbon Dioxide and the much larger molecules Tetrahydrofuran, phenol, furfural, 1-4 Benzoquinone. I will also present results for the four-body problem in which there are two target electrons involved in the collision. M4DW results will be presented for dissociative excitation-ionization of orientated D_2. I will show that M4DW calculations using a variational wave function for the ground state that included s- and p- orbital states give better agreement to the experimental measurements than a ground state approximated as a product of two 1s-type Dyson orbitals.

ACKNOWLEDGMENTS

I would like to thank to my wife for her support and continual patience. I am also very thankful to my mother and all my friends for encouraging and supporting throughout my graduate study.

I am also grateful to Prof. Don Madison for his guidance and support during my study. Without his valuable assistance and encouragements, this work not have been completed. I have also thank you to the faculty members who agreed to serve on my committee: Jerry Peacher, Michael Schulz, Daniel Fischer, and Richard Dawes.

Finally, I would like to thank the staff of faculty in the physics department at Missouri S&T for their support. I am thankful to the Ministry of Higher Education & Scientific Research in Libya for financial assistance scholarship.

TABLE OF CONTENTS

LIST OF ILLUSTRATIONS

PAPER III

PAPER IV

PAPER V

PAPER X

LIST OF TABLES

1. INTRODUCTION

Understanding the quantum mechanics of electrons interacting with atoms or molecules is fundamental in theoretical studies of atomic collisions, where the first experimental measurement of the total cross section for electrons colliding with atoms was in 1921 by Ramsauer [1]. During these early years, the theory was developed to explain the dynamical processes for total cross sections and good agreement with experiment was achieved. Despite these early successes, there are still a lot of challenges for theory such as describing fully differential cross sections for ionization of atoms or molecules or for describing the dissociative-ionization process for electron impact ionization of diatomic molecules. These problems are very important for many areas of practical applications. The fully differential cross sections represent the most severe test for theory so they are of primary interest to us. Unfortunately, these processes also tend to be the most demanding for computer resources.

One of the fundamental problems that cannot be solved analytically in physics is the few-body problem. Exact solutions of the Schrodinger equation are known only for the two body problem. Approximations are required to solve problems with more than 2 particles. There are a lot of different theoretical approaches for treating electron collisions with complicated atoms and molecules [2]. These approaches are based either upon perturbative or non-perturbative expansions and several successful theoretical methods have been developed to treat electron-impact ionization of atoms and molecules. The Distorted-Wave Born Approximation (DWBA) which treats single ionization of a complex target as a 3- body problem has been one of the most successful approximations. The standard DWBA does not contain the post-collision interaction (PCI) [3] in the final state wavefunction. Much better agreement between experiment and theory is achieved if the exact coulomb interaction (PCI) is included between the ejected and scatted electrons either exactly or approximately using the Ward-Macek approximation [4].

The fundamental process of electron-impact ionization of atoms or molecules, or more commonly known as (e,2e), plays a main role in understanding the physics of the upper atmosphere, Lasers, and plasmas. In this process, the projectile electron collides with the molecules or atoms, then the projectile electron will be scattered and the molecule or atom will ionize and eject an electron. Although, we don't know which one is the projectile

or ejected electron, we follow the standard procedure of calling the faster electron the projectile and the slower one as the ejected electron. Sometimes after scattering, the molecules or atoms will be left in an excited state, depending on the energy and momentum transferred to the target by projectile electron.

In a fully differential cross section (FDCS) measurement for an (e,2e) event the observation angles and energies of both final state electrons is determined. This is a 5-fold differential cross section (two angles for each electron and one energy - the other energy is determined from energy conservation). Normally, this is called a triply differential cross section (TDCS - two solid angles and one energy). For studying ionization of a molecule, a sixth parameter, the molecular alignment, must also be considered. For this case, the FDCS becomes the Quadruple Differential cross section (QDCS) [5].

In the late 1990's and early 2000's, (e,2e) studies for electron-molecule collisions were dominated by high energy (>1 KeV incident electron energy) electron collisions. For high energies, we can ignore the interaction between the fast free electrons and target, and the electron wavefunctions can be treated as plane waves. Under these circumstances, the differential cross section measurement becomes a measurement of the momentum space bound state wavefunction for the ionized electron. These measurements became known as Electron Momentum Spectroscopy (EMS) [6]. However, for low and intermediate incident electron energy, the dynamics of the collision become important and plane waves are not a good approximation for the continuum electron's wavefunction.

The object of this dissertation is to study electron-impact ionization of molecules for low to intermediate incident energy electrons using the molecular 3-body (M3DW) and 4-body distorted wave (M4DW) approximations. Calculated QDCS will be compared directly with experiment for measurements which determine the orientation of the molecule at the time of ionization. Most experimental measurements do not determine the orientation of the molecules. For this case, one must average over all possible orientations. Our group has previously proposed the orientation–averaged molecular orbital (OAMO) approximation which significantly reduces the required computer time. However, we have recently learned that this approximation is not valid for some molecules which means that we should take a proper average over all molecular orientations (huge amount of computer time) so I will present results for both types of calculations.

2. THEORETICAL METHODS

In this section I will present my theoretical approach for treating molecular collisions for electron impact using the molecular three-body distorted wave (M3DW) method for single ionization and the molecular four-body distorted wave (M4DW) method for simultaneous ionization and excitation of the molecule. To deal with these problems, we have to make several approximations to be able to calculate the Triple Differential cross section (TDCS) or Quardruple Differential cross section (QDCS).

2.1. THREE BODY PROBLEM

To calculate Triple Differential Cross Sections (TDCS) for single ionization of molecules by electron-impact using the Molecular 3-Body Distorted Wave approximation (M3DW), the cross section is calculated as follows [3,7]

$$\frac{d\sigma}{d\Omega_f d\Omega_e dE_e} = \frac{1}{(2\pi)^5}\frac{k_f k_e}{k_i}\left(\left|T_{dir}\right|^2 + \left|T_{exc}\right|^2 + \left|T_{dir} - T_{exc}\right|^2\right) \quad (1)$$

The exact t- matrix can be expressed

$$T_{fi} = \left\langle \chi_f^-(\mathbf{k}_f, \mathbf{r}_0)\chi_s^-(\mathbf{k}_s, \mathbf{r}_1)C_{f-s}(\mathbf{k}_{01}, \mathbf{r}_{01})\psi_{\text{Ion}}(\xi, \mathbf{R})\left|H - H_i\right|\psi_{\text{Target}}(\xi, \mathbf{r}_1, \mathbf{R})\ \chi_i^+(\mathbf{k}_i, \mathbf{r}_0)\right\rangle \quad (2)$$

Where T_{dir} is the direct scattering amplitude and T_{exc} is the exchange amplitude where $\mathbf{r}_0$ and $\mathbf{r}_1$ are exchanged for the final state wave function. The TDCS may be calculated either by taking a proper average over all molecular orientations (huge amount of computer time) or by using the orientation-averaged molecular orbital (OAMO) (significantly less computer time).

In our approximation, ($H - H_i$) depends only on the projectile electron ($\mathbf{r}_0$) and the active electron ($\mathbf{r}_1$). Since this term does not depend only on the passive electron coordinates ξ, we can do the integral over all these coordinates and define

$$\phi_{Dy}(\mathbf{r}_1, \mathbf{R}) \equiv \left\langle \psi_{\text{Ion}}(\xi, \mathbf{R})\left|\psi_{\text{Target}}(\xi, \mathbf{r}_1, \mathbf{R})\right.\right\rangle \quad (3)$$

Here $\phi_{Dy}(\mathbf{r}_1, \mathbf{R})$ is the initial bound-state Dyson molecular orbital for the active electron $\mathbf{r}_1$ with $\mathbf{R}$ of the orientation of the molecule. Defining the perturbation to be W, we have

$$T_{fi}(\mathbf{R}) = \left\langle \chi_f^-(\mathbf{k}_f, \mathbf{r}_0)\chi_s^+(\mathbf{k}_s, \mathbf{r}_1)C_{f-s}(\mathbf{k}_{01}, \mathbf{r}_{01})\right|\mathrm{W}\left|\phi_{Dy}(\mathbf{r}_1, \mathbf{R})\ \chi_i^+(\mathbf{k}_i, \mathbf{r}_0)\right\rangle \quad (4)$$

The Triple Differential cross section for some orientation **R** can be obtained from (considering only one amplitude for simplicity - could be either direct or exchange)

$$TDCS(\mathbf{R}) = \frac{1}{(2\pi)^5}\frac{k_f k_s}{k_i}\left|T_{fi}(\mathbf{R})\right|^2 \tag{5}$$

2.1.1. Proper Orientation Average. The proper orientation average (PA) cross section is calculated by averaging over all possible orientations [8]

$$PA = \frac{\int \mathrm{TDCS}(\mathbf{R})\ \mathrm{d}\Omega_R}{\int d\Omega_R} \tag{6}$$

In this case, we calculate the TDCS at each orientation and then average over all orientations of the molecule.

$$PA = \frac{\int \frac{1}{(2\pi)^5}\frac{k_f k_s}{k_i}\left|\int d^3r_0 d^3r_1 \chi_f^{-*}(\mathbf{k}_f,\mathbf{r}_0)\chi_s^{-*}(\mathbf{k}_s,\mathbf{r}_1)C_{f-s}(\mathbf{k}_{01},\mathbf{r}_{01})\mathrm{W}(\mathbf{r}_0,\mathbf{r}_1)\,\phi_{Dy}(\mathbf{r}_1,\mathbf{R})\chi_i^{+}(\mathbf{k}_i,\mathbf{r}_0)\right|^2 d\Omega_R}{\int d\Omega_R} \tag{7}$$

2.1.2. OAMO Approximation. In the OAMO (Orientation Averaged Molecular Orbital) approximation, we assume that we can commute the absolute value and integral over orientations in Eq. (7)

$$OAMO \simeq \frac{1}{(2\pi)^5}\frac{k_f k_s}{k_i}\frac{\left|\int d\Omega_R \{\int d^3r_0\ d^3r_1\ \chi_f^{-*}(\mathbf{k}_f,\mathbf{r}_0)\chi_s^{-*}(\mathbf{k}_s,\mathbf{r}_1)C_{f-s}(\mathbf{k}_{01},\mathbf{r}_{01})\mathrm{W}(\mathbf{r}_0,\mathbf{r}_1)\,\phi_{Dy}(\mathbf{r}_1,\mathbf{R})\chi_i^{+}(\mathbf{k}_i,\mathbf{r}_0)\}\right|^2}{\int d\Omega_R} \tag{8}$$

Since the only term in the integral that depends on the orientation is the Dyson orbital, we can interchange the order of integrations

$$OAMO \simeq \frac{1}{(2\pi)^5}\frac{k_f k_s}{k_i}\frac{\left|\int d^3r_0\ d^3r_1\ \chi_f^{-*}(\mathbf{k}_f,\mathbf{r}_0)\chi_s^{-*}(\mathbf{k}_s,\mathbf{r}_1)C_{f-s}(\mathbf{k}_{01},\mathbf{r}_{01})\mathrm{W}(\mathbf{r}_0,\mathbf{r}_1)\int \phi_{Dy}(\mathbf{r}_1,\mathbf{R})\,d\Omega_R\ \chi_i^{+}(\mathbf{k}_i,\mathbf{r}_0)\}\right|^2}{\int d\Omega_R} \tag{9}$$

We now define the OAMO Dyson wavefunction

$$\phi_{Dy}^{OA}(\mathbf{r}_1) = \frac{\int \phi_{Dy}(\mathbf{r}_1,\mathbf{R})d\Omega_R}{\int d\Omega_R} \tag{10}$$

$$\mathrm{OAMO} = \frac{1}{(2\pi)^5}\frac{k_f k_s}{k_i}\left|\int d^3r_0\ d^3r_1\ \chi_f^{-*}(\mathbf{k}_f,\mathbf{r}_0)\chi_s^{-*}(\mathbf{k}_s,\mathbf{r}_1)C_{f-s}(\mathbf{k}_{01},\mathbf{r}_{01})\mathrm{W}(\mathbf{r}_0,\mathbf{r}_1)\,\phi_{Dy}^{OA}(\mathbf{r}_1)\chi_i^{+}(\mathbf{k}_i,\mathbf{r}_0)\right|^2 \tag{11}$$

This is a T-matrix just like one we would evaluate for ionization of an atom or ionization of a single molecular orientation which does not take very much computer time.

2.1.3. Potential Scattering. In this section we discuss the calculation of the continuum wavefunctions for the electron. In principle, this is a very complicated many problem calculation. To simplify this problem, we replace the target by a spherically symmetric scattering potential $U(r)$. For neutral targets, this potential is asymptotically neutral and for ions it is asymptotically a Coulomb potential. These two methods are shown in Figures 2.1 and 2.2. For continuum electrons, the energy $E = \frac{k^2}{2} > 0$ so the electron is not bound. Let's start with the simplest scattering problem for real a potential $\mathrm{V}(r)$, the general form of the Schrodinger equation describing the scattering charged particle can be given by

$$\left(-\frac{1}{2}\nabla^2 + \mathrm{V}(r)\right)\chi(\mathbf{k},\mathbf{r}) = E\chi(\mathbf{k},\mathbf{r}) \tag{12}$$

the potential depends on r value only. In general, the solution of this equation can be expanded in terms of spherical harmonics ($Y_{\ell m}(\theta,\phi)$)

$$\chi(\mathbf{k},\mathbf{r}) = \sum_{\ell=0}^{\infty} R_\ell(r) Y_{\ell m}(\theta,\phi) \tag{13}$$

However, since, the potential is spherically symmetric, the wavefunction will only depend on the angle between the incident beam direction and the scattered electron momentum $\mathbf{k}$ direction. If we pick the incident direction along the z-axis, then the wavefunction will only depend on the angle θ between the z-axis and the direction of $\mathbf{k}$. Since the wave function does not depend on the azimuthal angle ϕ ($m = 0 \Rightarrow Y_{l0} = \sqrt{\frac{2l+1}{4\pi}} P_\ell(\cos)$). As a result

$$\chi(\mathbf{k},\mathbf{r}) = \sum_{\ell=0}^{\infty} R_\ell(r) Y_{\ell m}(\theta,\phi) \tag{14}$$

Using

$$\nabla^2 = \frac{1}{r^2}\frac{\partial}{\partial r}\left(r^2 \frac{\partial}{\partial r}\right) - \frac{L^2(\theta,\phi)}{r^2} \tag{15}$$

and

$$L^2(\theta,\phi)\, Y_{\ell m}(\theta,\phi) = \ell(\ell+1)\, Y_{\ell m}(\theta,\phi) \tag{16}$$

The Schrodinger equation (12) can be written as

$$\left(-\frac{1}{2}\left(\frac{1}{r^2}\frac{\partial}{\partial r}(r^2\frac{\partial}{\partial r})-\frac{L^2(\theta,\phi)}{r^2}\right)+\mathrm{V}(r)-\frac{k^2}{2}\right)R_\ell(r)Y_{\ell m}(\theta,\phi)=0 \tag{17}$$

The radial differential equation is given by

$$\left(\frac{d^2}{dr^2}+\frac{2}{r}\frac{d}{dr}-\frac{l(l+1)}{r^2}-U(r)+k^2\right)R_\ell(r)=0 \tag{18}$$

Let's introduce the reduced potential $U(r)=2\mathrm{V}(r)$. We can eliminate the second derivative function and make simpler solution of radial function by introducing the new radial function

$$\chi_\ell(r)=rR_\ell(r) \tag{19}$$

Then Eq. (17) becomes

$$\left(\frac{d^2}{dr^2}-\frac{l(l+1)}{r^2}-U(r)+k^2\right)\chi_\ell(r)=0 \tag{20}$$

To solve the eq. (20), there are two zones of potentials as shown in the Figure 2.3. For neutral atoms, there would be a charge of +Z (the nuclear charge) at the origin and a net charge of -Z distributed spherically symmetrically within a sphere of radius R. For spherically symmetric charge distributions, we know from Gauss's law $\int \vec{E}\bullet d\vec{A}=\frac{q_{enclosed}}{\varepsilon_0}$ that if we draw a sphere of radius r, the potential will be the same as the potential of a point charge $q_{enclosed}$ located at the origin. For $r<R$, the negative charge enclosed $q_{negative}<-Z$ and $\vec{E}=k\frac{q_{enclosed}}{r^2}$, where $k=\frac{1}{4\pi\varepsilon_0}$. For $r\geq R$, $q_{enclosed}=0$ and $\vec{E}=0$.

Zero potential

Let's first look at the solution of Eq. (19) for no potential. If $U(r)=0$, the solution of Eq. (19) is a Bessel function. Since it is a second order differential equation, there are two solutions, a regular and irregular Bessel function. The regular solution F_ℓ is zero at the origin and the irregular solution G_ℓ is infinite at the origin [9]. If $U(r)=0$ everywhere, the solution is the regular solution which is also a plane wave. The function

$$\frac{F_\ell(k,r)}{kr} = j_\ell(k,r) \tag{21}$$

where $j_\ell(k,r)$ is called the regular spherical Bessel function. We can plug this in eq. (14) , and get the solution for a plane wave

$$\chi(\mathbf{k},\mathbf{r}) = e^{i\mathbf{k}.\mathbf{r}} = e^{ikz} = e^{ikr\cos\theta} = \sum_{l=0}^{\infty}(2l+1)i^\ell j_\ell(k,r)P_\ell(\cos\theta) \tag{22}$$

The asymptotic forms of the regular and irregular solutions are:

$$F_\ell(kr) = \sin\,(kr - \frac{\ell\pi}{2}) \tag{23}$$

$$G_\ell(kr) = -\cos\,(kr - \frac{\ell\pi}{2}) \tag{24}$$

Consequently, the asymptotic form of Eq. (22) can be written as

$$\chi(\mathbf{k},\mathbf{r}) = \frac{1}{kr}\sum_{l=0}^{\infty}(2l+1)i^\ell \sin\left(kr - \frac{\ell\pi}{2}\right)P_\ell(\cos\theta), \qquad r \to \infty$$

Zone II

If $U(r) \neq 0$ everywhere, but is asymptotically zero, the asymptotic solution is a linear combination of the regular and irregular solutions

$$\begin{aligned}\chi_\ell(k,r) &= A_\ell\ F_\ell(k,r) - B_\ell\ G_\ell(k,r) \\ &\to A_\ell\ \sin\,(kr - \frac{\ell\pi}{2}) + B_\ell\ \cos\,(kr - \frac{\ell\pi}{2})\end{aligned} \tag{25}$$

and

$$\frac{\chi_\ell(k,r)}{kr} = A_\ell\ j_\ell(k,r) + B_\ell\ \eta_\ell(k,r) \tag{26}$$

Where

$$\eta_\ell(k,r) = -\frac{G_\ell(k,r)}{kr} \tag{27}$$

Is the irregular spherical Bessel function. Eq. (25) can be re-written

$$A_\ell\ \sin\,(kr - \frac{\ell\pi}{2}) + B_\ell\ \cos\,(kr - \frac{\ell\pi}{2}) = N_\ell\ \sin\,(kr - \frac{\ell\pi}{2} + \delta_\ell) \tag{28}$$

Where $N_\ell = \sqrt{A_\ell^2 + B_\ell^2}$ and

$$\tan\delta_\ell = \frac{B_\ell}{A_\ell} \tag{29}$$

Here δ_ℓ is called the phase shift since it represents the angular change in the solution relative to a plane wave. The full solution of the Schrödinger equation (12) can be obtained by summing all the partial wave components of Eq. (20)

$$\begin{aligned}\chi^+(\mathbf{k},\mathbf{r}) &= \frac{1}{kr}\sum_{\ell m}\ \chi_\ell(r)\,Y_{\ell m}(\theta,\phi)\,Y^*_{\ell m}(\hat{k}) \\ &= \frac{1}{kr}\sum_{\ell}\ \chi_\ell(r)\,\frac{2\ell+1}{4\pi}\,P_\ell(\cos\theta)\end{aligned} \tag{30}$$

The normalization of the radial partial waves $\chi_\ell(r)$ is determined by the boundary condition imposed by scattering theory and scattering theory requires that the asymptotic waveshould be a plane wave plus either an incoming or outgoing spherical wave. For outgoing waves

$$\chi^+(\mathbf{k},\mathbf{r}) \to e^{i\mathbf{k}\bullet\mathbf{r}} + f(\theta)\,\frac{e^{ikr}}{r} \tag{31}$$

The asymptotic form of $\chi_\ell(r)$ is given by Eq. (28). We can use some trigonometry to rearrange the asymptotic form into a plane wave plus scattered wave.

$$\sin(kr-\frac{\ell\pi}{2}+\delta_\ell) = \sin(kr-\frac{\ell\pi}{2})\cos\,\delta_\ell + \cos(kr-\frac{\ell\pi}{2})\sin\,\delta_\ell \tag{32}$$

$$e^{i(kr-\frac{\ell\pi}{2})} = \cos(kr-\frac{\ell\pi}{2}) + i\sin(kr-\frac{\ell\pi}{2}) \tag{33}$$

$$\cos(kr-\frac{\ell\pi}{2})\sin\,\delta_\ell = [e^{i(kr-\frac{\ell\pi}{2})} - i\sin(kr-\frac{\ell\pi}{2})]\sin\,\delta_\ell \tag{34}$$

$$\begin{aligned}\sin(kr-\frac{\ell\pi}{2}+\delta_\ell) &= \sin(kr-\frac{\ell\pi}{2})\cos\,\delta_\ell + [e^{i(kr-\frac{\ell\pi}{2})} - i\sin(kr-\frac{\ell\pi}{2})]\sin\,\delta_\ell \\ &= \sin(kr-\frac{\ell\pi}{2})(\cos\,\delta_\ell - i\sin\,\delta_\ell) + \sin\,\delta_\ell\,e^{i(kr-\frac{\ell\pi}{2})} \\ &= \sin(kr-\frac{\ell\pi}{2})\,e^{-i\,\delta_\ell} + \sin\,\delta_\ell\,e^{ikr}\,e^{-\frac{\ell\pi}{2}} \\ &= \sin(kr-\frac{\ell\pi}{2})\,e^{-i\,\delta_\ell} + \sin\,\delta_\ell\,e^{ikr}\,i^{-\ell}\end{aligned} \tag{35}$$

Now use Eq. (35) in Eq. (30) for the case where the z-axis is parallel to the incident beam direction

$$\chi^+(\mathbf{k},\mathbf{r}) = \frac{1}{kr}\sum_{\ell m}\ \chi_\ell(r)\ \frac{2\ell+1}{4\pi}\,P_\ell(\cos\theta)$$

$$\rightarrow \frac{1}{kr}\sum_{\ell m}\frac{2\ell+1}{4\pi}N_\ell\ [\sin(kr-\frac{\ell\pi}{2})\,e^{-i\,\delta_\ell}+\sin\,\delta_\ell\ e^{ikr}\ i^{-\ell}]P_\ell(\cos\theta) \tag{36}$$

Compare this to the required boundary condition

$$\begin{aligned}\chi^+(\mathbf{k},\mathbf{r}) &\rightarrow e^{i\mathbf{k}\bullet\mathbf{r}}+f(\theta)\frac{e^{ikr}}{r}\\ &=\sum_\ell i^\ell\ (2\ell+1)\ j_\ell(k,r)\,P_\ell(\cos\alpha)+f(\theta)\frac{e^{ikr}}{r}\\ &\rightarrow\sum_\ell i^\ell\ (2\ell+1)\frac{\sin(kr-\frac{\ell\pi}{2})}{kr}P_\ell(\cos\theta)+f(\theta)\frac{e^{ikr}}{r}\end{aligned} \tag{37}$$

Comparing (36) and (37), we can see that

$$N_\ell=4\pi\,i^\ell\ e^{i\,\delta_\ell} \tag{38}$$

$$f(\theta)=\frac{1}{k}\sum_{\ell m}(2\ell+1)\,e^{i\,\delta_\ell}\ \sin\,\delta_\ell\ P_\ell(\cos\theta) \tag{39}$$

The differential cross section is given by

$$\frac{d\sigma}{d\Omega}=\left|f(\theta)\right|^2 \tag{40}$$

And the total cross section

$$\sigma=\int\frac{d\sigma}{d\Omega}\,d\Omega=\frac{4\pi}{k^2}\sum_\ell(2\ell+1)\sin^2\delta_\ell \tag{41}$$

2.1.3.1. Alternate asymptotic form. For practical calculations, using sin and cos functions for matching the boundary conditions requires much larger r-values than necessary/practical. Instead, we use the second line of Eq. (35)

$$\begin{aligned}\sin(kr-\frac{\ell\pi}{2}+\delta_\ell)&=\sin(kr-\frac{\ell\pi}{2})e^{-i\,\delta_\ell}+\sin\,\delta_\ell\ e^{\,i(kr-\frac{\ell\pi}{2})}\\ &=\sin(kr-\frac{\ell\pi}{2})\,e^{-i\,\delta_\ell}+\sin\,\delta_\ell\,[\cos(kr-\frac{\ell\pi}{2})+i\sin(kr-\frac{\ell\pi}{2})]\end{aligned} \tag{42}$$

Use this in Eq. (30)

$$\begin{aligned}\chi^+(\mathbf{k},\mathbf{r})&=\frac{1}{kr}\sum_{\ell m}\ \chi_\ell(r)\,Y_{\ell m}(\hat{r})\,Y^*_{\ell m}(\hat{k})\\ &\rightarrow\frac{1}{kr}\sum_{\ell m}\ N_\ell\ \sin(kr-\frac{\ell\pi}{2}+\delta_\ell)\,Y_{\ell m}(\hat{r})\,Y^*_{\ell m}(\hat{k})\end{aligned}$$

$$= \frac{1}{kr} \sum_{\ell m} \; 4\pi \, i^{\ell} \, e^{i\delta_\ell} \, \{\sin\,(kr - \frac{\ell\pi}{2})\, e^{-i\delta_\ell} + \sin\,\delta_\ell \, [\cos(kr - \frac{\ell\pi}{2}) + i\,\sin(kr - \frac{\ell\pi}{2})]\} Y_{\ell m}(\hat{r})\, Y^{*}_{\ell m}(\hat{k})$$

$$= \frac{4\pi}{kr} \sum_{\ell m} i^{\ell} \{\sin\,(kr - \frac{\ell\pi}{2}) + e^{i\delta_\ell} \sin\,\delta_\ell \, [\cos(kr - \frac{\ell\pi}{2}) + i\,\sin(kr - \frac{\ell\pi}{2})]\} Y_{\ell m}(\hat{r})\, Y^{*}_{\ell m}(\hat{k})$$

$$= \frac{4\pi}{kr} \sum_{\ell m} i^{\ell} \{F_\ell\,(kr) + e^{i\delta_\ell} \sin\,\delta_\ell \, [-G_\ell\,(kr) + i\,F_\ell\,(kr)]\} Y_{\ell m}(\hat{r})\, Y^{*}_{\ell m}(\hat{k}) \tag{43}$$

Incorporating the normalization constant into the expansion coefficient, the general partial wave expansion is normally written as

$$\begin{aligned} \chi^{+}(\mathbf{k},\mathbf{r}) &= \frac{4\pi}{kr} \; \sum_{\ell m} i^{\ell} \; \chi_\ell(k,r)\, Y^{m}_{\ell}(\hat{\mathbf{k}})\, Y^{m*}_{\ell}(\hat{\mathbf{r}}) \\ &= \frac{1}{kr} \sum_{\ell} i^{\ell} \; (2\ell+1)\, \chi_\ell(k,r)\, P_\ell(\cos\gamma) \end{aligned} \tag{44}$$

Where asymptotically

$$\begin{aligned} \chi_\ell &\rightarrow F_\ell\,(kr) + e^{i\delta_\ell} \sin\,\delta_\ell \, [-G_\ell\,(kr) + i\,F_\ell\,(kr)] \\ &\equiv F_\ell\,(kr) + T_\ell \, [-G_\ell\,(kr) + i\,F_\ell\,(kr)] \end{aligned} \tag{45}$$

Where $T_\ell = e^{i\delta_\ell} \sin\,\delta_\ell$ is called the elastic scattering T-matrix.

2.1.3.2. 2nd Alternate asymptotic form of the partial wave. There are alternate forms of the asymptotic radial partial wave that can be useful. Starting with Eq. (45)

$$\begin{aligned} \chi_\ell &\rightarrow F_\ell\,(kr) + e^{i\delta_\ell} \sin\,\delta_\ell \, [-G_\ell\,(kr) + i\,F_\ell\,(kr)] \\ &= e^{i\delta_\ell} \{F_\ell\,(kr) e^{-i\delta_\ell} + \sin\,\delta_\ell \; [-G_\ell\,(kr) + i\,F_\ell\,(kr)]\} \\ &= e^{i\delta_\ell} \{F_\ell\,(kr) [\cos\,\delta_\ell - i \sin\,\delta_\ell\,] + \sin\,\delta_\ell \; [-G_\ell\,(kr) + i\,F_\ell\,(kr)]\} \\ &= e^{i\delta_\ell} [\cos\,\delta_\ell \; F_\ell\,(kr) - \sin\,\delta_\ell \; G_\ell\,(kr)] \end{aligned} \tag{46}$$

Notice that the quantity in brackets is real so that all the complex information is contained in $e^{i\delta_\ell}$. In the early days of computers, space was a premium and it required half the storage space to store a real array and one complex number so that was often done. The codes we are using use that method for calculating distorted waves.

2.1.3.3. Coulomb waves. All of the above is for asymptotically neutral potentials. Frequently, we wish to solve the Schrödinger equation for potentials that are asymptotically a Coulomb potential. This can be done essentially exactly as above since the asymptotic form for regular and irregular Coulomb functions are

$$F_\ell(kr) \to \sin[kr - \frac{\ell\pi}{2} - \lambda \ln(2kr)]$$
$$G_\ell(kr) \to \cos[kr - \frac{\ell\pi}{2} - \lambda \ln(2kr)] \quad (47)$$

The Somerfield parameter $\lambda = \frac{z_1 z_2}{k}$, and $z_1 z_2$ are particle charges. Consequently all the trig, the relations can be used in the same way. We have a subroutine that calculates either spherical Bessel functions or Coulomb waves depending on whether λ is zero or non-zero. The only additional complication associated with Coulomb waves is that there is an additional phase shift called the Coulomb phase shift σ_ℓ and this phase shift is included directly in the partial wave expansion

$$\chi^+(\mathbf{k},\mathbf{r}) = \frac{4\pi}{kr} \sum_{\ell m} i^\ell \, e^{i\sigma_\ell} \, \chi_\ell(k,r) \, Y_\ell^m(\hat{\mathbf{k}}) \, Y_\ell^{m*}(\hat{\mathbf{r}})$$
$$= \frac{1}{kr} \sum_{\ell} i^\ell \, e^{i\sigma_\ell} \, (2\ell+1) \, \chi_\ell(k,r) \, P_\ell(\cos\gamma) \quad (48)$$

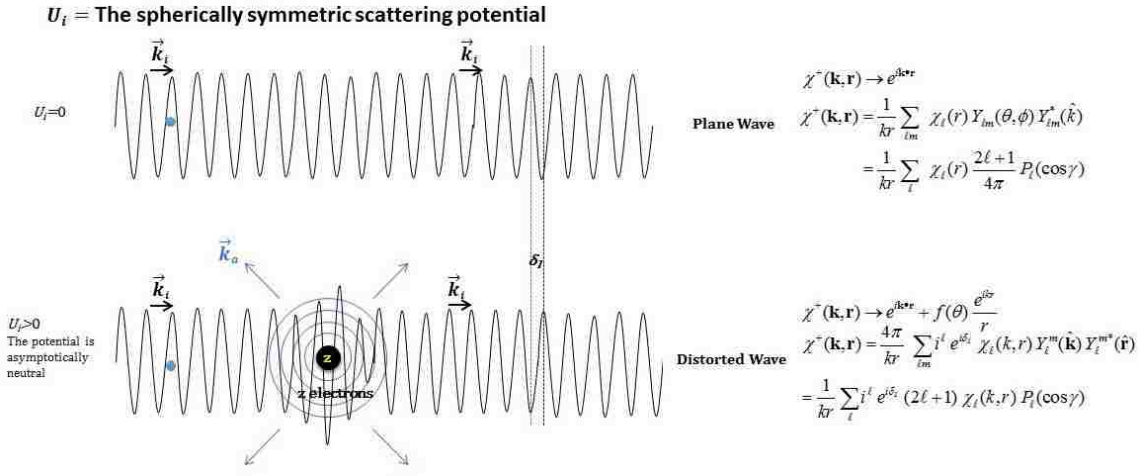

Figure 2.1. Asymptotically neutral potential wave diagram

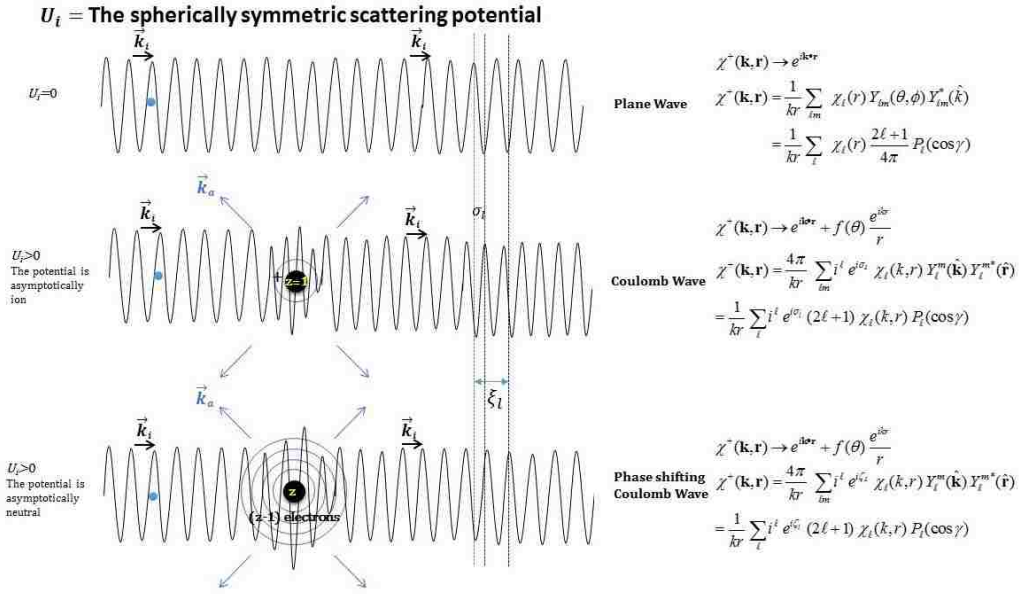

Figure 2.2. Asymptotically coulomb potential wave diagram

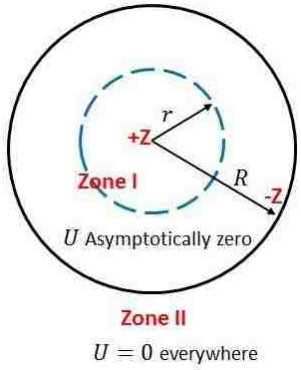

Figure 2.3. Charge distribution of neutral object

2.1.4. Calculation of the Perturbation. The exact T-matrix can be written

$$T_{fi} = \left\langle \Phi_f \left| \mathrm{W} \right| \Phi_i \right\rangle = \left\langle \Phi_f \left| H - H_0 \right| \Phi_i \right\rangle \tag{49}$$

Where the initial-state Hamiltonian H_0 is chosen to be

$$H_0 = H_{\text{target}} + K_i + U_i \tag{50}$$

where H_{target} is the Hamiltonian for the neutral target with eigenfunctions ψ_{target}, K_i is the kinetic energy operator for the projectile, and U_i is an initial-state spherically symmetric

potential for the projectile-target interactions (normally called the initial-state distorted potential).

The full Hamiltonian is given

$$H = H_{\text{target}} + K_i + V_i \tag{51}$$

where V_i is the initial state interaction between the incoming projectile electron and the target

$$\mathrm{W} = H - H_0 = V_i - U_i \tag{52}$$

The exact potential V_i can be expressed as two terms. The 1st term is the projectile electron-target electrons interaction V_{ele}, and the 2nd term is the projectile electron-target nuclei interaction V_N. The initial state potential is given by (see Fig. 2.10):

$$V_i = V_{ele} + V_N \tag{53}$$

We obtain this potential from the charge distribution of the target $\rho(\mathbf{r}_1, \mathbf{R})$. After we have calculated the Dyson orbital's wave function $\phi_{Dyson}(\mathbf{r}_1, \boldsymbol{R})$, we can calculate the charge density for neutral molecule as follows:

$$\rho(\mathbf{r}_1, \mathbf{R}) = \sum_{k=1}^{m} n_k \left| \phi_{Dyson}^{k}(\mathbf{r}_1, \mathbf{R}) \right|^2 \tag{54}$$

Where m is the number of orbitals in the molecule, and n_k is the occupation number of the orbital. From equation (54) the charge density depends on the orientation of the molecule. To obtain the spherically symmetric distorting potential, we average this density over all orientations to form the average radial charge density.

$$\rho^{ave}(r_1) = \left\langle \rho(\mathbf{r}_1, \mathbf{R}) \right\rangle \tag{55}$$

The angle dependent potential $V(\mathbf{r}_0)$ for the interaction between the free particle located at $\mathbf{r}_0$ and the target electrons is given by

$$\begin{aligned} V_{ele}(\mathbf{r}_0) &= z_p z_e \int \frac{\rho^{ave}(r_1)}{|\mathbf{r}_0 - \mathbf{r}_1|} r_1^2 \, dr_1 \, d\hat{r}_1 \\ &= -z_p \int \frac{\rho^{ave}(r_1)}{|\mathbf{r}_0 - \mathbf{r}_1|} r_1^2 \, dr_1 \, d\hat{r}_1 \end{aligned} \tag{56}$$

Where z_p is the charge of the projectile, the electron charge is $z_e = -1$, and $d\hat{r}_1 = \sin(\theta_1)\, d\theta_1\, d\phi = -d\cos(\theta_1)\, d\phi$. To get the spherically symmetric scattering potential, we average $V_{ele}(\mathbf{r}_0)$ over angles (θ_0, ϕ_0).

$$U_{\text{ele}}(r_0) = \frac{1}{4\pi}\int V_{ele}(\mathbf{r}_0)\, d\hat{r}_0 = \frac{-z_p}{4\pi}\iint \frac{\rho^{ave}(r_1)}{|\mathbf{r}_0 - \mathbf{r}_1|}\, r_1^2\, dr_1\, d\hat{r}_1\, d\hat{r}_0 \tag{57}$$

We now use a result from Jackson

$$\frac{1}{|\mathbf{r}_0 - \mathbf{r}_1|} = 4\pi\sum_{\ell m}\frac{1}{2\ell+1}\frac{r_<^\ell}{r_>^{\ell+1}}\, Y_{\ell m}^*(\hat{r}_0)\, Y_{\ell m}(\hat{r}_1) \tag{58}$$

$$\begin{aligned} U_{\text{ele}}(r_0) &= \frac{1}{4\pi}\int V_{ele}(\mathbf{r}_0)\, d\hat{r}_0 \\ &= \frac{-z_p}{4\pi}\iint \rho^{ave}(r_1)\sum_{\ell m}\frac{1}{2\ell+1}\frac{r_<^\ell}{r_>^{\ell+1}}\, Y_{\ell m}^*(\hat{r}_0)\, Y_{\ell m}(\hat{r}_1) r_1^2\, dr_1\, d\hat{r}_1\, d\hat{r}_0 \\ &= \frac{-z_p}{4\pi}\sum_{\ell m}\frac{1}{2\ell+1}\int \rho^{ave}(r_1)\frac{r_<^\ell}{r_>^{\ell+1}}\, Y_{\ell m}(\hat{r}_1) r_1^2\, dr_1\, d\hat{r}_1 \int Y_{\ell m}^*(\hat{r}_0)\, d\hat{r}_0 \end{aligned} \tag{59}$$

However, $Y_{00} = \frac{1}{\sqrt{4\pi}}$ and

$$\begin{aligned} \int Y_{\ell m}^*(\hat{r}_0)\, d\hat{r}_0 &= \sqrt{4\pi}\int Y_{00}(\hat{r}_0) Y_{\ell m}^*(\hat{r}_0)\, d\hat{r}_0 \\ &= \sqrt{4\pi}\, \delta_{\ell 0}\, \delta_{m0} \end{aligned} \tag{60}$$

Consequently

$$U_{\text{ele}}(r_0) = \frac{-z_p}{4\pi}\int \rho^{ave}(r_1)\frac{1}{r_>}\, r_1^2\, dr_1\, d\hat{r}_1 \tag{61}$$

Now the integral of $d\hat{r}_2$ is 4π so that

$$U_{\text{ele}}(r_0) = -z_p \int \rho^{ave}(r_1)\frac{1}{r_>}\, r_1^2\, dr_1 \tag{62}$$

For the perturbation, we assume that the actual nuclear interaction cancels the nuclear interaction in the distorting potential ($V_N \equiv U_N$).

Consequently, the perturbation becomes

$$V_i - U_i = V_{ele} + V_N - U_{ele} - U_N$$

$$V_i - U_i = -z_p \int \frac{\rho^{ave}(r_1)}{|\mathbf{r}_0 - \mathbf{r}_1|} r_1^2 \, dr_1 \, d\hat{r}_1 + z_p \int \rho^{ave}(r_1) \frac{1}{r_>} r_1^2 \, dr_1 \tag{63}$$

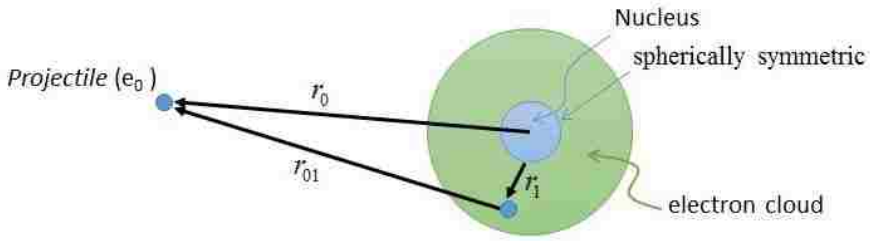

Figure 2.4. Interaction between projectile and spherically symmetric potential

2.1.5. Correlation-Polarization Potential. The projectile electron will polarize the target and this polarization changes the interaction between the projectile and target. Since this could be an important effect, we need to add a polarization potential to the distorting potential. The Perdue-Zunger correlation-polarization potential is a combination of the asymptotic dipole polarization potential and a short ranged correlation potential. For large r, the dipole polarization potential can be approximated as

$$v_p(r) \cong -\frac{1}{2}\left[\frac{\alpha_0}{r^4}\right] \tag{64}$$

Where α_0 is the polarizability of the target. This potential cannot be used for small r since it becomes infinite. The short range correlation potential is defined to be [10]

$$v_{co}(r) = \begin{cases} 0.0311 \ln r_s - 0.0584 + 0.00133 \, r_s \ln r_s - 0.0084 \ln r_s & r_s < 1 \\ \dfrac{\gamma\left(1 + \frac{7}{6}\beta_1\sqrt{r_s} + \frac{4}{3}\beta_2 r_s\right)}{\left(1 + \beta_1\sqrt{r_s} + \beta_2 r_s\right)^2} & r_s \geq 1 \end{cases} \tag{65}$$

where $\gamma = -0.1423$, $\beta_1 = 1.0529$, $\beta_2 = 0.3334$, and $r_s = \left[\frac{3}{4\pi}\rho(\vec{r})\right]^{\frac{1}{3}}$

The radial charge density is $\rho(\vec{r})$ is averaged over all angles as above. The correlation-Polarization potential depends only on the molecule charge density and polarizabilities. The idea is to use (65) for short range and Eq. (64) for long range. A plot of the absolute values of short range and long range potentials is shown in Fig. 2.5. When the two curves cross, we switch from the short range form to the long range form. The final potential is shown in Fig. 2.6.

If we draw the absolute values of correlation and polarization potential, we get

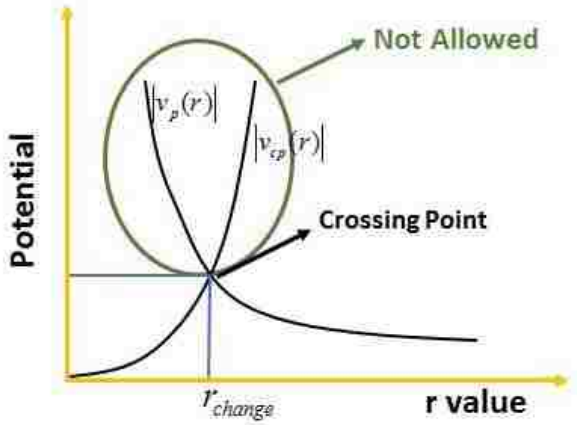

Figure 2.5. Shows the crossing point between the correlation and polarization potential

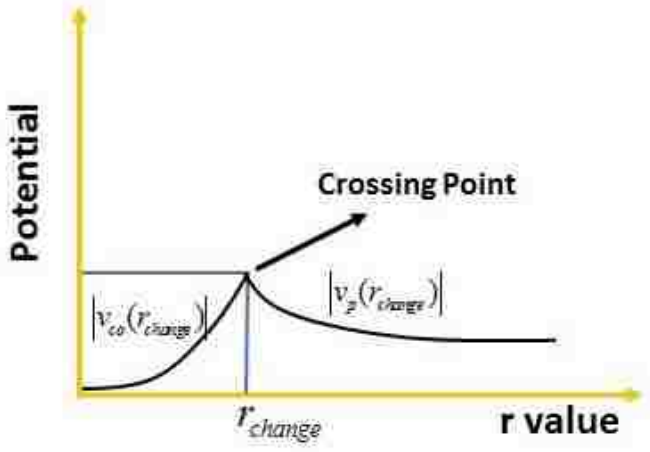

Figure 2.6. The final correlation-polarization potential

2.2. FOUR BODY PROBLEM

2.2.1. Excitation-ionization. Let us first consider the quadruple differential cross section (QDCS) for electron impact excitation-ionization of an aligned hydrogen molecule. After the collision, an electron is ejected and the molecule is left in an excited state.

$$e_i^-(\mathbf{k}_i) + H_2 \rightarrow (H_2^+)^* + e_{scat.}^-(\mathbf{k}_{scat.}) + e_{ejec.}^-(\mathbf{k}_{ejec.}) \tag{66}$$

where $e_i^-, e_{scat}^-,$ and e_{ejec}^- represents the incident, scattered, and ejected electrons with momenta $\mathbf{k}_i, \mathbf{k}_{scat.},$ and $\mathbf{k}_{ejec.}$ respectively (energies $E_i, E_{scat.},$ and $E_{eject.}$). H_2 is the neutral hydrogen molecule, and $(H_2^+)^*$ is the excited residual ion.

The momentum transfer is given by

$$\mathbf{q} = \mathbf{k}_i - \mathbf{k}_{scat.} \tag{67}$$

We can calculate the momentum transfer as shown in Figure 2.7 (66)

$$q = \sqrt{k_i^2 + k_{\text{scat.}}^2 - 2k_i k_{scat.} \cos\theta_{scat.}} \tag{68}$$

$$\begin{aligned} \mathbf{k}_i &= \mathbf{k}_{scat.} + \mathbf{k}_{eject.} + \mathbf{p} \\ \mathbf{p} &= \mathbf{k}_i - \mathbf{k}_{scat.} - \mathbf{k}_{eject.} \\ \mathbf{p} &= \mathbf{q} - \mathbf{k}_{eject.} \end{aligned} \tag{69}$$

If $\mathbf{p}$ is the momentum of the residual ion and

$$E_i = E_{scat.} + E_{eject.} + E_{ion} + E_{excite} \tag{70}$$

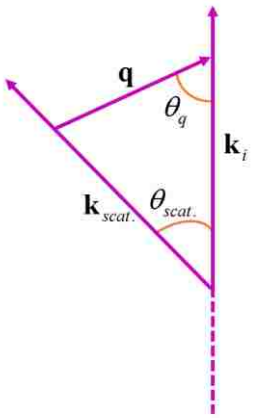

Figure 2.7. Schematic representation of the momentum transfer

where E_{ion} is the ionization energy and E_{excite} is the excitation energy from the ground state orbital to the excited state orbital. For example, the excitation energy from the H_2 ground state to the orbital state $2p\sigma_u$ is 18.1 eV, and the excitation energy to the $(2s\sigma_g + 2p\pi_u)$ state is 28.3 eV. That means the excitation-ionization energy ($E_{ion} + E_{excite}$) for the orbital state $2p\sigma_u$ is 37.1 eV, and for the orbital state $(2s\sigma_g + 2p\pi_u)$ is 40.3 eV.

2.2.2. Molecular 4-Body Distorted Wave. The QDCS (quadruple differential cross section) for excitation-ionization can be given by [5]

$$\frac{d^7\sigma}{d\Omega_{scat.}d\Omega_{ejec.}d\Omega_R dE_{ejec.}} = \frac{1}{(2\pi)^5}\frac{k_{scat.}k_{ejec.}}{k_i}\mu_{pa}\mu_{ie}\left|T_{fi}\right|^2 \tag{71}$$

where QDCS depends on the solid angles of the scattered and ejected electrons $(\Omega_{scat.}, \Omega_{ejec.})$, the solid angle of the aligned molecule Ω_R as show in figure (2.8), the ejected electron energy, and the excited state of the ion. In Eq. (56) μ_{pa} is the reduced mass of the projectile electron and molecule target H_2, and μ_{ie} is the reduced mass of the projectile electron and the residual ion H_2^+.

In the molecular 4 body Distorted wave (M4DW) approximation, the transition matrix T_{fi} is giving by

$$T_{fi} = \langle \chi^-_{scat.}(\mathbf{k}_{scat.}, \mathbf{r}_0)\, \chi^-_{ejec.}(\mathbf{k}_{ejec.}, \mathbf{r}_1)\, \phi^{Dy}_{ion}(\mathbf{r}_2, \mathbf{R})\, \mathrm{C}_{\text{scat.-ejec.}}(\mathbf{r}_{01}) \left|V_i - U_i\right| \psi_{\text{target}}(\mathbf{r}_1, \mathbf{r}_2, \mathbf{R})\, \chi^+_i(\mathbf{k}_i, \mathbf{r}_0)\rangle \tag{72}$$

Here $\chi^+_i, \chi^-_{scat.}$ and $\chi^-_{ejec.}$ are continuum state distorted wave functions for the incident, scattered, and ejected electrons with respective wave numbers $\mathbf{k}_i, \mathbf{k}_{scat.}$, and $\mathbf{k}_{ejec.}$. The "+" and "-" on the wavefunctions indicate outgoing and incoming wave boundary conditions. $\mathrm{C}_{\text{scat.-ejec.}}(\mathbf{r}_{01})$ is the Coulomb interaction between the scatted projectile and ejected electron. $\psi_{\text{target}}(\mathbf{r}_1, \mathbf{r}_2, \mathbf{R})$, and $\phi^{Dy}_{ion}(\mathbf{r}_2, \mathbf{R})$ are the ground state and excited state wave functions for the target molecule H_2 and residual ion wave function H_2^+ and $\mathbf{R}$ is the internuclear vector which determines the alignment of the molecule. Let's now look at the individual components of the T-matrix.

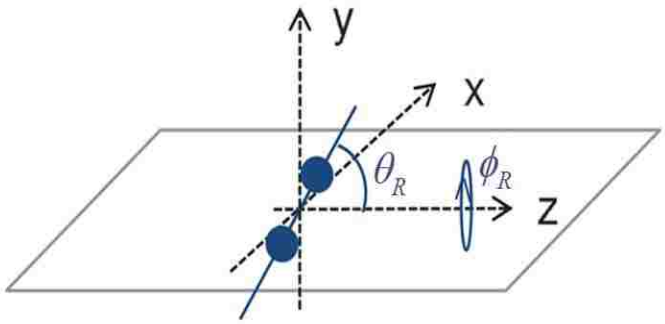

Figure 2.8. Shows the alignment of the molecular axis (θ_R, ϕ_R) for a diatomic molecule.

2.2.3. Ground State Wave Function for H_2. We have calculated the ground wave function for the H_2 molecule by using the variational method of Rosen [11].

We start with the Hamiltonian operator $\hat{\mathrm{H}}$ for an isolated H_2 molecule which is time independent (in atomic units) (see Fig.2.9 for the definition of coordinates)

$$\begin{aligned} H &= -\frac{1}{2}\nabla_1^2 - \frac{1}{2}\nabla_2^2 - \frac{1}{r_{A1}} - \frac{1}{r_{A2}} - \frac{1}{r_{B1}} - \frac{1}{r_{B2}} + \frac{1}{R} + \frac{1}{r_{12}} \\ &= -\frac{1}{2}\sum_{i=1}^{2}\nabla_i^2 - \sum_{i=1}^{2}\left(\frac{1}{r_{Ai}} + \frac{1}{r_{Bi}}\right) + \frac{1}{R} + \frac{1}{r_{12}} \end{aligned} \tag{73}$$

The first term in the Hamiltonian is sum in the kinetic energy for two electrons (we assume that the nuclei are stationary), the second term is the sum of the potential energy for the attraction between the electrons and nucleus, and the third term is the nuclear repulsion potential $\mathrm{V}_{NN} = \frac{1}{R}$ where R is the internuclear distance. Finally the last term is the potential energy of the two repulsive electrons.

The ground state wave function can be expressed as a product of a spatial part and a spin part

$$\psi(x, y, z) = \phi(x, y, z)\zeta(m_s) \tag{74}$$

Now the Hamiltonian operator has no effect on the spin function $\zeta(m_s)$

$$\hat{H}\psi(x, y, z) = \hat{H}\left[\phi(x, y, z)\zeta(m_s)\right] = \zeta(m_s)\hat{H}\phi(x, y, z) = E\left[\phi(x, y, z)\zeta(m_s)\right] \tag{75}$$

So, we get the same energies without spin. The only difference spin makes is to double the possible number of states. [12]

Denote the two nuclei for the H_2 molecule as A and B, and (r_{A1}, r_{B2}) as the distance of electrons 1 and 2 from the nuclei as shown in Fig. 2.9.

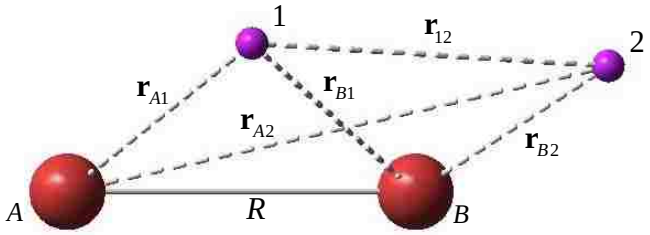

Figure 2.9. Coordinates used in the Rosen wave function

when $R = 0$, the molecule becomes a helium He atom. Following Rosen, we approximate the ground state wavefunction for the target $\psi_{\text{target}}(\mathbf{r}_1, \mathbf{r}_2)$ as

$$\psi_{\text{target}}(\mathbf{r}_1, \mathbf{r}_2) = N\left[\phi_{A1}(\mathbf{r}_{A1})\phi_{B2}(\mathbf{r}_{B2}) + \phi_{A2}(\mathbf{r}_{A2})\phi_{B1}(\mathbf{r}_{B1})\right] \tag{76}$$

Where ϕ_{A1} is a trial wave function which is expressed as a linear combination of a 1s and 2pz wave function.

$$\phi_{A1}(\mathbf{r}_{A1}) = N_0\left\{\phi_{1s}(\mathbf{r}_{A1}) + \sigma\,\phi_{2pz}(\mathbf{r}_{A1})\right\} \tag{77}$$

$$\phi_{B1}(\mathbf{r}_{A1}) = N_0\left\{\phi_{1s}(\mathbf{r}_{B1}) + \sigma\,\phi_{2pz}(\mathbf{r}_{B1})\right\} \tag{78}$$

Here σ is a parameter to minimize the energy and we have reproduced the value Rosen paper. The normalization factors are derived in Appendix A.

2.2.4. Excited State Wave Function for H_2^+ Ion. After the collision, one of the atomic electrons is ionized and other atomic electrons is left in an excited state of the H_2^+ ion. So, the Hamiltonian for H_2^+ (two protons separated by a distance R and a single electron) is given by

$$H = -\frac{1}{2}\nabla_1^2 - \frac{1}{r_{A1}} - \frac{1}{r_{B1}} + \frac{1}{R} \tag{79}$$

In this case, we don't have the mutual repulsion of the electrons. We use a Dyson orbital for the excited states ($2s\sigma_g, 2p\sigma_u,$ and $2p\pi_u$) which is provided by Chuangang Ning from

Tsinghua University, in Beijing, China. The Dyson orbital wave function is expressed as a linear combination of primitive Gaussian-type functions.

$$\psi(r,\theta,\varphi)=\sum_{i=1}^{2}\sum_{j=1}^{16}C_{ij}N_{ij}\ r_i^{n-1}\ e^{-\alpha_{ij}r_i^2}\ Y_{lm}^{R}(\theta,\varphi) \tag{80}$$

and real spherical harmonic functions $Y_{lm}^{R}(\theta,\varphi)$ are used. The radial part doesn't depend on the magnetic quantum number m

$$R_{nl}(r)=\sum_{i=1}^{2}\sum_{j=1}^{16}C_{ij}N_{ij}\ r_i^{n-1}\ e^{-\alpha_{ij}r_i^2} \tag{81}$$

Here C_{ij} and α_{ij} are parameters for the Gaussian wave function which are calculated by Ning. N_{ij} is the normalization constant for the Gaussian type orbitals (GTO). We assume the molecule lies along z-axis as shown in the Figure 2.10

The molecular coordinates are defined as follows

$$r_1=\sqrt{x^2+y^2+(z-R/2)^2} \qquad r_2=\sqrt{x^2+y^2+(z+R/2)^2} \tag{82}$$

$$\begin{aligned} \cos\theta_1&=\frac{z_1}{r_1}=\frac{z-R/2}{r_1} & \tan\varphi&=\frac{y_1}{x_1}=\frac{y}{x}\\ \cos\theta_2&=\frac{z_2}{r_2}=\frac{z+R/2}{r_2} & \tan\varphi&=\frac{y_2}{x_2}=\frac{y}{x} \end{aligned} \tag{83}$$

The normalization factor for each GTO is given by

$$N_{ij}=\sqrt{\left(\frac{2(2\alpha_{ij})^{n+1/2}}{\Gamma(n+1/2)}\right)} \tag{84}$$

The real spherical harmonic functions are given by

$$Y_{lm}^{R}(\theta,\varphi)=\sqrt{\frac{(2l+1)(l-m)!}{4\pi(l-m)!}}P_l^m(\theta)\phi_m(\varphi) \tag{85}$$

$$\phi_m(\varphi)=\begin{cases}\sqrt{2}\cos m\varphi & m>0\\ \sqrt{2}\,\mathrm{sim}|m|\varphi & m<0\\ 1 & m=0\end{cases} \tag{86}$$

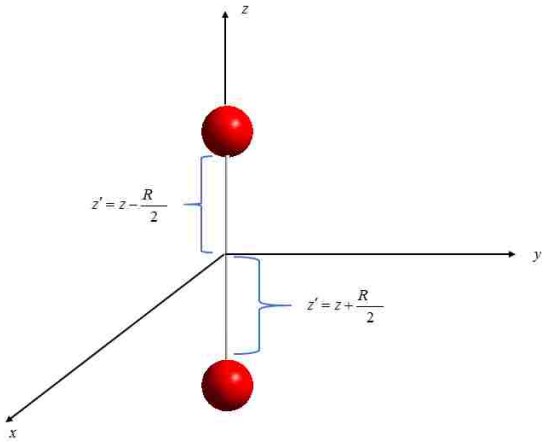

Figure 2.10. The diagram shows the molecule lying along z-axis.

2.2.5. Molecular States of H_2. We have studied four orbital states for the hydrogen molecule ($1s\sigma_g$, $2s\sigma_g$, $2p\sigma_u$, and $2p\pi_u$). There are two possible angular momentum projection states $|m|=0$ and $|m|=1$. The Greek letter σ corresponds to $|m|=0$ and π corresponds to $|m|=1$. The electronic wave functions can be classified as either even parity or odd parity. For even parity states, we use the subscript g (from the German word gerade, meaning even); and for odd parity states, we use u (from ungerade meaning odd). The Spatial electronic wave function $1s\sigma_g$ orbital is bonding and $1s\sigma^*_u$ orbital is antibonding.

All the excited states of H_2^+ will immediately dissociate. The dissociation energy D_e is the energy required to separate a molecule into atoms. Let's consider the dissociation energy for a diatomic moleculur bound electronic state. Figure 2.11 shows the potential energy as a function of internuclear distance. In the figure, R_e is the equilibrium internuclear distance, and as R goes to zero, the potential energy goes to infinity. The difference between the potential energy at $R=\infty$ and the potential energy at equilibrium is the equilibrium dissociation energy [12]

$$D_e \equiv U(\infty) - U(R_e) \tag{87}$$

The dissociation energy for the ground vibrational state is $D_0 \approx D_e - \frac{1}{2}h\upsilon$ where $\frac{1}{2}h\upsilon$ is the zero-point energy

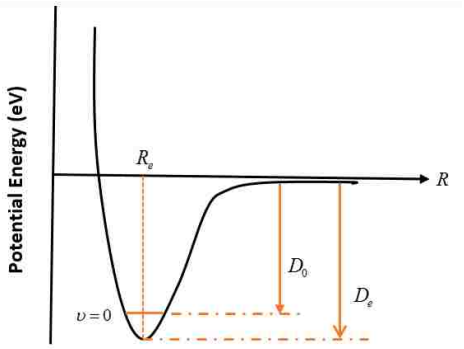

Figure 2.11. Schematic diagram showing the dissociation energy

PAPER

I- Triply differential (e,2e) studies of phenol

G. B. da Silva,[1, 2] R. F. C. Neves,[1, 3, 4] L. Chiari,[1,a)] D. B. Jones,[1] E. Ali,[5] D. H. Madison,[5] C. G. Ning,[6] K. L. Nixon,[4] M. C. A. Lopes, [4] and M. J. Brunger[1, 7, b)]

[1]*School of Chemical and Physical Sciences, Flinders University, GPO Box 2100,Adelaide, South Australia 5001, Australia*

[2]*Universidade Federal de Mato Grosso, Barra do Garças, MT 78600-000, Brazil*

[3]*Instituto Federal do Sul de Minas Gerais, Câmpus Poços de Caldas, MG, Brazil*

[4]*Departamento de Física, UFJF, Juiz de Fora, 36036-330, MG, Brazil*

[5]*Department of Physics, Missouri University of Science and Technology, Rolla, Missouri 65409, USA*

[6]*Department of Physics, State Key Laboratory of Low-Dimensional Quantum Physics, Tsinghua University, Beijing 100084, China.*

[7]*Institute of Mathematical Sciences, University of Malaya, 50603 Kuala Lumpur, Malaysia*

(Received 7 August 2014; accepted 8 September 2014; published online 24 September 2014)

We have measured (e,2e) triple differential cross sections (TDCS) for the electron-impact ionisation of phenol with coplanar asymmetrical kinematics for an incident electron energy of 250 eV. Experimental measurements of the angular distribution of the slow outgoing electrons at 20 eV are obtained when the incident electron scatters through angles of -5°, -10°, and -15°, respectively. The TDCS data are compared with calculations performed within the molecular 3-body distorted wave model. In this case, a mixed level of agreement, that was dependent on the kinematical condition being probed, was observed between the theoretical and experimental results in the binary peak region. The experimental intensity of the recoil features under all kinematical conditions was relatively small, but was still largely underestimated by the theoretical calculations. [http://dx.doi.org/10.1063/1.4896072]

I. INTRODUCTION

Electron-impact ionisation of atoms and molecules is a fundamental process which is relevant to understand and interpret a wide range of scientific phenomenon and technological applications, including plasma physics,[1] planetary atmospheres,[2] and radiation-interactions with living tissue.[3] With the exception of the simpler atomic species,[4] the mechanisms of how low- and intermediate-energy electrons ionise atoms and molecules are still not particularly well understood. Measurements of triple differential cross sections (TDCS) for electron impact ionisation of atoms and molecules, using so-called (e,2e) experiments, represent an ideal testing ground to assess the reliability and limitations of theoretical models aimed at describing the ionisation process. In (e,2e) experiments, an electron with well-defined energy and momentum ionises an atomic or molecular target, with the two outgoing electrons being detected in time coincidence. As both the energies and momenta of the two-outgoing electrons are determined in the experiment, a kinematically complete picture of the ionisation process is obtained.

Recently, the dynamical (e,2e) approach has received renewed attention through its ability to provide essential molecular scattering data that can assist in understanding and quantifying the effects of ionisation-related radiation damage in living tissues.[5, 6] It is now well established that a single high-energy ionising particle can liberate large numbers of low-energy secondary electrons that deposit energy as they thermalise in living tissue. In addition to the primary ionising particles (e.g., photons, protons, positrons), these low-energy electrons may also induce cell damage.[7] Thus, the way in which those electrons ionise atoms and molecules is, while being only one component in a complex picture, essential to understand the radiation induced damage. The fundamental atomic and molecular physics scattering data, obtained from experiment and theory, is now being exploited to develop sophisticated charged-particle simulation codes that will be essential for describing charged particle transport in the biological media.[8]

The successful approach of employing electron scattering data in characterising radiation-induced damage within biological systems can be equally applied to other physical systems. One such system is the treatment of biomass by atmospheric pressure plasmas.[9-12] Here, free-electrons or radicals produced within plasmas have the potential to overcome the natural resilience of biomass to degradation.[13,14] In particular, lignocellulose

may be broken down by electron impact to fermentable sugars, to intensify the enzymatic hydrolysis process, and improve bio-ethanol yields. However, to exploit charged-particle and plasma simulation of novel applications we require new and diverse sets of complete cross sections from prototypical molecules relevant to the application. Phenol (C_6H_5OH, see Fig. 1), has been identified as a potential target of electron-induced breakdown of lignin (a phenolic based species). Specifically, phenol is known to readily photo-dissociate through conical intersections.[15, 16] This has prompted recent theoretical and experimental investigations into electron-driven interactions with phenol[17,18] (and references therein) as a prototypical subunit of lignin. Electron-impact ionisation is also a potential strategy for biomass degradation, and makes the investigation into the dynamics of electron-impact ionisation of phenol relevant for some processes related to biofuel production.

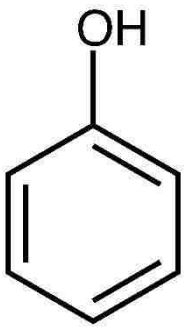

FIG. 1. A schematic representation for the structure of phenol.

To utilise collision cross sections in simulations, the data must adequately describe the physical processes over the complete and diverse range of kinematical conditions relevant to the process.[5,6] Unfortunately, our capability for obtaining experimental cross-sections over such a vast range of kinematics is quite limited owing to long experimental run times. This generates a pressing demand for new theoretical models that are able to accurately and efficiently compute those complete cross-section sets. The role of experiments is therefore to provide definitive tests to validate, or at least understand the limitations of, theoretical models.

In the present investigation, we utilise an (e,2e) technique to investigate the dynamics of electron impact ionization of phenol. These experiments are compared to

theoretical calculations obtained within a molecular 3-body distorted wave (M3DW) framework. Note that the M3DW approach has been demonstrated to be quite successful in reproducing collision cross section data for the low and intermediate-energy electron impact ionisation of atoms and molecules.[19] The present work extends our previous results for molecules of some biological interest, such as pyrimidine,[20] tetrahydrofuryl alcohol (THFA),[21,22] tetrahydrofuran (THF),[22,23] 1,4-dioxane,[23,24] and tetrahydropyran (THP).[24]

The structure of the present paper is as follows. In Sec. II, we discuss our experimental techniques and analysis procedures, while in Sec. III a brief description is provided in regard to the present computations. Thereafter, in Sec. IV, our results and a discussion of those results is presented, before some conclusions from the current investigation are drawn.

II. EXPERIMENTAL METHOD

We have used an (e,2e) coincidence technique, under coplanar asymmetric kinematical conditions, to obtain a selection of triple differential cross sections for electron-impact ionisation of phenol. A detailed description of the employed method can be found elsewhere.[20-24] Briefly, however, a well-collimated beam of electrons with energy $E_0 = 250$ eV collide with gaseous phenol at low pressure, with some electrons ionising the phenol target to yield two-outgoing electrons. The present high-purity sample of phenol was sourced from Ajax Unilab (assay > 99%), and is a solid at room temperature. Nonetheless, it readily sublimes under vacuum. To assist in producing a stable beam of phenol, the sample was heated to a modest temperature of 40-45^o C. Phenol-vapour was then introduced into the interaction region through a needle, with the flow rate being controlled by a variable leak valve. Note that our chamber and gas handling lines were heated to slightly higher temperatures to prevent the formation of phenol deposits within the chamber.

In the present asymmetrical kinematics of our experiments, we detect a fast electron with energy E_a, commonly referred to as the scattered electron, and a slow electron with energy E_b, usually referred to as the ejected electron, although of course the electrons are actually indistinguishable. Here, the scattered and ejected electrons are detected at angles referenced to the incident beam direction, θ_a and θ_b, respectively. In our experiment, a time

coincident technique is used to ensure that both electrons originated from the same ionisation event. The energy required to ionise the electron bound to phenol ε_i can then be determined through the conservation of energy,

$$\varepsilon_i = E_0 - E_b - E_a \quad (1)$$

Note that by keeping the incident electron and slow ejected electron energies fixed, binding energy spectra (BES) can be obtained by recording the number of true coincident events as the scattered electron energy is varied. The BES of phenol, measured with scattered and ejected electron angles of $\theta_a = -10^o$ and $\theta_b = 75^o$, respectively, is presented in Fig. 2. Note that the orbital assignments presented in Fig. 2 are taken from Kishimoto *et al*.,[25] and are supported by our own quantum chemistry calculations conducted as a part of this study (see later). Good qualitative agreement between the present BES, over the range of binding energies $\varepsilon_i \sim$ 7-16.5 eV, and the earlier He I ultraviolet photoelectron spectra (UPS) study of Kishimoto *et al*.[25] was found, although the superior energy resolution of the UPS technique ensured that more orbital-based features could be resolved. The coincidence energy resolution in the present measurements was estimated to be 1.1 eV (FWHM), while the Gaussian functions employed in our least-squares spectral deconvolution fit of the BES, as represented by the short-dashed curves (again see Fig. 2), possessed widths that were a convolution of the (e,2e) coincidence energy resolution and the natural widths of the various orbital manifolds, as taken from the UPS spectrum. The overall fit (solid line) to the coincidence data in our BES is seen to be very good, and clearly defines the unresolved highest-occupied molecular orbital (HOMO, $4a''$) and next highest-occupied molecular orbital (NHOMO, $3a''$) to be at $\varepsilon_i \sim$ 9 eV.

TDCS describing the angular distribution of the ejected electron E_b = 20 eV are obtained for the electron impact ionisation of the unresolved combination of the HOMO and NHOMO of phenol ($\varepsilon_i \sim$ 9 eV) when the scattered electrons were detected at fixed polar angles of $\theta_a = -5^o$, -10°, and -15°. For each angular position of the scattered electron analyser, the number of true coincident counts was recorded when the slow electron was detected in the angular ranges from θ_b = 55° to 120°, and from θ_b = 240° to 285°. Those

angular ranges encompass the so-called binary and recoil peak regions, respectively. Note that the angular range of our ejected electrons is largely limited by the considerable physical dimensions of the analysers. The kinematical conditions for this study were chosen to study ionisation dynamics at the bound Bethe-Ridge and below. The bound Bethe-Ridge is sometimes referred to as an ideal collision, where the recoil ion acts like a spectator (and so does not take any momentum). It happens exactly when the magnitude of the momentum transfer $|\mathbf{k}|$ is equal to that for the ejected electron $|\mathbf{k}_b|$. Here, the momentum transfer is defined as:

$$\mathbf{k} = \mathbf{k}_0 - \mathbf{k}_a \tag{2}$$

where $\mathbf{k}_0$ and $\mathbf{k}_a$ are the incident and scattered electron momenta, respectively. When the slow electron is ejected in a direction close to that of $\mathbf{k}$, it absorbs most of the momentum transferred in the collision, and the collision is said to be binary. Conversely, when the slow electron is directed in the direction anti-parallel to that of the momentum transfer, the ion possess substantial momentum and the collisions are said to be recoil in nature. The relative intensity of the TDCS in the binary and recoil regions therefore contain signatures relating to the dynamics of the ionisation process.[20-24]

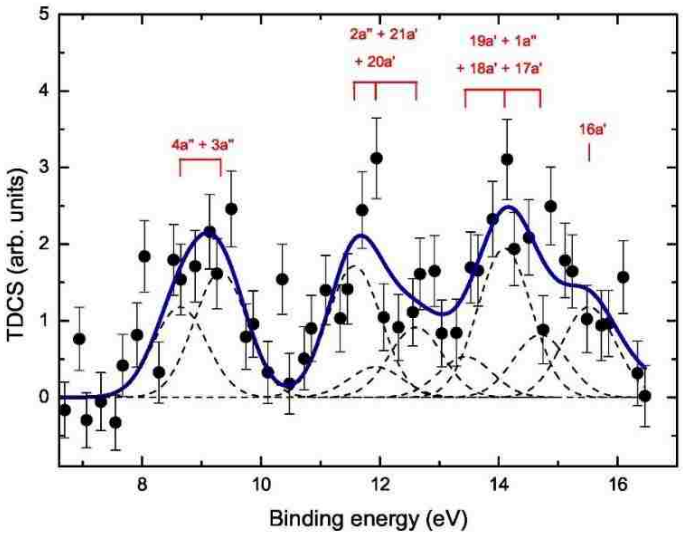

FIG. 2. Measured binding energy spectrum of phenol (•) obtained for an incident energy of 250 eV, and scattered and ejected electron detection angles of θ_a =-10° and θ_b = 75°, respectively. Also shown are the spectral deconvolutions of the measured spectra into contributions from each orbital feature (– –) and their sum (—). See text for further details.

III. THEORY

The theoretical results were calculated using the molecular three-body distorted wave approximation, coupled with an orientation-averaged molecular orbital (OAMO) approximation, and either an approximate or exact description of the post-collision interaction (PCI).[19] The direct-scattering T-matrix integral in this formalism is given by:

$$T_{dir} = \left\langle \underbrace{\chi_a^-(k_a, r_1)\chi_b^-(k_b, r_2)C_{scat-eject}(r_{12})}_{Final\ \text{state}} \middle| \frac{1}{r_{12}} - U_a(r_1) \middle| \underbrace{\phi_{DY}^{OA}(r_2)\chi_a^+(k_0, r_1)}_{Initial\ \text{state}} \right\rangle \qquad (3)$$

In this approach, the initial state consists of the incident distorted wave $\chi_a^+(k_0, r_1)$ and the orientation averaged Dyson orbital $\phi_{DY}^{OA}(r_2)$. This Dyson orbital defines the overlap of the many-electron wave functions of the initial and ionised states of the system, and can be approximated by the ionised Kohn- Sham orbitals under a frozen-core approach. The molecular wave functions were calculated using density functional theory (DFT), along with the standard hybrid B3LYP functional,[26] using ADF 2007 (the Amsterdam Density Functional program[27]) with a TZ2P (triple-zeta with two polarisation functions) Slater-type basis set. These orbitals were averaged over all molecular orientations within the so-called OAMO approach.[28] The potential U_a represents the spherically symmetric interaction between the projectile and the active electron, and r_{12} is the relative distance between the outgoing electrons. The final state consists of distorted waves $\chi_a^-(k_a, r_1)$ and $\chi_b^-(k_b, r_2)$ for the outgoing electrons multiplied by $C_{scat-eject}(r_{12})$, that is, a factor that describes the Coulomb interaction between the ejected and scattered electrons. The Coulomb interaction between those two electrons can be expressed as a product of a gamma (Γ) function and a confluent hypergeometric function ${}_1F_1$:

$$C_{scat-eject} = e^{\pi\gamma/2}\Gamma(1-i\gamma)\,{}_1F_1(i\gamma, 1, -i(k_{12}r_{12} + \mathbf{k}_{12}\bullet\mathbf{r}_{12})) \qquad (4)$$

In Eq. (4), $k_{12} = \mu v_{12}$, where μ is the reduced mass for two electrons, v_{12} is the relative velocity between them, and γ is the Sommerfeld parameter ($\gamma = 1/v_{12}$) that determines the strength of the interaction.

If one uses the Coulomb interaction as presented above, a numerical 6D integral is required to evaluate the T-matrix, demanding long computational times especially for large molecules. The difficulty arises from the hypergeometric function that cannot be factored out from the integral without appropriate simplification. Some authors have suggested that the PCI might be overestimated at lower energies,[19] and that the approximation given by Ward and Macek[29] for low energies can provide accurate results. In that approximation, r_{12} is replaced by an average value that is parallel to k_{12}. This simplifies the numerical calculation significantly, since the Coulomb interaction can now be factored from the T-matrix integral. Another further simplification can be made by just neglecting the hypergeometric function,[30,31] so approximating $\left|C_{scat-eject}\right|^2$ to the Gamow factor that is defined as:

$$N_{ee} = \left|e^{-\pi\gamma/2}\Gamma(1-i\gamma)\right|^2 . \tag{5}$$

The final TDCS cross-section is calculated using the direct and exchange-scattering amplitudes as follows:

$$\frac{d\sigma}{d\Omega_a d\Omega_b dE_b} = \frac{1}{(2\pi)^5}\frac{k_a k_b}{k_0}\left(\left|T_{dir}\right|^2 + \left|T_{exc}\right|^2 + \left|T_{dir} - T_{exc}\right|^2\right), \tag{6}$$

where T_{exc} is the exchange-scattering T-matrix that is calculated similar to T_{dir}, except that the particles 1 and 2 are interchanged in the final state.

In this work, the TDCS for single electron-impact ionisation of phenol was obtained using the M3DW approach with the Coulomb interaction treated either exactly, or approximated using the Ward-Macek approximation, or approximated by neglecting the hypergeometric function which is referred to as the Gamow approximation. In order to determine the importance of PCI, we also perform calculations, designated DWBA, that do not incorporate any postcollisional Coulomb interaction.

To assist in the interpretation of the present BES and TDCS results, quantum chemical calculations on phenol were also performed at the B3LYP/aug-cc-pVDZ level in GAUSSIAN09.[32] These calculations were employed to assist us in our orbital assignments and to derive orbital momentum profiles for the unresolved HOMO ($4a''$) and NHOMO (

$3a''$) studied experimentally. Those momentum profiles were calculated using the HEMS program described in Cook and Brion.[33]

IV. RESULTS AND DISCUSSION

Figure 3 shows the present triple differential crosssection angular distributions of the ejected electron produced in the ionisation of the HOMO+NHOMO of phenol, in the three asymmetric coplanar kinematical conditions for the scattered electron angles θ_a = -5°,-10°, and -15°. The data were taken as a function of the ejected electron angle, in the scattering plane, using E_0 = 250 eV and E_b = 20 eV. Momentum profiles for the ionised HOMO+NHOMO (π3 and π2) MOs are also presented in Fig. 4. In both the HOMO and the NHOMO, the ionised orbitals are dominated by out-of plane delocalised π orbitals, specifically by C(2p) and O(2p) electrons. The dominant "p-like" character of the ionised orbitals is clearly evident from the momentum profile, with a minimum at 0 a.u. Here, we note that under the present kinematical conditions, with intermediate to small incident and outgoing electron energies and a small momentum transferred to the target, the recoil momentum of the ion ($\mathbf{q}$), to conserve momentum, is not equal in magnitude and opposite in sign to the target electron's momentum at the instant of ionisation (as in electron momentum spectroscopy[34]). However, the momentum profiles should still provide clues to the observed experimental behaviour. For this purpose, in Fig. 4, we also show arrows that detail the region of recoil momentum covered, when the fast electron is detected at the specific scattering angles covered in our experiments.

The present experiments are obtained in a relative fashion, owing to the complexity and long experimental runtimes required to inter-normalize or place on an absolute scale.[35] We are therefore limited to assessing the angular distribution of the slow ejected electron for each scattering angle. From the theoretical perspective, the inclusion of different PCI models influences the absolute magnitude of the result. Thus, in order to assess the shapes of each calculation in reproducing the experimental data, we normalize all experimental and theoretical results to unity at a single point. The absolute numbers from our calculations are available on request.

Fig. 3 shows a varying level of agreement between the experimental data and the cross-section calculations. These variations are strongly dependant on the kinematical

condition in question. We begin by discussing the behaviour observed in the binary region. For θ_a = -5°, we observe excellent agreement in terms of the shape between the distorted wave calculations and the experimental measurement. This result is somewhat surprising in that previously the distorted wave calculations have failed to reproduce the experimental width of the binary feature of other molecular targets[20-24] under this same kinematical condition. However, when we consider the binary regions for the other kinematical conditions of θ_a =-10° or -15°, we see substantial differences between the experimental data and the distorted wave calculations.

Here, we note that all our theoretical calculations are largely consistent with one another, which suggests we rule out PCI effects as the origin of the observed discrepancies. The angular distribution for θ_a =-15° displays a deep minimum in the vicinity of the momentum transfer direction. This minimum is characteristic of the strong p-like character of the ionised orbital. Interestingly, the distorted wave calculations give maxima in the vicinity of the momentum transfer for both θ_a = -10° and -15°. This behaviour was noted in our previous investigations, however it was somewhat mitigated by the s-type or sp-hybrid nature of the orbitals ionised in those investigations. For phenol, where the HOMO+NHOMO is dominated by out-of-plane atomic 2p contributions, the failure of the orientation averaging approach becomes inherently obvious for the θ_a = -10° and -15° conditions. Indeed, we note that the orientation averaging approach is known to be problematic for the asymmetric p-like orbital contributions.[36] In a recent publication by Chaluvadi *et al.*,[37] the OAMO approximation was replaced by a proper average over orientation dependent cross sections and much better agreement with experiment was found for methane. Trial calculations have indicated that there is a high probability that, for p-type states, the proper average method will produce a split binary peak similar to that observed in the experimental data. Unfortunately, these proper average calculations are so computationally expensive that they can only run on very large computing clusters, such as the US Extreme Science and Engineering Discovery Environment (XSEDE). We currently have a pending proposal requesting time on the XSEDE clusters to calculate proper average cross sections for some of these large molecules that have been measured

at Flinders.[20-24] Overall, the effects of PCI are quite small with the largest difference found for θ_a=-10°. Interestingly, for all three measured cases, the Gamow approximation gives results that are slightly closer to experiment than the other two treatments.

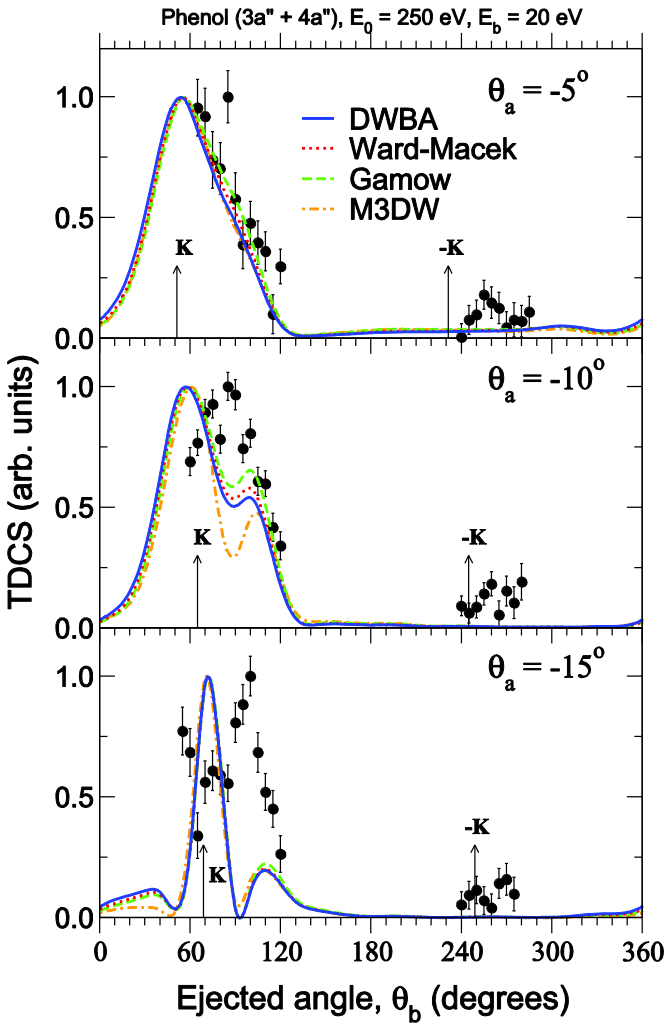

FIG. 3. TDCS for electron impact ionisation of the HOMO and NHOMO of phenol $(4a''+3a'')$ with E_0 = 250 eV, E_b = 20 eV and transferred momenta of 0.45 a.u. ($\theta_a = -5^O$), 0.77 a.u. (θ_a = −10°), and 1.12 a.u. (θ_a = −15°), respectively. The M3DW calculation results with the Coulomb interaction treated exactly (M3DW) and approximately are compared to the experimental results (•). The arrows represent the directions parallel (**K**) and anti-parallel (–**K**) to the transferred momentum.

Now we turn our attention to the recoil region. Here, the calculated TDCS underestimates the strength of the measured TDCS in the recoil region for all conditions.

This observation is consistent with previous studies employing the same theoretical approach for other molecular targets,[20-24] where the calculation persistently underestimates the strength of the TDCS in the recoil region. However, this observation is somewhat tempered for the HOMO+NHOMO of phenol by the absence of any significant recoil peak intensity across the range of kinematical conditions studied. We do, however, note that at θ_a = -5°, there is experimental evidence of a peak centred on $\theta_b \sim 260°$ (see Fig. 3). Here, all theoretical methods support the existence of a recoil feature, as all of the methods give rise to a small peak centred in the vicinity of $\theta_b \sim 300°$. The absence of any substantial experimental recoil peak intensity is particularly notable for the phenol target. In our earlier investigations on other molecular targets, conducted under similar kinematical conditions, prominent recoil peak intensities have been observed (especially for θ_a = -5°). Previously, Xu *et al*.[38] have commented that the strength of the recoil peak intensity could be related to the orbital momentum profile. In that work, they stated that the p-like profile, having a reduced binary maximum, may exhibit a larger recoil peak, relatively speaking. Based on these assumptions, one may therefore expect significant recoil peak intensity for the unresolved HOMO and NHOMO of phenol, being dominated by p-type orbital contributions. However, this is clearly not the case. One possible explanation for this behaviour is the nature of the ionised orbital. In this case, we note that the HOMO+NHOMO of phenol are both diffuse π-bonding orbitals. This differs significantly from the orbitals of THF, THFA, THP, and 1,4-dioxane studied in our earlier investigations,[20-24] where the ionised orbitals were dominated by O(2p) lone electron pairs that are centralised on the oxygen atom, which then couple to the carbon σ-frame. In phenol, the delocalisation of the orbital over the entire molecule may reduce electron-interactions with the nuclei that are classically required for recoil scattering. However, this notion requires detailed theoretical investigation before definitive conclusions can be deduced. From the theoretical perspective, the absence of recoil intensity in the M3DWframework may be explained by the absence of nuclear charge at the centre of mass. Here, the nuclear charge is re-distributed over spherical shells that are known to reduce the distortion experienced by the outgoing electron.[39]

The present investigation, together with our earlier studies, suggest that the dynamics of the ionisation process is governed by a multitude of factors, relating to both the nature of the ionised orbital and how that orbital interacts with localized nuclei. Indeed, computationally demanding proper-averaged calculations[37] may be required to shed further light into these issues.

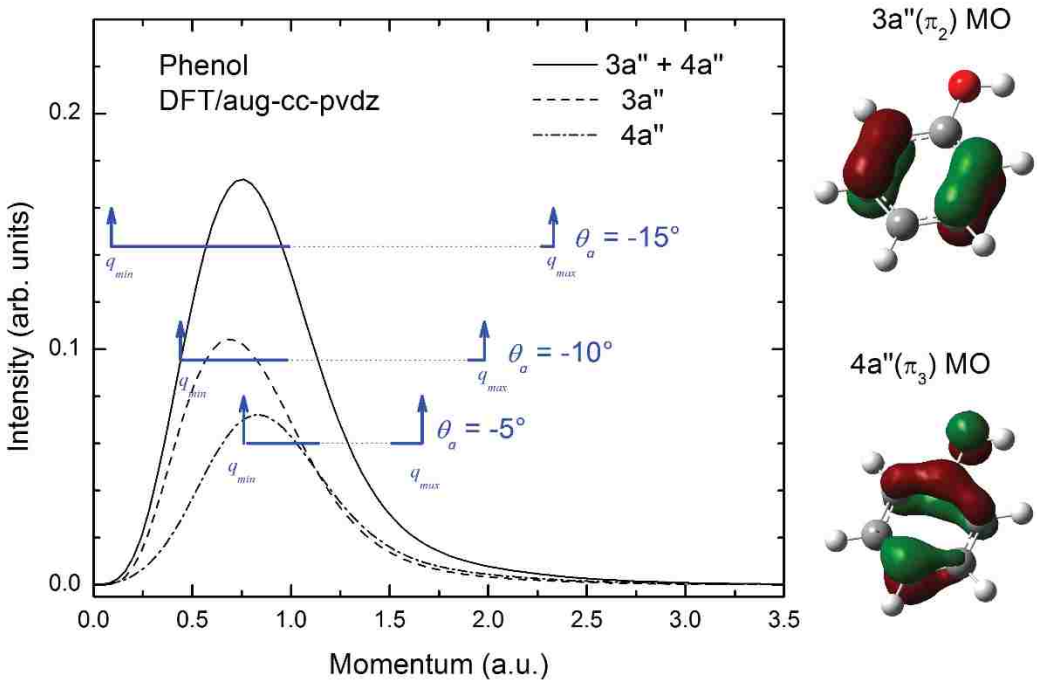

FIG. 4. Momentum profiles of the $4a''$ HOMO, $3a''$ NHOMO, and the sum $4a''+3a''$ of phenol. The arrows indicate the accessible range of recoil momentum values covered in the kinematical conditions of our experiment. Also shown are diagrammatic representations of the HOMO and NHOMO orbitals. See text for further details.

V. CONCLUSIONS

We have presented experimental and theoretical TDCS results for phenol. The approach used in the theoretical calculations of the TDCS was the M3DW, coupled with an orientation-averaged molecular orbital approximation, and with PCI treated either exactly or approximately. The TDCS data for the electron-impact ionisation of phenol were obtained under coplanar asymmetrical kinematics with incident energy of 250 eV. Here, the kinematical configurations were chosen to correspond to the region near the bound Bethe- Ridge. The experimental data were taken on the $4a''$ and $3a''$ orbitals, that

unfortunately could not be resolved, given our coincidence energy resolution. The level of agreement between the calculations and experimental data was strongly dependent on the kinematical configurations investigated in this work, being much better at smaller momentum transfer. The theoretical calculations further suggest that PCI is not necessarily playing an important role under these kinematical conditions and may be neglected in the first instance. The more important approximation is the OAMO and we expect that the properly averaged cross sections will be in better accord with experiment. We will perform the proper average cross sections as soon as we can obtain the necessary computational resources.

ACKNOWLEDGMENTS

This research was supported by the Australian Research Council (ARC) Centre of Excellence for Antimatter-Matter Studies, by the U.S. National Science Foundation (NSF) under Grant. No. PHY-1068237 (E.A. and D.H.M.), and by the National Natural Science Foundation of China (NNSFC) under Grant No. 11174175 (C.G.N.). G.B.S. thanks the Brazilian government through CAPES (Proc. No. BEX 17756/12-0) and Flinders University for financial assistance during his stay in Australia. D.B.J. gratefully acknowledges support provided through an ARC Discovery Early Career Researcher Award. R.F.C.N. also acknowledges CNPq for financial support that enabled him to study in Australia. M.C.A.L. acknowledges financial support from CNPq. Finally, M.J.B. acknowledges CNPq for his "Special Visiting Professor" appointment.

[1]L. G. Christophorou and J. K. Olthoff, *Fundamental Electron Interactions with Plasma Processing Gases* (Kluwer Academic, New York, 2004).

[2]L. Campbell and M. J. Brunger, Plasma Sources Sci. Technol. **22**, 013002 (2013).

[3]B. Boudaiffa, P. Cloutier, D. Hunting, M. A. Huels, and L. Sanche, Science **287**, 1658 (2000).

[4]I. Bray, D. Fursa, A. Kadyrov, A. Stelbovics, A. Kheifets, and A. Mukhamedzhanov, Phys. Rep. **520**, 135 (2012).

[5]A. G. Sanz, M. C. Fuss, A. Muñoz, F. Blanco, P. Limão-Vieira, M. J. Brunger, S. J. Buckman, and G. García, Int. J. Radiat. Biol. **88**, 71 (2012).

[6]R. D. White, W. Tattersall, G. Boyle, R. E. Robson, S. Dujko, Z. Lj. Petrovic, A. Bankovic, M. J. Brunger, J. P. Sullivan, S. J. Buckman, and G. Garcia, Appl. Radiat. Isot. **83**, 77 (2014).

[7]L. Sanche, Eur. Phys. J. D **35**, 367 (2005).

[8]H. Nikjoo, P. O'Neill, M. Terrissol, and D. Goodhead, Radiat. Environ. Biophys. **38**, 31 (1999).

[9]N. Schultz-Jensen, Z. Kádár, A. B. Thomsen, H. Bindslev, and F. Leipold, Appl. Biochem. Biotechnol. **165**, 1010 (2011).

[10]L. Klarhöfer, W. Viöl, and W. Maus-Friedrichs, Holzforschung **64**, 331 (2010).

[11]J. A. Souza-Corrêa, M. A. Ridenti, C. Oliveira, S. R. Araújo, and J. Amorim, J. Phys. Chem. B **117**, 3110 (2013).

[12]J. Amorim, C. Oliveira, J. A. Souza-Corrêa, and M. A. Ridenti, Plasma Process. Polym. **10**, 670 (2013).

[13]A. J. Ragauskas, C. K. Williams, B. H. Davison, G. Britovsek, J. Cairney, C. A. Eckert, W. J. Frederick, J. P. Hallett, D. J. Leak, C. L. Liotta, J. R. Mielenz, R. Murphy, R. Templer, and T. Tschaplinski, Science **311**, 484 (2006).

[14]M. E. Himmel, S.-Y. Ding, D. K. Johnson, W. S. Adney, M. R. Nimlos, J. W. Brady, and T. D. Foust, Science **315**, 804 (2007).

[15]M. N. R. Ashfold, B. Cronin, A. L. Devine, R. N. Dixon, andM. G. D. Nix, Science **312**, 1637 (2006).

[16]O. P. J. Vieuxmaire, Z. Lan, A. L. Sobolewski, and W. Domcke, J. Chem. Phys. **129**, 224307 (2008).

[17]E. M. de Oliveira, S. d'A. Sanchez, M. H. F. Bettega, A. P. P. Natalense, M. A. P. Lima, and M. T. do N. Varella, Phys. Rev. A **86**, 020701(R) (2012).

[18]D. B. Jones, G. B. da Silva, R. F. C. Neves, H. V. Duque, L. Chiari, E. M. de Oliveira, M. C. A. Lopes, R. F. da Costa, M. T. do N. Varella, M. H. F. Bettega, M. A. P. Lima, and M. J. Brunger, J. Chem. Phys. **141**, 074314 (2014).

[19]D. H. Madison and O. Al-Hagan, J. At. Mol. Opt. Phys. **2010**, 367180 (2010).

[20]J. Builth-Williams, S. M. Bellm, D. B. Jones, H. Chaluvadi, D. Madison, C. G. Ning, B. Lohmann, and M. J. Brunger, J. Chem. Phys. **136**, 024304 (2012).

[21]S. M. Bellm, J. D. Builth-Williams, D. B. Jones, H. Chaluvadi, D. H.Madison, C. G. Ning, F. Wang, X. G. Ma, B. Lohmann, and M. J. Brunger, J. Chem. Phys. **136**, 244301 (2012).

[22]D. B. Jones, J. D. Builth-Williams, S. M. Bellm, L. Chiari, H. Chaluvadi, D. H. Madison, C. G. Ning, B. Lohmann, O. Ingólfsson, and M. J. Brunger, Chem. Phys. Lett. **572**, 32 (2013).

[23]J. D. Builth-Williams, S. M. Bellm, L. Chiari, P. A. Thorn, D. B. Jones, H. Chaluvadi, D. H. Madison, C. G. Ning, B. Lohmann, G. B. da Silva, and M. J. Brunger, J. Chem. Phys. **139**, 034306 (2013).

[24]J. D. Builth-Williams, G. B. da Silva, L. Chiari, D. B. Jones, H. Chaluvadi, D. H. Madison, and M. J. Brunger, J. Chem. Phys. **140**, 214312 (2014).

[25]N. Kishimoto, M. Furuhashi, and K. Ohno, J. Electron Spectrosc. Relat. Phenom. **113**, 35 (2000).

[26]C. Lee, W. Yang, and R. G. Parr, Phys. Rev. B **37**, 785 (1988).

[27]G. te Velde, E. Baerends, C. Fonseca Guerra, S. van Gisbergen, J. Snijders, and T. Ziegler, J. Comput. Chem. **22**, 931 (2001).

[28]J. F. Gao, D. H. Madison, and J. L. Peacher, J. Chem. Phys. **123**, 204314 (2005).

[29]S. J. Ward and J. H. Macek, Phys. Rev. A **49**, 1049 (1994).

[30]J. Botero and J. H. Macek, Phys. Rev. Lett. **68**, 576 (1992).

[31]C. T. Whelan, R. J. Allan, and H. R. Walters, J. Phys. IV France 3(C6), 39 (1993).

[32]M. J. Frisch, G. W. Trucks, H. B. Schlegel *et al*., Gaussian 09, Revision B.01 Gaussian, Inc., Wallington, CT, 2010.

[33]J. P. Cook and C. Brion, Chem. Phys. **69**, 339 (1982).

[34]E. Weigold and I. McCarthy, *Electron Momentum Spectroscopy* (Kluwer Academic, New York, 1999).

[35]L. R. Hargreaves, M. A. Stevenson, and B. Lohmann, Meas. Sci. Technol.21, 055112 (2010).

[36]J. F. Gao, J. L. Peacher, and D. H. Madison, J. Chem. Phys. **123**, 204302 (2005).

[37]H. Chaluvadi, C. G. Ning, and D. Madison, Phys. Rev. A **89**, 062712 (2014).

[38]S. Xu, X. Ma, S. Yan, and P. Zhang, J. Chem. Phys. **136**, 237101 (2012).

[39]I. Tóth and L. Nagy, J. Phys. B **43**, 135204 (2010).

II. Comparison of experimental and theoretical electron-impact ionization triple differential cross sections for ethane

Esam Ali[1*], Kate Nixon[2,3], Andrew Murray[2], Chuangang Ning[4], James Colgan[5] and Don Madison[1]

[1]Department of Physics, Missouri University of Science and Technology, Rolla Missouri 65409, USA

[2]Photon Science Institute, School of Physics & Astronomy, University of Manchester, Manchester M13 9PL, United Kingdom

[3]School of Biology, Chemistry and Forensic Science, University of Wolverhampton, Wolverhampton WVl lLY, United Kingdom

[4]Department of Physics, State Key Laboratory of Low-Dimensional Quantum Physics, Tsinghua University, Beijing 100084, China

[5]Theoretical Division, Los Alamos National Laboratory, Los Alamos, New Mexico 87545, USA

(Received 31 August 2015; published 30 October 2015)

We have recently examined electron-impact ionization of molecules that have one large atom at the center, surrounded by H nuclei (H_2O, NH_3, CH_4). All of these molecules have ten electrons, however they vary in their molecular symmetry. We found that the triple differential cross sections (TDCs) for the highest occupied molecular orbitals (HOMOs) were similar, as was the character of the HOMO orbitals which had a *p*-type "peanut" shape. In this work, we examine ethane (C_2H_6) which is a molecule that has two large atoms surrounded by H nuclei, so that its HOMO has a "double-peanut" shape. The experiment was performed using a coplanar symmetric geometry (equal final-state energies and angles). We find the TDCS for ethane is similar to the single-center molecules at higher energies, and is similar to a diatomic molecule at lower energies.

DOI: 10.1103/PhysRevA.92.042711

*Corresponding author: eaagx2@mst.edu

I. INTRODUCTION

Studies of electron impact ionization of atoms and molecules play an important role for understanding the dynamical collisions of few-body systems. For the most elementary three-body problems, namely electron-impact ionization of atomic hydrogen and helium, the convergent close-coupling (CCC) method [1], the time-dependent close-coupling (TDCC) method [2], and the exterior complex scaling (ECS) technique [3] provide essentially exact results. A similarly accurate theory is however lacking for the larger atoms and molecules. Very recently, the *b*-spline *R*-matrix with pseudostates (BSR) and three-body distorted wave (3DW) approaches were shown to yield very good agreement with relatively absolute (ratios of cross sections are absolute) 3 dimensional (3D) measurements for 64 eV electron-impact ionization of Ne [4].

The distorted wave approach is the most versatile theoretical method since it can be applied with equal ease to atoms and molecules, and the molecular three-body distorted wave (M3DW) approximation has been shown to give reasonably accurate results for ionization of several molecules.

There have been many high-energy studies of electron-impact ionization of molecules. These greatly enhance our understanding of molecular wave functions, since in the high-energy collisions the measured cross section is proportional to the momentum space wave function. More recently, low-energy studies from molecules have begun to be reported. These studies are much more difficult for theory, since the cross sections are strongly dependent on the dynamics of the ionizing interaction. Initial studies were for the ionization of simple diatomic and triatomic molecules such as H_2 [5-10], N_2 [11-14], N_2O [15], CO_2 [14, 16] and H_2O [17-19]. More recently larger molecular targets such as CH_4 [20-23], NH_3 [24], formic acid [25] and DNA analogs such as phenol, pyrimidine and tetrahydrofuran among others [26-32] have been studied. Our previous studies on the isoelectronic series of H_2O [18], NH_3 [24] and CH_4 [22,23] each containing ten electrons, have been particularly insightful as they were all conducted in a similar energy regime and under the same kinematics. This allowed us to observe trends in the data across the molecular series. Also, all of these molecules have a large nucleus at, or near, the center of mass (CM) that is surrounded by lighter H nuclei. By contrast the symmetry of the molecular frame is different in each case, i.e., H_2O is planar, NH_3 is pyramidal and CH_4 is

tetrahedral. At the low energies used in these studies, it is expected that the ionization process will be dominated by the dynamics of the collision. Indeed, the measured triple-differential cross sections (TDCSs) for all of these molecular targets were found to be similar. Notwithstanding this, the influence of the orbital character could still be observed in the measured TDCS. The measured cross sections were found to be similar when scattering from target orbitals of the same character, that is, having *s*-like or *p*-like character, regardless of the target. This observation implies that the spatial arrangement of the atoms, or molecular symmetry, does not have a large effect on the ionization dynamics. Further, it was observed that the theoretical predictions did not show this variation with orbital character, suggesting that they are not sensitive to the character of the orbital. One suggestion to explain this observation in the experimental data is that the H atoms are light and may not contribute much to the scattering mechanism. The purpose of this work is hence to examine a molecule with two large nuclei which are similarly surrounded by lighter nuclei, to ascertain if the cross sections are similar to molecules such as H_2O, CH_4 or NH_3, or if they are similar to those of diatomic molecules. We can also observe the trends in the theoretical predictions to ascertain if they are influenced by the quasidiatomic nature of such a molecule. For this study, we have chosen the ethane molecule (C_2H_6), which is a relatively small molecule that has two large carbon nuclei and six light hydrogen nuclei.

Figure 1 compares the HOMO Dyson orbital for C_2H_6 with that for NH_3 and CH_4, both of which have a single large atom near the CM. As can be seen, the HOMO orbitals for these molecules are both *p*-type, showing a characteristic "peanut" shape. Also shown is the next highest-occupied molecular orbital (NHOMO) for the diatomic molecule N_2, since it also has this shape. While the orbitals for NH_3, CH_4 and N_2 are all *p*-type in character, C_2H_6 has a *double p*-type shape. From these orbitals, all of which exhibit *p*-like character, the obvious question is whether the cross section from ethane shows the same characteristics as the previous molecules with a single large atom near the center of mass or if the presence of the two large atoms within the molecule modifies the scattering dynamics yielding a cross section similar to a diatomic molecule or if the double *p*-type shape produces a totally different TDCS.

Theoretically it was found that the M3DW coupled with the orientation averaged molecular orbital (OAMO) approximation yielded qualitative agreement with experimental data for ionization of H_2O [18], NH_3 [24] and CH_4 [22,23]. However, a calculation doing a proper average (PA) over all orientations for CH_4 yielded much improved agreement with experimental data compared to the OAMO results [33]. Here we will compare experimental results for ethane with both M3DW-OAMO and PA results.

The experimental measurements were made using a coplanar symmetric geometry as shown in Fig. 2. In this geometry, both final state electrons are detected in the scattering plane with $E_a = E_b$ and $\theta_a = \theta_b$ where E_a is the energy of the scattered electron with momentum $\mathbf{k}_a$ observed at scattering angle θ_a , E_b and is the energy of the ejected electron with momentum $\mathbf{k}_b$ observed at scattering angle θ_b . Obviously the electrons cannot be distinguished, but for convenience we call one of the electrons the scattered projectile and the other the ejected electron. From energy conservation the binding energy (ε) is given by

$$\varepsilon = E_i - E_a - E_b \tag{1}$$

where E_i is the energy of the incoming electron with momentum $\mathbf{k}_i$.

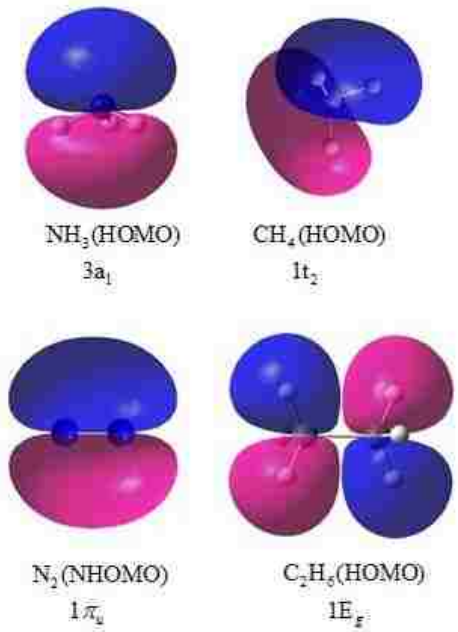

FIG. 1. (Color online) Dyson orbitals calculated for NH_3, CH_4, N_2, and C_2H_6.

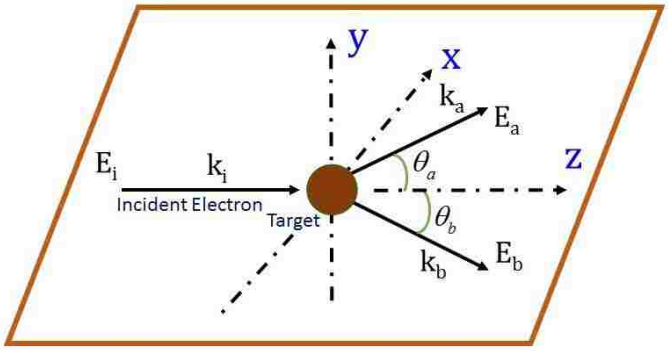

FIG. 2. (Color online) Coplanar symmetric geometry used for experimental measurements. See text for definition of the different variables.

In this paper we report experimental and theoretical results for electron-impact (e,2e) ionization of the HOMO orbital of the ethane molecule (C_2H_6) in coplanar symmetric scattering for four final state electron energies $E_a = E_b = 5, 10, 15,$ and $20\,eV$. We also compare the experimental ethane cross sections with those for CH_4, NH_3, and N_2. The experimental cross sections are then compared with theoretical M3DW calculations.

II. EXPERIMENT

The experimental data collected at the University of Manchester utilized a computer controlled and computer optimized (e,2e) spectrometer. This spectrometer has been fully described elsewhere [34], however the relevant details are again briefly given here for completeness. The incident electron beam is produced by an electron gun which uses a tungsten filament cathode and two three-element aperture lenses to transport and accelerate the electrons into a well collimated beam of the desired energy. The electron beam is crossed with the molecular target (high purity ethane, BOC [35]) effusing from a gas jet. The flow or ethane was controlled by a needle valve such that typical operating pressures were 1×10^{-5} torr. The outgoing electrons, resulting from a collision with the molecular target, are collected by two analyzers, each consisting of a three element lens and hemispherical energy selector. The transmitted electrons are detected by a channel electron multiplier. Each analyzer is mounted on an individual turntable that enables them to rotate independently around the detection plane over the angles of $35^o < \theta < 125^o$. To ensure that the spectrometer remained optimized over the time of data collection, the electrostatic

lenses in the apparatus were adjusted under computer control as the experiment progressed, so as to maximize the electron count rate in each analyzer. This corrected for any variation in the signals as the analyzers swept back and forth around the detection plane. The experimental data reported here are an average of several sweeps around the detection plane with the uncertainty being the standard error for the average at each particular angle. The uncertainty on the analyzer angle is estimated to be $\sim 3^o$ with contributions from the pencil angle of the incident electron beam and the acceptance angle of the analyzers. The coincidence energy resolution obtained in this study is ~ 0.9eV, as determined by the binding energy spectrum of helium.

III. THEORY

The molecular three-body distorted wave (M3DW) approximation is described in Refs. [36,37] and here we provide only a short review. The triple-differential cross section (TDCS) is given by

$$\frac{d^5\sigma}{d\Omega_a d\Omega_b dE_b} = \frac{1}{(2\pi)^5}\frac{k_a k_b}{k_i}\left(\left|T_{dir}\right|^2 + \left|T_{exc}\right|^2 + \left|T_{dir} - T_{exc}\right|^2\right) \tag{2}$$

where $\mathbf{k}_i, \mathbf{k}_a$ and $\mathbf{k}_b$ are the wave vectors for the initial, scattered, and ejected electrons, respectively, T_{dir} is the direct scattering amplitude, and T_{exc} is the exchange amplitude. The direct scattering amplitude is given by

$$T_{dir} = \left\langle \chi_a^-(\mathbf{k}_a, \mathbf{r}_0)\chi_b^-(\mathbf{k}_b, \mathbf{r}_1)\mathrm{C}_{ab}(\mathbf{r}_{01})\psi_{\mathrm{Ion}}(\xi, \mathbf{R})\left|\mathrm{V}_i - U_i\right|\psi_{\mathrm{Target}}(\xi, \mathbf{r}_1, \mathbf{R})\ \ \chi_i^+(\mathbf{k}_i, \mathbf{r}_0)\right\rangle \tag{3}$$

where $\chi_i^+(\mathbf{k}_i, \mathbf{r}_0)$ is a continuum-state distorted for wave number $\mathbf{k}_i$ and the (+) indicates outgoing wave boundary conditions, $\chi_a^-(\mathbf{k}_a, \mathbf{r}_0), \chi_b^-(\mathbf{k}_b, \mathbf{r}_1)$ are the scattered and ejected electron distorted waves with incoming wave boundary conditions, the factor $\mathrm{C}_{ab}(\mathbf{r}_{01})$ is the final state Coulomb-distortion factor between the two electrons – normally called postcollision interaction (PCI), $\psi_{\mathrm{Target}}(\xi, \mathbf{r}_1, \mathbf{R})$ is the initial state molecular wavefunction which depends on the orientation of the molecule $\mathbf{R}$, the active electron $\mathbf{r}_1$, and all the passive electrons ξ, and finally $\psi_{\mathrm{Ion}}(\xi, \mathbf{R})$ is the final state ion wave function which depends on the orientation and on the passive electrons. In the approximation we use for the perturbation $(\mathrm{V}_i - U_i)$, this only depends on the projectile electron (r_0) and active

electron (r_1) . Since the perturbation does not depend on the passive electron coordinates ξ, we can integrate over all these coordinates and define

$$\phi_{Dy}(\mathbf{r}_1,\mathbf{R}) = \left\langle \psi_{\text{Ion}}(\xi,\mathbf{R}) \middle| \psi_{\text{Target}}(\xi,\mathbf{r}_1,\mathbf{R}) \right\rangle \tag{4}$$

Here $\phi_{Dy}(\mathbf{r}_1,\mathbf{R})$ is the initial bound-state wave function which is commonly called the Dyson molecular orbital for the active electron, which depends both on $\mathbf{r}_1$ and $\mathbf{R}$. Defining the perturbation to be *W*, we have

$$T_{dir}(\mathbf{R}) = \left\langle \chi_a^-(\mathbf{k}_a,\mathbf{r}_0)\chi_b^-(\mathbf{k}_b,\mathbf{r}_1)\mathrm{C}_{ab}(\mathbf{r}_{01}) \middle| \mathrm{W} \middle| \phi_{Dy}(\mathbf{r}_1,\mathbf{R}) \;\; \chi_i^+(\mathbf{k}_i,\mathbf{r}_0) \right\rangle \tag{5}$$

The exchange *T*-matrix is the same as Eq. (5) except that $\mathbf{r}_0$ and $\mathbf{r}_1$ are interchanged in the final state wavefunction. The triple differential cross section (TDCS) for a given orientation $\mathbf{R}$ with respect to the laboratory frame can be obtained from

$$\sigma^{TDCS}(\mathbf{R}) = \frac{1}{(2\pi)^5}\frac{k_a k_b}{k_i}\left(\left|T_{dir}(\mathbf{R})\right|^2 + \left|T_{exc}(\mathbf{R})\right|^2 + \left|T_{dir}(\mathbf{R}) - T_{exc}(\mathbf{R})\right|^2 \right) \tag{6}$$

A. Proper average (PA) over molecular orientations

To take the proper average (PA) over all molecular orientations, the TDCS is calculated for each orientation and then averaged over all possible orientations so that

$$\sigma^{PA} = \frac{\int \sigma^{\text{TDCS}}(\mathbf{R})\, \mathrm{d}\Omega_R}{\int d\Omega_R} \tag{7}$$

Looking only at the direct scattering amplitude as an example, this leads to

$$\sigma^{PA} = \frac{\int \frac{1}{(2\pi)^5}\frac{k_a k_b}{k_i}\left| \int d^3r_0 d^3r_1 \chi_a^{-*}(\mathbf{k}_a,\mathbf{r}_0)\chi_b^{-*}(\mathbf{k}_b,\mathbf{r}_1)\mathrm{C}_{ab}(\mathbf{r}_{01})\mathrm{W}(\mathbf{r}_0,\mathbf{r}_1)\,\phi_{Dy}(\mathbf{r}_1,\mathbf{R})\chi_i^+(\mathbf{k}_i,\mathbf{r}_0) \right|^2 d\Omega_R}{\int d\Omega_R} \tag{8}$$

B. OAMO approximation

In the OAMO (orientation averaged molecular orbital) approximation [36], we assume that the absolute value and integral over molecular orientations in Eq. (8) commute, so that

$$\sigma^{OAMO} \simeq \frac{1}{(2\pi)^5}\frac{k_a k_b}{k_i}\frac{\left|\int d\Omega_R \{\int d^3r_0\, d^3r_1\, \chi_a^{-*}(\mathbf{k}_a,\mathbf{r}_0)\chi_b^{-*}(\mathbf{k}_b,\mathbf{r}_1)\mathrm{C}_{ab}(\mathbf{r}_{01})\mathrm{W}(\mathbf{r}_0,\mathbf{r}_1)\,\phi_{Dy}(\mathbf{r}_1,\mathbf{R})\chi_i^{+}(\mathbf{k}_i,\mathbf{r}_0)\}\right|^2}{\int d\Omega_R} \tag{9}$$

Since the only term in the integral that depends on the orientation is the Dyson orbital, we can interchange the order of integration, so that

$$\sigma^{OAMO} \simeq \frac{1}{(2\pi)^5}\frac{k_a k_b}{k_i}\frac{\left|\int d^3r_0\, d^3r_1\, \chi_a^{-*}(\mathbf{k}_a,\mathbf{r}_0)\chi_b^{-*}(\mathbf{k}_b,\mathbf{r}_1)\mathrm{C}_{ab}(\mathbf{r}_{01})\mathrm{W}(\mathbf{r}_0,\mathbf{r}_1)\int \phi_{Dy}(\mathbf{r}_1,\mathbf{R})d\Omega_R\chi_i^{+}(\mathbf{k}_i,\mathbf{r}_0)\right|^2}{\int d\Omega_R} \tag{10}$$

We now define the OAMO Dyson wavefunction

$$\phi_{Dy}^{OAMO}(\mathbf{r}_1) = \frac{\int \phi_{Dy}(\mathbf{r}_1,\mathbf{R})d\Omega_R}{\int d\Omega_R} \tag{11}$$

so that

$$\sigma^{\mathrm{OAMO}} = \frac{1}{(2\pi)^5}\frac{k_a k_b}{k_i}\left|\int d^3r_0\, d^3r_1\, \chi_a^{-*}(\mathbf{k}_a,\mathbf{r}_0)\chi_b^{-*}(\mathbf{k}_b,\mathbf{r}_1)\mathrm{C}_{ab}(\mathbf{r}_{01})\mathrm{W}(\mathbf{r}_0,\mathbf{r}_1)\,\phi_{Dy}^{OAMO}(\mathbf{r}_1)\chi_i^{+}(\mathbf{k}_i,\mathbf{r}_0)\right|^2 \tag{12}$$

This is a *T*-matrix just like one we would evaluate for ionization of an atom, or for ionization of a single molecular orientation. The advantage of this approximation is that this calculation does not take much computer time. By contrast, the PA calculation can take an enormous amount of computer time, depending on the number of orientations required for suitable convergence.

IV. RESULTS

In Fig. 3 we compare the present experimental ethane cross sections with previously published data for CH_4 [22], NH_3 [24], and N_2 [12]. As absolute data have not been measured, each of the data sets i normalized to unity at its most intense point. From the figure, it is seen that the TDCS measurements are similar for all four molecules at the two highest energies of 20 and 15 eV. All of them show high intensity at low angles, a minimum at $\theta \sim 90°$ followed by the cross section increasing again at high analyzer angles. A signature of a *p*-like orbital observed in the isoelectronic targets is a small "dip" in the large peak at low angles which is also present in the ethane data, but less obvious in N_2.

By contrast, at 10 and 5 eV ethane shows a very different character from the two molecules that have a single heavy atom near the CM. At 10 eV ethane is very similar to the diatomic molecule N_2, and at 5 eV ethane is quasi-isotropic and therefore different from all the other measurements. These observations suggest that for the higher energies, the incoming electron scatters from one of the "peanut-like" orbitals, with very little influence from the second orbital, or the diatomic nature of the molecule. As the energy is lowered to 10 eV, the results look more like a diatomic molecule, suggesting that the outer six H nuclei do not play an important role but that the two-center nature of the target influences the dynamics. As the energy is further lowered to 5 eV, it appears that the interactions become much more complicated and the data cannot be explained by these simple ideas.

Figure 4 compares experimental and theoretical results for electron-impact ionization of ethane. Both the data and theoretical calculations have been normalized to unity at their largest values. The solid (red) curves are the proper average (PA) results and the dashed (blue) curves are the OAMO results. For the highest energies of 15 and 20 eV, there is qualitative agreement between experiment and theory for the small angle peak. For 20 eV, the PA results are in somewhat better agreement with experiment than the OAMO calculation, in that the location of the forward peak is closer to the data, and also shows a "dip" in this peak. At 15 eV, both theories have small angle peaks which have shifted to larger scattering angles. Since both PA and OAMO have the exact electron-electron PCI repulsion, this shift suggests that the theoretical repulsion is stronger than observed. There is a second large angle peak at high scattering angles in the experimental data that is present in the OAMO theory but is not predicted by the PA calculations.

For the two lowest energies, the agreement between experiment and theory is less satisfactory. At 10 eV, the OAMO predicts three peaks, which is similar to the data. However, the first peak is much too small and the third one appears to be too big. The PA, on the other hand, has a single small angle peak. Unfortunately, the PA peak is shifted to a much larger angle than is found in the experiment. While the experimental data show a second peak for large angles, the PA calculation only shows a shoulder in this angular range. The lack of a significant large angle peak for 15 and 10 eV may indicate that the nuclear scattering is underestimated in the PA model since it has been previously found that a strong interaction with the nucleus is necessary to obtain both outgoing electrons at

large angles [9]. At 5 eV, the data shows little variation with angle, unlike the theoretical results. However, the data appear to have (at least) three peaks in this angular range which is also predicted by the PA calculation. The PA results are an improvement over that of the OAMO, in that OAMO predicts a single narrow peak at large angles while the PA predicts multiple peaks of comparable heights, similar to the data.

V. CONCLUSIONS

We have presented experimental and theoretical results for electron-impact ionization from the ethane (C_2H_6) HOMO for coplanar symmetric scattering. Both electrons in the final state have equal energies and are detected at equal angles on opposite sides of the incident beam direction. Four different final state energies between 5 to 20 eV have been examined.

Ethane can be considered as a quasidiatomic molecule of C_2 surrounded by six H nuclei, and the HOMO looks like two *p*-type "peanut" states side by side. We have compared the experimental measurements with equivalent data for electron-impact ionization of NH_3 and CH_4, which have a *p*-type HOMO state with one large atom near the CM surrounded by H nuclei. We also compared with experimental data for the NHOMO state of N_2. N_2 is of course not surrounded by H nuclei, but has the same two heavy atom molecular frame and, further, its NHOMO orbital also has a "peanut" shape. We found that at the two highest energies of 15 and 20 eV, the cross sections for all four molecules were similar, suggesting that the projectile electron scatters from one of the ethane orbitals with little influence from the second. At 10 eV, the ethane results were quite different from NH_3 and CH_4 but were similar to N_2. This suggests that as the energy is lowered, the electron "sees" an effective diatomic molecule with little influence from the surrounding H nuclei. At the lowest energy of 5 eV, the ethane data were different to any of the other three molecules (but closest to N_2), suggesting that the scattering process is more complicated.

We also compared the ethane experimental data with theoretical M3DW results calculated using both the OAMO approximation and a proper average (PA) over all orientations. For the highest energy of 20 eV, the PA results were in reasonable agreement with experiment for the small angle peak, while at 15 and 10 eV the agreement was more qualitative, with the theoretical peak shifting to increasingly larger angles as the energy

decreases. For 5 eV, the PA calculation was again in qualitative agreement with experiment. In all cases, the PA results agreed with experimental data more closely than the OAMO results, as would be expected.

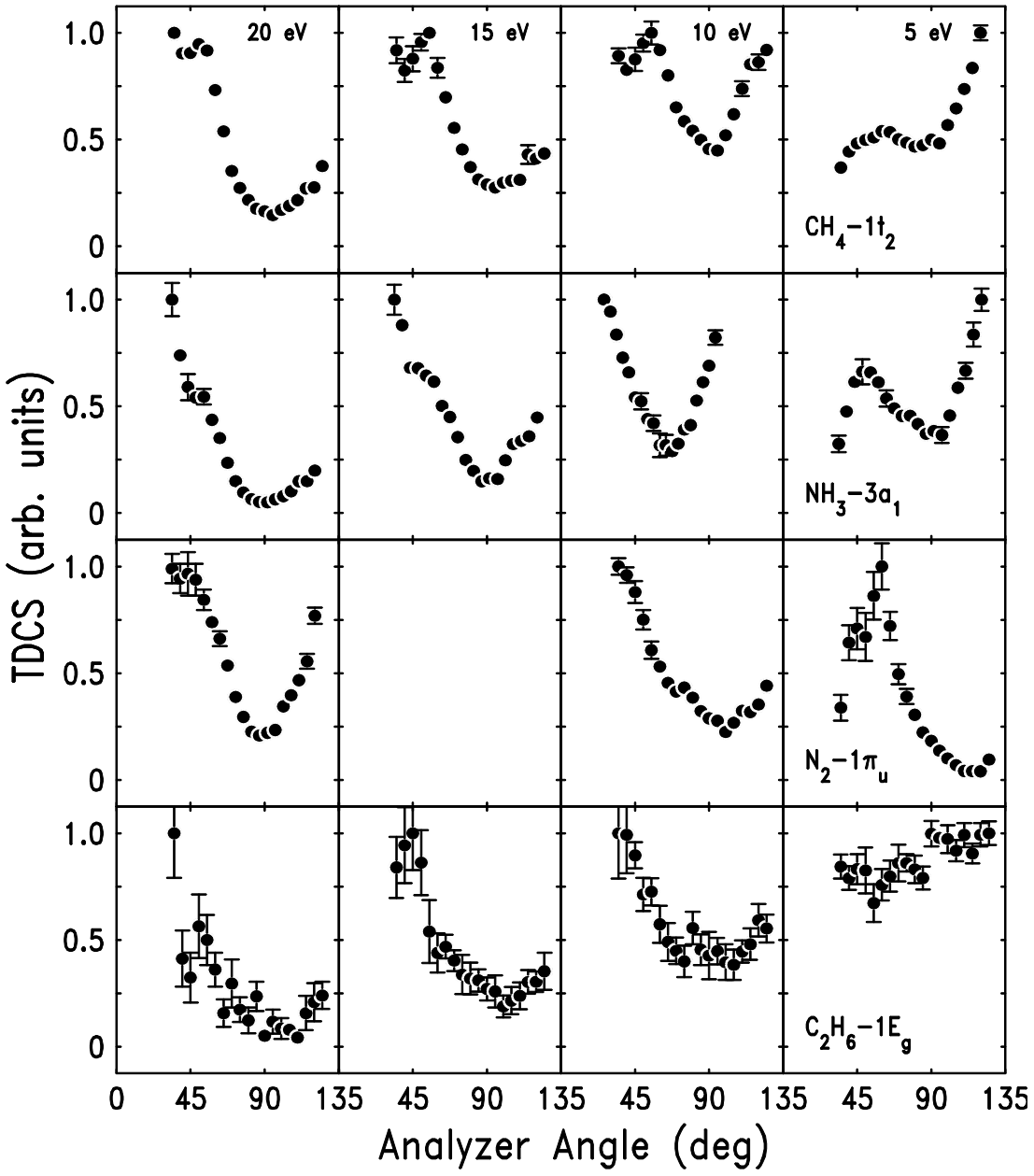

FIG. 3. Experimental TDCS for coplanar symmetric electron-impact ionization of NH_3, CH_4, N_2, and C_2H_6 as a function of electron detection angle, for a series of outgoing electron energies. Both final-state electrons have equal energies as listed in the top row, and both are detected at equal angles as shown in fig. 2. For each set of energies, the largest measured data have been normalized to unity.

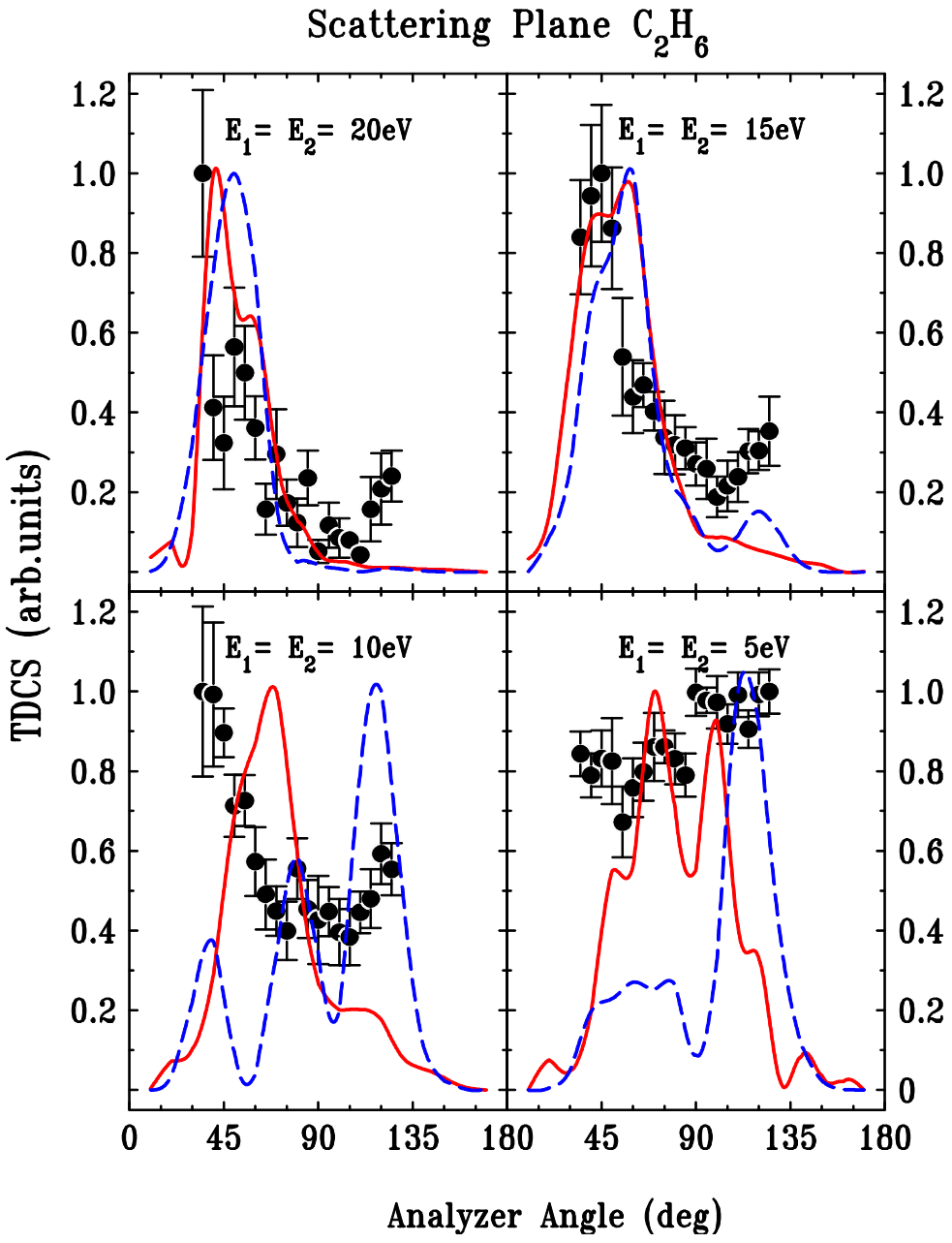

FIG. 4. (Color online) Experimental and theoretical TDCS for electron-impact ionization of ethane (C_2H_6) as a function of electron detection angle, using the geometry in fig. 2. For both experimental data and theoretical calculations, the largest cross sections have been normalized to unity for each set of energies. The theoretical curves are: solid (red) is PA and dashed (blue) is OAMO.

ACKNOWLEDGEMENTS

K.N. would like to thank the European commission for a Marie Curie International Incoming Fellowship undertaken at the University of Manchester. We would like to thank

the technicians in the Schuster laboratory for providing excellent support for the experimental apparatus. This work was partly supported by the US National Science Foundation under Grant. No. PHY-1505819 and by the National Natural Science Foundation of China under Grants No. 11174175. Computational work was performed with Institutional Computing resources made available through the Los Alamos National Laboratory and XSEDE resources provided by the Texas Advanced Computing Center (Grant No. TG-MCA07S029). The Los Alamos National Laboratory is operated by Los Alamos National Security, LLC, for the National Nuclear Security Administration of the US Department of Energy under Contract No. DE-AC5206NA25396.

[1] I. Bray and A. T. Stelbovics, Phys. Rev. A 46, 6995 (1992).

[2] J. Colgan and M. S. Pindzola, Phys. Rev. A 74, 012713 (2006).

[3] T. N. Rescigno, M. Baertschy, W. A. Isaacs, and C. W. McCurdy, Science 286, 2474 (1999).

[4] X. Ren, S. Amami, O. Zatsarinny, T. Pfluger, M. Weyland, W. Y. Baek, H. Rabus, K. Bartschat, D. Madison, and A. Dorn, *Phys. Rev*. A **91**, 032707 (2015).

[5] A. Senftleben, T. Pflueger, X. Ren, O. Al-Hagan, B. Najjari, D. Madison, A. Dorn, and J. Ullrich, *J. Phys. B* **43**, 081002 (2010).

[6] D. S. Milne-Brownlie, M. Foster, J. Gao, B. Lohmann, and D. H. Madison, *Phys. Rev. Lett*. **96**, 233201 (2006).

[7) A. J. Murray, *J. Phys. B* **38**, 1999 (2005).

[8] E. M. Staicu Casagrande, A. Naja, F. Mezdari, A. LahmamBennani, P. Bolognesi, B. Joulakian, O. Chuluunbaatar, O. AlHagan, D. H. Madison, D. V. Fursa, and I. Bray, *J. Phys. B* **41**, 025204 (2008).

[9] O. Al-Hagan, C. Kaiser, D. H. Madison, and A. J. Murray, *Nat. Phys. 5*, 59 (2009).

[10] J. Gao, D. H. Madison, J. L. Peacher, A. J. Murray, and M. J. Hussey, *J. Chem. Phys*. **124**, 194306 (2006).

[11] A. J. Murray, M. J. Hussey, I. Bray, J. Gao, and D. H. Madison, *J. Phys. B* **39**, 3945 (2006).

[12] M. J. Hussey and A. J. Murray, *J. Phys. B* **35**, 3399 (2002).

[13] L. R. Hargreaves, C. Colyer, M. A. Stevenson, B. Lohmann, O. Al-Hagan, D. H. Madison, and C. G. Ning, *Phys. Rev*. A **80**, 062704 (2009).

[14] A. Lahmam-Bennani, E. M. Staicu Casagrande, and A. Naja, J. Phys. B **42**, 235205 (2009).

[15] S. J. Cavanagh and B. Lohmann, *J. Phys. B* **32**, L261 (1999).

[16] M. J. Hussey and A. J. Murray, *J. Phys. B* **38**, 2965 (2005).

[17] D. S. Milne-Brownlie, S. J. Cavanagh, B. Lohmann, C. Champion, P. A. Hervieux, and J. Hanssen, . A **69**, 032701 (2004).

[18] K. L. Nixon, A. J. Murray, O. Al-Hagan, D. H. Madison, and C. Ning, J. Phys. B **43**, 035201 (2010).

[19] C. Kaiser, D. Spieker, J. Gao, M. Hussey, A. Murray, and D. H. Madison, J. Phys. B **40**, 2563 (2007).

[20] A. Lahmam-Bennani, A. Naja, E. M. Staicu Casagrande, N. Okumus, C. Dal Cappello, I. Charpentier, and S. Houamer, J. Phys. B **42**, 165201 (2009).

[21] S. Xu, H. Chaluvadi, X. Ren, T. Pfluger, A. Senftleben, C. G. ¨ Ning, S. Yan, P. Zhang, J. Yang, X. Ma, J. Ullrich, D. H. Madison, and A. Dorn, J. Chem. Phys. **137**, 024301 (2012).

[22] K. L. Nixon, A. J. Murray, H. Chaluvadi, C. G. Ning, and D. H. Madison, J. Chem. Phys. **134**, 174304 (2011).

[23] K. L. Nixon, A. J. Murray, H. Chaluvadi, S. Amami, D. H. Madison, and C. G. Ning, J. Chem. Phys. **136**, 094302 (2012).

[24] K. L. Nixon, A. J. Murray, H. Chaluvadi, C. G. Ning, J. Colgan, and D. H. Madison, J. Chem. Phys. **138**, 174304 (2013).

[25] C. J. Colyer, M. A. Stevenson, O. Al-Hagan, D. H. Madison, C. G. Ning, and B. Lohmann, J. Phys. B **42**, 235207 (2009).

[26] J. D. Builth-Williams, S. M. Bellm, L. Chiari, P. A. Thorn, D. B. Jones, H. Chaluvadi, D. H. Madison, C. G. Ning, B. Lohmann, G. B. da Silva, and M. J. Brunger, J. Chem. Phys. **139**, 034306 (2013).

[27] D. B. Jones, J. D. Builth-Williams, S. M. Bellm, L. Chiari, H. Chaluvadi, D. H. Madison, C. G. Ning, B. Lohmann, O. Ingolfsson, and M. J. Brunger, Chem. Phys. Lett. **572**, 32 (2013).

[28] S.M. Bellm, J. D. Builth-Williams, D. B. Jones, H. Chaluvadi, D. H. Madison, C. G. Ning, F. Wang, X. G. Ma, B. Lohmann, and M. J. Brunger, J. Chem. Phys. **136**, 244301 (2012).

[29] S.M. Bellm, C. J. Colyer, B. Lohmann, and C. Champion, Phys. Rev. A **85**, 022710 (2012).

[30] J. D. Builth-Williams, S. M. Bellm, D. B. Jones, H. Chaluvadi, D. H. Madison, C. G. Ning, B. Lohmann, and M. J Brunger, J. Chem. Phys. **136**, 024304 (2012).

[31] C. J. Colyer, S. M. Bellm, B. Lohmann, G. F. Hanne, O. AlHagan, D. H. Madison, and C. G. Ning, J. Chem. Phys. **133**, 124302 (2010).

[32] G. B. da Silva, R. F. C. Neves, L. Chiari, D. B. Jones, E. Ali, D. H. Madison, C. G. Ning, K. L. Nixon, M. C. A. Lopes, and M. J. Brunger, J. Chem. Phys. **141**, 124307 (2014).

[33] H. Chaluvadi, C. G. Ning, and D. Madison, Phys. Rev. A **89**, 062712 (2014).

[34] A. J. Murray, B. C. H. Turton, and F. H. Read, Rev. Sci. Instrum. **63**, 3346 (1992).

[35] BOC Industrial Gases UK, http://www.boconline.co.uk.

[36] J. Gao, J. L. Peacher, and D. H. Madison, J. Chem. Phys. **123**, 204302 (2005).

[37] D. H. Madison and O. Al-Hagan, J. At., Mol., Opt. Phys. **2010**, 367180 (2010).

III. Electron- and photon-impact ionization of furfural

D. B. Jones,[1] E. Ali,[2] K. L. Nixon,[3,4] P. Limão-Vieira,[5,a)] M.-J. Hubin-Franskin,[6] J. Delwiche,[6] C. G. Ning,[7] J. Colgan,[8] A. J. Murray,[9] D. H. Madison[2,a)] and M. J. Brunger[1,10,a)]

[1]*School of Chemical and Physical Sciences, Flinders University, GPO Box 2100, Adelaide, SA 5001, Australia*

[2]*Department of Physics, Missouri University of Science and Technology, Rolla, Missouri 65409, USA*

[3]*Departamento de Física, Universidade Federal de Juiz de Fora, Juiz de Fora, MG, Brazil*

[4]*School of Biology, Chemistry and Forensic Science, University of Wolverhampton, Wolverhampton WV1 1LY, UK*

[5]*Laboratório de Colisões Atómicas e Moleculares, CEFITEC, Departamento de Física, Faculdade de Ciências e Tecnologia, Universidade Nova de Lisboa, 2829-516 Caparica, Portugal*

[6]*Département de Chimie, Université de Liège, Institut de Chimie-Bât. B6C, B-4000 Liège 1, Belgium*

[7]*Department of Physics, State Key Laboratory of Low-Dimensional Quantum Physics, Tsinghua University, Beijing 100084, China*

[8]*Theoretical Division, Los Alamos National Laboratory, Los Alamos, NM 87545, USA*

[9]*Photon Science Institute, School of Physics & Astronomy, University of Manchester, Manchester M13 9PL, UK*

[10]*Institute of Mathematical Sciences, University of Malaya, 50603 Kuala Lumpur, Malaysia*

(Received 24 August 2015; accepted 29 October 2015; published online 12 November 2015)

[a)] Authors to whom correspondence should be addressed. Electronic addresses: plimaovieira@fct.unl.pt ; madison@mst.edu; and michael.brunger@flinders.edu.au

The He(I) photoelectron spectrum of furfural has been investigated, with its vibrational structure assigned for the first time. The ground and excited ionized states are assigned through *ab initio* calculations performed at the outer-valence Green's function level. Triple differential cross sections (TDCS) for electron-impact ionization of the unresolved combination of the 4a″+21a′ highest and next-highest occupied molecular orbitals have also been obtained. Experimental angular distributions of the TDCS are recorded in asymmetric coplanar kinematics. TDCS are also measured under doubly-symmetric coplanar kinematics. The experimental TDCS are compared to theoretical calculations, obtained within a molecular 3-body distorted wave framework that employed either an orientation average or proper TDCS average. The proper average calculations suggest that they may resolve some of the discrepancies regarding the angular distributions of the TDCS, when compared to calculations employing the orbital average.
[http://dx.doi.org/10.1063/1.4935444]

I. INTRODUCTION

Furfural or 2-furaldehyde ($C_5H_4O_2$) is an important chemical in the petroleum, plastics, agro-chemical and pharmaceutical industries.[1] It has also been identified as a key platform chemical[2,3] in the commercial realisation of bio-refineries.[4] At this stage, no direct synthetic methods for furfural production exist, and it is solely produced on the industrial scale through the thermochemical treatment of biomass.[1] Hybrid interdisciplinary strategies are currently being investigated to optimize and control the chemical conversion of biomass into desirable chemicals. These include utilizing atmospheric plasma pre-treatments,[5,6] or electron-beam irradiation[7,8] to overcome the natural recalcitrance of biomass. A knowledge of electron- and photon-driven processes with key bio-refinery compounds will also play an important role in understanding the chemical kinetics associated with non-thermal plasma-assisted combustion of complex biofuel-air mixtures, where conventional high-temperature combustion models may not be applicable.[9] A detailed understanding of the quantum chemical structure of the biomass sub-unit furfural, and its reaction dynamics, is therefore an important part of developing innovative

techniques that can improve the energy and conversion efficiency for the processing and for the realisation of next-generation biofuels.

To partially address these requirements, an investigation into the photon- and electron-impact ionization of furfural is reported in this manuscript. Furfural is a planar molecule that can exist in either a *trans*- or *cis*-conformation (see Fig. 1). The preferred furfural structure and its rotational barrier have been the subject of many investigations (see Refs. 10 and 11 and references therein), so that it is now well established that in the gas phase the *trans* conformer is preferred, and that the relative conformation populations are *trans* (79.5%) and *cis* (20.5%). For the ionization dynamics of furfural, to the best of our knowledge there has only been one low-resolution photoelectron study undertaken.[12] A high-resolution photo-ionization study has therefore been carried out here, in order to characterise the vibrational structure of its low-lying ionic states. This study complements allied investigations into the electron- and photon-impact discrete excitation of furfural.[13] The dynamics of photon- and electron-impact ionization of complex polyatomic species also furthers understanding about the influence of target structure in the dynamics of the ionization process. In this respect, the triple-differential cross sections (TDCS) for the electron-impact ionization reaction have been measured,

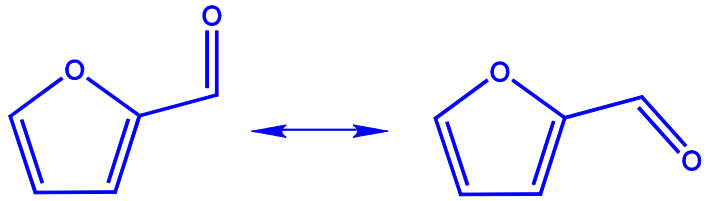

FIG. 1. Schematic representation of furfural in its *cis*- and *trans*-conformations.

$$e_0^-\left(E_0,\mathbf{k}_0\right)+M\rightarrow M^+\left(\epsilon,\mathbf{q}\right)+e_1^-\left(E_1,\mathbf{k}_1\right)+e_2^-\left(E_2,\mathbf{k}_2\right). \tag{1}$$

Here, an incident electron with energy E_0 and momentum $\mathbf{k}_0$, $e_0^-\left(E_0,\mathbf{k}_0\right)$, ionizes the furfural target M (assumed to be at rest) with an ionization energy ϵ, to produce a furfural ion M^+ recoiling with a momentum $\mathbf{q}$ to conserve momentum. The energies $(E_i's)$ and momenta $(\mathbf{k}_i's)$ of both outgoing electrons ($i = 1$ or 2) are then determined so as to observe

a kinematically complete reaction. This study of furfural is performed here with a combination of asymmetric coplanar and doubly symmetric coplanar scattering geometries, as depicted in Fig. 2.

This combination of experiments, performed over a range of scattering kinematics, provides a strong test of theoretical calculations aimed at describing the electron-impact ionization process. Here we have performed calculations at the molecular three body distorted wave (M3DW) level, that either employ an orbital average or a proper TDCS average to account for the random orientation of the molecules in the experimental studies.[14] In this way the validity and limitation of approximations made in calculating electron scattering cross sections across a range of scattering regimes can be assessed. This also builds on earlier studies evaluating the role of molecular structure in electron-impact ionization scattering dynamics from key organic compounds.[15-20]

The outline of this manuscript is as follows. In Section II details of the experimental configurations are presented, while in Section III, the scattering and quantum chemistry calculations are outlined. The experimental and theoretical results are then presented and discussed in Section IV. Finally conclusions from this work are drawn in Section V.

II. EXPERIMENTAL DETAILS

A. Furfural sample

In all of the experiments described here, vapour from a liquid furfural sample (Sigma Aldrich; 99% assay) was used. The samples were employed without further purification, except that they were subjected to repeated freeze pump-thaw cycles to remove dissolved gases.

B. Photoelectron experimental details

He(I) (21.22 eV) photoelectron spectra of furfural were recorded at the Université de Liège, Belgium. The apparatus that was employed has been described in detail previously.[21] Briefly, the spectrometer consists of a 180° cylindrical electrostatic analyser with a mean radius of 5 cm. The analyser is used in constant energy pass mode. The incident photons are produced by a DC discharge in a two stage differentially pumped lamp. The energy scale was calibrated using the well-known xenon lines ($^2P_{3/2}$ = 12.130 eV and $^2P_{1/2}$ = 13.435 eV).[22,23] The resolution of the present spectrum is 30 meV as determined from the full width half maximum (FWHM) of the Xe peaks in the presence of

furfural. The intensities in the spectrum were corrected for the transmission of the analysing system. The accuracy of the energy scale is estimated to be ± 2 meV.

C. Asymmetric coplanar kinematics experimental configuration at Flinders

Triple differential cross sections (TDCS) for the electron impact ionization of the unresolved combination of the highest occupied and next-highest occupied molecular orbitals of furfural (HOMO+NHOMO; 4a″+21a′) have been measured on an apparatus housed at Flinders University. This apparatus has been described previously,[24] so only those details relating to the present measurements are repeated here. These measurements were performed in an asymmetric coplanar geometry, as depicted in Fig. 2 (a). Here an incident electron beam, with energy E_0 = 250 eV, was crossed with a beam of furfural vapour. A coincidence technique[25] was employed to measure the angular distributions of the slow ejected electron, with energy E_2 = 20 eV, while detecting the fast scattered electron at fixed scattering angles of either θ_1 = -5, -10 or -15°. Note that the scattered electron energy was selected to conserve energy in the ionization of the unresolved HOMO+NHOMO (IP ~ 9.2 eV). Here the coincidence energy resolution was typically ~1.1 eV (FWHM). The angular distributions for fixed scattering angles were then inter-normalised, by measuring the angular distribution of the scattered electron when the ejected electron angle is fixed at $\theta_2 = 90^o$. In this way, theoretical TDCSs can be compared to the measured experimental data through a single normalisation factor applied to all experimental data. This normalisation factor was determined using a least squares technique applied to the experimental data in the binary region of the $\theta_1 = -10^o$ angular distribution.

In the asymmetric coplanar geometry, the detection energy and angle of the fast scattered electron define the momentum transferred to the target ($\mathbf{K} = \mathbf{k}_0 - \mathbf{k}_1$) during the ionization process. When the slow electron leaves the collision in the direction close to that of the momentum transfer, this is considered as a binary interaction with the target. Conversely, when the slow electron is ejected in directions close to being anti-parallel to the momentum transfer direction, the residual ion must recoil with substantial momentum. These angular regions of the TDCS are then described either as the binary or

recoil regions, depending on if they lie close to parallel or anti-parallel to the momentum transfer direction, respectively.

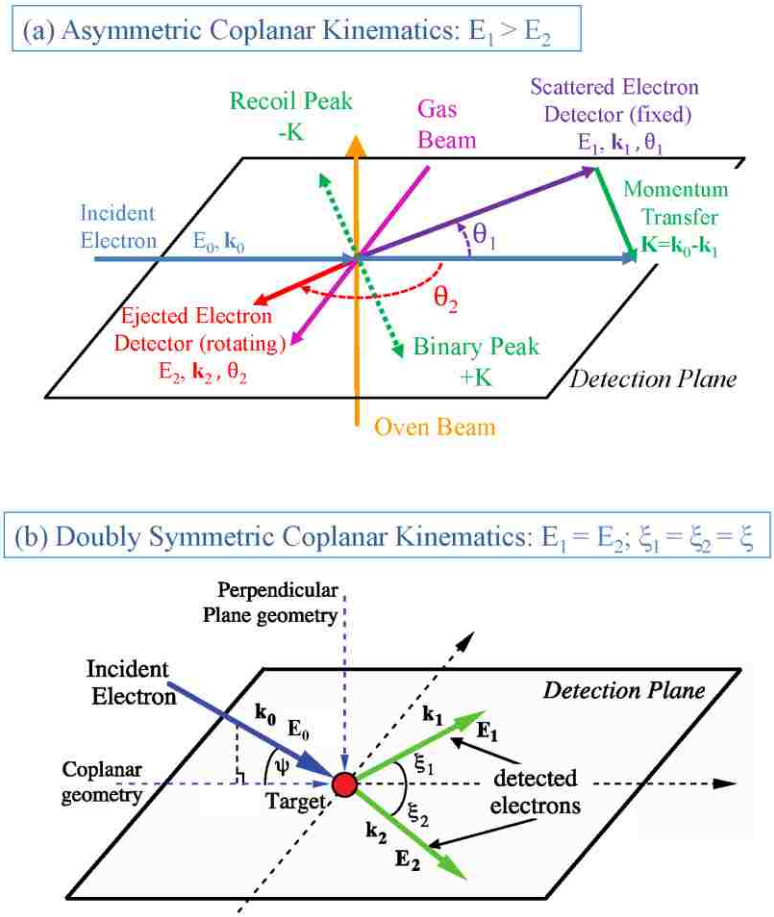

FIG. 2. Schematic diagrams of the present electron impact ionization scattering geometries. (a) The asymmetric coplanar geometry. (b) The doubly symmetric geometry, which becomes coplanar $\psi = 0^o$ when all three electrons are confined to the detection plane. The analyser angles (ξ_1 and ξ_2) are measured with respect to the projection of the incident electron beam $\mathbf{k_0}$ onto this plane as shown. See text for further details.

D. Doubly symmetric coplanar kinematics experimental configuration at Manchester

The experimental data collected at the University of Manchester utilised a computer controlled and computer optimised (*e*,2*e*) spectrometer. This spectrometer is described elsewhere,[26] however the relevant details are briefly given here for completeness. The incident electron beam is produced by a two-stage electron gun. The outgoing electron

analyzers are mounted on individual turntables that enable them to rotate independently around the detection plane. For this study, the spectrometer was operated in a coplanar geometry [see Fig. 2 (b)], where the momentum of the incident electron $\mathbf{k_0}$ lies in the detection plane defined by the two outgoing electrons $\mathbf{k_1}$, and $\mathbf{k_2}$. Doubly-symmetric kinematics were adopted with $E_1 = E_2 = E$ and $\xi_1 = \xi_2 = \xi$. In this case, E = 20 eV and ξ was scanned over the range from 35° to 120°. To ensure the spectrometer remained optimised over the time of data collection, the electrostatic lenses in the apparatus were adjusted under computer control at each angle of ξ, to maximise the electron count rate in each analyser. This corrected for any variation in the signal as the analysers swept back and forth around the detection plane. The typical coincidence energy resolution for this apparatus was determined to be ~ 1.4 eV (FWHM) from the measurement of the binding energy spectrum of helium.

As furfural is a liquid at room temperature it was necessary at both Flinders and Manchester to heat the sample and the gas handling lines to obtain sufficient target density for the measurements. In addition to this, the vacuum chamber at Manchester was also heated to ~40°C. High purity furfural was admitted at Manchester into the interaction region via a gas jet. The flow of furfural was regulated by a needle valve so that the vacuum in the chamber was raised from a base pressure of $\sim 1\times10^{-7}$ torr to a stable working pressure of $\sim 7\times10^{-6}$ torr. As a large background was observed in the coincidence timing spectrum, it was necessary to use a low incident electron beam current of ~150nA to improve the coincidence signal to background ratio.

The incident electron energy of the spectrometer was calibrated by measuring the coincidence binding energy spectrum of the outer valence orbitals of furfural. The incident electron energy was then set to match the energy of the structure corresponding to the unresolved HOMO and NHOMO states within the binding energy spectrum.

The data presented here for a coplanar geometry have been normalised to unity at ξ = 45°, since absolute measurements of the TDCS were not obtained. The theoretical calculations, obtained within different frameworks, are also normalised to unity in the region of ξ = 45° to enable a comparison with the data. The uncertainty in the measurements at each angle ξ was generated from the standard error, determined from averaging the data at a given angle for all sweeps of the detection plane. Six sweeps were used to produce the TDCS, with

data being accumulated at each angle for 2000 seconds. The angular uncertainties in the measurements were estimated to be ~ ± 3°.

III. COMPUTATIONAL METHODS

To assist in the assignment of the present spectra, quantum chemical calculations have been performed at the outer valence Green's function (OVGF)[27] level using an augmented correlation consistent valence double zeta basis set (aug-cc-pVDZ).[28,29] The ionized orbital characters were also studied using a Density Functional Theory framework employing the B3LYP functional[30] with the same aug-cc-pVDZ basis. Here we calculated spherically-averaged orbital momentum profiles for the ionized orbitals that were studied experimentally. Those momentum profiles were obtained using the HEMS program outlined in Cook and Brion.[31] Note that those quantum chemical calculations were performed within the Gaussian 09 package.[32]

To investigate the dynamics of the electron impact ionization process, triple differential cross sections were calculated at the molecular 3-body distorted wave (M3DW) level. These calculations were performed for both the asymmetric coplanar and doubly symmetric coplanar scattering geometries. The triple differential cross section for electron-impact ionization can be obtained through:

$$\frac{d\sigma}{d\Omega_a d\Omega_b dE_b} = \frac{1}{(2\pi)^5}\frac{k_1 k_2}{k_0}\left(|T_{dir}|^2 + |T_{exc}|^2 + |T_{dir} - T_{exc}|^2\right), \quad (2)$$

where T_{dir} is the direct ionization scattering amplitude described by:

$$T_{dir} = \chi_1^-(\boldsymbol{k}_1, \boldsymbol{r}_1)\,\chi_2^-(\boldsymbol{k}_2, \boldsymbol{r}_2)\,C_{scat-ejec}(\boldsymbol{r}_{12})|V - U_0|\phi_{DY}^{OA}(\boldsymbol{r}_2)\,\chi_0^+(\boldsymbol{k}_0, \boldsymbol{r}_1). \quad (3)$$

The exchange scattering amplitude, T_{exc}, is calculated in the same way as the direct scattering amplitude, except that the outgoing electrons in the final state are interchanged. In calculating scattering amplitudes, the initial state is the product of the incident distorted wave, $\chi_0^+(\boldsymbol{k}_0, \boldsymbol{r}_1)$, and the orientation averaged Dyson orbital $\phi_{DY}^{OA}(\boldsymbol{r}_2)$. The final state is described as the product of distorted waves for the two outgoing electrons, $\chi_1^-(\boldsymbol{k}_1, \boldsymbol{r}_1)$ and $\chi_2^-(\boldsymbol{k}_2, \boldsymbol{r}_2)$, and a Coulomb distortion factor $C_{scat-ejec}(\boldsymbol{r}_{12})$. Here $\boldsymbol{r}_{12}$ is the distance between the two out-going electrons. If we neglect the Coulomb distortion factor in the final state, the M3DW reduces to the distorted-wave Born approximation (DWBA).

To calculate a TDCS employing a proper average, the fixed-in-space Dyson orbital replaces the orientation averaged Dyson orbital in the description of the initial state. The proper-averaged TDCS can then be obtained from the TDCS for fixed-in-space molecules by numerically performing a subsequent spherical averaging procedure.[14]

For furfural, the orientation-averaged or fixed-in-space Dyson orbitals are obtained using a frozen-orbital approximation. The Dyson orbital is then described by the ionized Kohn-Sham orbital (either 4a″ or 21a′) calculated within a Density Functional Theory framework employing the standard hybrid B3LYP functional[30] with a TZ2P (triple-zeta with two polarization functions) Slater type basis set within the ADF 2007 (Amsterdam Density Functional) program.[33] More details about the M3DW method can be found in Madison and Al-Hagan.[34]

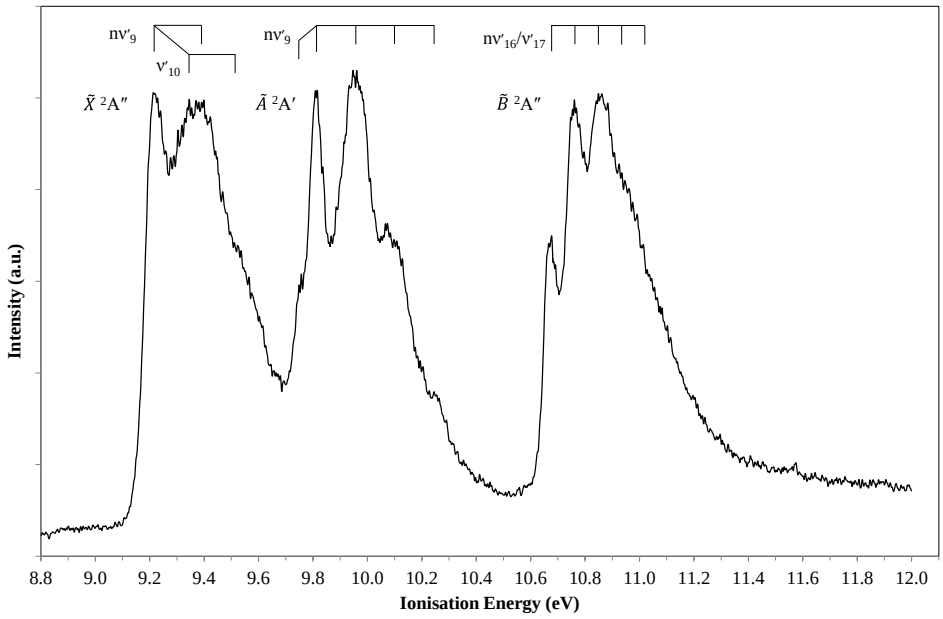

FIG. 3. The present He(I) photoelectron spectrum of furfural as measured in the 8.8 – 12.0 eV binding energy region.

In order to compare the calculated TDCS to the data, the TDCS were calculated for the HOMO and NHOMO of furfural in both the *cis* and *trans* conformers. A relative conformer population weighting of 0.205×(*cis*) and 0.795×(*trans*) was then applied, which is in line with the known relative populations of the two conformers in the gas phase under the experimental conditions.[10,11] Owing to the high computational cost of performing the

proper average calculations, these calculations were only performed for the NHOMO of the *trans* geometry which displayed a larger cross section at the M3DW level. As the proper average calculations are only performed for the NHOMO, we apply a normalisation factor to rescale this calculation so it can be compared with the experimental data and M3DW calculation. That normalisation factor was determined using a least squares fitting procedure applied to the normalised experimental data of the binary region of the θ_1 = -10° angular distribution.

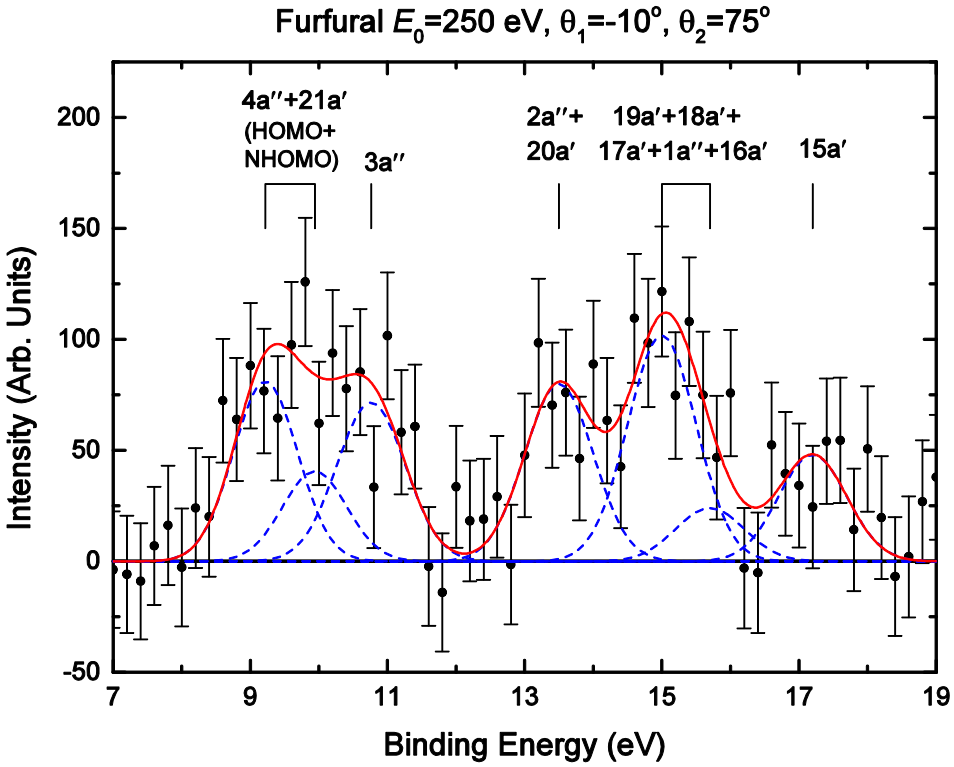

FIG. 4. A representative binding energy spectrum of furfural obtained in asymmetric coplanar kinematics with E_0 = 250 eV, E_2 = 20 eV and the scattered and ejected electrons being detected at $\theta_1 = -10^o$ and $\theta_2 = 75^o$, respectively.

IV. RESULTS AND DISCUSSION

A. Photon and electron impact ionization and state assignments

In Figures 3 and 4, we present our high resolution photoelectron spectrum and the (*e*,2*e*) binding energy spectrum obtained in the asymmetric coplanar geometry. In Table 1, we further present a summary of the electronic state assignments, and where possible the

assignments of the vibrational substructure for the ionic states of furfural. Those assignments are additionally compared to results from the calculations, and those made using the photoelectron spectrum previously reported by Klapstein and co-workers.[12] The high resolution photoelectron spectra displays three distinct bands, peaking at 9.223 ± 0.002 eV (4a″, π), 9.956 ± 0.002 (21a′, n_O) and 10.678 ± 0.002 (3a″, π) eV. These values are largely consistent with the early photoelectron spectroscopic investigation.[12] The ionization processes of these three features either relates to the removal of electrons from the π-bonding structure of the 5-member ring, or to the oxygen lone-pair (n_O) in the carbonyl group. We do however note that in the 21a′ orbital, the in-plane oxygen lone electron pair (n_O) does couple to the carbon frame through a σ–like interaction. The calculated values, shown in Table 1, further suggest that both the *cis* and *trans* conformers all have very similar ionization energies. The measured low-lying vertical ionization energies of furfural in both conformations agree reasonably well, to within ±0.5 eV, with the OVGF theoretical predictions. Here the OVGF theory is consistent with results from the Density Functional Theory calculations at the B3LYP/aug-cc-pVDZ level, in that the ordering of the HOMO and NHOMO are 4a″ and 21a′, respectively.

The high-resolution photoelectron spectra also shows substantially more detail for each of the initial three ionic bands than had been previously observed. The structures within each of these features are reminiscent of those observed in previous studies on furan,[35] its methyl derivative,[36] and 2-vinyl furan.[37] The first adiabatic energy of furfural is 9.223 ± 0.002 eV (Figure 3 and Table 1), followed by a vibrational peak centred at 9.382 eV, which is 0.159 eV from the 0–0 transition. This peak is quite broad and asymmetric, and on the low energy side, a structure may be tentatively positioned at 0.123 eV from the origin. The weak broad band at higher energy (9.52(7) eV) may be mainly assigned to combination and overtone bands of these two vibrations. However, the relatively poorer apparent resolution here compared with the corresponding band in furan[35] and the other furan derivatives[36,37] suggests that many vibrations may be actively adding to the line width. This assignment of vibrational states is further complicated by the observation of Fermi resonances in the infrared vibrational excitation spectra.[38] We therefore tentatively propose the following possible vibrational mode assignments (with ground state vibration energies for *trans*- and *cis*-conformers, respectively): to the main 0.159 eV peak, ν_9 (0.169

eV) with other possible contributing vibrational modes ν_6 (0.195 and 0.194 eV), ν_7 (0.182 and 0.183 eV) and ν_8 (0.173 eV), and to the 0.123 eV feature, ν_{10} (0.155 and 0.158 eV). All these vibrations are totally symmetric (a′)[38] and involve displacement of the heavier atoms (C and O).[39] For the next ionic band, $\tilde{A}\,^2A'$, the peak at 9.813 ± 0.002 eV is assigned to the 0–0 transition. The peak at 9.956 eV, is therefore 0.143 eV from this origin. A possible contributing vibrational mode in this case is (with ground state vibration energies for *trans*- and *cis*-conformers, respectively) ν_9 (0.169 eV). A weak shoulder appears on the low energy side of the 0–0 transition, around 0.048 eV, and may be due to a hot-band involving mode ν_{18} (0.062 eV). As far as the third ionic band is concerned, we assign the structure to either excitation of mode ν_{16} (0.109 eV) or ν_{17} (0.094 eV). As a consequence we have labelled its features in Figure 3 and Table 1 as ν_{16} / ν_{17}.

TABLE 1. Experimental and theoretical ionization potentials (eV) of furfural. Also presented are the ionic vibrational state assignments and calculated pole strengths.

	Present PES						*cis*-furfural OVGF/aug-cc-pvdz		*trans*-furfural OVGF/aug-cc-pvdz	
Present (e,2e)	Energy (eV)	$\Delta\nu'$ (eV)	$\Delta\nu'$ (eV)	Assignment	PES[12]	State	Energy (eV)	PS	Energy (eV)	PS
9.2	9.223[a]	…	…	ν_{00}	9.22	$(4a'')^{-1}$	9.25	0.90	9.18	0.90
	9.346	0.123	…	$1\nu'_{10}$	9.32					
	9.382	…	0.159	$1\nu'_{9}$[b]	9.39					
	9.52(7)[c]	…	0.181	$1\nu'_{10}+1\nu'_{9}$[b]	9.57					
9.9	9.765	0.048	…	ν_{18}	…	$(21a')^{-1}$	10.46	0.88	10.49	0.88
	9.813[a]	…	…	ν_{00}	9.80[a]					
	9.956[d]	…	0.143	$1\nu'_{9}$	9.94[d]					
	10.07(4)[c]	…	0.118	$2\nu'_{9}$	10.08					
	10.24(8)[c]	…	0.174	$3\nu'_{9}$	10.22					
10.8	10.678	…	…	ν_{00}	10.67	$(3a'')^{-1}$	10.78	0.89	10.74	0.89
	10.765	0.087	…	$1\nu'_{16}/1\nu'_{17}$	10.76					
	10.860	0.095	…	$2\nu'_{16}/2\nu'_{17}$	10.86					
	10.92(9)[c]	0.069	…	$3\nu'_{16}/3\nu'_{17}$	10.96					
	11.02(6)[c]	0.097	…	$4\nu'_{16}/4\nu'_{17}$	…					
13.5					13.5	$(2a'')^{-1}$	13.76	0.83	13.79	0.83
						$(20a')^{-1}$	13.81	0.90	13.85	0.90
					14.3	$(19a')^{-1}$	14.57	0.90	14.52	0.90
15.0					14.8	$(18a')^{-1}$	14.72	0.89	14.68	0.89
15.7					15.97	$(17a')^{-1}$	15.74	0.87	15.30	0.88
						$(1a'')^{-1}$	15.77	0.76[e]	15.76	0.75[e]
						$(16a')^{-1}$	15.89	0.86	16.42	0.87
17.2					17.2	$(15a')^{-1}$	17.97	0.85	17.91	0.86

[a] Adiabatic value.
[b] See text for more detail.
[c] Shoulder structure (the last decimal of the energy value is given in brackets for these less-resolved features).
[d] Vertical value.
[e] Here the one-particle picture of ionization is breaking down.

B. Electron impact ionization dynamics

In Fig. 5, triple differential cross sections (TDCS) for the electron impact ionization of the unresolved HOMO+NHOMO (4a″+21a′) are presented, measured in the doubly symmetric coplanar geometry with a detected electron energy of 20 eV. The measured TDCS are compared to theoretical calculations performed at the distorted wave Born approximation (DWBA) and the molecular three-body distorted wave (M3DW) level. In order to facilitate a qualitative comparison between the experiment and different calculations, both the theoretical and experimental results have been normalised to unity at $\xi_1 = \xi_2 = \xi = 45°$ as noted above. In this comparison, it is observed that the DWBA calculation adequately reproduces the shape of the data in the 35-65° range. However, the DWBA calculation gives unphysical behaviour in the limit of $\xi = 0°$, where the TDCS must be zero owing to the repulsive Coulombic interaction between the outgoing electrons. The M3DW calculation correctly accounts for this asymptotic behaviour, however it fails to predict the correct shape of the experimental TDCS. Note that the TDCS data increases in intensity as the angle of detection increases from 100-120°. Interestingly, however, both the DWBA and M3DW calculations predict decreasing intensity as this angle increases.

Triple differential cross sections (TDCSs) have also been measured in an asymmetric coplanar geometry, with the results presented in Fig. 6. Here angular distributions of the ejected electrons (E_2 = 20eV) were measured while the scattered electrons were detected at fixed angles of (a) $\theta_1 = -5^o$, (b) $\theta_1 = -10^o$, and (c) $\theta_1 = -15^o$. The TDCS are compared with corresponding results from M3DW calculations (for the HOMO+NHOMO) that either employ an orientation average molecular orbital (OAMO) or include a proper average to account for the random orientation of the target in the experiment. Here we again note that as the experimental angular distributions for each scattered electron angle have been inter-normalised, only a single normalisation factor is employed between the M3DW calculation and the experimental data. We reiterate that this factor was determined using a least squares technique in the binary region of the $\theta_1 = -10^o$ angular distribution.

In contrast to the doubly symmetric coplanar geometry, the M3DW calculations using an OAMO approach (dashed red line) qualitatively reproduce the shape and relative

magnitude of the TDCS for the scattering angles of $\theta_1 = -5^o$ and -10° (see Fig. 6). However, the M3DW (OAMO) calculations fail to reproduce the experimental behaviour observed when the scattered electron angle is changed to $\theta_1 = -15^o$. Specifically, the M3DW (OAMO) predicts that the TDCS has a maximum intensity in the direction of the momentum transfer, while experimentally a minimum is observed. The M3DW (OAMO) calculation also predicts a greater recoil intensity than that observed experimentally at $\theta_1 = -5^o$ and -15°.

To try to understand these deficiencies in the M3DW (OAMO) model, calculations employing a proper TDCS average were also performed. These calculations are computationally demanding, so they were restricted to electron-impact ionization of the NHOMO. This restriction, being different from that which is measured in the experiments, led us to normalise those proper average calculations to the experimental data. It is hoped that these computationally demanding calculations for the NHOMO will still provide some insights into the merits of the proper TDCS averaging procedure in general. These results are represented by the solid green lines in Fig. 6.

The proper average result has more success in resolving the observed discrepancies in the angular distribution of the binary region for a scattered electron angle of $\theta_1 = -15^o$. Further, the proper average result displays relative binary and recoil peak intensities that are somewhat consistent with those observed experimentally. This suggests that the proper average might resolve the deficiencies within the OAMO approach. However the significant computational cost, thus only allowing for the calculation of the proper average TDCS for the NHOMO, while experimentally the HOMO and NHOMO are investigated, does limit our ability to fully assess the merits of this theoretical approach.

It is therefore important to try to understand the sources of the discrepancies observed between experiment and theory at the M3DW (OAMO) level, particularly given this high computational cost of carrying out the proper average calculations. To assist in this, TDCS obtained at the M3DW level (with an orbital average) for the HOMO and NHOMO of both conformers are presented in Fig 7. Additionally in Fig. 8 we present orbital momentum profiles and schematic diagrams of the ionized orbitals. In Fig. 7, it is seen that the TDCS calculated for the NHOMO is substantially larger in magnitude than

that for the HOMO, for almost the entire angular distribution of each scattered electron angle considered. When the spherically averaged momentum profiles for the HOMO and NHOMO are considered in Fig. 8, it is only in the smallest (< ~0.3 a.u.) or largest (> ~1.3 a.u.) momentum regions that the NHOMO displays larger intensity than that for the HOMO. Note that in high-impact energy electron impact ionization kinematics where the collision can be described impulsively, the TDCS is proportional to the modulus squared of the spherically averaged orbital momentum profile (*i.e.* so called electron momentum spectroscopy[25,40]). While the present asymmetric coplanar kinematical conditions substantially differ from those required to probe the orbital structure, we have previously observed that the underlying orbital character still persists in the angular distribution of the dynamical TDCS under similar conditions.[16-20] Here, we note that the influence of an orbital's character to TDCS behaviour was first discussed in Xu *et al*.[41] in this study, the range of recoil momenta magnitudes covered in these asymmetrical kinematics are 0.77-1.66 a.u., 0.44-1.98 a.u. and 0.10-2.33 a.u for $\theta_1 = -5^o$, -10^o and -15°, respectively. For this reason, it appears that the calculations for the TDCS of the M3DW (OAMO) HOMO may be substantially underestimated. Note also that the M3DW failed to describe the observed angular distribution for the HOMO+NHOMO of phenol.[19] In the case of phenol, both the HOMO and NHOMO are dominated by orbital contributions that form an out-of-plane π-bonding network. This is similar to the HOMO of furfural, which can also be described as an out-of-plane π-bonding orbital. We therefore suspect that the inverse symmetry, or a substantial delocalisation of these orbital contributions away from the nucleons, is the cause of the reduction in the TDCS intensity of the HOMO within the orbital average M3DW framework. This therefore represents a limitation in the application of that theoretical approach.

V. CONCLUSIONS

In this manuscript an in-depth study into the photon and electron impact ionization to low-lying ionic states of furfural has been presented. Measurement of high resolution He(I) photoelectron spectra has provided the first vibrational spectral assignments of the ionic states. The dynamics of the electron-impact ionization process has been evaluated in asymmetric coplanar and doubly symmetric coplanar geometries. These results have been compared to those from sophisticated molecular three-body distorted wave calculations

that employ either an orbital or proper average to account for the random orientation of the target. It was observed that in asymmetric kinematics, the orientation average failed to accurately reproduce the angular dependence of the measurements over the complete set of kinematical conditions studied experimentally. The inter-normalisation of the experimental TDCS measurements for different scattered angles also revealed discrepancies with the absolute scale of the M3DW calculations within the orbital average formulation. TDCSs calculated using a proper average appear to resolve some of these problems, however their high computational cost makes them prohibitive for calculating all possible contributing states (the results presented here took over one year to calculate using all of the available computing resources at our disposal). It therefore remains desirable to understand the limitations within the orientation average M3DW model. Clearly, strategies for reducing the computational demands of the proper average calculations are desirable so that the merits of this approach can be definitively assessed.

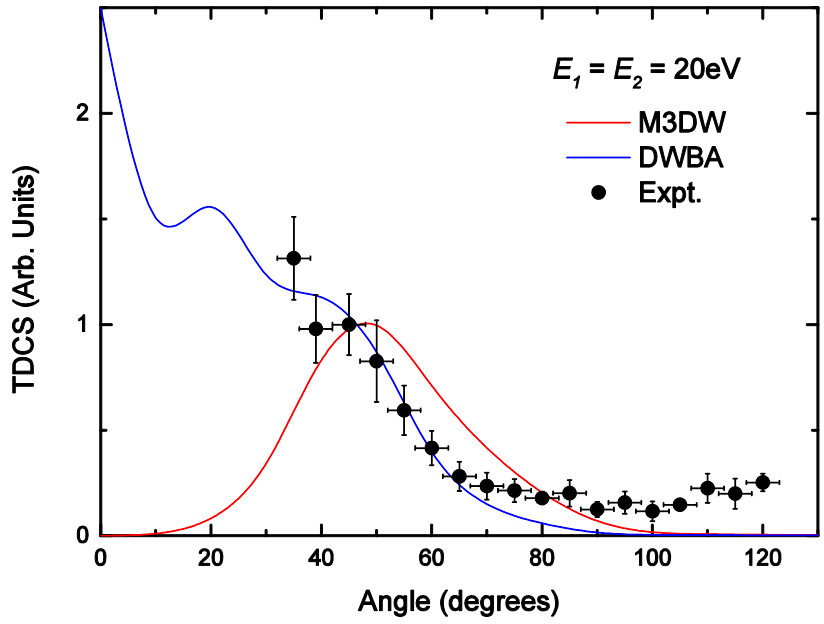

FIG.5. Experimental and theoretical triple differential cross sections for electron impact ionization of the unresolved HOMO+NHOMO (4a″+21a′) of furfural in the double symmetric coplanar geometry. Here the electrons were detected with $E_1 = E_2 = 20$ eV. See also legend in figure.

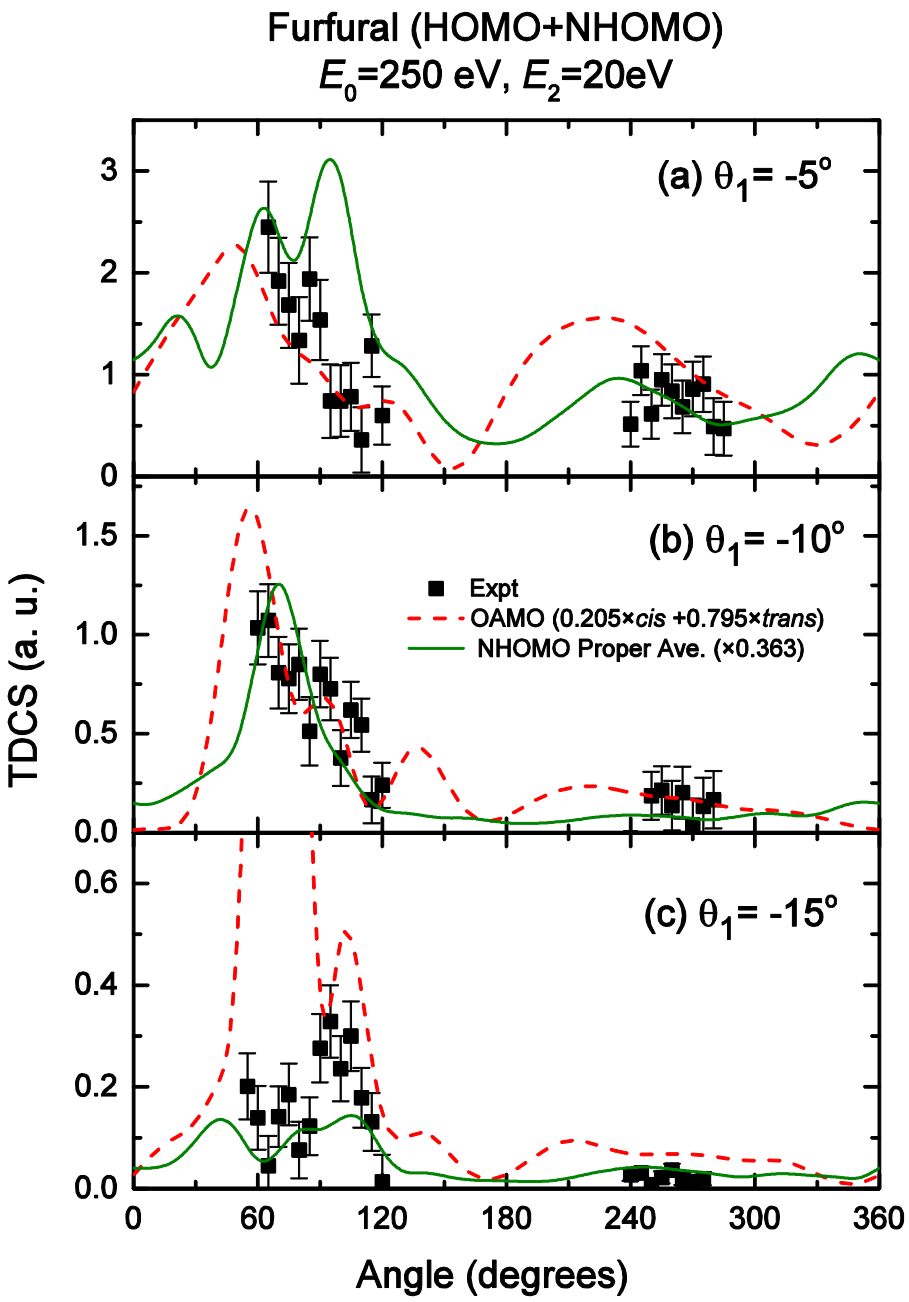

FIG. 6. Experimental and theoretical triple differential cross sections for electron impact ionization of the HOMO+NHOMO (4a″ +21a′) of furfural in the asymmetric kinematics with E_0 = 250 eV, E_2 = 20 eV, and with the scattered electron being detected at (a) $\theta_1 = -5^o$, (b) $\theta_1 = -10^o$, and (c) $\theta_1 = -15^o$. See text and legend in figure for further details. Note that a.u. here represents atomic units.

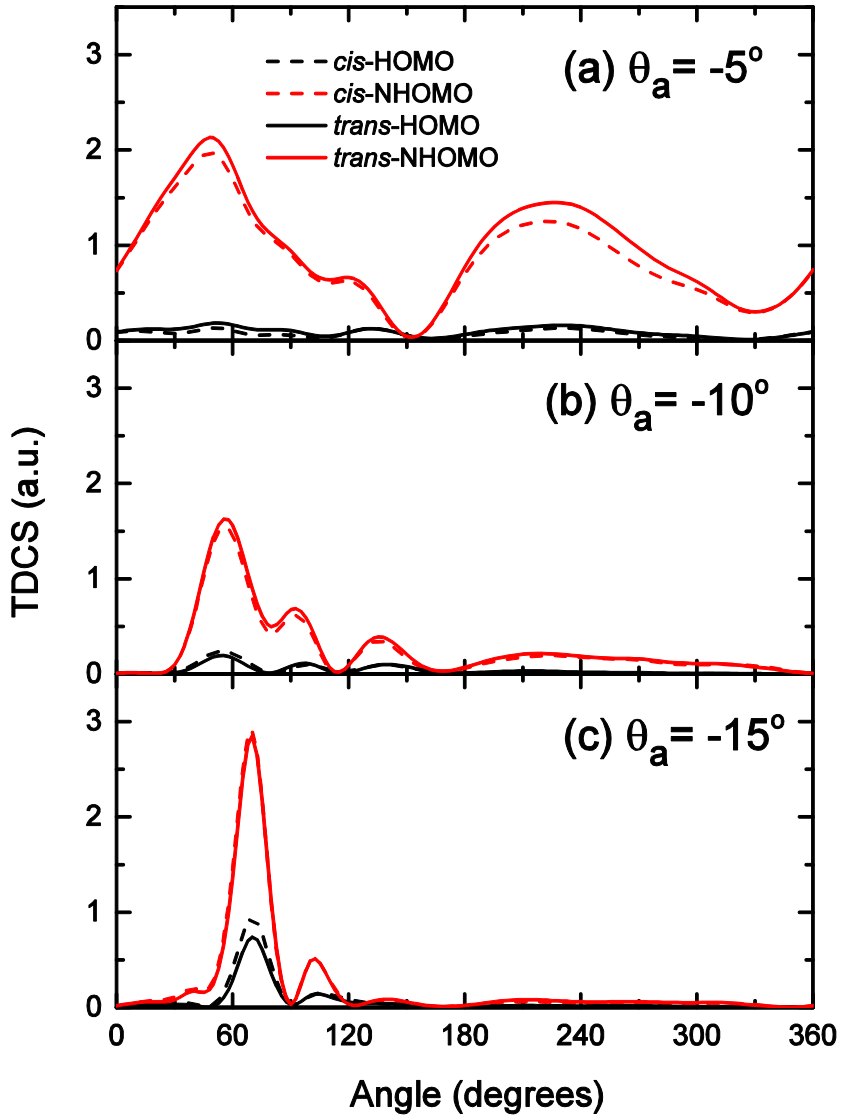

FIG. 7. Theoretical M3DW orientation averaged molecular orbital (OAMO) triple differential cross sections for electron impact ionization of the HOMO and NHOMO of each furfural conformer. Results are for asymmetric coplanar kinematics with E_0 = 250 eV, E_2 = 20 eV, and with the scattered electrons being detected at(a) $\theta_1 = -5^o$, (b) $\theta_1 = -10^o$, and (c) $\theta_1 = -15^o$. Note that a.u. here represents atomic units. See also legend in figure.

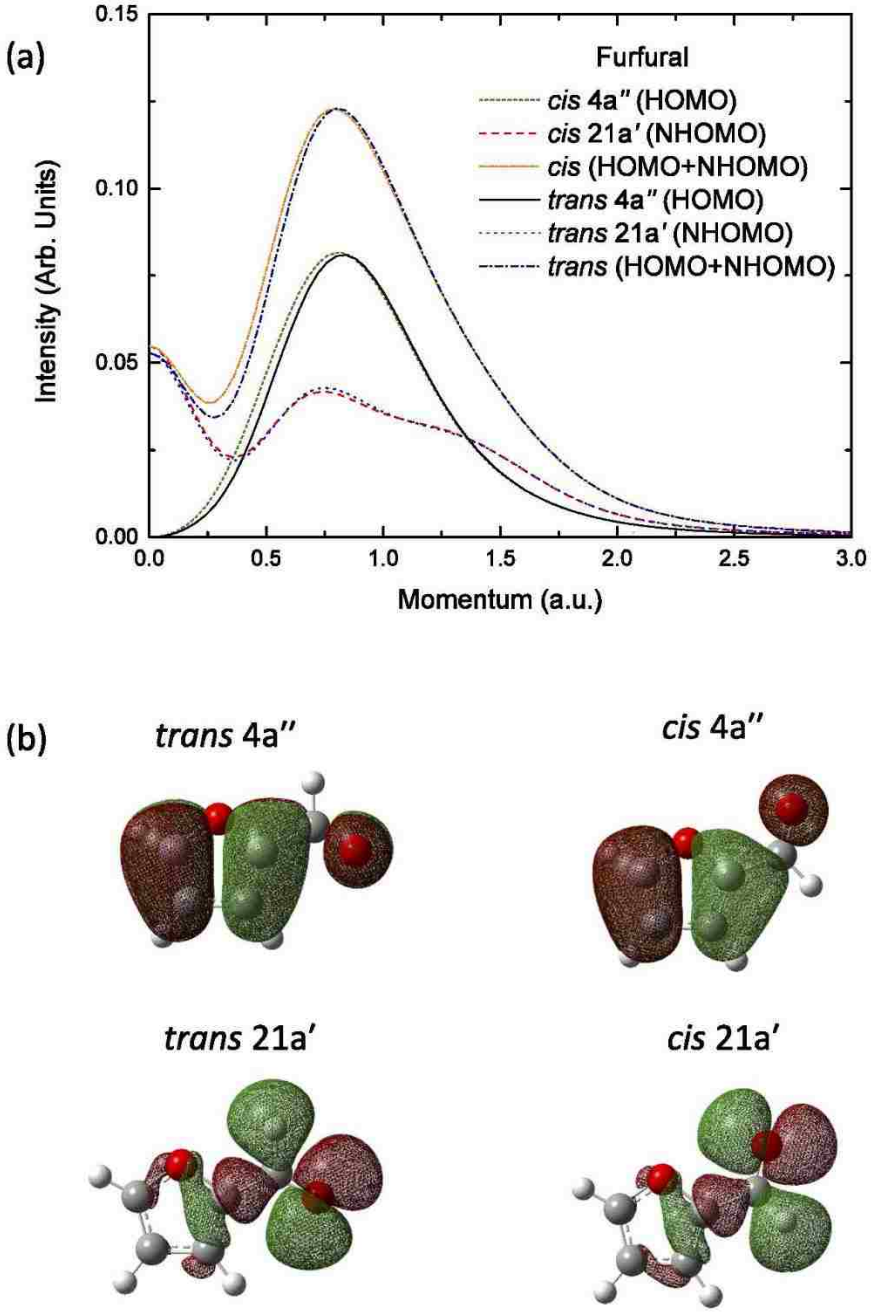

FIG**.** 8. (a) Theoretical spherically averaged momentum profiles and (b) molecular orbital representations of the HOMO and NHOMO of furfural in both the *cis* and *trans* conformers. See also legend in figure.

ACKNOWLEDGMENTS

PLV acknowledges the Portuguese Foundation for Science and Technology (FCT-MEC) through research grants PTDC/FIS-ATO/1832/2012, SFRH/BSAB/105792/2014 and UID/FIS/00068/2013. He also acknowledges his Visiting Professor position at Flinders

University and together with M-JH-F the Portuguese–Belgian joint collaboration. The Patrimoine of the University of Liège, the Fonds National de la Recherche Scientifique and the Fonds de la Recherche Fondamentale Collective of Belgium have supported this research. DBJ thanks the Australian Research Council for financial support provided through a Discovery Early Career Research Award, while MJB also thanks the Australian Research Council for financial support. E.A. and D.H.M. acknowledge support of the U.S. National Science Foundation (NSF) under Grant. No. PHY-1068237 and XSEDE resources provided by the Texas Advanced Computing Center (Grant No. TG-MCA07S029). Computational work was performed with Institutional Computing resources made available through the Los Alamos National Laboratory. The Los Alamos National Laboratory is operated by Los Alamos National Security, LLC, for the National Nuclear Security Administration of the US Department of Energy under Contract No. DE-AC5206NA25396. C.G.N. acknowledges support of the National Natural Science Foundation of China (NNSFC) under Grant No. 11174175. KLN would like to thank CNPq for an 'Attracting Young Talent' grant and also thanks the Royal Society for funding her visit to the University of Manchester as a Newton Alumni. We all thank Rafael Neves for some assistance in operating the spectrometer at Flinders.

[1]A. S. Mamman, J.-M. Lee, Y.-C. Kim, I. T. Hwang, N.-J. Park, Y. K. Hwang, J.-S. Chang and J.-S. Hwang, Biofuel. Bioprod. Bior. **2**, 438 (2008).

[2]H. Gomez Bernal, L. Bernazzani and A. M. Raspolli Galletti, Green Chemistry **16**, 3734 (2014).

[3]J.-P. Lange, E. van der Heide, J. van Buijtenen and R. Price, ChemSusChem **5**, 150 (2012).

[4]A. J. Ragauskas, C. K. Williams, B. H. Davison, G. Britovsek, J. Cairney, C. A. Eckert, W. J. Frederick, J. P. Hallett, D. J. Leak, C. L. Liotta, J. R. Mielenz, R. Murphy, R. Templer and T. Tschaplinski, Science **311**, 484 (2006).

[5]J. Amorim, C. Oliveira, J. A. Souza-Corrêa and M. A. Ridenti, Plasma Process. Polym. **10**, 670 (2013).

[6]N. Schultz-Jensen, F. Leipold, H. Bindslev and A. Thomsen, Appl. Biochem. Biotechnol. **163**, 558 (2011).

[7]J. S. Bak, J. K. Ko, Y. H. Han, B. C. Lee, I.-G. Choi and K. H. Kim, Bioresource Technol. **100**, 1285 (2009).

[8]A. W. Khan, J. P. Labrie and J. McKeown, Biotechnol. Bioeng. **28**, 1449 (1986).

[9]V. A. Igor and R. L. Walter, Plasma Physics and Controlled Fusion **57**, 014001 (2015).

[10]K. K. Baldridge, V. Jonas and A. D. Bain, J. Chem. Phys. **113**, 7519 (2000).

[11]T. S. Little, J. Qiu and J. R. Durig, Spectrochim. Acta A **45**, 789 (1989).

[12]D. Klapstein, C. D. MacPherson and R. T. O'Brien, Can. J. Chem. **68**, 747 (1990).

[13]F. Ferreira da Silva, E. Lange, P. Limão-Vieira, N. C. Jones, S. V. Hoffmann, M.-J. Hubin-Franskin, J. Delwiche, M. J. Brunger, R. F. C. Neves, M. C. A. Lopes, E. M. de Oliveira, R. F. da Costa, M. T. do N. Varella, M. H. F. Bettega, F. Blanco, G. García, M. A. P. Lima and D. B. Jones, J. Chem. Phys. (submitted, 2015).

[14]H. Chaluvadi, C. G. Ning and D. Madison, Phys. Rev. A **89**, 062712 (2014).

[15]S. M. Bellm, J. D. Builth-Williams, D. B. Jones, H. Chaluvadi, D. H. Madison, C. G. Ning, F. Wang, X. G. Ma, B. Lohmann and M. J. Brunger, J. Chem. Phys. **136**, 244301 (2012).

[16]J. Builth-Williams, S. M. Bellm, D. B. Jones, H. Chaluvadi, D. Madison, C. G. Ning, B. Lohmann and M. J. Brunger, J. Chem. Phys. **136**, 024304 (2012).

[17]J. D. Builth-Williams, S. M. Bellm, L. Chiari, P. A. Thorn, D. B. Jones, H. Chaluvadi, D. H. Madison, C. G. Ning, B. Lohmann, G. B. da Silva and M. J. Brunger, J. Chem. Phys. **139**, 034306 (2013).

[18]D. B. Jones, J. D. Builth-Williams, S. M. Bellm, L. Chiari, H. Chaluvadi, D. H. Madison, C. G. Ning, B. Lohmann, O. Ingolfsson and M. J. Brunger, Chem. Phys. Lett. **572**, 32 (2013).

[19]G. B. da Silva, R. F. C. Neves, L. Chiari, D. B. Jones, E. Ali, D. H. Madison, C. G. Ning, K. L. Nixon, M. C. A. Lopes and M. J. Brunger, J. Chem. Phys. **141**, 124307 (2014).

[20]J. D. Builth-Williams, G. B. da Silva, L. Chiari, D. B. Jones, H. Chaluvadi, D. H. Madison and M. J. Brunger, J. Chem. Phys. **140**, 214312 (2014).

[21]J. Delwiche, P. Natalis, J. Momigny and J. E. Collin, J. Electron Spectrosc. Relat. Phenom. **1**, 219 (1972).

[22]J. H. D. Eland, *Photoelectron spectroscopy*. (Butterworth & Co Ltd., London, 1984).

[23]D. R. Lide, *Handbook of Chemistry and Physics*. (CRC Press, New York, 1992).

[24]S. J. Cavanagh and B. Lohmann, J. Phys. B: At. Mol. Opt. Phys. **32**, L261 (1999).

[25]A. J. Murray, B. C. H. Turton and F. H. Read, Rev. Sci. Instrum. **63**, 3346 (1992).

[26]W. von Niessen, J. Schirmer and L. S. Cederbaum, Computer Physics Reports **1**, 57 (1984).

[27]T. H. Dunning, J. Chem. Phys. **90**, 1007 (1989).

[28]R. A. Kendall, T. H. Dunning and R. J. Harrison, J. Chem. Phys. **96**, 6796 (1992).

[29]C. Lee, W. Yang and R. G. Parr, Phys. Rev. B **37**, 785 (1988).

[30]J. P. D. Cook and C. E. Brion, Chem. Phys. **69**, 339 (1982).

[31]M. J. Frisch *et al.*, *Gaussian 09, Revision B.01*, Gaussian Inc., Wallington CT, USA (2010).

[32]G. te Velde, F. M. Bickelhaupt, E. J. Baerends, C. Fonseca Guerra, S. J. A. van Gisbergen, J. G. Snijders and T. Ziegler, J. Comput. Chem. **22**, 931 (2001).

[33]D. H. Madison and O. Al-Hagan, Journal of Atomic, Molecular, and Optical Physics **2010**, 367180 (2010).

[34]E. E. Rennie, C. A. F. Johnson, J. E. Parker, D. M. P. Holland, D. A. Shaw, M. A. MacDonald, M. A. Hayes and L. G. Shpinkova, Chem. Phys. **236**, 365 (1998).

[35]A. Giuliani, J. Delwiche, S. V. Hoffmann, P. Limão-Vieira, N. J. Mason and M.-J. Hubin-Franskin, J. Chem. Phys. **119**, 3670 (2003).

[36]A. Giuliani, I. C. Walker, J. Delwiche, S. V. Hoffmann, C. Kech, P. Limão-Vieira, N. J. Mason and M.-J. Hubin-Franskin, J. Chem. Phys. **120**, 10972 (2004).

[37]M. Rogojerov, G. Keresztury and B. Jordanov, Spectrochim. Acta A **61**, 1661 (2005).

[38]T. Kim, R. S. Assary, L. A. Curtiss, C. L. Marshall and P. C. Stair, Journal of Raman Spectroscopy **42**, 2069 (2011).

[39]E. Weigold and I. E. McCarthy, *Electron Momentum Spectroscopy* (Kluwer Academic/Plenum Publishers, New York, 1999).

[40]M. Takahashi, Bull. Chem. Soc. Jpn. **82**, 751 (2009).

IV. Comparison of experimental and theoretical triple differential cross sections for the single ionization of CO_2 ($1\pi_g$) by electron impact

Zehra N. Ozer*[1], Esam Ali[2], Mevlut Dogan[1], Murat Yavuz[1], O. Alwan[3,4], A. Naja[3], O. Chuluunbaatar[5], B. B. Joulakian[4], C. Ning[6], James Colgan[7] and Don Madison[2]

[1]Department of Physics, e-COL Laboratory, Afyon Kocatepe University, 03200, Afyon, Turkey

[2]Department of Physics, Missouri University of Science and Technology, Rolla MO 65409, USA

[3]Lebanese University, LPM, EDST, Tripoli, Lebanon

[4]Universitè de Lorraine, SRSMC (UMR CNRS 7565), 1 bld Arago, bat. ICPM 57078 Metz Cedex 3, France

[5]Joint Institude for Nuclear Research, Dubna, Moscow Region 141980

[6]Department of Physics, State Key Laboratory of Low-Dimensional Quantum Physics, Tsinghua University, Beijing 100084, China

[7]Theoretical Division, Los Alamos National Laboratory, Los Alamos, NM 87545

Experimental and theoretical triple differential cross sections (TDCSs) for intermediate energy (100 eV – 400 eV) electron-impact single ionization of the CO_2 are presented for three fixed projectile scattering angles. Results are presented for ionization of the outer most $1\pi_g$ molecular orbital of CO_2 in a coplanar asymmetric geometry. The experimental data are compared to predictions from the three center Coulomb continuum (ThCC) approximation for triatomic targets, and the molecular three body distorted wave (M3DW) model. It is observed that while both theories are in reasonable qualitative agreement with experiment, the M3DW is in the best overall agreement with experiment.

1. INTRODUCTION

Electron impact single ionization of molecules is of interest not only due to practical applications, but also due to obtaining a better understanding of fundamental physics. On the practical application side, studies of electron impact ionization of atmospheric molecules are useful for controlling and monitoring global warming. Information on single ionization of atmospheric molecules is also important both for understanding the development of planetary atmospheres and controlling the events in the ionosphere and its neighboring regions

For a number of reasons, CO_2 is one of the most important gases on Earth. Plants use CO_2 to produce sugars and starches in photosynthesis that are necessary for the survival of life. CO_2 in the atmosphere is also important because it absorbs heat radiated from the Earth's surface and increasing levels of CO_2 in the atmosphere may be responsible for long term changes in the earth's climate.

CO_2 is also an important molecule in applied fields from astrophysics to plasma chemistry and it is the main component in the atmospheres of Venus and Mars so it is an important molecule to study and understand. Fully differential electron-impact ionization studies, called (e,2e), provide the richest information for understanding the dynamics of the reaction process and also the dynamics of the target for ionization of atoms/molecules. The motivation of this work is to present new experimental and theoretical results to further study the dynamics of such reactions. Since CO_2 is a linear triatomic molecule, it is a good starting point, which could motivate studies of more complicated polyatomic molecules.

Due to the growing interest on the behavior of this molecule, some reviews have been published for different types of cross sections [1]-[4]. Several groups have measured the angular distribution of electrons elastically scattered from CO_2 for intermediate [5] and low energies [6]-[7]. Some works have concentrated on determining the absolute scale of the cross sections [8]-[10]. Comprehensive sets of cross sections have been presented for a number of processes (total, elastic scattering, momentum transfer, excitation, ionization and electron attachment) [11] to provide benchmark data. There are a few studies on the double differential cross sections (DDCSs) of secondary electrons ejected from CO_2 at intermediate energies in literature [12]-[13]. The results indicate good agreement between

theory and other experimental results. However, significant differences are observed for higher energies [13].

Despite all this work, detailed experimental and theoretical examinations of triple differential cross section (TDCS) for electron-CO_2 collisions have been relatively few. The first experimental (e,2e) study was done by Hussey and Murray [14]. They presented differential ionization cross sections for low energy electron scattering from the $1\pi_g$ and $4\sigma_g$ orbitals of CO_2 for 10-80 eV incident electron energies in coplanar symmetric (e,2e) experiments. The results were compared with the same energy range results for the diatomic molecule N_2. A double forward peak was observed at low angles and energies for the CO_2 $1\pi_g$ state but not N_2 [14]. TDCSs for CO_2 and N_2 molecules in coplanar asymmetric geometry at incident electron energies around 500-700 eV were measured by Lahmam-Bennani *et al.* [15] for cases corresponding to large momentum transferred to the ion which yields larger recoil scattering. The experimental data are compared to theoretical calculations using the first Born approximation-two center continuum (FBA-TCC) approach [16] and the theoretical description was not able to explain the origin of the main structures for the binary and recoil regions.

In this work, we will compare experiment with the two center Coulomb continuum (TCC) and the molecular 3-body distorted wave (M3DW) approximation. Chuluunbaatar and Joulakian extended the TCC model to three centers to obtain a better theoretical description for ionizing linear polyatomic targets, and used the new model to determine differential cross sections for the outer most and inner shell orbitals of CO_2 [15][17]. We will label this approach as the three center continuum (ThCC) approximation. The theory was further modified to use Dyson Gaussian orbitals and the results gave better agreement with the experimental data [18].

The M3DW has previously been applied to several molecular targets. A summary of this work up to 2010 was given by Madison and Al Hagan [19]. More recently, studies have been performed for ionization of CH_4 [20], [21], tetrahydrofuran and tetrahydrofurfuryl [22], NH3 [23], the cyclic ethers tetrahydrofuran, tetrahydropyran and 1,4-dioxane [24], tetrahydropyran and 1,4-dioxane [25], phenol [26], N_2 [27], ethane [28], and furfural [29]. The M3DW has not been previously applied to CO_2.

In this work, experimental and theoretical coplanar TDCS results will be presented for ionization of the CO_2 $1\pi_g$ state for an incident electron energy of 250 eV, an ejected electron energy of 37 eV, and for three fixed faster electron angles of (10^0, 20^0, 30^0).

A schematic diagram of the geometry is presented in Fig. 1. The incident electron has energy E_i and momentum k_i, the faster final-state electron is detected at an angle θ_a with energy E_a and momentum k_a and the slower final-state electron is detected at an angle θ_b with energy E_b and momentum k_b. The momentum transfer direction is defined by

$$\mathbf{q} = \mathbf{k}_i - \mathbf{k}_a \tag{1}$$

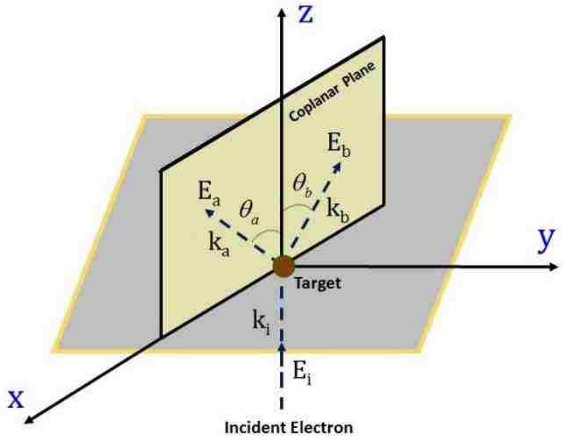

FIG.1. (Color online) Schematic drawing of the experimental geometry.

II. EXPERIMENTAL PROCEDURE

The measurements have been carried out using an (e,2e) coincidence spectrometer. The experimental geometry used is coplanar asymmetric geometry which means that the incident, scattered and ejected electrons are in a single plane. The scattered electron is detected at a fixed forward angle in coincidence with ejected electron angles ranging from 30^0 to 130^0. The experimental conditions for these measurements were incident electron energy E_i=250 eV, faster final state electron angle θ_a= 10^0-30^0, slower final state electron energy E_b= 37 eV. The binding energy of the CO_2 $1\pi_g$ orbital is 11.7 eV. The faster final state electron energy is E_a= 201.3 eV which is determined by energy conservation. Of

course, we do not know which electron is the scattered electron and which electron is the ejected electron but, for discussion purposes, we call the faster final state electron the scattered electron and the slower final state electron the ejected electron.

Since the apparatus is of a conventional design, only a brief description will be given here. Electrons emitted from a tungsten filament are accelerated and focused to the interaction region to produce a beam of desired energy which can range between 40-350 eV by using the electrostatic lenses of an electron gun. The beam is then perpendicularly crossed with the gas beam. The outgoing electrons are energy selected by using two rotatable hemispherical electrostatic energy analyzers at different angles (Figure 2) and detected by single channel electron multipliers (CEM) housed on the exit of analyzers. From the width of the peak representing elastically scattered electrons, we determined the spectrometer resolution to be about 0.9 eV full width at half maximum (FWHM). All the components of the electron spectrometer are housed in a stainless steel cylindrical vacuum chamber fitted with a μ metal.

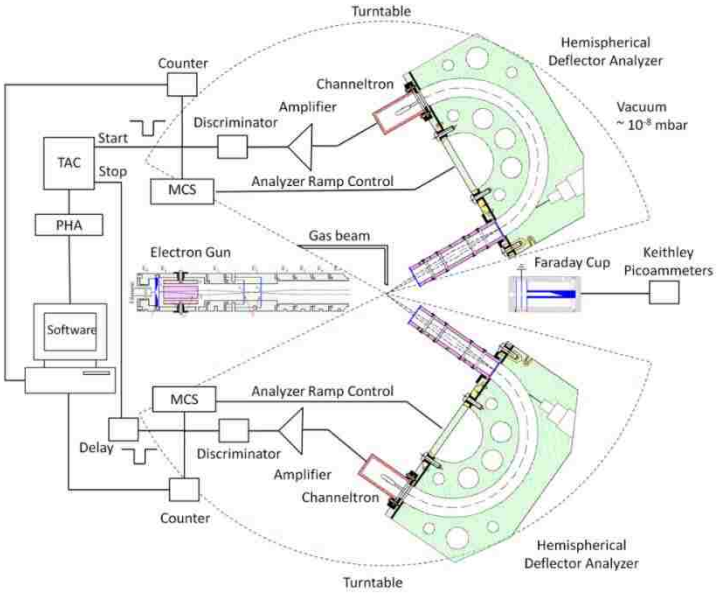

FIG. 2. Schematic view of experimental setup and coincidence electronics.

The outgoing electrons analyzed with respect to their energies and scattering angles are detected in coincidence. True coincidences are selected by setting conditions on the peak in the coincidence time spectrum. Further experimental details may be found in [30]-[33].

Using the (e,2e) experimental technique, it is possible to study either the electronic structure of the target or the dynamics of the ionization process. Here we report experiments performed using this set up to study the ionization process of for the CO_2 ($1\pi_g$) orbital. Although there have been a few previous studies of CO_2, there have been no studies in the kinematical range of interest here.

III. THEORETICAL FRAMEWORK

A. Molecular three-body distorted wave

The molecular three-body distorted wave (M3DW) approximation has been presented in previous publications [19], [21], [34] and here we provide only a brief description. The triple-differential cross section (TDCS) is given by

$$\frac{d^5\sigma}{d\Omega_a d\Omega_b dE_b} = \frac{1}{(2\pi)^5}\frac{k_a k_b}{k_i}\left(|T_{dir}|^2 + |T_{exc}|^2 + |T_{dir} - T_{exc}|^2\right) \tag{2}$$

where T_{dir} and T_{exc} are the direct and exchange scattering amplitudes. The direct amplitude is given by

$$T_{dir} = \left\langle \chi_a^-(\mathbf{k}_a, \mathbf{r}_0)\chi_b^-(\mathbf{k}_b, \mathbf{r}_1)\mathrm{C}_{ab}(\mathbf{r}_{01})\middle|\mathrm{V}_i - U_i\middle|\phi_{Dy}(\mathbf{r}_1, \mathbf{R})\,\chi_i^+(\mathbf{k}_i, \mathbf{r}_0)\right\rangle \tag{3}$$

where $\chi_i^+(\mathbf{k}_i, \mathbf{r}_0)$ is a continuum-state distorted for wave, $\chi_a^-(\mathbf{k}_a, \mathbf{r}_0)$ and $\chi_b^-(\mathbf{k}_b, \mathbf{r}_1)$ are the scattered and ejected electron distorted waves, $\phi_{Dy}(\mathbf{r}_1, \mathbf{R})$ is the initial bound-state electronic wave function, commonly called the Dyson molecular orbital for the active electron, which depends both on the spacial coordinate $\mathbf{r}_1$ and the molecular orientation $\mathbf{R}$. The Dyson wavefunction is defined to be the overlap between the final molecular wavefunction for the ion and the initial molecular wavefunction for the neutral molecule. The molecular wave functions were calculated using DFT (density functional theory) along with the standard hybrid B3LYP [35] functional by means of the ADF 2007 (Amsterdam Density Functional) program [36] with the TZ2P (triple-zeta with two polarization functions) Slater type basis sets. The initial state interaction potential between the projectile and the neutral molecule is V_i, and U_i is a spherically symmetric approximation for V_i. Consequently $\mathrm{V}_i - U_i$ is the non-spherical part of the initial state projectile-target interaction. The factor $\mathrm{C}_{ab}(\mathbf{r}_{01})$ is the final state Coulomb-distortion factor between the two final-state electrons – normally called the post collision interaction (PCI). We call

results obtained using the above T-matrices M3DW (molecular 3-body distorted wave). Since the final state Coulomb interaction is included in the final state wavefunction, the M3DW contains PCI to all orders of perturbation theory.

The exchange *T*-matrix T_{exc} is the same as Eq. (3) except that $\mathbf{r}_0$ and $\mathbf{r}_1$ are interchanged in the final state wavefunction.

The TDCS of Eq. (2) depends on the orientation of the molecule and most experiments do not determine the orientation of the molecule at the time of ionization. Consequently, the theory needs to average over all orientations [20]. To take the average over all molecular orientations, the TDCS is calculated for each orientation and then averaged over all possible orientations so that (to simplify the notation, we will label the TDCS of Eq. (2) as $\sigma^{\mathrm{TDCS}}(\mathbf{R})$)

$$\sigma^{M3DW} = \frac{\int \sigma^{\mathrm{TDCS}}(\mathbf{R})\, d\Omega_R}{\int d\Omega_R} \tag{4}$$

B. Three center continuum model

We have also used the three center continuum model with Dyson type orbitals for the ionization of the ($1\pi_g$) level of CO_2. In this approach, the triple differential cross section (TDCS) of eq. (2) is obtained by averaging the multiply differential cross section for fixed orientation of the molecule over all molecular orientations. The orientation of the molecule is given by the polar θ_R and azimuthal φ_R angles defined in the laboratory frame of reference, which has its z axis parallel to the incidence direction of the projectile.

$$\frac{d^5\sigma}{d\Omega_a d\Omega_b dE_b} = \frac{1}{4\pi}\int d\Omega_R \frac{d^7\sigma}{d\Omega_R d\Omega_a d\Omega_b dE_b} \tag{5}$$

With

$$\frac{d^7\sigma}{d\Omega_R d\Omega_a d\Omega_b dE_b} = \frac{k_a k_b}{2k_i}\left[\left|T_{dir}^{m=1}\right|^2 + \left|T_{dir}^{m=-1}\right|^2\right] \tag{6}$$

For the asymmetric regime of the present paper (E_0=250 eV, E_b=37 eV) we consider only the direct term of the transition matrix element which is given by

$$T_{dir}^{m} = \frac{1}{2\pi}\int \overrightarrow{dr_1}\int \overrightarrow{dr_0} \exp(i(\vec{k}_i.\vec{r}_0 - \vec{k}_a.\vec{r}_0)\chi(\vec{k}_b.\vec{r}_1)V\phi_{1\pi_g}^{m}(\vec{r}_1) \tag{7}$$

The details concerning the different terms of this expression are given in [17],[18]. $\chi(\vec{k}_b.\vec{r}_1)$ represents the three center continuum function, $\phi^m_{1\pi_g}(\vec{r}_1)$ is the Dyson orbital [37],[38] for the initially bound electron obtained from the coupled cluster results [39],[40] by calculating the overlap between the N state of the target and the (N-1) state of the ionized ion. V represents the model potential describing the interaction of the incident electron with the target.

IV. RESULTS

The M3DW has yielded reasonably good agreement with experiment for several different molecular targets but it has not been previously applied to CO_2. In the past, the two-center Coulomb continuum (TCC) model, which applies two center Coulomb continuum functions obtained from the solution of the Schrödinger equation for a free electron in the Coulomb field of two fixed charged nuclei, was extended to three-center targets (ThCC), and has been applied to the ionization of CO_2 [17] for higher incident (~ 500 eV) energy asymmetric cases. In [18], it was slightly modified by the introduction of a supplementary parameter, which adds some flexibility to the function and adapts it to more general situations. Five types of calculations were done, with different model potential parameters for the interaction of the incident electron with the target. In this work, we will consider the type 5, which takes into account all the screening of the inactive electrons of the target borrowed from [41]. The electronic structure of CO_2 is described by Dyson orbitals. To avoid cumbersome calculations, the incident and scattered electrons are, at this stage, are described by plane waves. We think that for the incident energy domain (250 eV) of the present experiment, this could be considered as a compromise, which should be improved in the future.

The present M3DW model contains the post collision interaction (PCI) between scattered and ejected electrons to all orders of perturbation theory which has been shown to be very important for several other cases. In the M3DW model, the in- and outgoing electrons are described by a wave distorted by the perturbing potential, i.e., the interaction with the target. With the inclusion of PCI, TDCS can be calculated that agree reasonably well with experiments down to relatively low impact energies. There are no adjustable parameters in the M3DW.

The aim of this work is to compare experimental and theoretical results for (e,2e) ionization of CO_2 for intermediate energies. From previous works for ionization, it has been found that the typical (e,2e) coplanar cross sections have a large peak in the forward direction. This peak is called the binary peak since it is close to the direction that a classical particle would leave a collision for elastic scattering of two equal mass particles (the momentum transfer direction $+\mathbf{q}$). Also typically, there is a much smaller peak at large angles which is normally close to $180°$ from the binary peak (the negative of the momentum transfer direction $-\mathbf{q}$) and this small peak is called the recoil peak since it is attributed to a binary electron being back scattered from the nucleus. Figure 3 shows the CO_2 $1\pi_g$ orbital. It is seen that it has the appearance of two atomic p-type states. It is also known that, for an atomic p-state, the binary peak often is split into two peaks with a minimum at the direction of momentum transfer.

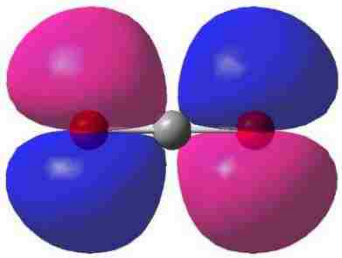

FIG. 3. (color online). The CO_2 $1\pi_g$ orbital. The center small ball is the carbon atom, the two balls on either side are the oxygen atoms, and the larger oval shapes are the electron wavefunction of either positive or negative sign.

Figure 4 shows the comparison of the experimental results with the predictions of the M3DW and ThCC (type5) models. Since the experimental data are not absolute, experiment is normalized to the M3DW at the binary peak. The ThCC model predicts cross sections a little larger than the M3DW for all the cases we considered. Consequently, we multiplied the ThCC results by 0.8 so that the theoretical cross sections have the same magnitude for the largest cross section ($\theta_a = 10^0$ binary peak). It is seen that both experiment and theory predict a single binary peak at $\theta_a = 10^0$ and a double binary peak at

$\theta_a = 20^0$ which is a known characteristic for ionization of atomic p-states. The ThCC predicts the relative heights of the two peaks better than the M3DW at 20^0. However, for $\theta_a = 30^0$, both theories predict a double peak while experiment only has a single peak. Also shown in Fig. 4 is the location of the momentum transfer ($+\mathbf{q}$) and location of the expected recoil peak ($-\mathbf{q}$). It is seen that, at $\theta_a = 10^0$, the experiment and M3DW have binary peaks at a larger angle than the momentum transfer which would be attributed to PCI.

The similarity of the present results and atomic p-type cross sections is further enhanced by noting that, in both experiment and theory, single peaks occur near the momentum transfer direction and, for double peaks, the minimum between the two peaks occurs near the momentum transfer direction which is the same as the atomic case. There have been several papers published for ionization of argon 3p for similar kinematics [42]-[46]. For 10^0 scattering, all theories and experiment had a single binary peak for ejected electron energies above 10 eV which is consistent with the present results. For 20^0 scattering, all theories and experiment indicated a double peak again similar to the present case. Unfortunately, we could not find any 30^0 measurements which is disappointing since it would be very interesting to see if other works found a single peak or double peak for 30^0. To our knowledge, a way to predict when to expect a single or double peak has not been found.

For this kinematics, there is almost no recoil peak in the experimental data except for a slight hint that there might be a small one for $\theta_a = 10^0$ but at angles larger than the expected recoil peak location. The ThCC predicts a very broad recoil type peak that is qualitatively in agreement with experiment at $\theta_a = 10^0$ while the M3DW predicts a very small peak near the expected recoil peak location. For $\theta_a = 20^0$ and 30^0, the ThCC predicts a double recoil peak with a minimum at $-\mathbf{q}$ and the magnitude is much larger than the data. For $\theta_a = 20^0$ and 30^o, the M3DW and experimental data have very small cross sections in the recoil region.

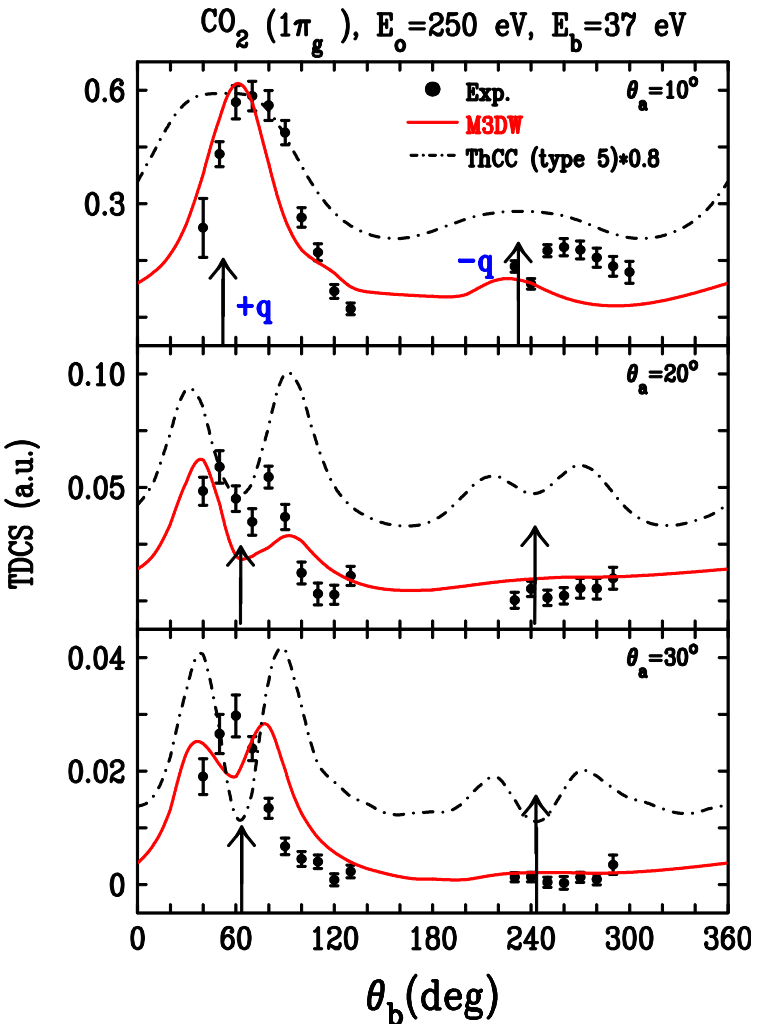

FIG. 4. (Color online) TDCS in atomic units (a.u.) for electron-impact ionization of the $1\pi_g$ state of CO_2 plotted as a function of the ejection angle for the 37 eV ejected electron. The experimental results are normalized to the M3DW calculations at the binary peak. The arrow near 60^0 is the momentum transfer direction ($+\mathbf{q}$) and the arrow near 240^0 is the negative momentum transfer direction ($-\mathbf{q}$).

As can be seen from the figure, there is qualitative agreement between theory and experiment. The ThCC qualitatively predicts the shape of the binary peak for $\theta_a = 10^0$ and 20^0 but not $\theta_a = 30^0$ and it predicts a larger cross section than seen in experiment for the two larger scattering angles. The M3DW gives the best overall agreement with data except for predicting a double binary peak at $\theta_a = 30^0$.

V. CONCLUSION

The scattering of electrons by a polyatomic linear molecular target is one of the basic problems in molecular collisions. There have been a limited number of (e,2e) studies for electron-impact ionization of CO_2 but none for the intermediate kinematics examined here. In this work, we compared experiment and theory for intermediate energy electron-impact ionization of the $1\pi_g$ state of CO_2. The $1\pi_g$ state has the shape of a double atomic p-state which typically can have a double binary peak (but not always) with the minimum located near the momentum transfer direction. We compared M3DW and ThCC (type 5) theoretical results with experimental data and found p-state evidence in the binary peak both experimentally and theoretically. Both the ThCC and M3DW predicted a double peak structure for both the two larger scattering angles while experiment found a double peak for the middle angle only. There was an indication of a recoil peak only for the smallest projectile scattering angle. The M3DW was in the best overall agreement with experiment except for the prediction of a double binary peak for the largest projectile scattering angle.

ACKNOWLEDGMENTS

This work was supported by the Scientific and Technological Research Council of Turkey (TUBITAK) through Grant No. 109T738 and by BAPK through Grant No. 15.HIZ.DES.130. EA and DM would like to acknowledge the support of the US National Science Foundation under Grant. No. PHY-1505819 and CN would like to acknowledge the support of the National Natural Science Foundation of China under Grant No. 11174175. Computational work was performed with Institutional Computing resources made available through the Los Alamos National Laboratory. The Los Alamos National Laboratory is operated by Los Alamos National Security, LLC, for the National Nuclear Security Administration of the US Department of Energy under Contract No. DE-AC5206NA25396.

[1] H. Tanaka, T. Ishikawa, T. Masai, T. Sagara, L. Boesten, M. Takekawa, Y. Itikawa, and M. Kimura, Phys. Rev. A **57**,1798 (1798).

[2] M. Kimura, M. Inokuti, K-I. Kowari, M. A. Dillon, A. Pagnamenta, Argonne National Laboratory, Argonne, Illinois 60439 (1989).

[3] T. Shirai, T. Tabata, H. Tawara, Atomic Data and Nuclear Data Tables, **79**, 143 (2001).

[4] G. P. Karwasz, R. S. Brusa and A. Zecca, Rivista del Nuovo Cimento **24**, 1 (2001).

[5] G. N. Ogurtsov, J. Phys. B: At. Mol. Opt. Phys. **28**, 1805 (1998).

[6] D.F. Register, H. Nishimura, S. Trajmar, J. Phys. B: At. Mol. Opt. Phys. **13**, 1651 (1980).

[7] T. W. Shyn, W. E. Sharp, and G. R. Carignan, Phys. Rev. A **17**, 1855 (1978).

[8] R. McDiarmid and J. P. Doering, J. Chem. Phys. **80**, 648 (1984).

[9] K. Anzai, H. Kato, M. Hoshino, H. Tanaka, Y. Itikawa, L. Campbell, M. J. Brunger, S. J. Buckman, H. Cho, F. Blanco, G. Garcia, P. Limão-Vieira, and O. Ingólfsson, Eur. Phys. J. D **66**, 36 (2012).

[10] M. A. Green, P. J. O. Teubner, L. Campbell, M. J. Brunger, M. Hoshino, T. Ishikawa, M. Kitajima, H. Tanaka, Y. Itikawa, M. Kimura and R. J. Buenker, J. Phys. B: At. Mol. Opt. Phys. **35**, 567 (2002).

[11] Y. Itikawa, Journal of Physical and Chemical Reference Data, **31**, 749 (2002).

[12] T. W. Shyn and W. E. Sharp, Phys. Rev. A **20**, 2332 (1979).

[13] C. B. Opal, W. K. Peterson, and E. C. Beaty, Chem. Phys. **55**, 4100 (1971).

[14] M. J. Hussey and A. J. Murray, J. Phys. B: At. Mol. Opt. Phys. **38**, 2965 (2005).

[15] A. Lahmam-Bennani, E. M. Staicu Casagrande and A. Naja , J. Phys. B: At. Mol. Opt. Phys. **42**, 235205 (2009).

[16] B. Joulakian, J. Hanssen, R. Rivarola, and A. Motassim, Phys. Rev. A **54**, 1473 (1996).

[17] O. Chuluunbaatar and B. Joulakian, J. Phys. B: At. Mol. Opt. Phys. **43**, 155201 (2010).

[18] O. Alwan, O. Chuluunbaatar, X. Assfeld, A. Naja and B. Joulakian. J. Phys.B: At. Mol. Opt. Phys. **47**, 225201 (2014).

[19] D. H. Madison and O. Al-Hagan, Journal of Atomic, Molecular and Optical Physics **2010** 367180 (2010).

[20] S. Xu, Hari Chaluvadi, X. Ren, T. Pflüger, A. Senftleben, C. G. Ning, S. Yan, P. Zhang, J. Yang, X. Ma, J. Ullrich, D. H. Madison, and A. Dorn, J. Chem. Phys. **137**, 024301 (2012).

[21] H. Chaluvadi, C. G. Ning and D. Madison, Phys. Rev. A **89**, 062712 (2014).

[22] D. Jones, J. D. Builth-Williams, S. M. Bellm, L. Chiari, H. Chaluvadi, D. Madison, C. Ning, B. Lohmann, O. Ingólfsson, and M. Brunger, Chem. Phys. Let. **572**, 32 (2013).

[23] K. L. Nixon, A. J. Murray, H. Chaluvadi, C. Ning, J. Colgan, and D. H. Madison, J. Chem. Phys. **138**, 174304 (2013).

[24] J. D. Builth-Williams, S. M. Bellm, L. Chiari, P. A. Thorn, D. B. Jones, H. Chaluvadi, D. H. Madison, C. G. Ning, B. Lohmann, G. da Silva, and M. J. Brunger, J. Chem. Phys. **139**, 034306 (2013).

[25] J. D. Builth-Williams, G. B. da Silva, L. Chiari, D. B. Jones, H. Chaluvadi, D. H. Madison, and M. J. Brunger, J. Chem. Phys. **140**, 214312 (2014).

[26] G. B. da Silva, R. F. C. Neves, L. Chiari, D. B. Jones, E. Ali, D. H. Madison, C. G. Ning, K. L. Nixon, M. C. A. Lopes, and M. J. Brunger, J. Chem. Phys. 141, 124307 (2014).

[27] H. Chaluvadi, Z. N. Ozer, M. Dogan, C. Ning, J. Colgan and D. Madison, J. Phys. B **48**, 155203 (2015).

[28] E. Ali, K. Nixon, A. Murray, C. Ning, J. Colgan, and D. Madison, Phys. Rev. A **92**, 042711 (2015).

[29] D. B. Jones, E. Ali, K. L. Nixon, P. Limão-Vieira, M.-J. Hubin-Franskin, J. Delwiche, C. G. Ning, J. Colgan, A. J. Murray, D. H. Madison, and M. J. Brunger, J. Chem. Phys. **143**, 184310 (2015).

[30] Z. N. Ozer, H. Chaluvadi, M. Ulu, M. Dogan, B. Aktas, and D. Madison, Phys. Rev. A **87**, 042704 (2013).

[31] S. Amami, M. Ulu, Z. N. Ozer, M. Yavuz, S. Kazgoz, M. Dogan, O. Zatsarinny, K. Bartschat, and D. Madison, Phys. Rev. A **90**, 012704 (2014).

[32] M. Dogan, M. Ulu, Z. N. Ozer, M. Yavuz, and G. Bozkurt, Journal of Spectroscopy, (2013).

[33] H. Chaluvadi, Z. N. Ozer, M. Dogan, C. Ning, J. Colgan, and D. Madison, J. Phys.B: At. Mol. Opt. Phys. **48**, 155203 (2015).

[34] J. Gao, D. H. Madison, and J. L. Peacher, J. Chem. Phys. **123** 204302 (2005).

[35] C. F. Guerra, J. G. Snijders, G. Te Velde, and E. J. Baerends, Theoretical Chemistry Accounts, **99**, 391 (1998).

[36] C. L. W. Yang, and R. G. Parr, Phys. Rev. B **37**, 785 (1988).

[37] I. G. Kaplan, B. Barbiellini, and A. Bansil, Phys. Rev. B **68**, 235104 (2003).

[38] R. J. F. Nicholson, I. E. McCarthy, and W. Weyrich, J. Phys.B: At. Mol. Opt. Phys. **32** 3873 (1999).

[39] C. M. Oana and A. I. Krylov, J. Chem. Phys. **127**, 234106 (2007).

[40] C. M. Oana and A. I. Krylov, J. Chem. Phys. **131**,1241143 (2009).

[41] F. J. Rogers, B. G. Wilson, and C. A. Iglesias, Phys. Rev. A **38**, 5007 (1998).

[42] M Stevenson, G J Leighton, A Crowe, K Bartschat, O K Vorov and D H Madison, J. Phys. B: At. Mol. Opt. Phys. **40,** 1639 (2007).

[43] X. Ren, A. Senftleben, T. Pflueger, A. Dorn, K. Bartschat and J. Ullrich, J. Phys. B: At. Mol. Opt. Phys. **43,** 035202 (2010).

[44] Xueguang Ren, Arne Senftleben, Thomas Pflueger, Alexander Dorn, Klaus Bartschat, and Joachim Ullrich, Phys.Rev. A **83**, 052714 (2011).

[45] M. Ulu, Z. N. Ozer, M. Yavuz, O. Zatsarinny, K. Bartschat, M. Dogan and A. Crowe, J. Phys. B: At. Mol. Opt. Phys. **46,** 115204 (2013).

[46] S. Amami, M. Ulu, Z. N. Ozer, M. Yavuz, S. Kazgoz, M. Dogan, O. Zatsarinny, K. Bartschat, and D. Madison, Phys. Rev A **90**, 012704 (2014).

V. Experimental and theoretical triple-differential cross sections for tetrahydrofuran ionized by low-energy 26-eV electron-impact

Esam Ali[1], XueGuang Ren[2], Alexander Dorn[2], Chuangang Ning[3], James Colgan[4] and Don Madison[1]

[1]Department of Physics, Missouri University of Science and Technology, Rolla MO 65409, USA

[2]Max-Planck-Institut für Kernphysik, Saupfercheckweg1, 69117 Heidelberg, Germany

[3]Department of Physics, State Key Laboratory of Low-Dimensional Quantum Physics, Tsinghua University, Beijing 100084, China

[4]Theoretical Division, Los Alamos National Laboratory, Los Alamos, NM 87545

We report an experimental and theoretical study of low energy electron-impact ionization of Tetrahydrofuran, which is a molecule of biological interest. The experiments were performed using an advanced reaction microscope specially built for electron-impact ionization studies. The theoretical calculations were performed within the molecular 3-body distorted wave model. Reasonably good agreement is found between experiment and theory.

DOI: 10.1103/PhysRevA.93.062705

I. INTRODUCTION

The interactions of electrons with atoms, molecules and clusters are of great importance in a wide range of scientific and practical applications [1]. For example, in medical radiation therapy, it has been discovered that significant damage to DNA is induced by electrons with energies below 100 eV [2,3], which are the most abundant secondary species in media penetrated by high-energy ionizing radiation [4]. Even slow electrons with energies below the ionization threshold (≤ 10 eV) can produce considerable DNA strand breaks via dissociative electron attachment resonances. Above this energy range the damage to DNA is dominated by a superposition of various nonresonant mechanisms related to excitation, ionization and dissociation. Therefore, a number of experimental and theoretical works examining electron interactions with biomolecules have been carried out to study the dynamics of electrons in biological media, see e.g.[5-13]. Here, tetrahydrofuran (THF, C_4H_8O) has been used frequently since it is one of the simplest molecular analogues of the DNA bases.

A comprehensive way to characterize the dynamics of electron-impact ionization of matter is to detect the two outgoing electrons in coincidence, the so-called (e, 2e) method which serves as a powerful tool to understand the electron trajectory in a media. This is a kinematically complete experiment, in which the linear momentum vectors of all final-state particles are determined. The quantity measured in such experiments is the triple-differential cross section (TDCS), i.e., a cross section that is differential in the solid angles of both electrons and the energy of one of them (energy conservation determines the energy of the second electron). Such (e, 2e) experiments for THF have been recently performed at high collision energy (250 eV) [5-13]. In the present work, we study low-energy (E_0 = 26.5 eV) electron-impact ionization of THF to understand the features of low-energy electrons in biological systems using the kinematically complete (e,2e) experiments. For low energy electrons, the effects of post collision interaction (PCI), electron exchange, and electron-target interactions are expected to become more pronounced which might significantly influence the electron trajectory in matter[14,15]. The TDCSs were measured for an ejected electron energy of 3.5 eV, for a range of projectile scattering angles (θ_a = 15°, 25°, and 35°) and resolving different fragmentation channels ($C_4H_8O^+$, $C_4H_7O^+$, and $C_3H_6^+$). The experimental data were compared with theoretical predictions from the distorted-wave

Born approximation (DWBA) with inclusion of the post-collision interaction (PCI) using the Ward-Macek method [16] and the molecular three-body distorted-wave (M3DW) approach, (see e.g. [17,18]).

II. EXPERIMENTAL METHODS

The experiment was performed using an advanced reaction microscope specially built for electron-impact ionization studies [19]. Details of the setup were described elsewhere [20]. A brief outline will be given here. A well-focused (~1 mm diameter), pulsed electron beam crosses a supersonic gas jet with internal temperature of T ~10 K. It is produced by supersonic gas expansion from a 30 μm nozzle and two-stage differential pumping system. Here, helium gas with a partial pressure of 2 bar mixed with THF with a partial pressure of 500 mbar was used. The pulsed electron beam is emitted from a recently developed photoemission electron gun ($\Delta E < 0.5$ eV), in which a pulsed ultraviolet laser beam ($\lambda = 266$ nm, $\Delta t < 0.5$ ns) illuminates a tantalum photocathode. The projectile beam axis (defining the longitudinal direction) is adjusted parallel to the electric and magnetic extraction fields, which are used to guide electrons and ions onto two position- and time-sensitive multi-hit detectors equipped with fast delay-line readout.

Experimental data were measured using the triple coincidences method in which both outgoing electrons (the faster electron E_a and the slower electron E_b) and the fragment ion are recorded. From the positions of the hits and the times of flight (TOF), the vector momenta of the detected particles can be determined. Note that the projectile beam is adjusted exactly parallel to the electric and magnetic extraction fields. After passing through the target gas jet, the beam arrives at the electron detector, where a central hole in the multichannel plates allows for the undeflected electrons to pass without inducing a hit. The detection solid angle for electrons is close to 4π, apart from the acceptance holes at small forward and backward angles where the electrons end up in the detector bore. In the fragmentation processes of molecules, the dissociated ions are usually created with some kinetic energy. In order to cover a large solid angle for the detection of the fragment ions, a pulsed electric field has been applied for ion extraction. In this way, significantly improved mass and energy resolutions have been achieved [20,21].

III. THEORETICAL METHODS

In this paper, we have used the M3DW (molecular 3-body distorted wave) approach which is described in Refs. [22-24]. For the 3-body problem, the triple differential cross section (TDCS) which we evaluate numerically is given by

$$\frac{d^5\sigma}{d\Omega_a d\Omega_b dE_b} = \frac{1}{(2\pi)^5}\frac{k_a k_b}{k_i}\left(|T_{dir}|^2 + |T_{exc}|^2 + |T_{dir} - T_{exc}|^2\right) \quad (1)$$

where T_{dir} and T_{exc} are the direct and exchange scattering amplitudes. The direct amplitude is given by

$$T_{dir} = \left\langle \chi_a^-(\mathbf{k}_a, \mathbf{r}_0)\chi_b^-(\mathbf{k}_b, \mathbf{r}_1)\mathrm{C}_{ab}(\mathbf{r}_{01})\middle| W \middle| \phi_{Dy}^{OA}(\mathbf{r}_1)\ \ \chi_i^+(\mathbf{k}_i, \mathbf{r}_0)\right\rangle \quad (2)$$

Here $\chi_i^+(\mathbf{k}_i, \mathbf{r}_0)$ is an initial-state distorted wave for the incoming electron with wave number $\mathbf{k_i}$ and the (+) indicates outgoing wave boundary conditions, $\chi_a^-(\mathbf{k}_a, \mathbf{r}_0)$ and $\chi_b^-(\mathbf{k}_b, \mathbf{r}_1)$ are the final state distorted wave functions for the faster and slower electrons with wave numbers $\mathbf{k}_a$ and $\mathbf{k}_b$ respectively, the (-) indicates incoming wave boundary conditions. We, of course, do not know which electron is the scattered projectile and which electron is the ejected electron but, for discussion purposes, we call the faster electron the scattered electron and the slower electron the ejected electron. The perturbation $W = V_i - U_i$ where V_i is the initial state interaction between the projectile and neutral target, and U_i is a spherically symmetric approximation for V_i. $\phi_{Dy}^{OA}(\mathbf{r}_1)$ is an initial bound-state Dyson molecular orbital averaged over all orientations [24] and $\mathbf{r}_1$ is the active electron coordinate. $\mathrm{C}_{ab}(\mathbf{r}_{01})$ is the Coulomb interaction between the projectile and ejected electron [normally called the post collision interaction (PCI)] which can be expressed as:

$$\mathrm{C}_{ab}(\mathbf{r}_{01}) = e^{\frac{-\pi\gamma}{2}}\Gamma(1-i\gamma)\ {}_1F_1(i\gamma, 1, -i(k_{ab}r_{01} + \mathbf{k}_{ab}\bullet\mathbf{r}_{01})) \quad (3)$$

Here Γ is the gamma function, $\mathbf{k}_{ab} = \mu\mathbf{v}_{ab}$ is the relative electron-electron wave number which depends on the relative velocity $\mathbf{v}_{ab}$ and the reduced mass for the two electrons μ, ${}_1F_1$ is a confluent Hypergeometric function, and γ is the Somerfield parameter ($\gamma = 1/\mathbf{v}_{ab}$). In the Ward-Macek approximation [16], one replaces the actual final state

electron-electron separation $\mathbf{r}_{01}$ by an average value directed parallel to $\mathbf{k}_{ab}$. The average separation is defined as

$$r_{01}^{ave} = \frac{\pi^2}{16\varepsilon_t}\left(1+\frac{0.627}{\pi}\sqrt{\varepsilon_t}\ln\varepsilon_t\right)^2 \tag{4}$$

where ε_t is the total energy of the scattered and ejected electrons. In the Ward-Macek approximation, PCI is approximated as

$$\mathrm{C}_{ab}(r_{01}^{ave}) = e^{\frac{-\pi\gamma}{2}}\Gamma(1-i\gamma)\ {}_1F_1(i\gamma,1,-2ik_{ab}\,r_{01}^{ave}) \tag{5}$$

which does not depend on electron coordinates and can be removed from the integral in the T-matrix. With the PCI term removed from the integral, the T-matrix becomes the standard DWBA (distorted wave Born) approximation. We will label results using the Ward-Macek approximation for PCI as WM and results using the exact PCI of eq. (3) as M3DW (molecular 3-body distorted wave). The only difference between the two calculations is the treatment of PCI.

The exchange amplitude T_{exc} is the same as Eq. (2) with $\mathbf{r}_0$ and $\mathbf{r}_1$ interchanged in the final state wavefunction.

IV. RESULTS

A schematic diagram of the geometry for coplanar scattering is presented in Fig. 1 where the scattering plane is the xz-plane. Here we will present results for $E_0 = 26.5$ eV, $E_b = 3.5$ eV, faster final state electron scattering angles $\theta_a = 15°, 25°,$ and $35°$, and ejected electron angles θ_b ranging from 0^0 – 360^0 measured clockwise.

In the experiment, the scattered and ejected electrons are measured in coincidence with one fragment ion. The detected cations are $C_4H_8O^+$, $C_4H_7O^+$ and $C_3H_6^+$. It has been identified in ref. [20] that the cation $C_4H_8O^+$ is attributed to the ionization of 9b i.e. the highest occupied molecular orbital (HOMO) of THF, the cation $C_4H_7O^+$ is attributed to the ionization of the 9b (20%) and 11a orbital (80%) (next highest occupied molecular orbital "NHOMO") of THF. The most abundant ion in the fragmentation of THF has been identified as the $C_3H_6^+$ fragment which is attributed to the ionization of the 11a (12%), 10a (46%) (next-next highest occupied molecular orbital "N-NHOMO"), 8b (21%), and 9a

(21%) orbitals of THF. There are two conformers for THF labeled C_s and C_2 and the above weights are for C_2. Figure 2 shows the two conformers for HOMO, NHOMO and N-NHOMO which make the dominant contributions to the three measured cations. For the theoretical calculations, the TDCS for the two conformers are summed using the ratios $55\%\ C_s + 45\%\ C_2$ [25,26]. Figures 3-5 show the calculated conformer cross sections for the three measured cations in atomic units. As is seen, the two cross sections are very similar so the conformer weights are relatively unimportant.

Figure 6 compares theoretical and experimental results for ionization of the THF HOMO (ionization energy of 9.7 eV) state which leads to the $C_4H_8O^+$ cation. Since the ratios of the experimental data for different angles and different ionized orbitals are absolute, the experiment has been normalized to theory using a single normalization factor for all scattering angles and the three measured states. This normalization factor was chosen for best visual fit of experimental and M3DW cross sections for ionization of the THF HOMO state and $\theta_a = 15°$ (Fig. 6, top panel) . Both theories are absolute (in atomic units) with no normalization. The solid (red) curves are the results of the M3DW calculation and the dashed (blue) curves are the results using the Ward-Macek (WM) approximation for PCI. Overall, the M3DW results are in better agreement with experiment than the WM although the WM does predict the experimental dip seen near $160°$ for $\theta_a = 25°, \text{ and } 35°$. The M3DW predicts the shape of the data much better for small projectile scattering angles and small ejected electron angles. From studies of electron-impact ionization of atoms, it has been found that the typical (e,2e) coplanar cross sections have a large peak in the forward direction. This peak is called the classical binary peak since it is close to the direction that a classical particle would leave a collision for elastic scattering of two equal mass particles (the momentum transfer direction $+\mathbf{q}$). Also typically, there is a much smaller peak at large angles which is normally close to $180°$ from the binary peak (the negative of the momentum transfer direction $-\mathbf{q}$) and this small peak is called the recoil peak since it is attributed to a binary electron being back scattered from

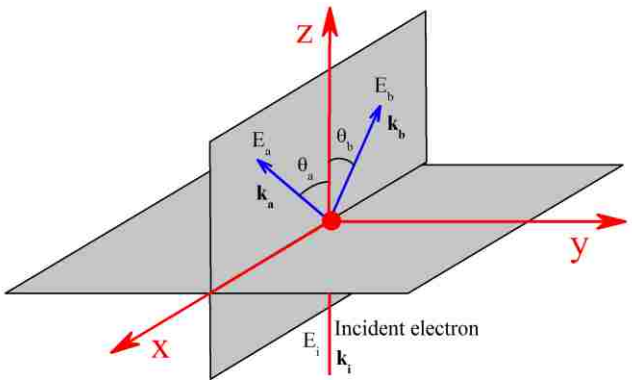

FIG.1. Schematic diagram of coplanar geometry

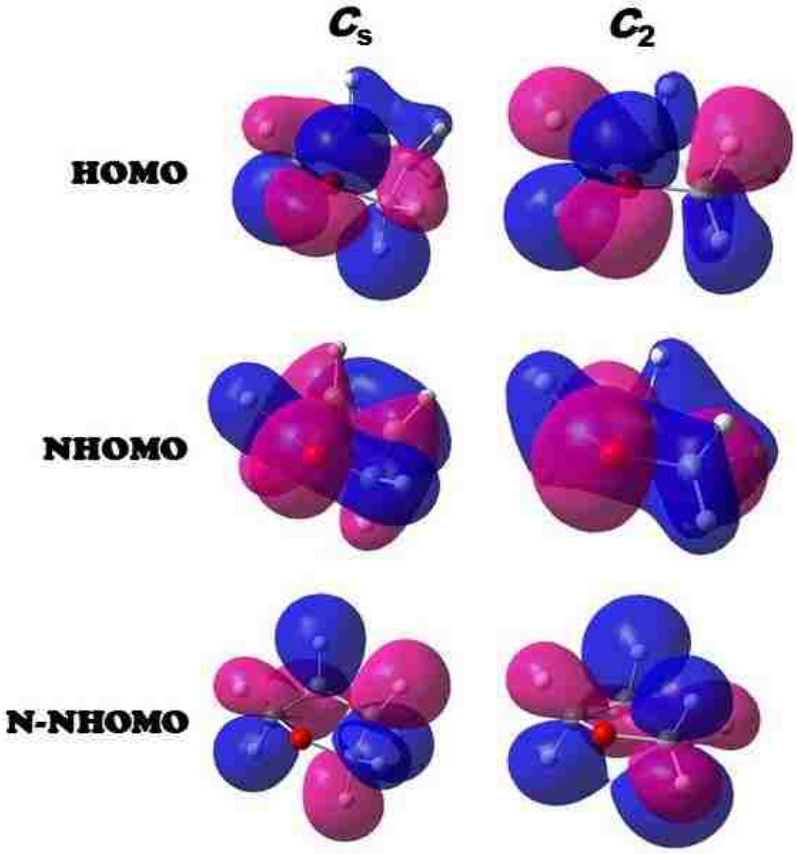

FIG. 2. THF conformers C_s and C_2 for the HOMO, NHOMO, and N-NHOMO states.

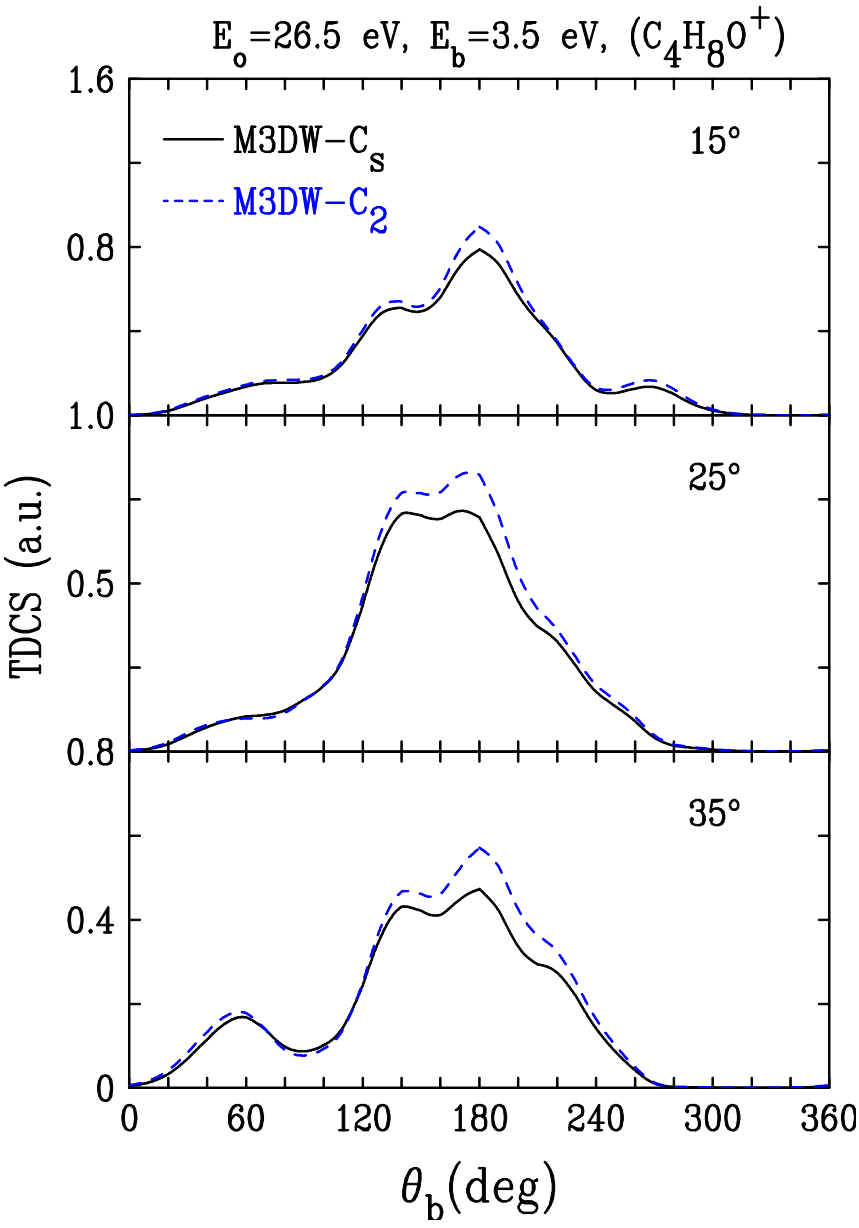

FIG. 3. Theoretical TDCS in atomic units for 26.5 eV electron-impact ionization of the THF HOMO state which leads to the cation $C_4H_8O^+$ as a function of the ejected electron scattering angle θ_b. The faster electron scattering angle is θ_a is indicated in each panel. The solid (black) lines are the M3DW results for the C_s conformer and dashed (blue) lines are the M3DW results for the C_2 conformer.

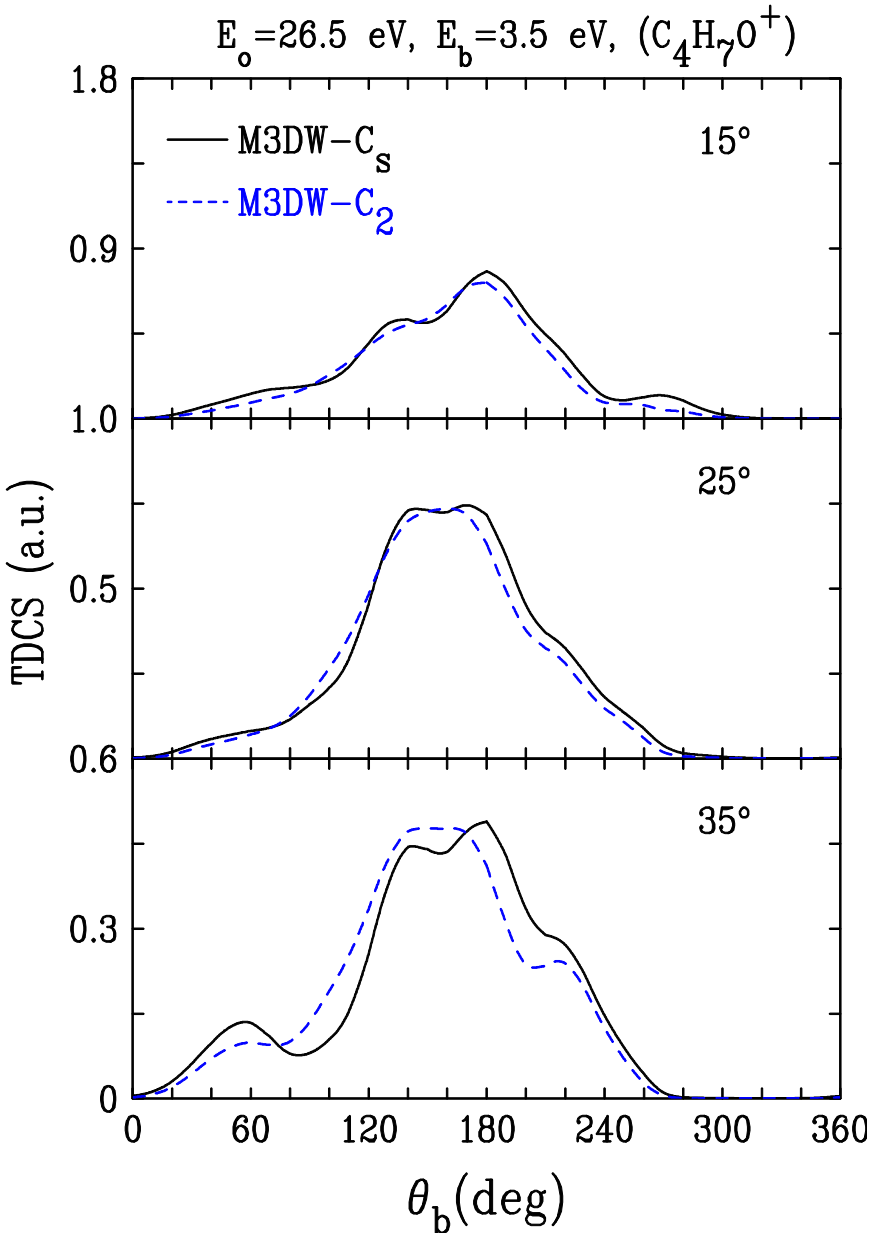

FIG. 4. Theoretical TDCS in atomic units for 26.5 eV electron-impact ionization of the THF combination of states which leads to the cation $C_4H_7O^+$ as a function of the ejected electron scattering angle θ_b. The faster electron scattering angle is θ_a is indicated in each panel. The solid (black) lines are the M3DW results for the C_s conformer and dashed (blue) lines are the M3DW results for the C_2 conformer.

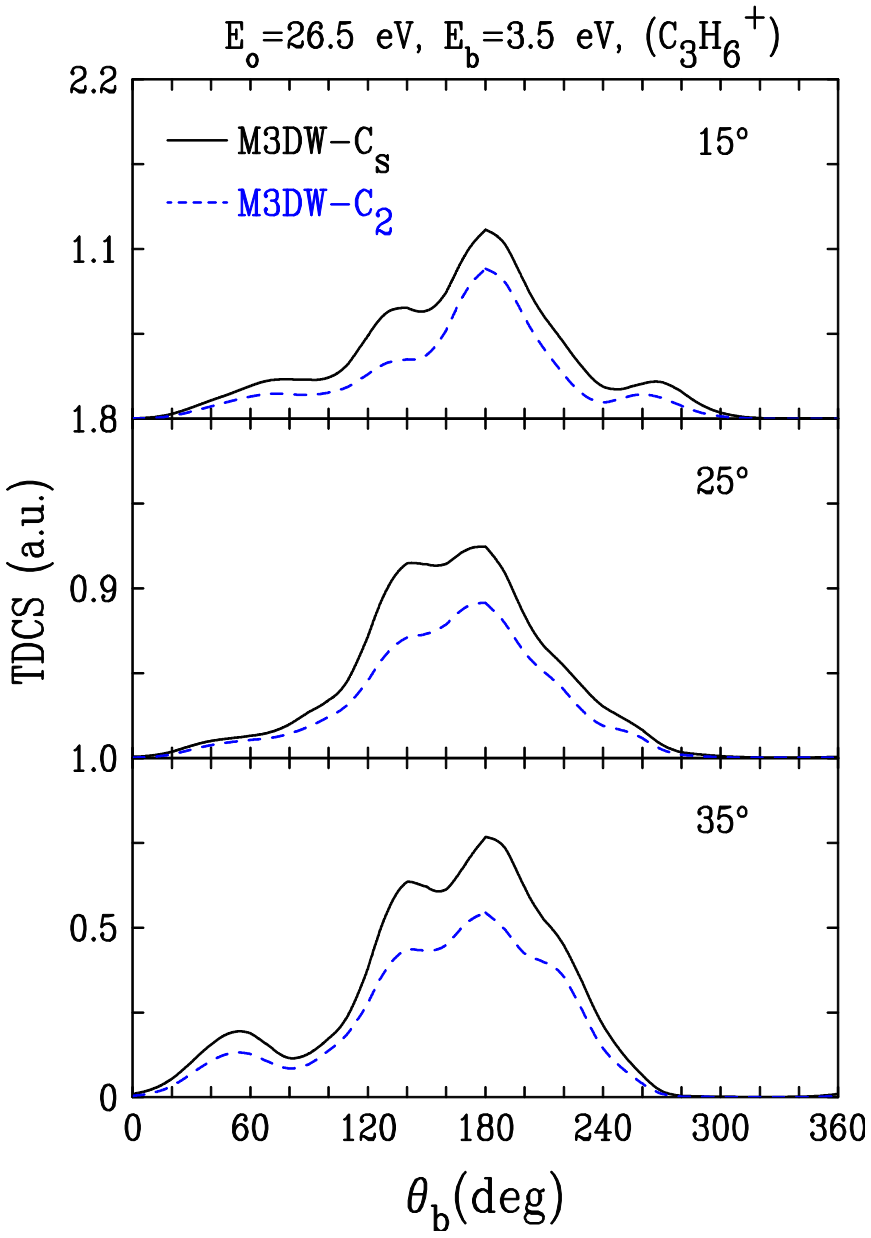

FIG. 5. Theoretical TDCS in atomic units for 26.5 eV electron-impact ionization of the THF combination of states which leads to the cation $C_3H_6^+$ as a function of the ejected electron scattering angle θ_b. The faster electron scattering angle is θ_a is indicated in each panel. The solid (black) lines are the M3DW results for the C_s conformer and dashed (blue) lines are the M3DW results for the C_2 conformer.

the nucleus. The location of these two directions is shown by the vertical arrows in the figure. It is seen that the experimental data shows no indication of a binary peak but possibly a recoil peak. The WM approximation has a peak near the binary direction but shifted to larger angles and a peak near the recoil direction but shifted to smaller angles. Angular shifts like this would normally be attributed to PCI repulsion but we think that this is an unlikely explanation since WM has PCI only to first order and the shifts are bigger than one would expect to first order. Similar to the experimental data, M3DW has no peaks in the binary region for the two smaller projectile scattering angles and a small peak at the largest angle. The experimental data also has a small hint of a binary type peak for $\theta_a = 35°$. The M3DW also has a large angle peak at considerably smaller angles than the expected recoil direction. What is very clear is that these cross sections do not have the standard two peak binary and recoil structure normally found in atomic ionization. Consequently, it appears that the shape of the TDCS for these more complicated multi-center targets and at the present low impact energy probably cannot be explained by simple classical models.

Figure 7 compares experimental and theoretical results for ionization of the combination of THF states which lead to the $C_4H_7O^+$ cation. The comparison between theory and experiment is similar to the HOMO state. For this case the M3DW is again in better overall agreement with experiment. The WM results predict a peak near the recoil direction that is much larger than experiment especially for the smaller projectile scattering angles. The agreement between experiment and the M3DW is very good for the smallest projectile scattering angle. Although qualitatively similar, the agreement with experiment for the $35°$ projectile scattering angle is not as good as it was for the HOMO state. Figure 8 compares experimental and theoretical results for ionization of the combination of THF states which lead to the $C_3H_6^+$ cation and again the results are similar to the previous two states. However for this case, the agreement of M3DW with the $25°$ and $35°$ data is better than for the other two states. Interestingly, the WM results are in quite good agreement with the $25°$ data for all three cases. Overall the theoretical cross sections are highest in the vicinity of $\theta_b = 180°$ which is in accordance with the strong PCI effects present for

two outgoing electrons with low energies ($E_a = 10-13$ eV , $E_b = 3.5$ eV) and the resulting preferred back-to-back emission of both electrons.

It is interesting to note that the cross section patterns are not particularly sensitive to the specific initial orbital being ionized. This is also the case for the two THF conformers C_s and C_2 which show essentially identical TDCS as was shown in Figs. 3-5. This may seem surprising since the orbital spatial structures differ greatly (Fig. 2), even belonging to different symmetries. Nevertheless, their orbital momentum distributions (MDs) are rather similar if the molecular alignment is not resolved. The spherically averaged MDs for various orbitals of THF have been measured by Ning et al. [26]. We are concerned with the MD of the HOMO (binding energy 9.7 eV) and a group involving the NHOMO and N-NHOMO orbitals (up to 12 eV binding energy). Both MDs are very similar. They range from zero up to about 2 a.u. with two maxima in that range which are only slightly differently positioned in both cases. Thus, the effect of the MD of the initially bound electron which is present in the momentum and angular distributions of the ejected electron will be similar for these orbitals. In addition, the spatial charge density distributions of all these orbitals are spread out over the whole molecule as can be seen in Fig. 2. Thus, the resulting multi-center potential of the singly charged ion which is experienced by the outgoing electrons will not be strongly different for ionization of the various orbitals. Consequently, rescattering processes in the ionic potential which give rise, e.g. to the typical recoil peak observed in the (e,2e) studies at higher energies should also be similar for the different orbitals. As a result, it is perhaps not so surprising that we have found no large variation in the electron emission pattern for the different orbitals.

V. CONCLUSIONS

In summary, we have measured relatively absolute cross sections for ionization of THF states which lead to three different cations. This means that there is only one normalization factor used for the experiment for all three states and all three projectile scattering angles (9 panels in all). We have found reasonably good agreement between experiment and theory (both shape and magnitude) for the final state cations $C_4H_8O^+$, $C_4H_7O^+$, and $C_3H_6^+$ of THF for a relatively low incident electron energy of 26.5 eV. Although there is considerable structure in the measured and calculated cross sections, they

do not have the traditional binary and recoil peaks which is not surprising considering the complicated multi-center scattering centers for a large molecule such as this. Overall the M3DW is in fairly good agreement, both in magnitude and shape, with all the measured states and scattering angles. These results indicate that the theoretical M3DW TDCS could reliably be used in the track structure modelling calculations for biological media.

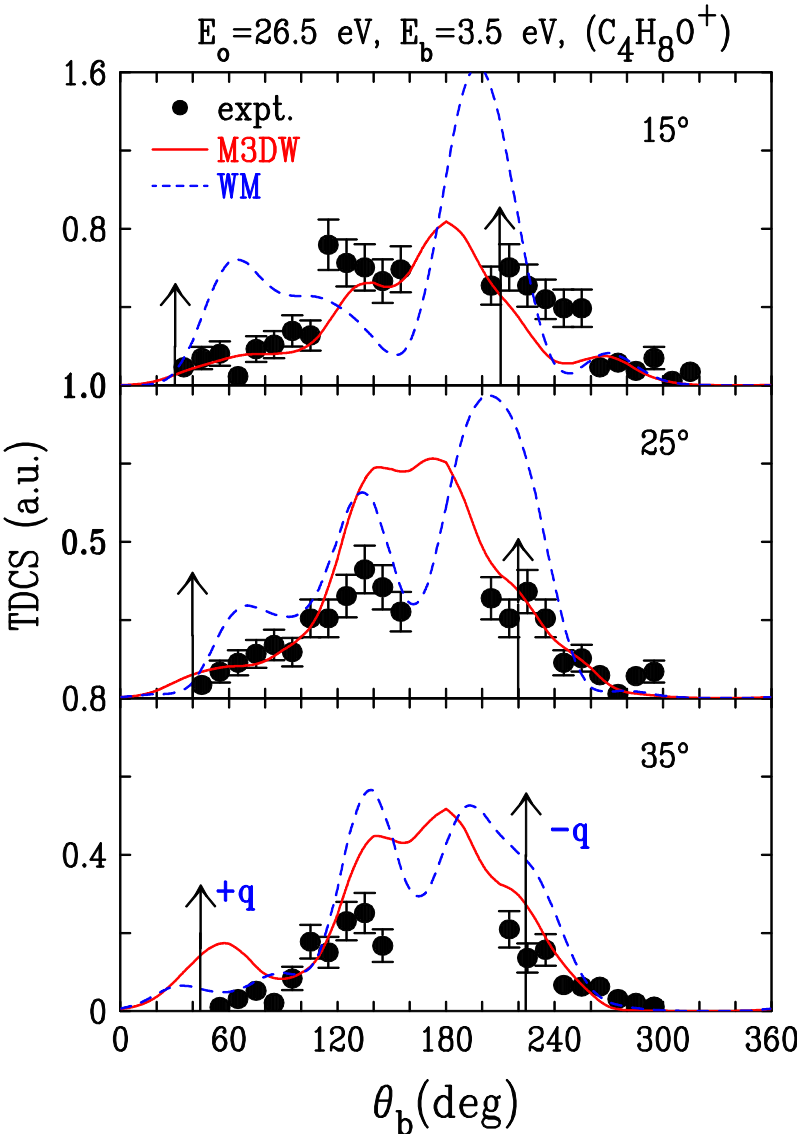

FIG. 6. Experimental and theoretical TDCS in atomic units for 26.5 eV electron-impact ionization of the THF HOMO state which leads to the cation $C_4H_8O^+$ as a function of the ejected electron scattering angle θ_b. The faster electron scattering angle is θ_b is indicated in each panel. The experimental data are the circles, the solid (red) lines are the M3DW results and the dashed (blue) lines are the WM results. The theoretical results are in atomic units and one normalization factor for experiment has been used for all panels of fig. 6-8.

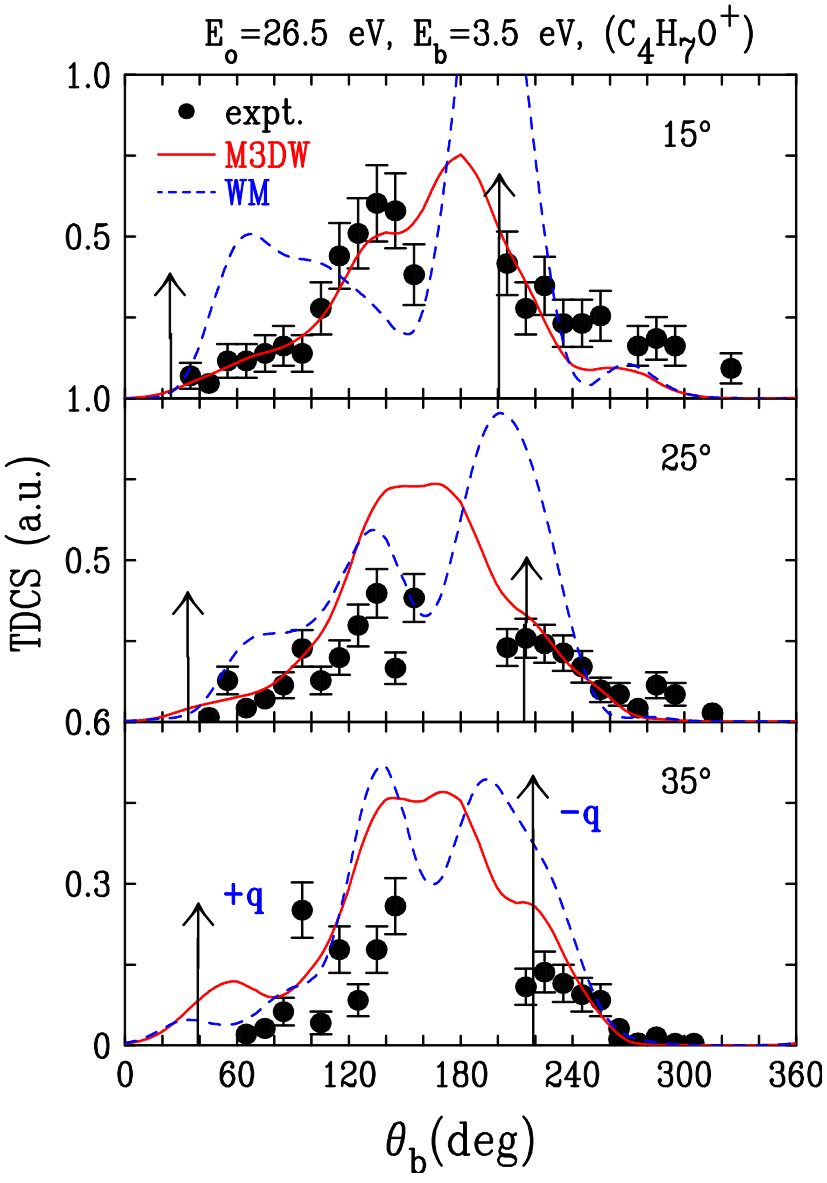

FIG. 7. Experimental and theoretical TDCS in atomic units for 26.5 eV electron-impact ionization of the combination of THF states which leads to the cation $C_4H_7O^+$ as a function of the ejected electron scattering angle θ_b. The faster electron scattering angle is θ_a is indicated in each panel. The experimental data are the circles, the solid (red) lines are the M3DW results and the dashed (blue) lines are the WM results. The theoretical results are in atomic units and one normalization factor for experiment has been used for all panels of fig. 6-8.

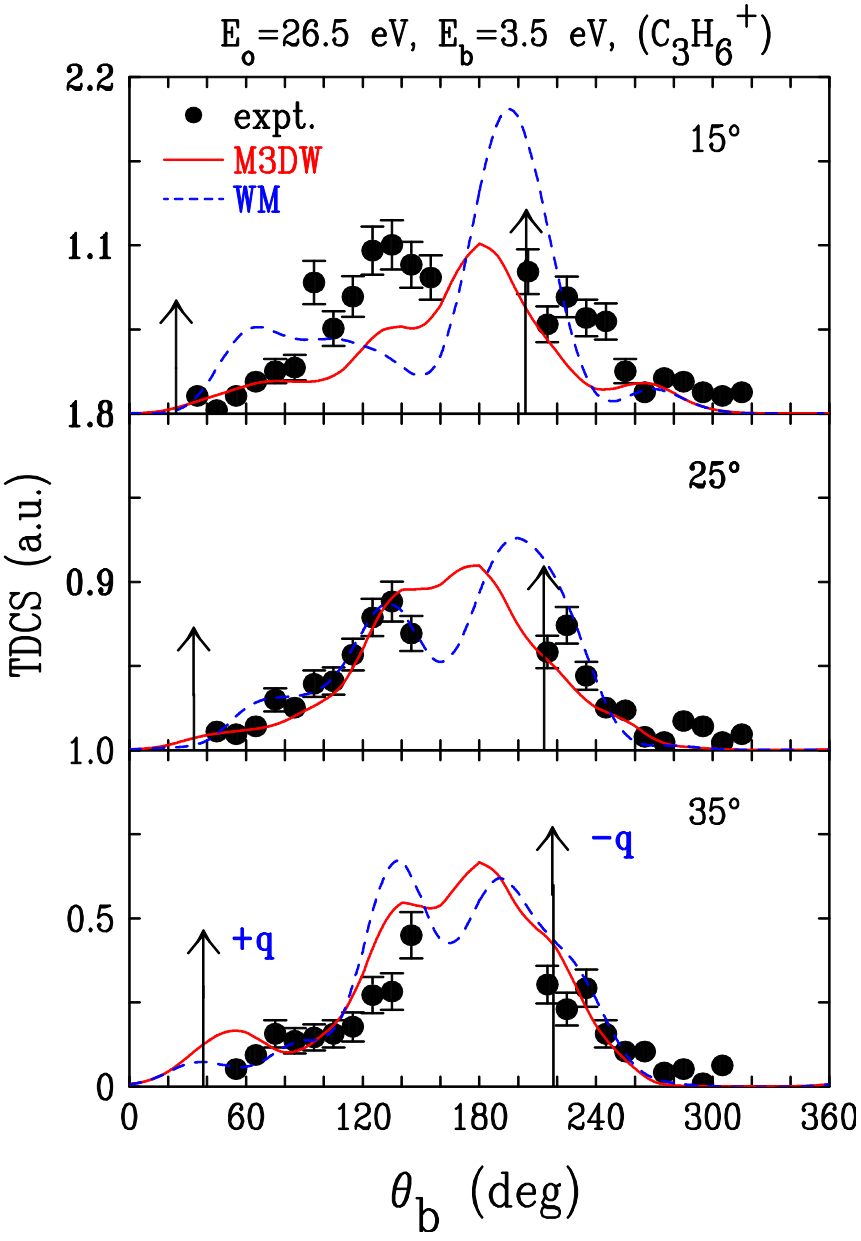

FIG. 8. Experimental and theoretical TDCS in atomic units for 26.5 eV electron-impact ionization of the combination of THF states which leads to the cation $C_3H_6^+$ as a function of the ejected electron scattering angle θ_b. The faster electron scattering angle is θ_a is indicated in each panel. The experimental data are the circles, the solid (red) lines are the M3DW results and the dashed (blue) lines are the WM results. The theoretical results are in atomic units and one normalization factor for experiment has been used for all panels of fig. 6-8.

ACKNOWLEDGMENTS

EA and DM would like to acknowledge the support of the US National Science Foundation under Grant. No. PHY-1505819 and CN would like to acknowledge the support of the National Natural Science Foundation of China under Grant No. 11174175. Computational work was performed with Institutional Computing resources made available through the Los Alamos National Laboratory. The Los Alamos National Laboratory is operated by Los Alamos National Security, LLC, for the National Nuclear Security Administration of the US Department of Energy under Contract No. DE-AC5206NA25396.

[1] B. C. Garrett et al. Chem. Rev. **105**, 355 (2005).

[2] M.A. Huels, B. Boudaiffa, P. Cloutier, D. Hunting, and L. Sanche, J. Am. Chem. Soc.**125**, 4467 (2003).

[3] E. Alizadeh, T. M. Orlando, and L. Sanche, Annual Review of Physical Chemistry **66**, 379 (2015).

[4] S. M. Pimblott and J. A. LaVerne, Radiation Physics and Chemistry **76**, 1244 (2007).

[5] M. Fuss, A. Muñoz, J. C. Oller, F. Blanco, D. Almeida, P. Limão Vieira, T. P. D. Do, M. J. Brunger, and G. Garc´ia, Phys. Rev.A **80**, 052709 (2009).

[6] A. Zecca, C. Perazzolli, and M. J. Brunger, J. Phys. B **38**, 2079 (2005).

[7] P. Moz˙ejko, E. Ptasin´ska-Denga, A. Domaracka, and C. Szmytkowski, Phys. Rev.A **74**, 012708 (2006).

[8] W. Y. Baek, M. Bug, H. Rabus, E. Gargioni, and B. Grosswendt, Phys. Rev. A **86**, 032702 (2012).

[9] L. Chiari, E. Anderson, W. Tattersall, J. R. Machacek, P. Palihawadana, C. Makochekanwa, J. P. Sullivan, G. Garcia, F. Blanco, R. P. McEachran, M. J. Brunger, and S. J. Buckman, J. Chem. Phys. **138**, 074301 (2013).

[10] M. Allan, J. Phys. B **40**, 3531 (2007).

[11] C. J. Colyer, V. Vizcaino, J. P. Sullivan, M. J. Brunger, and S. J. Buckman, New J. Phys. **9**, 41 (2007).

[12] M. Dampc, A. R. Milosavljevic´, I. Linert, B. P. Marinkovic´, and M. Zubek, Phys. Rev.A **75**, 042710 (2007).

[13] A. Gauf, L. R. Hargreaves, A. Jo, J. Tanner, M. A. Khakoo, T. Walls, C. Winstead, and V. McKoy, Phys. Rev. A **85**, 052717 (2012).

[14] J. D. Builth-Williams, S. M. Bellm, L. Chiari, P. A. Thorn, D. B. Jones, H. Chaluvadi, D. H. Madison, C. G. Ning, B. Lohmann, G. B. da Silva, and M. J. Brunger, J. Chem. Phys. **139**, 034306 (2013).

[15] X. Ren, S. Amami, O. Zatsarinny, T. Pfluger, M. Weyland, W. Y. Baek, H. Rabus, K. Bartschat, D. Madison, and A. Dorn, Phys. Rev. A **91**, 032707 (2015).

[16] S. J. Ward and J. H. Macek, Phys. Rev. A **49**, 1049 (1994).

[17] O. Al-Hagan, C. Kaiser, A. J. Murray, and D. Madison, Nat Phys **5**, 59 (2009).

[18] O. Al-Hagan, A. J. Murray, C. Kaiser, J. Colgan, and D. H. Madison, Phys. Rev. A **81**, 030701 (2010).

[19] J. Ullrich, R. Moshammer, A. Dorn, R. Doerner, L. Schmidt, and H. Schmidt-Boecking, Rep. Prog. Phys. **66**, 1463 (2003).

[20] X. Ren, T. Pflueger, M. Weyland, W. Y. Baek, H. Rabus, J. Ullrich, and A. Dorn, J. Chem. Phys. **141**, 134314 (2014).

[21] X. Ren, T. Pflueger, M. Weyland, W. Y. Baek, H. Rabus, J. Ullrich, and A. Dorn, J. Chem. Phys. **142**, 174313 (2015).

[22] J. Gao, D.H. Madison, and J.L. Peacher, J. Chem. Phys. **123** 204314 (2005).

[23] J. Gao, D.H. Madison, and J.L. Peacher, Phys. Rev. A **72** 032721 (2005).

[24] J. Gao, D.H. Madison, and J.L. Peacher, J. Chem. Phys. **123** 204302 (2005).

[25] Tiecheng Yang, Guolin Su, Chuangang Ning, Jingkang Deng, Feng Wang, Shufeng Zhang, Xueguang Ren, and Yanru Huang, J. Phys. Chem. A, **111**, 4927-4933 (2007).

[26] C. G. Ning, Y. R. Huang , S. F. Zhang , J. K. Deng , K. Liu , Z. H. Luo and F. Wang, J. Phys. Chem. A, **112**, 11078-11087 (2008).

VI. Electron impact ionization dynamics of *para*-benzoquinone

D. B. Jones,[1,a)] E. Ali,[2] C. G. Ning,[3] J. Colgan,[4] O. Ingólfsson,[5] D. H. Madison[2] and M. J. Brunger[1,6,a)]

[1]*School of Chemical and Physical Sciences, Flinders University, GPO Box 2100, Adelaide, SA 5001, Australia*

[2]*Department of Physics, Missouri University of Science and Technology, Rolla, Missouri 65409, USA*

[3]*Department of Physics, State Key Laboratory of Low-Dimensional Quantum Physics, Tsinghua University, Beijing 100084, China*

[4]*Theoretical Division, Los Alamos National Laboratory, Los Alamos, New Mexico 87545, USA*

[5]*Science Institute and Department of Chemistry, University of Iceland, Dunhagi 3, 107 Reykjavík, Iceland*

[6]*Institute of Mathematical Sciences, University of Malaya, 50603 Kuala Lumpur, Malaysia*

(Received 4 September 2016; accepted 10 October 2016; published online 27 October 2016)

Triple differential cross sections (TDCS) for the electron impact ionization of the unresolved combination of the 4-highest occupied molecular orbitals ($4b_{3g}$, $5b_{2u}$, $1b_{1g}$ and $2b_{3u}$) of *para*-benzoquinone are reported. These were obtained in an asymmetric coplanar geometry with the scattered electron being observed at the angles -7.5°, -10.0°, -12.5° and -15.0°. The experimental cross sections are compared to theoretical calculations performed at the molecular 3-body distorted wave level, with a marginal level of agreement between them being found. The character of the ionized orbitals, through calculated momentum profiles, provides some qualitative interpretation for the measured angular distributions of the TDCS.

a) Authors to whom correspondence should be addressed. Electronic addresses: darryl.jones@flinders.edu.au and michael.brunger@flinders.edu.au

I. INTRODUCTION

Oxygenic photosynthesis is the principle energy convertor on earth,[1] converting H_2O and CO_2 into sugars and O_2. An understanding of the individual processes within the photosynthetic cycle thus have broad implications for technological development. Specifically, it is desirable to increase the light capturing efficiency and to identify and then remove competitive chemical pathways that offer less efficient oxygenation reactions.[2] This has the potential to improve biomass generation which may in turn increase the viability of a sustainable biofuel industry. Enhancing our understanding of naturally occurring photosynthesis may also drive innovation in photovoltaics and photocatalysis,[3] and also the creation of hybrid photo-bioelectrochemical technologies.[4] Quinones play a particularly important role in photochemical systems through their ability to undergo reversible reduction (i.e. from plastoquinone to plastoquinol). The ability to undergo reversible reduction also makes quinones an important substance within the electron transport chain of cellular respiration. The unique electrochemical properties of quinones have further enabled their use as a low-cost and sustainable material for energy storage applications.[5,6]

para-Benzoquinone (2,5-cyclohexadiene-1,4-dione, $C_6H_4O_2$, see Figure 1), hereafter referred to as pBQ, is the simplest quinone. It has therefore served as a prototypical structure in a number of studies aiming to understanding photo-induced and electrochemical behaviour of quinones in general. Correspondingly the structures of its ground, excited, anionic and cationic states,[7-10] as well as that of its derivatives[11] and complexes[12] have attracted significant theoretical attention over an extended period of time. There has also been extensive experimental studies into the photo-dynamics of pBQ[8,13-16] and the bulk of the spectroscopic and theoretical studies conducted have been reviewed by Itoh in 1995,[17] and a fairly comprehensive literature overview is given in Ómarsson and Ingólfsson.[18] From an electron scattering perspective, however, it is only vibrational and electronic excitation,[19] negative ion formation and the resonances[18,20-26] of pBQ and its derivatives that have been investigated. The cationic forms of pBQ and its derivatives have also been investigated experimentally through photoionization,[27-30] Penning ionization[31] and matrix isolation spectroscopy.[32] The interpretation of the cationic structure of pBQ has, however, been controversial as vibronic coupling occurs between the

outermost orbitals that lie close in energy,[32] while there is also a strong influence of electron correlation in the cationic states.[11] Further knowledge of the cationic structure and the ionization dynamics of pBQ is therefore important in understanding chemical reactivity within the quinone family of compounds.

In this paper we present a combined experimental and theoretical investigation into electron impact ionization of the unresolved combination of the four-highest occupied molecular orbitals ($4b_{3g}$, $5b_{2u}$, $1b_{1g}$ and $2b_{3u}$) of pBQ. Here we employed an (e,2e) coincident technique using the asymmetric coplanar kinematics depicted in Fig. 2, with an intermediate impact energy (E_0). This kinematically complete electron impact ionization process is described through:

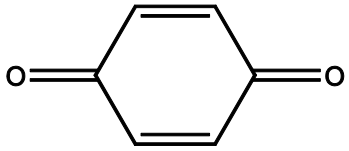

FIG. 1. Schematic representation of *para*-benzoquinone (pBQ, 1,4-benzoquinone).

$$e_0^-(E_0,k_0) + \mathrm{pBQ} \rightarrow \mathrm{pBQ}^+(\varepsilon_i) + e_1^-(E_1,k_1) + e_2^-(E_2,k_2)\,. \qquad (1)$$

Here E_j and k_j ($j = 0,1,$ or 2) are the energies and momenta of the incident, fast-scattered and slow-ejected electrons, respectively. The conservation of energy requires that:

$$\varepsilon_i = E_0 - (E_1 + E_2)\,, \qquad (2)$$

where ε_i is the energy required to ionize the *i*th-orbital of pBQ. The ion created recoils from the collision with momentum,

$$q = k_0 - (k_1 + k_2)\,. \qquad (3)$$

Angular distributions of the triple differential cross section for the ejected electron were obtained when the faster electron was scattered through a fixed angle of either $\theta_1 =$ -7.5°, -10.0°, -12.5° or -15.0°. Under these conditions, a change to the fixed scattered electron angle reflects a change in the momentum transferred ($\mathbf{K} = \mathbf{k}_0 - \mathbf{k}_1$) to the molecule during the ionization process. Such conditions are important for establishing a link between high

impact ionization phenomena that can probe the internal structure of molecules,[33-35] and low impact energy collisions that investigate the collision dynamics.[36] These kinematical conditions are also similar to those employed in our previous investigations on the ionization dynamics of larger molecules.[37-43] Further, our current experimental investigations relate to the ionization dynamics of biologically relevant molecular targets that contain oxygen atoms in varying chemical environments.[40-43] In this way we can experimentally assess the role of the oxygen atom's bonding network and its proximity to the surrounding functional groups in the collisional dynamics. In the current contribution, we chose to study the angular distributions of the triple differential cross section (TDCS) over a finely spaced range of scattered electron angles in order to investigate how rapidly the TDCS varies. This was prompted by recent experimental and theoretical investigations into the electron impact ionization of argon, under comparable intermediate energy asymmetric kinematic conditions.[44-46] Those argon studies revealed that the magnitude of the TDCS changed rapidly with the scattered electron angle. We therefore wished to evaluate how the magnitude of the TDCS varied as a function of the scattered electron angle for a more complicated, molecular target.

The final, more general, point we wish to make is the importance of studies such as the present in the development of models of electron transport in matter. One such model, the low-energy particle track simulation (LEPTS) code from Garcia and colleagues,[47-50] currently describes the ionization process through the total ionization cross section and empirical double differential cross sections (derived from average energy-loss distributions and elastic scattering angular distributions), with the ejected secondary electron moving off in the direction of the momentum transfer (+K) vector.[51] In effect, this neglects all consideration of the shape of the TDCS in the binary region, and discounts the possibility of recoil scattering. The present study, and our earlier studies,[37-43] which includes work on bio-molecules, explicitly investigates the angular distribution of the TDCS under different kinematical conditions, and so directly probes the validity of the ionization model currently used by Garcia and his co-workers.[47-50]

The outline of the remainder of our paper is as follows. In Section II the details of our experimental and theoretical methods are summarised. We then present and discuss

our results in Section III. Finally, in Section IV, some conclusions are drawn from this investigation.

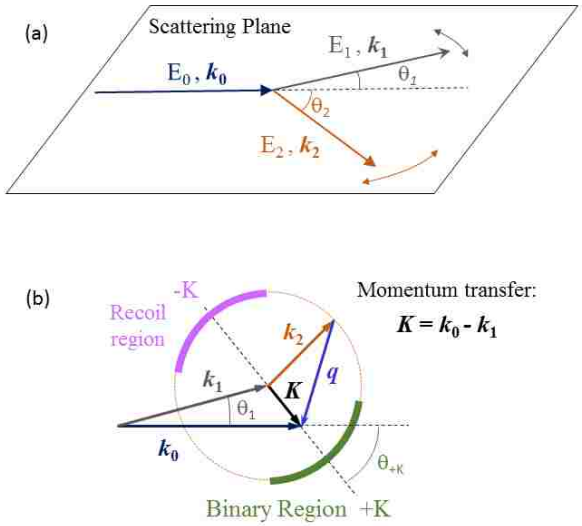

FIG. 2. (a) Schematic representation of the asymmetric coplanar kinematics used in the present measurements for electron impact ionization of pBQ. (b) A diagrammatic representation of the momentum transferred to the target (***K***) and the conservation of momentum within the present asymmetric coplanar kinematics. Here ***q*** represents the recoil momentum of the residual ion. The Binary and Recoil regions represent the angular ranges where the ejected electron (having momentum $\boldsymbol{k_2}$,) leaves the collision in the directions close to parallel and antiparallel to the momentum transfer direction (θ_{+K} θ_{+K}), respectively. See text for further details.

II. EXPERIMENTAL AND THEORETICAL DETAILS

Triple differential cross sections for the electron impact ionization of pBQ have been measured using an electron-electron coincidence technique. The details of the (e,2e) coincidence spectrometer have been described previously in Cavanagh and Lohmann.[52] In brief, an electron beam intersects an effusive beam of pBQ with scattered and ejected electrons being detected using energy selective analysers that are mounted on independently rotatable turntables. The pBQ beam is produced from *para*-benzoquinone (98% assay, Sigma-Aldrich) that was degassed prior to use. *para*-Benzoquinone is a solid at room temperature that readily sublimes at reduced pressure. Its vapour pressure is, however, relatively low for collision studies (0.1 mmHg at 25°C) and we found pBQ to be

a particularly challenging target for us to investigate experimentally. In this study, our most stable experimental conditions were achieved when the gas handling lines and the scattering chamber were heated to 40°C, with the pBQ sample being heated to ~30°C. Heating the sample to higher temperatures resulted in recrystallization within the inlet system, ultimately causing a blockage in our sample handling system. Under our optimal running conditions, the experiments were conducted with a gauge-corrected chamber pressure of ~9×10^{-7} torr.

An electron impact ionization binding energy spectrum for pBQ was first obtained by recording the number of true coincident electron impact ionization events while repeatedly scanning over a range of scattered electron energies. Here the incident and ejected electron energies were fixed at 250 eV and 20 eV, respectively. For these measurements, both the scattered and ejected electron analyser positions were fixed at -10.0° and 75.0°, respectively. A typical example of a pBQ binding energy spectrum from the present electron impact ionization investigation is given in Figure 3. Angular distributions of the electron impact ionization triple differential cross section are obtained by fixing the scattered electron analyser position (in this case at -7.5°, -10.0°, -12.5° or -15.0°), and scanning over a range of ejected electron angles. Here the incident and ejected electron energies are again fixed at 250 eV and 20 eV, respectively, while the scattered electron energy is fixed to investigate the unresolved combination of the 4 highest occupied molecular orbitals (see Figure 3). As our coincidence energy resolution is ~1.1 eV (FWHM), the fixed scattered electron energy for the angular distribution measurements was taken to be the centre of the band for the $4b_{3g}+5b_{2u}+1b_{1g}+2b_{3u}$ orbitals (E_1 ~ 219.5 eV). With all four of the outermost orbitals lying within 1 eV of energy, we believe that all orbitals should contribute equally within the experimental TDCS angular distribution measurement. The measured triple differential cross sections angular distributions for different scattered electron angles were then inter-normalised by fixing the ejected electron detector at 90° and measuring the TDCS while scanning over the range of scattered electron angles examined. The present experimental angular distributions are shown in Figure 4.

In order to interpret our measured spectra, quantum chemical calculations were performed in Gaussian 09.[53] The pBQ geometry was first optimised at the B3LYP/aug-cc-pVDZ level of theory, with the optimum geometry being in excellent accord with

previously reported experimental and theoretical values that have been previously summarised in Ref [10]. The optimized geometry was then used for subsequent calculations performed at the B3LYP/aug-cc-pVDZ and OVGF/aug-cc-pVDZ levels of theory. As the pBQ electronic structure has been extensively studied using sophisticated methods, [7,11] our calculations were primarily done to assist us further in interpreting our measurements. We do note that we achieved excellent agreement with previous calculations performed at a similar level of theory.[11] The B3LYP/aug-cc-pVDZ calculations are used here to visualise the ionized orbitals and to obtain spherically averaged orbital momentum profiles through the HEMS program.[54] The spatial orbital representations and momentum profiles can be found in Figure 5.

To calculate triple differential cross sections (TDCS) for the electron impact ionization of pBQ, we used the molecular three-body distorted wave (M3DW) approximation. This approach has been described elsewhere,[55,56] so we only provide a short overview here. The TDCS within the M3DW framework is given by:

$$\frac{d^5\sigma}{d\Omega_1 d\Omega_2 dE} = \frac{1}{(2\pi)^5}\frac{k_1 k_2}{k_0}\left(\left|T_{dir}\right|^2 + \left|T_{exc}\right|^2 + \left|T_{dir} - T_{dir}\right|^2\right) \tag{4}$$

As before k_0 $\mathrm{k_0}$, k_1 $\mathrm{k_1}$and k_2 are the wave vectors for the initial, scattered, and ejected electrons, respectively. T_{dir} is the direct scattering amplitude, and T_{exc} $\mathrm{T_{exc}}$ is the exchange amplitude. The direct scattering amplitude is given by:

$$T_{dir} = \left\langle \chi_1^-(k_1, r_0)\chi_2^-(k_2, r_1)C_{12}(r_{01})\middle|\mathrm{V_0} - U_0\middle|\phi_{Dy}(r_1)\chi_0^+(k_0, r_0)\right\rangle \tag{5}$$

where $\chi_0^+(k_0, r_0)$ $\chi_0^+(\mathrm{k_0}, \mathrm{r_0})$ is a continuum-state distorted wave for an incident electron with wave number k_0 $\mathrm{k_0}$and the (+) indicates outgoing wave boundary conditions. Further, $\chi_1^-(k_1, r_0)$ $\chi_1^-(\mathrm{k_1}, \mathrm{r_0})$ and $\chi_2^-(k_2, r_1)$ $\chi_2^-(\mathrm{k_2}, \mathrm{r_1})$are the scattered and ejected electron distorted waves with incoming wave boundary conditions. The factor $C_{12}(r_{01})$ $\mathrm{C_{12}(r_{01})}$ is the final state Coulomb-distortion factor between the two outgoing electrons – normally called the post collision interaction (PCI), and $\phi_{Dy}(r_1)$ $\phi_{\mathrm{Dy}}(\mathrm{r_1})$is the one-electron Dyson orbital averaged over all molecular orientations.[55] Calculations at the distorted wave Born

approximation (DWBA) level, where we do not include the post collision interaction term, were also carried out.

III. RESULTS AND DISCUSSION

A typical binding energy spectrum for electron impact ionization of pBQ is presented in Figure 3. To assist in the interpretation of this spectrum, our calculated ionization energies and a summary of previous experimental photoelectron spectroscopy data is given in Table 1. In Figure 3 we see a strong band for the unresolved combination of the 4 highest occupied molecular orbitals ($4b_{3g}$, $5b_{2u}$, $1b_{1g}$ and $2b_{3u}$). These orbitals have traditionally been described as symmetric and asymmetric non-bonding oxygen 2p orbitals [$4b_{3g}$ (n_-), $5b_{2u}$ (n_+)] and the out of plane π–ring bonding contributions [$1b_{1g}$ (π), $2b_{3u}$ (π)]. It is important to note that these 4-highest occupied orbitals are well separated from other molecular orbitals in pBQ, and they therefore form the subject of our ionization dynamics investigation.

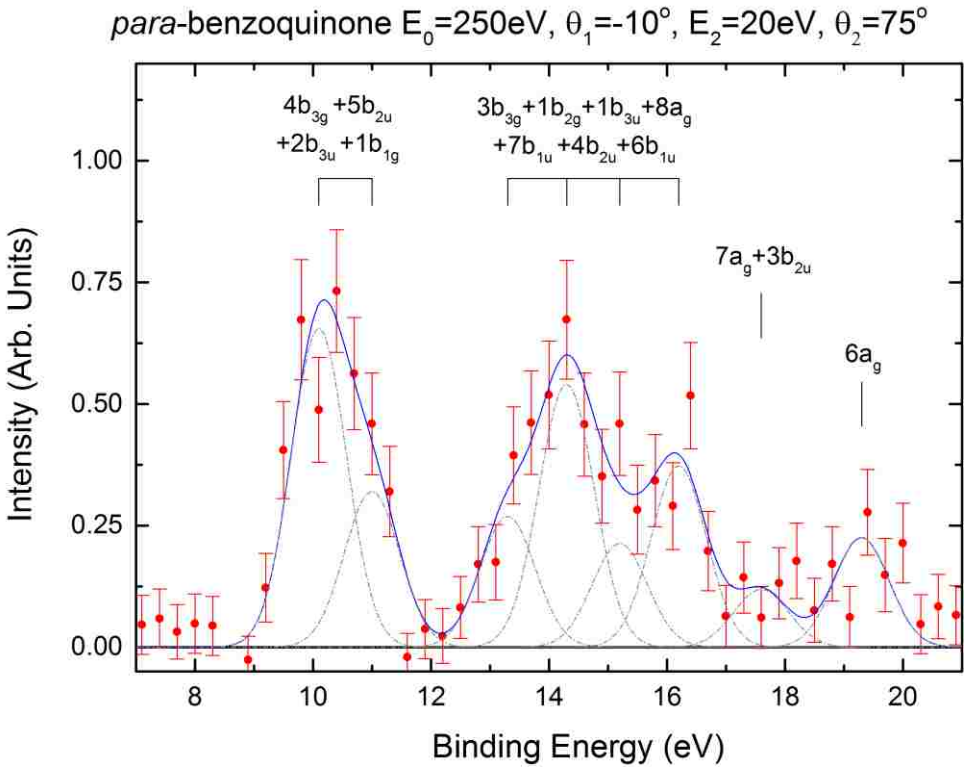

FIG. 3. The (e,2e) binding energy spectrum of *para*-benzoquinone obtained using an incident electron energy of 250 eV. The scattered electron energy was scanned for a fixed angle of detection, $\theta_1 = -10.0°$, while the ejected electron energy was detected at $\theta_2 = 75°$ with an energy of 20 eV. See text for further details.

TABLE 1**.** Present (e,2e) and previous photoelectron spectroscopy (PES) experimental ionization potentials and presently calculated theoretical ionization potentials of pBQ (para-benzoquinone). See text for further details.

	PES[7,29]	PES[30]	PES[27]	PES[28]	OVGF/aug-cc-pVDZ		
Present (e,2e) Energy (eV)	Energy (eV)	Energy (eV)	Energy (eV)	Energy (eV)	IP (eV)	Pole strength	Assignment
10.1	10.11	9.99	9.99	10.05	10.36	0.888	$(4b_{3g})^{-1}$ [n_-]
	10.40	10.29	10.29	10.33	10.78	0.877	$(5b_{2u})^{-1}$ [n_+]
11.0	11.06	10.93	10.93	11.08	10.89	0.887	$(2b_{3u})^{-1}$ [π_+]
	11.5	11.0	11.1	11.08	10.90	0.903	$(1b_{1g})^{-1}$ [π_-]
13.3	13.4	13.5			14.08	0.877	$(3b_{3g})^{-1}$
	13.4				14.12	0.831	$(1b_{2g})^{-1}$
14.3	14.3	14.3			14.68	0.892	$(8a_g)^{-1}$
	14.8	14.9/15.0			15.05	0.847	$(1b_{3u})^{-1}$
15.2	14.7	14.8			15.26	0.885	$(7b_{1u})^{-1}$
	15.3	15.5			15.62	0.879	$(4b_{2u})^{-1}$
16.2	16.2	16.2/16.7			16.74	0.867	$(6b_{1u})^{-1}$
17.6	17.0	17.0			17.04	0.867	$(3b_{2u})^{-1}$
					17.29	0.861	$(7a_g)^{-1}$
19.3	19.5	19.5					

Angular distributions for the triple differential cross sections for the unresolved combination of the four outermost orbitals are shown in Figure 4. These were measured for an incident electron energy of 250 eV and when the scattered electron was detected at θ_1 = -7.5°, -10.0°, -12.5° or -15.0°. Experimental angular distribution were observed in the binary and recoil regions, where the ejected electron leaves the collision in a direction that is close to parallel and anti-parallel with the momentum transfer direction, respectively. We note that we did attempt to measure the TDCSs in the recoil regions at θ_1 θ_1 = -7.5° and -15.0° but we could not achieve acceptable statistics for those angular distributions. This suggests that the TDCSs in the recoil regions for θ_1 = -7.5° and -15.0° are particularly small. Even for the TDCSs at θ_1 = θ_1 -10.0° and -12.5°, for which we were able to obtain acceptable true coincident signals in the recoil region, the uncertainties were of the order of ~45%. To provide the reader with further clarity of the difficulties associated with these (e,2e) measurements, we note that our TDCS angular distribution data was obtained in an experimental runtime of ~6 months. In order to compare with our theoretical results, the

experimental data was normalised to the M3DW at a single point (θ_2 θ_2 = 70°) in the binary region of the θ_1 = -7.5° angular distribution. This single normalisation factor has been applied to the experimental data measured across all of the scattered electron angles. We now discuss and compare the experimental and theoretical TDCS data in more detail.

We begin with discussions of the binary peak region. Here we can immediately see from Figure 4 that the shape and magnitude of the binary peak is changing as the scattered electron angle increases. For example, for a scattered electron angle of -7.5°, the maximum intensity of the TDCS occurs close to the momentum transfer direction (+K). As θ_1 increases we now see that the maximum intensity shifts away from the momentum transfer direction. Indeed, we also observe a local minimum in the vicinity of the momentum transfer direction for θ_1 = θ_1 -15.0°. This behaviour resembles that previously observed for the ionization of the unresolved 4a″+3a″ orbitals of phenol, under similar kinematical conditions.[39] The 4a″ and 3a″ orbitals of phenol are both out-of-plane ring bonding/O(2p) orbitals, which therefore resemble the $2b_{3u}$ and $1b_{1g}$ orbitals of pBQ. This raises the intriguing possibility that out-of-plane ring bonding/O(2p) orbitals may possess a characteristic TDCS angular distribution, although further work to confirm this is clearly needed.

We now compare the present experimental data to our theoretical calculations (see Figure 4). The M3DW calculation produces an angular distribution that has a peak in the binary direction that is similar to that observed in the experimental profile for the scattered electron angle of -7.5°, although the theoretical distribution does not exhibit the particularly broad nature of the binary lobe seen experimentally at the larger ejected electron angles, θ_2 = 90-120°. As the scattered electron angle increases the agreement between the shape of the TDCS in the binary region for the experimental data and that predicted by the M3DW calculation worsens. Specifically, while the M3DW TDCS calculations at larger scattering angles show a principal maximum in the momentum transfer direction, this is not seen experimentally. Regarding the absolute scale, the theoretical TDCS predicts an intensity in the binary region that increases as the scattered electron angle increases. This behaviour is consistent with the experimental observation from θ_1 = θ_1 =-7.5° to -10.0°, where the

absolute intensity of the TDCS in the binary region is also seen to increase. However, differences exist in the absolute intensity behaviour between theory and experiment, with the experimental TDCS reaching its maximum TDCS intensity at θ_1 = -10.0° before it decreases as the scattered electron angle increases to -15.0°, while the intensity of the M3DW binary region TDCS continues to increase as the scattered electron angle becomes larger. We note that this behaviour of the M3DW cross sections was also observed in our study on furfural.[38] In terms of the DWBA calculations, we found that these give TDCS angular distributions that are very similar to those calculated using the M3DW method at each θ_1, although the DWBA calculations gave a slightly larger absolute value for the TDCS across most angular regions for each scattering angle. Finally, we highlight the significant variation in the absolute scale of the TDCS as the scattered electron angle varies. This result illustrates the importance of obtaining absolute experimental cross section data in order to provide a full assessment of the validity of the theoretical calculations.

As neither of the M3DW or DWBA methods were able to quantitatively reproduce the experimental results, we are thus interested to try and qualitatively explain the experimental observations with a view to improving the theoretical description of the electron impact ionization dynamics of complex molecules. To this end, we consider the relevant orbital momentum profiles of the ionized orbitals shown in Fig. 5. Our approach originates from electron momentum spectroscopy [33-35], where the internal electronic structure of the target is probed through impulsive collisions at high-impact energies. Under the present asymmetric coplanar kinematic conditions at intermediate impact energies, the impulse approximation breaks down and the collisional and structural components become intertwined. However, consideration of the momentum profiles within an impulse approximation (the momentum of the ionized target's electron is equal in magnitude but opposite in sign to the ion recoil momentum) may provide some qualitative explanation of the present observed TDCS.[39,41,57] In this context the range of possible recoil momentum values available to conserve momentum is also shown in Fig. 5 for each experimental scattered electron angle considered. Here the recoil momentum of the ion is at its minimum, q_{min}, in the direction of the momentum transfer (+K), while it is at its

maximum, q_{max}, in the direction anti-parallel to the momentum transfer (-K); see also Fig. 2b.

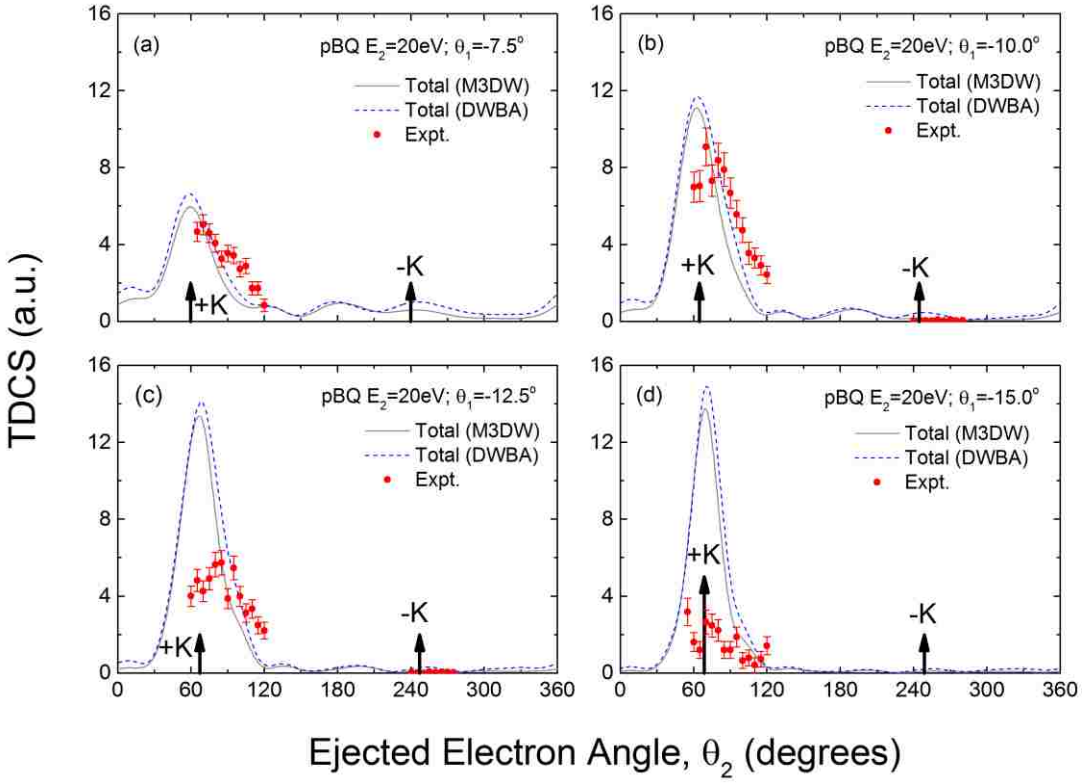

FIG. 4. Experimental and theoretical triple differential cross sections for the electron impact ionization of the unresolved combination of the $4b_{3g}+5b_{2u}+1b_{1g}+2b_{3u}$ orbitals of pBQ for (a) $\theta_1 = -7.5°$, (b) $\theta_1 = -10.0°$, (c) $\theta_1 = -12.5°$, and (d) $\theta_1 = -15.0°$. Here the incident electron energy is 250 eV and the ejected electron energy is 20 eV. See text for further details. Note here that a.u. represents atomic units.

From Figure 5 we can see that for a scattered electron angle of -7.5°, the momentum profile is at its maximum for the minimum magnitude of the recoil momentum, q_{min}. As the scattering angle increases, the range of possible recoil momentum values increases and it becomes possible to sample different sections of the momentum profile. Specifically, the intensity of the orbital momentum profile sampled in the momentum transfer direction (+K) decreases, which in turn results in a local minimum in this direction. The maximum in the momentum profile is then located away from the momentum transfer directions and gives rise to the lobe structures observed in the TDCS, with these becoming more pronounced as the scattered electron angle increases. This interpretation thus qualitatively

provides some explanation of the experimentally observed phenomena. It also suggests that one possible issue with the current theoretical methods involves the spherically averaging approximations used in the calculations. Both the molecular orbital used for the bound state wavefunction and the distorting potential used to calculate the continuum electron wavefunctions are averaged over all orientations so the lack of agreement between theory and experiment might indicate strong orientation dependent effects.

We finally consider the behaviour of the triple differential cross sections for the electron impact ionization of the unresolved combination of the $4b_{3g}+5b_{2u}+1b_{1g}+2b_{3u}$ orbitals within the recoil region (see Fig. 4). Experimentally, no significant intensity is observed in the recoil region for any of the scattered electron angles considered. From the theoretical perspective, both the M3DW and DWBA calculations also indicate weak recoil peak intensities. The absence of significant recoil intensity in pBQ under the current kinematical conditions is not particularly surprising. Previously we have investigated the (e,2e) TDCS for the 4a″ and 3a″ orbitals of phenol under comparable conditions[39] and similar to the current study these did not possess any significant recoil peak intensity. The 4a″ and 3a″ orbitals of phenol are both out-of-plane ring bonding/O(2p) orbitals, which therefore resemble the $2b_{3u}$ and $1b_{1g}$ orbitals of pBQ investigated as a part of this work. The absence of significant recoil structure in phenol was attributed to the delocalisation of the electron density over the molecule, thus weakening any electron-nuclei scattering that is generally required to produce a significant recoil peak intensity. We believe that this is also likely to be the case for pBQ. This is supported by the M3DW calculations, where for both pBQ and phenol the out of plane orbitals have negligible recoil intensity under the present kinematical conditions. We also note that the behaviour of the angular distributions of the TDCS in the binary regions for pBQ and phenol show strong similarities, adding further support to our explanation. Correspondingly this observation supports our assertion regarding the similarity observed in the binary peak region for pBQ and phenol, hence, that the ionization dynamics for similar types of molecular orbitals may possess a characteristic TDCS angular distribution profile.

Lastly, we reflect that the lack of recoil region intensity for pBQ suggests that the ionization model employed within the LEPTS framework,[47-50] may be a good first approximation for describing electron transport through pBQ. However, as the sensitivity

requirements on charged-particle track simulations improves, it appears that ionization treatment must be expanded to consider scattering processes where the secondary electron is ejected at angles away from the momentum transfer direction. This is especially true for larger momentum transfer collisions, where the maximum of the TDCS angular distribution does not often lie on the momentum transfer direction. However, until theoretical methods are developed that can robustly describe/explain scattering phenomena for complex molecular targets over a range of kinematical regimes, the ionization model described within the LEPTS framework appears reasonable. However, it is highly desirable to develop robust, theoretical description of the ionization behaviour of complex molecules as this will ultimately improve the quality of charged-particle track simulations.

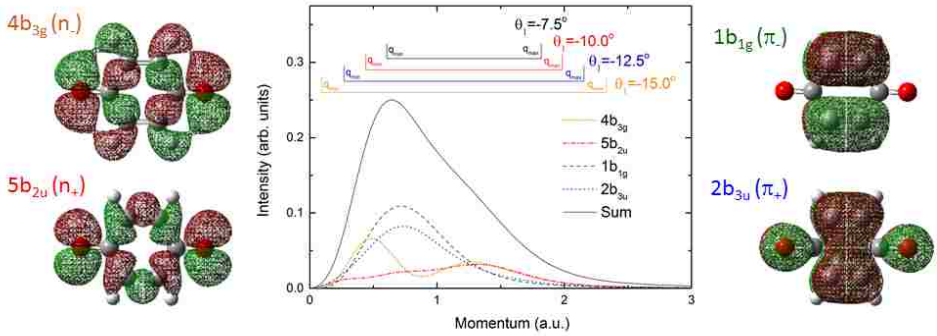

FIG. 5. Theoretical spatial orbital representation and momentum profiles of the pBQ orbitals we examined experimentally. Here the range of linear momenta examined under each kinematical condition is also depicted on the momentum profile. The summed momentum profile for the contributing orbitals is also presented. See text for further details.

IV. CONCLUSION

Experimental triple differential cross sections for the unresolved combination of the four outermost orbitals of *para*-benzoquinone were presented. These cross sections were experimentally inter-normalised to enable in depth evaluation of the angular distribution and an absolute scale for comparison with predictions using different theoretical models. Unfortunately, our theoretical calculations, performed at the molecular 3-body distorted wave and distorted wave Born approximation levels of theory, were unable to quantitatively describe the observed behaviour of the TDCSs. Nonetheless, by considering the orbital momentum profiles of the ionized orbitals we were able to provide

a qualitative description of the experimentally observed phenomena. The results presented in Figure 4 highlight the need for developing tractable theoretical scattering calculations that can adequately describe the molecular targets valence electronic structure. Finally, our systematic investigation into the ionization dynamics of this and similar molecules suggested that certain molecular orbitals may exhibit characteristic TDCS angular distributions.

ACKNOWLEDGMENTS

One of us (MJB) acknowledges the Australian Research Council for some financial support. CGN acknowledges the support from the National Natural Science Foundation of China (NSFC) (Grant No.11174175). Computational work was carried out using LANL Institutional Computing Resources. The Los Alamos National Laboratory is operated by Los Alamos National Security, LLC for the National Nuclear Security Administration of the U.S. Department of Energy under Contract No. DE-AC5206NA25396. This work was partly supported by the US National Science Foundation under Grant. No. PHY-1505819 (EA and DM).

[1]A. Zouni, H.-T. Witt, J. Kern, P. Fromme, N. Krauss, W. Saenger and P. Orth, Nature **409**, 739 (2001).

[2]A. J. Ragauskas, C. K. Williams, B. H. Davison, G. Britovsek, J. Cairney, C. A. Eckert, W. J. Frederick, J. P. Hallett, D. J. Leak, C. L. Liotta, J. R. Mielenz, R. Murphy, R. Templer and T. Tschaplinski, Science **311**, 484 (2006).

[3]M. Hambourger, G. F. Moore, D. M. Kramer, D. Gust, A. L. Moore and T. A. Moore, Chem. Soc. Rev. **38**, 25 (2009).

[4]O. Yehezkeli, R. Tel-Vered, J. Wasserman, A. Trifonov, D. Michaeli, R. Nechushtai and I. Willner, Nat. Comm. **3**, 742 (2012).

[5]B. Huskinson, M. P. Marshak, C. Suh, S. Er, M. R. Gerhardt, C. J. Galvin, X. Chen, A. Aspuru-Guzik, R. G. Gordon and M. J. Aziz, Nature **505**, 195 (2014).

[6]Y. Ding and G. Yu, Angew. Chem. Int. Ed. **55**, 4772 (2016).

[7]Y. Honda, M. Hada, M. Ehara and H. Nakatsuji, J. Phys. Chem. A **106**, 3838 (2002).

[8]G. Ter Horst and J. Kommandeur, Chem. Phys. **44**, 287 (1979).

[9]R. Pou-Amérigo, M. Merchán and E. Ortí, J. Chem. Phys. **110**, 9536 (1999).

[10]J. Weber, K. Malsch and G. Hohlneicher, Chem. Phys. **264**, 275 (2001).

[11]S. Knippenberg and M. S. Deleuze, J. Electron Spectrosc. Relat. Phenom. **178–179**, 61 (2010).

[12]T. N. V. Karsili, D. Tuna, J. Ehrmaier and W. Domcke, Phys. Chem. Chem. Phys. **17**, 32183 (2015).

[13]P. Brint, J.-P. Connerade, P. Tsekeris, A. Bolovinos and A. Baig, J. Chem. Soc., Faraday Trans. 2: Mol. Chem. Phys. **82**, 367 (1986).

[14]D. A. Horke, Q. Li, L. Blancafort and J. R. R. Verlet, Nat. Chem. **5**, 711 (2013).

[15]T. M. Dunn and A. H. Francis, J. Mol. Spectrosc. **50**, 14 (1974).

[16]J. M. Hollas, Spectrochimica Acta **20**, 1563 (1964).

[17]T. Itoh, Chem. Rev. **95**, 2351 (1995).

[18]B. Ómarsson and O. Ingólfsson, Phys. Chem. Chem. Phys. **15**, 16758 (2013).

[19]M. Allan, Chem. Phys. **84**, 311 (1984).

[20]L. G. Christophorou, J. G. Carter and A. A. Christodoulides, Chem. Phys. Lett. **3**, 237 (1969).

[21]P. M. Collins, L. G. Christophorou, E. L. Chaney and J. G. Carter, Chem. Phys. Lett. **4**, 646 (1970).

[22]C. D. Cooper, W. T. Naff and R. N. Compton, J. Chem. Phys. **63**, 2752 (1975).

[23]M. Allan, Chem. Phys. **81**, 235 (1983).

[24]S. A. Pshenichnyuk, N. L. Asfandiarov, V. S. Fal'ko and V. G. Lukin, Int. J. Mass Spectrom. **227**, 281 (2003).

[25]C. W. West, J. N. Bull, E. Antonkov and J. R. R. Verlet, J. Phys. Chem. A **118**, 11346 (2014).

[26]O. G. Khvostenko, P. V. Shchukin, G. M. Tuimedov, M. V. Muftakhov, E. E. Tseplin, S. N. Tseplina and V. A. Mazunov, Int. J. Mass Spectrom. **273**, 69 (2008).

[27]D. Dougherty and S. P. McGlynn, J. Am. Chem. Soc. **99**, 3234 (1977).

[28]J. F. Stanton, K. W. Sattelmeyer, J. Gauss, M. Allan, T. Skalicky and T. Bally, J. Chem. Phys. **115**, 1 (2001).

[29]C. R. Brundle, M. B. Robin and N. A. Kuebler, J. Am. Chem. Soc. **94**, 1466 (1972).

[30]L. Åsbrink, G. Bieri, C. Fridh, E. Lindholm and D. P. Chong, Chem. Phys. **43**, 189 (1979).

[31]N. Kishimoto, K. Okamura and K. Ohno, J. Chem. Phys. **120**, 11062 (2004).

[32]K. Piech, T. Bally, T. Ichino and J. Stanton, Phys. Chem. Chem. Phys. **16**, 2011 (2014).

[33]E. Weigold and I. E. McCarthy, *Electron Momentum Spectroscopy* (Kluwer Academic/Plenum Publishers, New York, 1999).

[34]M. J. Brunger and W. Adcock, J Chem Soc Perk T 2, 1 (2002).

[35]M. Takahashi, Bull. Chem. Soc. Jpn. **82**, 751 (2009).

[36]A. Lahmam-Bennani, J. Electron Spectrosc. Relat. Phenom. **123**, 365 (2002).

[37]J. D. Builth-Williams, S. M. Bellm, D. B. Jones, H. Chaluvadi, D. H. Madison, C. G. Ning, B. Lohmann and M. J. Brunger, J. Chem. Phys. **136**, 024304 (2012).

[38]D. B. Jones, E. Ali, K. L. Nixon, P. Limão-Vieira, M.-J. Hubin-Franskin, J. Delwiche, C. G. Ning, J. Colgan, A. J. Murray, D. H. Madison and M. J. Brunger, J. Chem. Phys. **143**, 184310 (2015).

[39]G. B. da Silva, R. F. C. Neves, L. Chiari, D. B. Jones, E. Ali, D. H. Madison, C. G. Ning, K. L. Nixon, M. C. A. Lopes and M. J. Brunger, J. Chem. Phys. **141**, 124307 (2014).

[40]J. D. Builth-Williams, G. B. da Silva, L. Chiari, D. B. Jones, H. Chaluvadi, D. H. Madison and M. J. Brunger, J. Chem. Phys. **140**, 214312 (2014).

[41]D. B. Jones, J. D. Builth-Williams, S. M. Bellm, L. Chiari, H. Chaluvadi, D. H. Madison, C. G. Ning, B. Lohmann, O. Ingolfsson and M. J. Brunger, Chem. Phys. Lett. **572**, 32 (2013).

[42]J. D. Builth-Williams, S. M. Bellm, L. Chiari, P. A. Thorn, D. B. Jones, H. Chaluvadi, D. H. Madison, C. G. Ning, B. Lohmann, G. B. da Silva and M. J. Brunger, J. Chem. Phys. **139**, 034306 (2013).

[43]S. M. Bellm, J. D. Builth-Williams, D. B. Jones, H. Chaluvadi, D. H. Madison, C. G. Ning, F. Wang, X. G. Ma, B. Lohmann and M. J. Brunger, J. Chem. Phys. **136**, 244301 (2012).

[44]O. Zatsarinny and K. Bartschat, Phys. Rev. A **85**, 032708 (2012).

[45]X. Ren, A. Senftleben, T. Pflüger, A. Dorn, K. Bartschat and J. Ullrich, Phys. Rev. A **83**, 052714 (2011).

[46]M. Ulu, Z. N. Ozer, M. Yavuz, O. Zatsarinny, K. Bartschat, M. Dogan and A. Crowe, J. Phys. B: At. Mol. Opt. Phys. **46**, 115204 (2013).

[47]A. G. Sanz, M. C. Fuss, A. Muñoz, F. Blanco, P. Limão-Vieira, M. J. Brunger, S. J. Buckman and G. García, Int. J. Radiat. Biol. **88**, 71 (2012).

[48]M. C. Fuss, A. G. Sanz, A. Muñoz, F. Blanco, M. J. Brunger, S. J. Buckman, P. Limão-Vieira and G. García, Appl. Radiat. Isotopes **83, Part B**, 159 (2014).

[49]M. C. Fuss, L. Ellis-Gibbings, D. B. Jones, M. J. Brunger, F. Blanco, A. Muñoz, P. Limão-Vieira and G. García, J. Appl. Phys. **117**, 214701 (2015).

[50]M. J. Brunger, K. Ratnavelu, S. J. Buckman, D. B. Jones, A. Muñoz, F. Blanco and G. García, Eur. Phys. J. D **70**, 46 (2016).

[51]F. Blanco, A. Muñoz, D. Almeida, F. Ferreira da Silva, P. Limão-Vieira, M. C. Fuss, A. G. Sanz and G. García, Eur. Phys. J. D **67**, 199 (2013).

[52]S. J. Cavanagh and B. Lohmann, J. Phys. B: At. Mol. Opt. Phys. **32**, L261 (1999).

[53]M. J. Frisch, G. W. Trucks, H. B. Schlegel, G. E. Scuseria, M. A. Robb, J. R. Cheeseman, G. Scalmani, V. Barone, B. Mennucci, G. A. Petersson, H. Nakatsuji, M. Caricato, X. Li, H. P. Hratchian, A. F. Izmaylov, J. Bloino, G. Zheng, J. L. Sonnenberg, M. Hada, M. Ehara, K. Toyota, R. Fukuda, J. Hasegawa, M. Ishida, T. Nakajima, Y. Honda, O. Kitao, H. Nakai, T. Vreven, J. A. Montgomery, J. E. Peralta, F. Ogliaro, M. Bearpark, J. J. Heyd, E. Brothers, K. N. Kudin, V. N. Staroverov, R. Kobayashi, J. Normand, K. Raghavachari, A. Rendell, J. C. Burant, S. S. Iyengar, J. Tomasi, M. Cossi, N. Rega, J. M. Millam, M. Klene, J. E. Knox, J. B. Cross, V. Bakken, C. Adamo, J. Jaramillo, R. Gomperts, R. E. Stratmann, O. Yazyev, A. J. Austin, R. Cammi, C. Pomelli, J. W. Ochterski, R. L. Martin, K. Morokuma, V. G. Zakrzewski, G. A. Voth, P. Salvador, J. J. Dannenberg, S. Dapprich, A. D. Daniels, Ö. Farkas, J. B. Foresman, J. V. Ortiz, J. Cioslowski and D. J. Fox, *Gaussian 09, Revision B.01*. (2010).

[54]J. P. D. Cook and C. E. Brion, Chem. Phys. **69**, 339 (1982).

[55]D. H. Madison and O. Al-Hagan, Journal of Atomic, Molecular, and Optical Physics **2010**, 367180 (2010).

[56]J. Gao, J. L. Peacher and D. H. Madison, J. Chem. Phys. **123**, 204302 (2005).

[57]S. Xu, X. Ma, S. Yan and P. Zhang, J. Chem. Phys. **136**, 237101 (2012).

VII. Electron-impact ionization of H_2O at low projectile energy: Internormalized triple-differential cross sections in three-dimensional kinematics

Xueguang Ren[1], Sadek Amami[2], Khokon Hossen[1], Esam Ali[2],ChuanGang Ning[3], James Colgan[4], Don Madison[2], and Alexander Dorn[1]

[1]*Max-Planck-Institut fur Kernphysik, 69117 Heidelberg, Germany*

[2]*Physics Department, Missouri University of Science and Technology, Rolla, Missouri 65409, USA*

[3]*Department of Physics, State Key Laboratory of Low-Dimensional Quantum Physics, Tsinghua University, Beijing 100084, China*

[4]*Theoretical Division, Los Alamos National Laboratory, Los Alamos, New Mexico 87545, US*

We report a combined experimental and theoretical study on the electron-impact ionization of water (H_2O) at the relatively low incident energy of E_0 = 81 eV in which either the $1b_1$ or $3a_1$ orbitals are ionized leading to the stable H_2O^+ cation. The experimental data were measured by using a reaction microscope, which can cover nearly the entire 4π solid angle for the secondary electron emission over a range of ejection energies. We present experimental data for the scattering angles of 6^o and 10^o for the faster of the two outgoing electrons as function of the detection angle of the secondary electron with energies of 5 eV and 10 eV. The experimental triple-differential cross sections are internormalized across the measured scattering angles and ejected energies. The experimental data are compared with predictions from two molecular three-body distorted-wave approaches: One applying the orientation-averaged molecular orbital (OAMO) approximation and one using a proper-average (PA) over orientation-dependent cross sections. The PA calculations are in better agreement with the experimental data than the OAMO calculations, for both the angular dependence and the relative magnitude of the observed cross-section structures.

I. **INTRODUCTION**

Electron-impact ionization dynamics of atoms and molecules have been of great interest from both theoretical and experimental points of view. It plays a crucial role in a variety of scientific and practical applications ranging from radiation chemistry and biology to astrophysics and atmospheric sciences [1,2]. It has been discovered recently that low-energy electrons can significantly induce breaks in DNA strands via the dissociative electron attachment resonances and a superposition of various nonresonant mechanisms related to excitation dissociation and ionization processes [3,4].

The water molecule (H_2O) is important in this respect, since it is ubiquitous on earth and surrounds all biological matter. Understanding the ionization dynamics requires a detailed knowledge of the interaction probabilities (i.e., the cross sections). A comprehensive way of characterizing the electron-impact ionization dynamics is to detect the two outgoing electrons in coincidence, the so-called (e,2e) studies [5,6], which determine the momentum vectors of all final-state particles. The quantity measured in the (e, 2e) experiments is the triple-differential cross section (TDCS), i.e., a cross section that is differential in the solid angles of both electrons and the energy of one of them. The energy of the other electron is given by energy conservation [7,8]. Such kinematically complete experiments serve as a powerful tool to comprehensively test theoretical models that account for the quantum few-body dynamics which are important to aid in the development of theoretical models and to provide the input parameters in Monte Carlo simulation in medical radiation therapy.

In recent years, theory has made tremendous progress in describing the electron-impact ionization dynamics of simple atoms and molecules, see e.g., [9-17]. Much more challenging, however, is the treatment of more complex targets, like heavy atoms and molecules. Electron-impact ionization dynamics of the water molecule has been previously studied by the Lohmann group in the coplanar asymmetric geometry at E_o=250 eV by using a conventional (e, 2e) spectrometer to examine ionization of the $2a_1$, $1b_2$, $3a_1$ and $1b_1$ states of H_2O [18]. Murray and co-workers performed coplanar symmetric and asymmetric (e, 2e) studies for the $1b_1$ state of H_2O [19] and symmetric coplanar and noncoplanar studies for the $3a_1$ state of H_2O at low impact energies [20]. Several models have been developed

to describe the ionization dynamics of H_2O. The agreement between theories and experiments, however, is not as good as the results for the ionization of simple targets; see e.g., Refs. [18-26]. Recent calculation of (e, 2e) on CH_4 using the molecular three-body distorted-wave approximation found that the method with proper averages (PA) is in much better agreement with experiment than the orientation-averaged molecular orbitals (OAMO) calculations [27]. On the other hand, experimental techniques were recently developed that allow for simultaneously accessing a large fraction of the entire solid angle and a large range of energies of the continuum electrons in the final state [28,29], the entire angular acceptance for the slow ejected electron within the scattering plane [30] and, more recently, the measurements of internormalized cross sections [13,31,32]. Thus, Thus, theories can be tested significantly more comprehensively over a large range of the final-state phase space.

In the present work, we perform a kinematically complete study of electron-impact ionization of H_2O at low projectile energy (E_o= 81 eV). Ionization of either the $1b_1$ or $3a_1$ orbitals is observed (we do not resolve the individual states) where the residual ion is stable and does not dissociate.

$$e_o + H_2O \rightarrow H_2O^+ + e_1 + e_2 \tag{88}$$

The TDCSs were measured by covering a large part of the full solid angle for the emitted electron. Since the experimental data are internormalized for different kinematical situations, a single common scaling factor is sufficient to fix the absolute value of all the experimental data which then can be compared with the theoretical predictions. The measurements reported here cover two ejected-electron energies (E_2=5.0 eV and 10.0 eV) and two projectile scattering angles ($\theta_1 = 6^o$ and 10.0^o). The experimental data are compared with theoretical predictions from two different versions of the molecular three-body distorted-wave approximation (M3DW). While both include the final-state postcollision interaction (PCI) exactly, they treat the averaging over spatial molecular alignment with different degrees of sophistication [27].

This paper is organized as follows: After a brief description of the experimental apparatus in Sec. II, we summarize the essential points of the two theoretical models in

Sec. III. The results are presented and discussed in Sec. IV, before we finish with conclusions in Sec. V. Unless specified otherwise, atomic units (a.u.) are used throughout.

II. EXPERIMENTAL METHOD

The experiment was performed by using a reaction microscope [28] that was specially built for electron-impact ionization studies. It was recently updated with a pulsed photoemission electron gun [33,34]. Since details of the experimental setup can be found in Refs. [28,33,34], only a brief outline will be given here. The well-focused ($\approx$ 1 mm diameter), pulsed electron beam with an energy of E_o= 81 eV is crossed with a continuous supersonic gas jet, which is produced using a $30\ \mu m$ nozzle and two-stage supersonic gas expansion. Here, helium gas with a partial pressure of 1 bar mixed with water vapor with a partial pressure of about 400 mbar was used. The electron beam is generated by illuminating a tantalum photocathode with a pulsed ultraviolet laser beam $(\lambda = 266\ nm,\ \Delta t < 0.5\ ns)$. The energy and temporal width of the electron pulses are about 0.5 eV (ΔE_o) and 0.5 ns (Δt_o), respectively.

Homogeneous magnetic and electric fields guide electrons and ions from the reaction volume onto two position- and time-sensitive microchannel plate detectors that are equipped with fast multihit delay-line readout. The projectile beam axis (defining the longitudinal z direction) is aligned parallel to the electric and magnetic extraction fields. Therefore, after crossing the target gas jet, the unscattered primary beam reaches the center of the electron detector, where a central bore in the multichannel plates allows it to pass without inducing a signal. The detection solid angle for H_2O^+ ions is 4π. The acceptance angle for detection of electrons up to an energy of 15 eV is also close to 4π, except for the acceptance holes at small forward and backward angles where the electrons end up in the detector bore.

Experimental data are recorded by triple-coincidence detection of two electrons $(e_1$ and $e_2)$ and the H_2O^+ cation. The three-dimensional momentum vectors and, consequently, kinetic energies and emission angles of final-state electrons and ions are determined from the individually measured time-of-flight and position of particles hitting on the detectors. The electron binding energy $(\varepsilon_b = E_o - E_1 - E_2)$ resolution of $\Delta\varepsilon_b \approx 2.5$ eV has been obtained in the present experiment. Since the complete

experimentally accessible phase space is measured simultaneously, all relative data are cross-normalized and only a single global factor fixing the absolute scale is required in comparison of theory and experiment [13,31,32].

III. THEORETICAL MODELS

We used two theoretical methods to describe the present electron-impact ionization process. Although they have been described previously [35-38] we summarize the essential ideas and the particular ingredients for the current cases of interest in order to make this paper self-contained. More detailed information can be found in the references given. The direct-scattering amplitude is given by

$$T_{dir} = \left\langle \underbrace{\chi_a^-(\mathbf{k}_a,\mathbf{r}_0)\chi_b^-(\mathbf{k}_b,\mathbf{r}_1)C_{ab}(\mathbf{r}_{01})}_{Final\ \text{state}} \right| \mathrm{W} \left| \underbrace{\phi_{Dy}(\mathbf{r}_1,\mathbf{R})\chi_i^+(\mathbf{k}_i,\mathbf{r}_0)}_{Initial\ \text{state}} \right\rangle, \tag{89}$$

where $\mathbf{k}_i, \mathbf{k}_a$ and $\mathbf{k}_b$ are the wave vectors for the initial, scattered, and ejected electrons, respectively, $\chi_i^+(\mathbf{k}_i,\mathbf{r}_0)$ is an initial-state continuum distorted wave and the (+) indicates outgoing-wave boundary conditions, $\chi_a^-(\mathbf{k}_a,\mathbf{r}_0), \chi_b^-(\mathbf{k}_b,\mathbf{r}_1)$ are the scattered and ejected-electron distorted waves with incoming-wave boundary conditions, and the factor $\mathrm{C}_{ab}(\mathbf{r}_{01})$ is the final-state Coulomb-distortion factor between the two electrons normally called the postcollision interaction (PCI). Here we use the exact final-state electron-electron interaction and not an approximation for it such as the Ward-Macek factor [39]. The perturbation $\mathrm{W}=\mathrm{V}_i - U_i$, where V_i is the initial-state interaction potential between the incident electron and the neutral molecule, and U_i represents the spherically symmetric interaction between the projectile and the active electron which is used to calculate the initial-state distorted wave $\chi_i^+(\mathbf{k}_i,\mathbf{r}_0)$. Here $\phi_{Dy}(\mathbf{r}_1,\mathbf{R})$ is the initial bound-state wave function, which is commonly called the Dyson molecular orbital, for the active electron and it depends both on $\mathbf{r}_1$ and the orientation of the molecule which is designated by $\mathbf{R}$. The triple-differential cross section (TDCS) for a given orientation $\mathbf{R}$ with respect to the laboratory frame can be obtained from

$$\sigma^{TDCS}(\mathbf{R}) = \frac{1}{(2\pi)^5}\frac{k_a k_b}{k_i}\left[\left|T_{dir}(\mathbf{R})\right|^2 + \left|T_{exc}(\mathbf{R})\right|^2 + \left|T_{dir}(\mathbf{R}) - T_{exc}(\mathbf{R})\right|^2\right], \quad (90)$$

where the exchange-scattering T_{exc} is calculated similarly to T_{dir} except that the particles 1 and 2 are interchanged in the final-state wave function. To take the proper average (PA) over all molecular orientations [37], the TDCS is calculated for each orientation and then averaged over all possible orientations so that

$$\sigma^{PA} = \frac{\int \sigma^{\mathrm{TDCS}}(\mathbf{R})\, \mathrm{d}\Omega_R}{\int d\Omega_R} \quad (91)$$

The only term in the integral for the *T* matrix that depends on the orientation is the Dyson wave function. In the orientation averaged molecular orbital (OAMO) approximation [35], we average the wave function over all orientations and then we calculate a single TDCS. This approximation save a lot of computer time since the PA needs thousands of processors to do a single calculation whereas the OAMO needs less than hundred.

IV. RESULTS AND DISCUSSION

Water (H_2O) contains 10 electrons and has five molecular orbitals: $1a_1$, $2a_1$, $1b_2$, $3a_1$ and $1b_1$. The reported valence electron binding energies of water monomer are 32.4 eV, 18.7 eV, 14.8 eV and 12.6 eV corresponding to $(2a_1)^{-1}$, $(1b_2)^{-1}$, $(3a_1)^{-1}$ and $(1b_1)^{-1}$ states, [40] respectively. We study electron-impact ionization of H_2O with the formation of the stable H_2O^+ cation which results from the ionization of either the $1b_1$ or $3a_1$ orbitals. In the present experiment, the $1b_1$ and $3a_1$ orbitals are not resolved due to the limited binding-energy resolution, thus, the experimental data represent the summed TDCS for the ionization of the $1b_1$ and $3a_1$ orbitals of H_2O. Figure 1 shows the experimental and theoretical TDCS for ionization of H_2O by 81 eV electron impact as three-dimensional (3D) polar plots for a projectile scattering angle of $\theta_1 = -10^o$ as a function of the emission direction of a slow ejected electron with E_2= 10 eV energy. Figure 1(a) corresponds to the experimental data, while Fig. 1(b) shows the calculated result from

the OAMO method. The projectile enters from the bottom with momentum $\mathbf{k}_i$ and is scattered to the left with momentum $\mathbf{k}_a$ (hence the minus in the notation for the scattering angle). These two vectors define the scattering (xz) plane, as indicated by the solid (red) frame in Fig. 1(a). The momentum transferred to the target $\mathbf{q} = \mathbf{k}_i - \mathbf{k}_a$, is also shown on the figures.

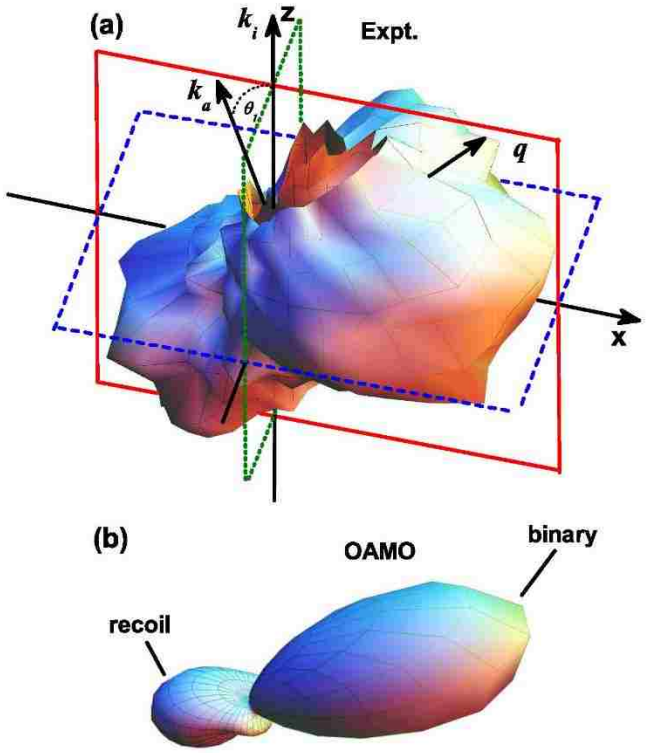

FIG. 1. Summed TDCS for experiment (top panel) and OAMO theory (bottom panel) presented as 3D images for electron-impact (E_0 = 81 eV) ionization of $1b_1$ and $3a_1$ orbitals of H_2O. The scattering angle is $\theta_1 = -10^o$, and the ejected electron energy is E_2= 10 eV. The experimental and theoretical data are normalized to unity for the binary peaks.

In these 3D plots, the TDCS for a particular direction is given as the distance from the origin of the plot to the point on the surface which is intersected by the ejected electron's emission direction. The kinematics chosen displays exemplarily the principal features of the emission pattern: it is governed by the well-known binary and recoil lobes. The binary lobe is oriented roughly along the direction of the momentum transfer $\mathbf{q}$, which would corresponds to electrons emitted after a single binary collision with the projectile. In the opposite direction the recoil lobe is found, where the outgoing slow electron, initially

moving in the binary direction, additionally backscatters in the ionic potential. For ionization from *p* orbitals, the binary peak often exhibits a minimum along the momentum transfer direction and there is a small minimum seen in the experimental data. This is the result of the characteristic momentum profile of the *p*-like $1b_1$ and $3a_1$ orbitals of H_2O that has a node for vanishing momentum [40]. The experimental and theoretical 3D plots are normalized to unity for the binary peaks. We see that the theoretical recoil peak is too small and the size of the out-of-scattering-plane cross section is strongly underestimated by OAMO. Furthermore, the minimum along the momentum transfer direction indicated in the experimental pattern is not present in the theoretical result. For the PA calculation no full 3D image was obtained since this theory is orders of magnitude computationally more expensive and so calculations were restricted to major cutting planes which are discussed in the following. However, the PA approach does predict a minimum similar to the experimental data.

For a quantitative comparison between experiment and both the OAMO and PA methods, the cross sections in three orthogonal planes are presented in Figs. 2-4. These are cuts through the 3D TDCS image as indicated in Fig. 1(a) by the solid, dashed and dotted frames. The experimental data represent the summed TDCS for the ionization of both the $1b_1$ and $3a_1$ orbitals of H_2O while for theories, both the summed cross sections as well as the the separate $1b_1$ and $3a_1$ cross sections are shown in Figs. 2-4. The studied kinematical conditions correspond to projectile scattering angles of $\theta_1 = -6^o$ and -10^o, and to ejected-electron energies of E_2 = 5 eV and 10 eV, respectively. The scaling factor used to normalize the experimental data to the theories was found by achieving a good visual fit of experiment and the PA calculations for the TDCS in the scattering plane at $\theta_1 = -6^o$ and E_2= 10 eV [Fig. 2(h)]. This factor was subsequently applied to all other kinematics and planes, i.e., the experimental data are consistently cross-normalized to each other. The OAMO theoretical results are multiplied by a factor of ten in order to compare with the results from experiment and PA calculations.

Figure 2 shows the results for detection of the secondary electron in the scattering plane, i.e., the xz plane of Fig. 1(a). It is obvious that, for the TDCS summed over $1b_1$ and

$3a_1$ orbitals, the OAMO strongly overestimate the size of the binary peak relative to the recoil peak. While both theories predict a double binary peak for all four cases, the PA calculations have a broader double binary peak with a minimum near the momentum transfer direction which is in better agreement with experiment. For the OAMO results, the second peak is much smaller and shifted to much larger angles. In experiment, the minimum in the binary lobe is not observed except for the case $\theta_1 = -10^o$ and E_2 = 10 eV where a minimum is hinted at about the momentum transfer direction. While both the OAMO and PA results predict a single peak structure for the recoil lobe, the PA predicts a shoulder at the large angle side consistent with the experimental data. Although the cross section close to 180^o cannot be accessed experimentally, the available data suggest a very broad recoil peak similar to PA especially for $\theta_1 = -10^o$ and E_2 = 5 eV. Overall, regarding the relative angular dependence of the TDCSs, The PA is in much better agreement with experiment than the OAMO.

It can be seen in Fig. 2 that the two theories differ strongly from each other especially for the separate $1b_1$ calculations. The OAMO TDCS for ionization of the $1b_1$ orbital shows a much stronger binary peak than recoil peak while the PA results exhibit a stronger recoil peak than binary peak consistent with the experimental data. Both the OAMO and PA results have double binary peaks with minimum shifted to larger angles than the momentum transfer direction. However, the OAMO minimum is shifted to much larger angles and the PA minimum is closer to experiment for the cases where experiment sees a double binary peak. On the other side, the predicted patterns for $3a_1$ are rather similar between OAMO and PA with a small binary peak and larger recoil peak.

Figure 3 shows a comparison between experiment and theory for the yz .plane (half-perpendicular plane). For this plane, symmetry considerations require the cross sections to be symmetric about 180^o, which can indeed be seen in both theory and experiment. In experiment, there is an indication of a three-lobe structure for all the cases. It can be seen in the 3D plot of Fig.1(a) that this plane cuts through the binary peak which results two symmetric maxima in the ranges $\theta_2 = 30^o - 90^o$ and $\theta_2 = 270^o - 330^o$, respectively. In addition, the recoil lobe gives rise to the central maximum at $\theta_2 = 180^o$. Concerning the

central peaks, the PA is in much better agreement with experiment than the OAMO. Here, the OAMO predicts a minimum or a flat distribution at $\theta_2 = 180^o$ except for the case of $\theta_1 = -6^o$ for E_2 = 10 eV. In all panels, the predicted cross sections are significantly smaller than observed experimentally for $\theta_2 \leq 90^o$ and, by symmetry, for $\theta_2 \geq 270^o$. Both PA and OAMO underestimate the out-of-the scattering plane size of the binary lobes. It is again interesting to note that significant discrepancies are seen between OAMO and PA in particular for the separate $1b_1$ calculations where the OAMO exhibits a minimum at $\theta_2 = 180^o$ with two maximums at about 120^o and 240^o while the PA predicts a strong maximum at $\theta_2 = 180^o$ with two side peaks at about 90^o and 270^o. The calculations for $3a_1$ are again rather similar between OAMO and PA.

Figure 4 shows the comparison between experiment and theories for the full-perpendicular plane (i.e., the xy-plane). Here, the experimental angular acceptance covers the entire $0^o - 360^o$ range, but the cross sections are again symmetric with respect to 180^o. The binary and recoil peaks are observed in the vicinity of $\phi_2 = 0^o$ and 180^o, respectively. The two theories in this case agree rather well in shape for the summed and the separate $1b_1$ and $3a_1$ TDCS, and they are in rather good agreement with the experimental data, except that the relative intensity of the recoil peaks are too low for Fig4.b and too high for Fig4.c in the OAMO curves.

V. CONCLUSIONS

We have reported a comprehensive study of the electron-impact ionization dynamics of H_2O for a projectile energy of 81 eV. Experimentally, the three-dimensional momentum vectors of the final-state particles are determined for a large part of the solid angle for the slow emitted electron. Thus, full three-dimensional representations of the cross sections are accessible. The summed triple-differential cross sections for ionization of $1b_1$ and $3a_1$ orbitals of H_2O obtained experimentally were internormalized across the scattering angles $\theta_1 = -6^o$ and -10^o and ejected electron energies E_2 = 5 eV and 10 eV, thus providing a thorough test for the theoretical models. The experimental data were

compared with predictions from the molecular three-body distorted-wave approximation coupled with OAMO and PA methods.

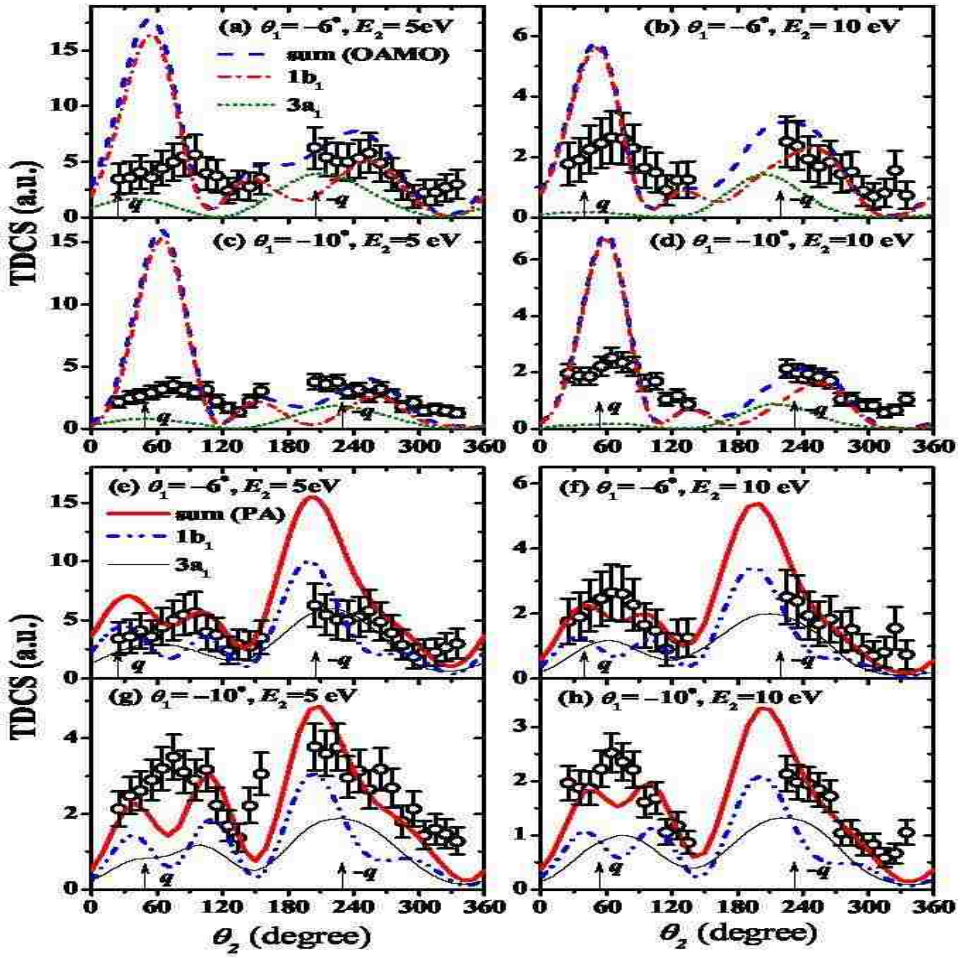

FIG. 2. Experimental and theoretical triple-differential cross sections (TDCS) for electron-impact (E_0 = 81 eV) ionization of $1b_1$ and $3a_1$ orbitals of H_2O presented as a function of the ejected electron (e_2) emission angle at scattering angles $\theta_1 = -6^o$ and $\theta_1 = -10^o$ for ejected-electron energies E_2 = 5 eV (left column) and E_2 = 10 eV (right column). Experimental data (open circles with error bars) are the summed TDCS and theoretical calculations (lines) for the summed and the separate $1b_1$ and $3a_1$ TDCS are obtained by OAMO (top two rows) and PA (bottom two rows) methods. The magnitude of OAMO calculations have been multiplied by a factor of 10. The vertical arrows indicate the momentum transfer direction, $\mathbf{q}$ and its opposite, $-\mathbf{q}$. The results are for the scattering plane, i.e., the xz-plane of Fig. 1(a)

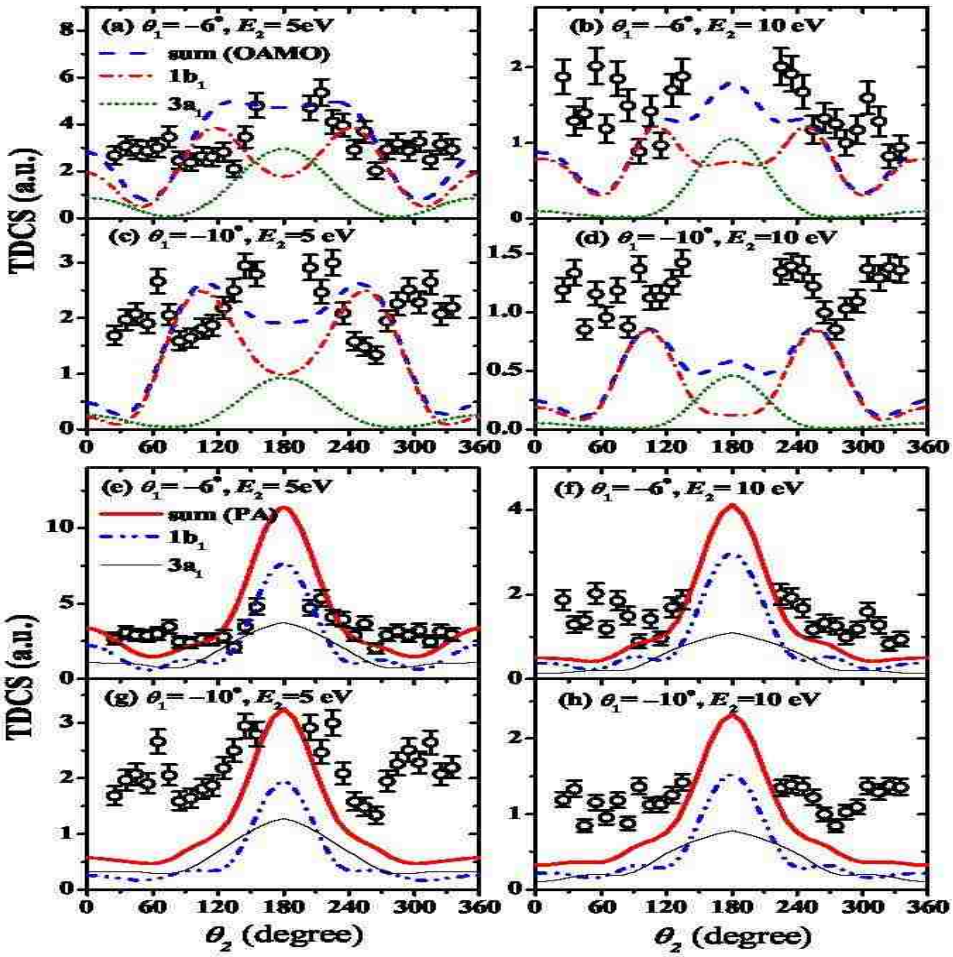

FIG. 3. Same as Fig. 2 for the "half-perpendicular" plane, i.e., the yz plane of Fig. 1(a).

There is overall much better agreement between the PA predictions and the experimental data than the OAMO concerning both the angular dependence of the cross sections and the relative magnitude over the entire range of angle and energy conditions analyzed. Noticeable systematic discrepancies occur in the half-perpendicular plane (Fig. 3), where both OAMO and PA predictions are significantly smaller than that observed experimentally in the angular ranges $\theta_2 \leq 90^o$ and, by symmetry, $\theta_2 \geq 270^o$. In comparison, for ionization of the atomic target Ne which has the same number of bound electrons as H_2O, the three-body distorted-wave theory reveals an unprecedented degree of agreement with experiment [13, 31]. The two calculations based on the three-body distorted-wave theory differ strongly from each other in both the relative shape and the

magnitude of the cross sections. This illustrates the fact that the theoretical treatment of electron-impact ionization of molecule is complicated and the results are very sensitive to the details of the model employed. The fact that the PA calculation agrees better with experiment for the scattering plane than the other two planes suggests that second Born terms which are not included in the present treatment may be more important in the out-of-the scattering plane than in the scattering plane. The present work indicates that it is more accurate to perform a proper average over orientation-dependent cross sections than to use the orientation-averaged molecular orbital for calculations. The computational cost of the proper average method, however, is much higher than the orientation-averaged molecular orbital approximation. OAMO calculations can be easily performed by using less than 100 processors while PA calculations require several thousand processors!

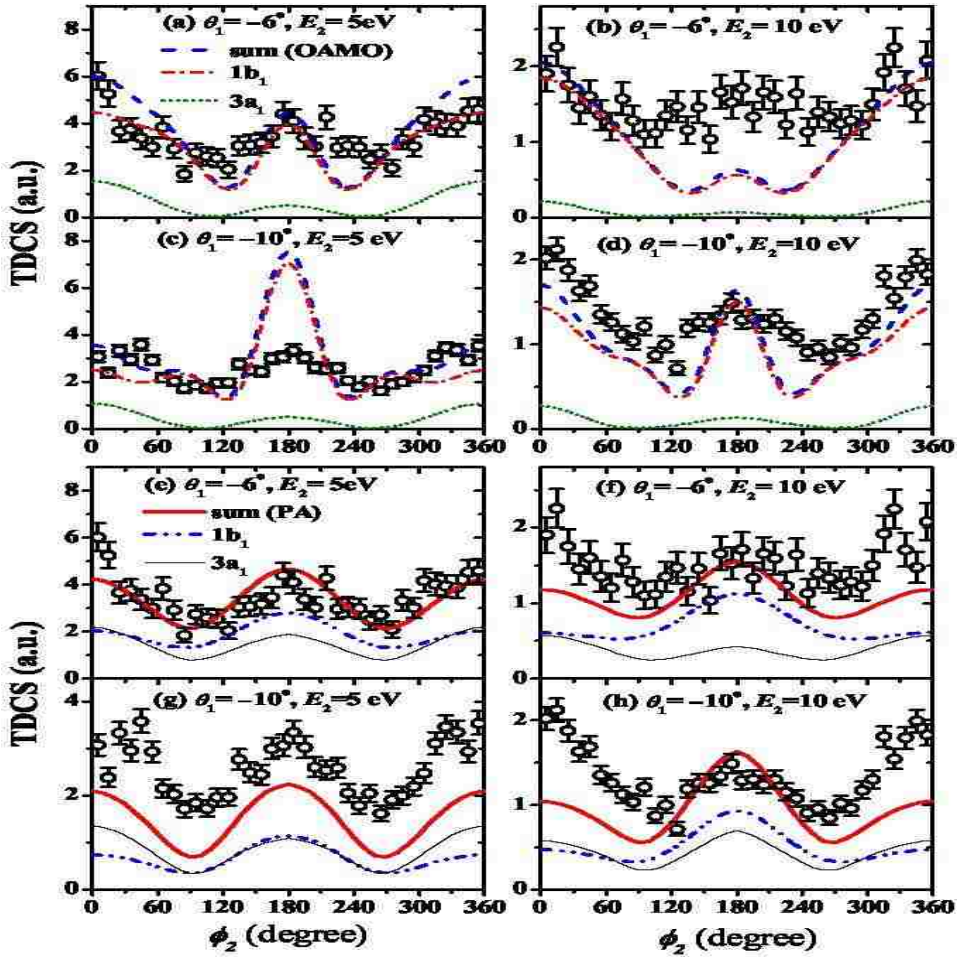

FIG. 4. Same as Fig. 2 for the “full-perpendicular" plane, i.e., the xy plane of Fig. 1(a).

ACKNOWLEDGMENTS

This work was supported, in part, by the United States National Science Foundation under grant No. PHY-1505819 (SA, EA, and DM) and by the National Natural Science Foundation of China under Grant No. 11174175 (CN). Computational work was performed with Institutional Computing resources made available through the Los Alamos National Laboratory. The Los Alamos National Laboratory is operated by Los Alamos National Security, LLC, for the National Nuclear Security Administration of the US Department of Energy under Contract No. DE-AC5206NA25396. EA and SA would also like to thank the Libyan Ministry of Higher Education's Scholarship for financial support.

[1] E. Alizadeh, T. M. Orlando, and L. Sanche, Annu. *Rev. Phys. Chem*. **66**, 379 (2015).

[2] B. C. Garrett, D. A. Dixon, D. M. Camaioni, D. M. Chipman, M. A. Johnson, C. D. Jonah, G. A. Kimmel, J. H. Miller, T. N. Rescigno, P. J. Rossky, S. S. Xantheas, S. D. Colson, A. H. Laufer, D. Ray, P. F. Barbara, D. M. Bartels, K. H. Becker, K. H. Bowen, S. E. Bradforth, I. Carmichael, J. V. Coe, L. R. Corrales, J. P. Cowin, M. Dupuis, K. B. Eisenthal, J. A. Franz, M. S. Gutowski, K. D. Jordan, B. D. Kay, J. A. LaVerne, S. V. Lymar, T. E. Madey, C. W. McCurdy, D. Meisel, S. Mukamel, A. R. Nilsson, T. M. Orlando, N. G. Petrik, S.M. Pimblott, J. R. Rustad, G. K. Schenter, S. J. Singer, A. Tokmakoff, L.-S.Wang, and T. S. Zwier, *Chem. Rev*. (Washington, DC, USA) **105**, 355 (2005).

[3] M. A. Huels, B. Boudaiffa, P. Cloutier, D. Hunting, and L. Sanche, *J. Am. Chem. Soc*. **125**, 4467 (2003).

[4] S.M. Pimblott and J. A. LaVerne, Radiat. *Phys. Chem*. **76**, 1244 (2007).

[5] H. Ehrhardt, M. Schulz, T. Tekaat, and K.Willmann, *Phys. Rev. Lett*. **22**, 89 (1969).

[6] U. Amaldi, A. Egidi, R. Marconero, and G. Pizzella, *Rev. Sci. Instrum*. **40**, 1001 (1969).

[7] H. Ehrhardt, K. Jung, G. Knoth, and P. Schlemmer, Z. *Phys. D: At., Mol. Clusters* **1**, 3 (1986).

[8] A. Lahmam-Bennani, *J. Phys. B: At., Mol. Opt. Phys*. **24**, 2401 (1991).

[9] T. N. Rescigno, M. Baertschy, W. Isaacs, and C. McCurdy, Science **286**, 2474 (1999).

[10] I. Bray, D. Fursa, A. Kadyrov, A. Stelbovics, A. Kheifets, and A. Mukhamedzhanov, *Phys. Rep*. **520**, 135 (2012).

[11] X. Ren, A. Senftleben, T. Pfl¨uger, K. Bartschat, O. Zatsarinny, J. Berakdar, J. Colgan, M. S. Pindzola, I. Bray, D. V. Fursa, and A. Dorn, *Phys. Rev*. A **92**, 052707 (2015).

[12] O. Zatsarinny and K. Bartschat, *Phys. Rev. Lett*. **107**, 023203 (2011).

[13] T. Pfl¨uger, O. Zatsarinny, K. Bartschat, A. Senftleben, X. Ren, J. Ullrich, and A. Dorn, *Phys. Rev. Lett*. **110**, 153202 (2013).

[14] X. Ren, A. Senftleben, T. Pfl¨uger, A. Dorn, J. Colgan, M. S. Pindzola, O. Al-Hagan, D. H. Madison, I. Bray, D. V. Fursa, and J. Ullrich, *Phys. Rev*. A **82**, 032712 (2010).

[15] O. Al-Hagan, C. Kaiser, A. J. Murray, and D. Madison, *Nat. Phys*. **5**, 59 (2009).

[16] X. Ren, T. Pfl¨uger, S. Xu, J. Colgan, M. S. Pindzola, A. Senftleben, J. Ullrich, andA.Dorn,Phys. *Rev. Lett.* **109**, 123202 (2012).

[17] M. C. Zammit, J. S. Savage, D. V. Fursa, and I. Bray, *Phys. Rev. Lett.* **116**, 233201 (2016).

[18] D. S. Milne-Brownlie, S. J. Cavanagh, B. Lohmann, C. Champion, P. A. Hervieux, and J. Hanssen, *Phys. Rev*. A **69**, 032701 (2004).

[19] C. Kaiser, D. Spieker, J. Gao, M. Hussey, A. Murray, and D. H. Madison, *J. Phys. B: At., Mol. Opt. Phys*. **40**, 2563 (2007).

[20] K. L. Nixon, A. J. Murray, O. Al-Hagan, D. H. Madison, and C. Ning, *J. Phys. B: At., Mol. Opt. Phys*. **43**, 035201 (2010).

[21] C. Champion, C. Dal Cappello, S. Houamer, and A. Mansouri, *Phys. Rev*. A **73**, 012717 (2006).

[22] C. Dal Cappello, Z. Rezkallah, S. Houamer, I. Charpentier, P. A. Hervieux, M. F. Ruiz-Lopez, R. Dey, and A. C. Roy, *Phys. Rev*. A **84**, 032711 (2011).

[23] I. T´oth, R. I. Campeanu, and L. Nagy, Eur. *Phys. J*. D **66**, 1 (2012).

[24] M. Sahlaoui, M. Bouamoud, B. Lasri, and M. Dogan, *J. Phys. B: At., Mol. Opt. Phys*. **46**, 115206 (2013).

[25] C.-Y. Lin, C. W. McCurdy, and T. N. Rescigno, *Phys. Rev*. A **89**, 012703 (2014).

[26] S. B. Zhang, X. Y. Li, J. G.Wang, Y. Z. Qu, and X. Chen, *Phys. Rev*. A **89**, 052711 (2014).

[27] H. Chaluvadi, C. G. Ning, and D. Madison, *Phys. Rev*. A **89**, 062712 (2014).

[28] J. Ullrich, R. Moshammer, A. Dorn, R. D¨orner, L. Schmidt, and H. Schmidt-B¨ocking, *Rep. Prog. Phys*. **66**, 1463 (2003).

[29] M. D¨urr, C. Dimopoulou, A. Dorn, B. Najjari, I. Bray, D. V. Fursa, Z. Chen, D. H. Madison, K. Bartschat, and J. Ullrich, *J. Phys. B: At., Mol. Opt. Phys*. **39**, 4097 (2006).

[30] M. A. Stevenson and B. Lohmann, *Phys. Rev*. A **77**, 032708 (2008).

[31] X. Ren, S. Amami, O. Zatsarinny, T. Pfl¨uger, M.Weyland,W. Y. Baek, H. Rabus, K. Bartschat, D. Madison, and A. Dorn, *Phys. Rev.* A **91**, 032707 (2015).

[32] X. Ren, S. Amami, O. Zatsarinny, T. Pfl¨uger, M. Weyland, A. Dorn, D. Madison, and K. Bartschat, *Phys. Rev*. A **93**, 062704 (2016).

[33] X. Ren, T. Pfl¨uger, M.Weyland,W.Y. Baek,H.Rabus, J.Ullrich, and A. Dorn, *J. Chem. Phys*. **141**, 134314 (2014).

[34] X. Ren, E. Jabbour Al Maalouf, A. Dorn, and S. Denifl, Nat. Commun. **7**, 11093 (2016).

[35] J. Gao, J. L. Peacher, and D. H. Madison, *J. Chem. Phys*. **123**, 204302 (2005).

[36] D. H. Madison and O. Al-Hagan, *J. At. Mol. Opt. Phys*. **2010**, 24 (2010).

[37] E. Ali, K. Nixon, A. Murray, C. Ning, J. Colgan, and D. Madison, *Phys. Rev.* A **92**, 042711 (2015).

[38] A. Sakaamini, S. Amami, A. J. Murray, C. Ning, andD.Madison, *J. Phys. B: At., Mol. Opt. Phys*. **49**, 195202 (2016).

[39] S. J. Ward and J. H. Macek, *Phys. Rev.* A **49**, 1049 (1994).

[40] Y. R. Miao, C. G. Ning, and J. K. Deng, *Phys. Rev*. A **83**, 062706 (2011).

VIII. Experimental and theoretical cross sections for molecular-frame electron-impact excitation-ionization of D_2

Julian C. A. Lower[1], Esam Ali[2], Susan Bellm[3], Erich Weigold[3],Allison Harris[4], C G Ning[5], and D. H. Madison[2]

[1]Institut fur Kernphysik, Max-van-Lane-Strasse 1, 60438 Frankfurt am Main, Germany

[2]Missouri University of Science and Technology, Rolla, MO 65409, USA

[3]AMPL,RSPE, The Australian National University, Canberra, Australian Capital Territory 0200, Australia

[4]Illinois State University, Normal, IL, 61761, USA

[5]Department of Physics and State Key Laboratory of Low-Dimensional Quantum Physics, Tsinghua University, Beijing 100084, China

We present both experimental and theoretical results for the dissociative ionization of D_2 molecules induced by electron impact. Cross sections are determined in the molecular frame and are fully differential in the energies and emission angles of the dissociation fragments. Transitions are considered from the $X^1\Sigma_g^+$ electronic ground state of D_2 to the $2s\sigma_g$, $2p\pi_u$ and $2p\sigma_u$ excited states of D_2^+. The experimental results are compared to calculations performed within the molecular four-body distorted wave (M4DW) framework to describe the multi-centre nature of the scattering process. The cross sections reveal a dramatic dependence on both the *alignment* of the internuclear axis with respect to the direction of the projectile momentum and on the *symmetry* of the excited dissociating state which is energetically resolved.

DOI: *10.1103/PhysRevA.88.062705*

I INTRODUCTION

The electron impact-induced ionization and fragmentation of molecules is a ubiquitous process of biological, industrial and theoretical relevance. It plays a central role in the physics and chemistry of the upper atmosphere, the operation of discharges and lasers, radiation-induced damage in biological material and plasma etching processes [1-3]. It is a process which describes both the removal of a parent molecule from a chemical environment accompanied with the liberation of atoms and molecules in neutral and charged states. The fragments themselves are often highly reactive due to unpaired electrons or their charge state and drive additional reactions in their local environment.

From a technological perspective, the extent to which such processes can be controlled is limited by our understanding of the physical mechanisms which underpin them and our ability to predict reaction rates under disparate physical conditions. Of great assistance to achieving these goals are measurements in which fragments are measured in time coincidence and in which the reaction kinematics are fully determined. Such measurements provide highly-differential cross sections which describe how the reaction probabilities for particular reaction pathways depend on the momenta of the projectile electron and the scattered electrons and on the momenta and internal energy states of the parent molecule and its charged and neutral fragmentation products. Crucial to the interpretation of such results is careful comparison with calculations. The generation of fully-differential cross sections for the molecular-fragmentation process considered here is extremely challenging due to complexities in describing electron scattering from a many-centred scattering potential and modeling the many-body dynamics which is mediated through the Coulomb potential. Comparison of theory with experimental data can be used to hone theory, establishing the relative merits and ranges of validity for the various approximations presently required to render calculations tractable. If a sound theoretical framework can be established to describe the problem, it can then be used to predict reaction rates and pathways in kinematical regions uncovered by or inaccessible to experimental investigation.

Previous studies of alignment-resolved (e,2e) studies of H_2 were extensively reviewed in [4] so only a brief account will be given here. Pioneering experiments were undertaken by the Sendai group [5-8] who, using hemispherical electrostatic energy

analyzers, performed measurements under conditions of high-momentum-transfer. Experimental and theoretical results were presented at impact energies of 1.2 keV and 2.0 keV to the $2s\sigma_g$ and $2p\sigma_u$ states and for molecular alignments where the internuclear axis was directed orthogonally to the projectile-electron direction. A strong alignment dependence in the measured (e,2e) count rate was observed with indications that for transitions to the $2p\sigma_u$ state, the two outgoing electrons escape preferentially so as to leave the ion recoil momenta along the molecular axis.

In contrast, measurements at lower impact energies were performed by the Heidelberg group [9-12]. Using a reaction microscope their measurements were performed at an impact energy of 200 eV under conditions of highly-asymmetric energy-sharing between the two (e,2e) electrons [9,10] and at lower impact energies of 31.5 eV [12] and 54 eV [11] in later publications. All of these studies focused on transitions from the $X^1\Sigma_g^+$ electronic ground state of H_2 to the vibrational continuum of the $1s\sigma_g$ ground state of H_2^+. [9,10]the experimental results were compared to molecular three-body distorted wave (M3DW) calculations [13-15] and another calculation involving atomic cross sections multiplied by an alignment-dependent interference factor [16]. In [12] the effects of projectile-nucleus scattering were explored through measurements in non-coplanar scattering geometry under which conditions these effects are enhanced [17] and the results were compared to those for electron-helium scattering under similar kinematics. Comparison of the experimental results was made to time-dependent close-coupling (TDCC) [18-21] and convergent close coupling (CCC) [22,23] calculations in addition to M3DW results.

Other low energy measurements were reported by the Canberra group [24]. At an impact energy of 178 eV they investigated transitions to the $2s\sigma_g$ and $2p\pi_u$ excited states of H_2^+. In contrast to the pioneering work of the Sendai group [5,6,8] they were able to study *all* molecular alignments, not just “side-on collisions” of the primary electron with the target molecule. However, due to limitations in their ion-energy measurement-range,

they were unable to access transitions to the $2p\sigma_u$ state of H_2^+ as achieved by the Sendai group.

Here we present experimental- and theoretical-results for the dissociative ionization of D_2 at an electron impact energy of 178 eV. From the perspective of its electronic structure and geometry, the D_2 (H_2) molecule presents the simplest neutral molecular target to explore mechanisms of dissociative ionization. The present experimental results extend on earlier results [24] for H_2 which were measured under identical reaction kinematics but restricted to transitions to the $2s\sigma_g$ and $2p\pi_u$ excited states of the H_2^+ ion. While the electronic structure of D_2 is essentially the same as that of H_2, its greater nuclear masses leads to substantially-lower fragment velocities associated with dissociative transitions. These lower fragment velocities, in conjunction with improvements made to our ion spectrometer, enabled us to increase the amount of ion-momentum phase space over which we could simultaneously measure compared to our previous work. As a consequence we are able to measure transitions to the $2p\sigma_u$ in addition to those to the $2s\sigma_g$ and $2p\pi_u$ excited states of the D_2^+ ion. By measuring deuterons and electrons in a coincidence experiment we are able to determine not only the dependence of the dissociative ionization process on the *alignment* of the internuclear axis with respect to the momenta of the projectile- and scattered-electrons, but also its dependence on the *symmetry* of the D_2 electronic state excited in the process.

II. REACTION GEOMETRY AND REACTION PATHWAYS

A schematic representation of the dissociative ionization process under consideration and the adopted reaction kinematics is shown schematically in Fig. 1. Mathematically, it can be described by the equation:

$$e_i^-(\mathbf{p_i}) + D_2(\theta_D,\phi_D) \rightarrow D(n,\mathbf{p_D}) + D^+(\mathbf{p_{D^+}}) + e_a^-(\mathbf{p_a}) + e_b^-(\mathbf{p_b}) \qquad (1)$$

Here $e_i^-(\mathbf{p_i})$, $e_a^-(\mathbf{p_a})$, and $e_b^-(\mathbf{p_b})$ represent incident, scattered and ejected electrons of respective momenta $\mathbf{p_i}$, $\mathbf{p_a}$, and $\mathbf{p_b}$ (energies E_i, E_a, and E_b). The momentum transfer from the projectile to the target is characterized by the momentum-transfer vector $\mathbf{K}$, defined through the expression $\mathbf{K} = \mathbf{p_i} - \mathbf{p_a}$, where $\mathbf{p_a}$ is the faster of the two final-state

electrons. Due to the imaging properties of our electron energy-analyzers, only collision events for which the momenta of the incident electron and the two final-state continuum-electrons are constrained to a common plane, the so-called scattering plane, are measured in the present experiment. $D_2(\theta_D,\phi_D)$ represents the parent deuterium molecule at rest in the laboratory frame and in the electronic ground state. Its alignment angle with respect to the scattering plane and the projectile momentum-vector is described by the polar coordinates (θ_D,ϕ_D). $D(n,\mathbf{p_D})$ represents the fragment deuterium atom of momentum $\mathbf{p_D}$ and principle quantum number n and $D^+(\mathbf{p_{D^+}})$ represents a deuteron of momentum $\mathbf{p_{D^+}}$ (energy E_{D^+}).

Deuterons emitted over the full 4π solid angle are detected in the present measurement. Both the fragmentation rate *and* the n-state distribution of the deuterium fragment atoms are shown to depend strongly on the alignment angle (θ_D,ϕ_D). For the low impact energy and low values of momentum transfer $\mathbf{K}$ considered, momentum transfer from the incident electron to the D_2 centre-of-mass and momentum transfer between the scattered electrons and the fragment nuclei is negligible. Thus, on dissociation of the excited D_2^+, $\mathbf{p_{D^+}} \cong -\mathbf{p_D}$ and for a known value of, determination of $\mathbf{p_a}$, $\mathbf{p_b}$ and $\mathbf{p_{D^+}}$ completely determines the reaction kinematics. Furthermore, by invoking energy conservation, the appearance energy $A(n)$ for transitions to the quantum state n of the residual deuterium atom is determined through the relation

$$A(n) = \varepsilon_b - 2E_{D^+} \tag{2}$$

Here ε_b is the electron binding energy, defined by the expression $\varepsilon_b = E_i - E_a - E_b$, and $2E_{D^+}$ accounts for the kinetic energy shared between the deuteron and the deuterium atom. This expression allows ionization events to be sorted according to the dissociation limits of the respective transitions with which they are associated. Finally, determination of $\mathbf{p_{D^+}}$ enables the molecular alignment at the time of ionization to be inferred and alignment-resolved data to be obtained [25].

Figure 2 shows a simplified potential energy diagram for the deuterium molecule and molecular ion. Only the four states of D_2^+ are shown which, under the adopted reaction

kinematics and for the processes presently under investigation, are involved in the strongest transitions. Dissociative ionization of the D_2 molecule may occur through a number of distinct pathways. First, it can proceed directly via transitions from the $X^1\Sigma_g^+$ electronic ground state of D_2 to the vibrational continuum of the $1s\sigma_g$ ground state of D_2. Deuterons and deuterium atoms produced through these transition are released with low values of kinetic energy (typically $\ll 1$eV). This ground-state dissociation process (termed GSD in [9]) has been extensively studied [5-11] in recent years. Second, dissociation may occur by the direct excitation of both target electrons. In this double-electron-excitation (DEE) process, one electron is excited to the ionization continuum and the other to an excited state of D_2^+ (all excited states of D_2^+ are dissociative), leading to deuterons and deuterium atoms of higher values of kinetic energy (typically 2-10 eV). This ionization-excitation process is the dominant dissociative ionization mechanism under the present kinematics and is the focus of this study. In contrast to the first pathway involving the electronic excitation of only a single electron, this double-electron-excitation process presents a considerably greater challenge to theory since it must be treated as a 4-body problem instead of an effective 3-body problem. Third, dissociative ionization may also occur *indirectly* through transitions to intermediate autoionizing states of D_2 [9,10] (termed AI in [9]). However, in the present measurement only emitted-electron energies above 30 eV are considered, thereby avoiding contributions from this resonance pathway. This restriction serves to simplify the data analysis by restricting the number of participating reaction pathways.

III. EXPERIMENT

Details of the measurement procedure have been described previously [24,27] so only a short summary will be given here. A schematic representation of the experimental arrangement is presented in Fig. 2 of [24]. Briefly, an electron beam is generated through photoionization of a strained GaAs crystal photo-cathode under illumination by laser light. The beam is accelerated to 178 eV and focused onto an effusive jet of D_2 molecules, crossing the jet orthogonally to form a localized interaction region (around 1 mm extent in all three spatial directions). Electrons emitted within a plane containing the primary-electron beam are collected in one of two toroidal-sector electrostatic electron analyzers

(see [28] for details). Each analyzer employs a position-and-time sensitive delay-line detector [29], enabling electron momenta to be reconstructed from the spatial and temporal

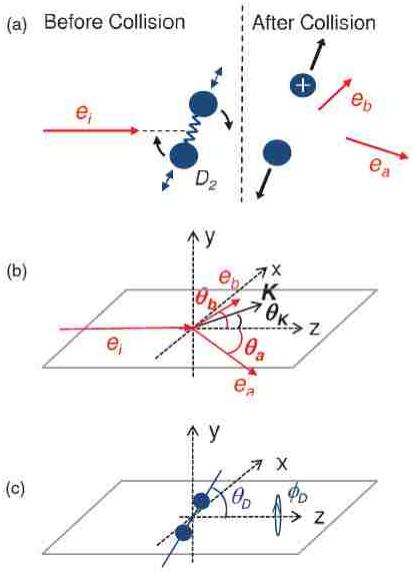

FIG. 1. Panel (a): Schematic representation of dissociative ionization process considered in this paper. A projectile electron e_i collides with a deuterium molecule, liberating two scattered electrons e_a and e_b, a deuteron and a deuterium atom in its ground- or in one of its excited-states. Panel (b): Reaction kinematics. The two scattered electrons are detected in a plane containing the incident electron beam and are detected at angles θ_a and θ_b on opposite sides of the beam. The direction of momentum transfer θ_k varies with the scattering angle θ_a. Panel (c): The alignment of the molecular axis, at the instant of ionization, is defined through the angles (θ_D, ϕ_D) and is inferred from the asymptotic trajectory of the deuteron fragment. The dissociation rate depends on the molecular alignment, the momenta of the projectile- and scattered-electrons and on the molecular- and ionic-states involved in the dissociative transition.

electron-arrival coordinates. One analyzer is adjusted to transmit electrons in the energy range ΔE_a where 90 eV $\leq E_a \leq$ 110 eV over the angular range $10^\circ \leq \theta_a \leq 50^\circ$ on one side of the electron beam. The second analyzer measures electrons in the energy range ΔE_b where 30 eV $\leq E_b \leq$ 50 eV over the angular range $40^0 \leq \theta_b \leq 80^0$ on the other side of the electron beam (see FIG. 1). We note here that the projectile-electron energy E_i and the average energies $\bar{E}_a$ and $\bar{E}_b$ for the two emitted electrons correspond to de Broglie-wavelengths of 0.92, 1.2, and 1.9 A° respectively; in contrast the equilibrium internuclear

separation for D_2 is around $0.58\,A^{o}$. Deuterons emitted over a 4π solid angle were focused by a pulsed-field ion-spectrometer onto a third delay-line detector. A schematic of the spectrometer showing simulated ion trajectories for 10 eV N^+ ions produced by Simion [31] software is shown in Fig. 3. From measurement of the deuteron arrival-positions and arrival-times, their momenta were uniquely determined and the molecular alignment, at the instant of ionization, was inferred. The combined momentum coordinates of electrons and ions enabled partial cross sections describing transitions to the $2s\sigma_g$ and $2p\pi_u$ and to the $2p\sigma_u$ excited states of D_2^+ to be determined.

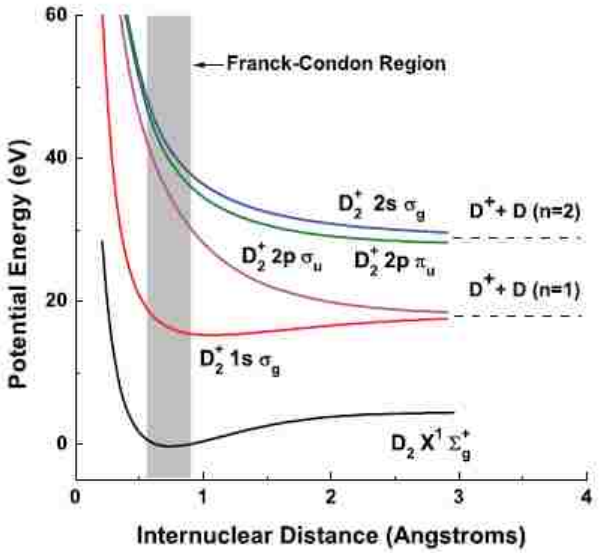

FIG. 2. Potential energy of D_2 and D_2^+ (approximated by fitting hydrogen data from [26]) as a function of internuclear distance, for the states relevant to the present study. The measurement energetically-resolves transitions to the $2s\sigma_g$ and $2p\pi_u$ states from those to the $1s\sigma_g$ and $2p\sigma_u$ states due to the 10.2 eV separation between their respective dissociation limits (indicated by the dashed lines). Transitions to the $1s\sigma_g$ and $2p\sigma_u$ states can be easily resolved from one another due to their well-separated deuteron energy-distributions.

Crucial to be the success of the present measurement was the application of time-dependent fields to identify, in time coincidence, two electrons and a deuteron derived from individual dissociative-ionization events and to suppress background signal resulting from dissociative-ionization events for which the associated (e,2e) pair remained undetected (the

electron analyzers, although highly efficient, measure <0.1% of all ionization events). The timing scheme we employed is shown schematically in Fig. 4.

Briefly, the primary electron beam was pulsed with a 30 % duty-cycle at a frequency of 125 kHz with a temporal pulse width of $2.5\ \mu s$. Between each electron pulse a "cleaning cycle" was implemented to sweep away residual deuterons from the interaction region by applying a fast-rise-time 252 V positive potential V_n to the gas needle through which the molecular beam is introduced. If, at a time $t_{(e,2e)}$, an (e,2e) ionization event was identified by the time-correlated arrival of two electrons at the electron detectors, an extraction field was generated within the ion-spectrometer to collect deuteron fragments (see Fig. 3). This was achieved by applying a potential of 300 V to mesh M1 which is electrically bridged to the first ten extraction electrodes and the grounded mesh M2 through a resistor chain. Due to the finite flight times for electrons traversing the electron analyzers and the finite response time of our pulse-processing electronics, the time delay between the instant of ionization at time t_i and the time at which the extraction voltages were applied t_{ext} was ~ 120 ns, i.e., $t_i < t_{(e,e2)} < t_{ext}$ with $t_{ext} - t_i \sim 120$ ns. The extraction field was maintained for a period of $8\ \mu s$, a sufficient time for the associated deuteron fragment of up to 12 eV kinetic energy to reach the ion detector. At the same time the needle potential was raised to the potential V_n, the value of 252 V chosen to optimize deuteron focussing onto the ion detector. Furthermore, upon detection of an (e,2e) event and to reduce deuteron background, the electron-beam pulsing sequence was interrupted during the period of ion extraction by prematurely turning off the electron beam. This was achieved through the operation of a fast optical shutter positioned between the laser source and the photocathode.

Without the application of electron-beam pulsing and ion-cleaning cycles, a problem would have arisen from low-energy deuterons, predominantly generated through GSD, accumulating in the neighbourhood of the interaction volume between (e,2e)-instigated deuteron extractions. In that case, the deuteron associated with a measured (e,2e) event would have been accompanied by many other deuterons created at earlier times for whose (e,2e) pairs were undetected. The presence of such a deuteron background would have greatly reduced the accuracy of the data. Furthermore, as we employed only single-

hit time-to-digital converters in our time measurements, the measurement of multiple deuterons in a given extraction would have necessarily distorted the measured deuteron energy-distribution as only the first detected deuteron in each extraction pulse is registered; thus by employing the above pulsing scheme high levels of background deuterons were avoided. By implementing the timing technique illustrated in Fig. 4, we were able to achieve a triple-coincidence electron-electron-deuteron count rate of around 1 count/s for dissociative ionization with an associated deuteron background rate of 0.1 Hz at a time-average beam-current of around 60 pA. In particular, the efficiency loss resulting from pulsing the electron-beam with a 30 % duty cycle was more than compensated for by the massive reduction in background signal. The small background that remains is mainly due to GSD-related (e,2e) events, which dominate the (e,2e) count rates. These are easily eliminated due to their much-lower associated electron binding energies. The remaining background events are spread over a large area of the two-dimensional phase-space defined by deuteron kinetic energy and electron binding energy. To take an approximate account of the effects of the remaining background-deuteron contribution in the spectra we present here, we have subtracted the recorded (e,2e) deuteron energy-distribution for non-dissociative ionization from that dissociative-ionization with a scale factor chosen to achieve zero counts in regions of the dissociative-ionization energy spectrum where no states exist.

Since our previous measurement on H_2 [24] and N_2 [27], the electrical shielding of the detector circuits against high-frequency pickup from the few-nanosecond rise times of the extraction- and needle-potentials was greatly improved, as was the response time of our pulsing electronics. As a result, considerably higher extraction fields could be employed and the range of accessible fragment-ion energies could be extended. In addition, switching from the molecular target H_2 to D_2 reduced, by a factor of $\sqrt{2}$, the distance traversed by the ionic fragments between the instant of ionization t_i and the time of extraction t_{ext}, improving ion focusing and further extending the range of ion energies which could be measured. Together these changes and improvements extended the energy range in which fragment could be collected and momentum analyzed over the full 4π solid angle of emission to 12 eV. As a result we are able to measure transitions to the dissociative $2p\sigma_u$

excited molecular-ion state, in addition to transitions to the $2s\sigma_g$ and $2p\pi_u$ excited states which we measured for H_2. Transitions to the former state are associated with higher average deuteron energies than those to the latter two (see Fig. 2). The formula for appearance energy $A(n)$ [Eq. (2)] was employed to sort events according to whether they corresponded to transitions to the $2p\sigma_u(n=1)$ or to the $2s\sigma_g$ and $2p\pi_u(n=2)$ states respectively. An appearance energy resolution of better than 2 eV Full-Width-at-Half-Maximum (FWHM) was achieved for all momentum coordinates within the range of measured momentum phase space. Given this fact and the fact that $A(n=2)$ and $A(n=1)$ are separated by 10.2 eV, transitions to the $2p\sigma_u$ and the $2s\sigma_g$ and $2p\pi_u$ states could be unambiguously distinguished from one another.

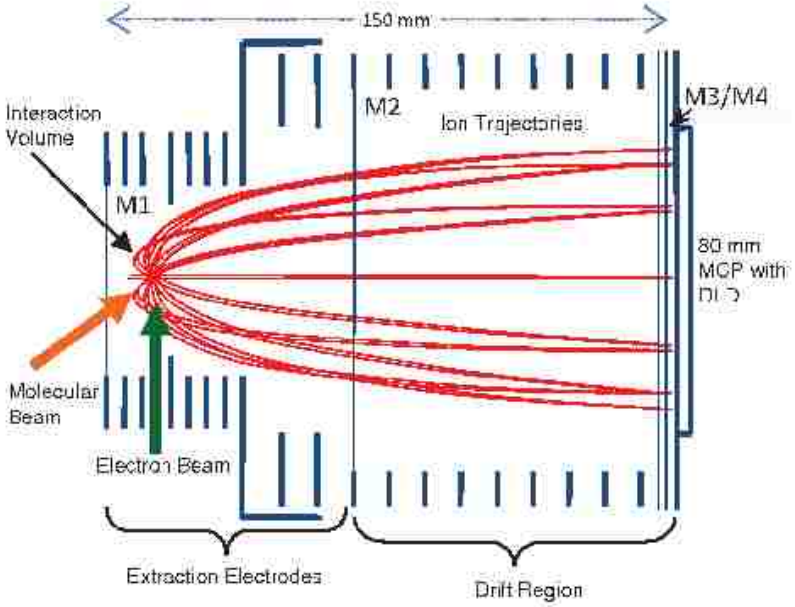

FIG. 3. Cross-sectional view of the ion spectrometer. The molecular beam is admitted through a 0.8 mm internal-bore needle (not shown) and crosses the electron beam at an angle of 90°. Ions are extracted by pulsing the potential of the mesh M1 which is coupled to the extraction electrodes and the grounded mesh M2 through a voltage-dividing resistor chain. The electrodes between meshes M2 and M3 and the meshes M3 and M4 themselves are maintained at a constant potential. The combination of separate ion acceleration- and drift-regions and the action of the lensing surface, arising from the potential difference across M2, creates conditions for spatial and temporal time-focusing [30]. Ions are detected on an 80 mm-diameter microchannel-plate detector (MCP) equipped with a delay-line

detector (DLD). Trajectories, simulated by SIMION software [31], are shown for 10 eV N^+ ions for emission angles in 30 angular steps. See text for details.

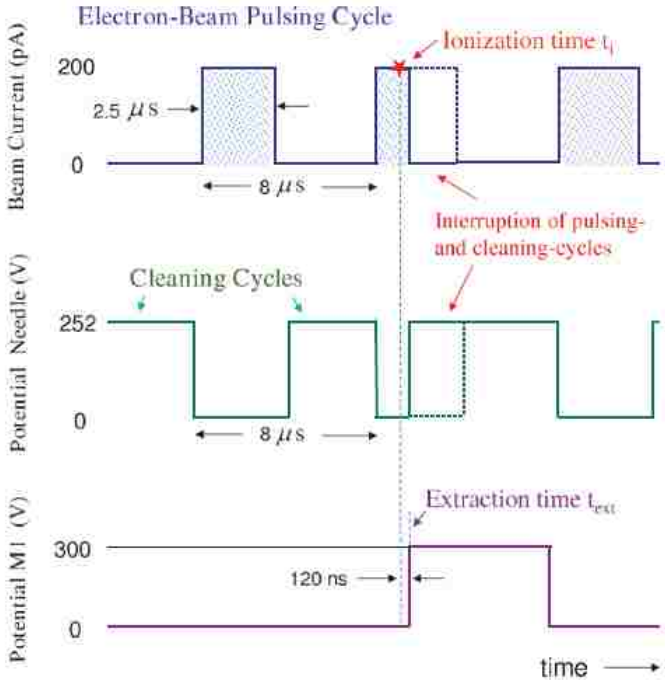

FIG. 4. Pulsing scheme for the electron beam, for the potential applied to target-gas needle and for the potential applied to the mesh M1. The detection of an (e,2e) ionization event, occurring shortly after ionization at time t_i , triggers the extraction of ions by raising the potentials of M1 and the needle to their optimum values for ion focusing. The electron beam and needle potentials are periodically pulsed to mitigate against the buildup of low-energy deuterons in the vicinity of the target region. See text for details.

IV. FOUR-BODY DISTORTED-WAVE THEORY

A. Formalism

In this section we present the theoretical framework within which calculations to describe the experimental data were performed. We emphasize here that an accurate description of the DEE dissociative-ionization process presents a great challenge, not only due to the inherent difficulty in describing electron scattering in a two-centred scattering potential, but also because the reaction involves a two-electron excitation leading to an electronic excitation of the residual molecular ion. Consequently, the DEE process poses a much greater theoretical challenge than that presented by the GSD process treated

previously [11,12] and one which must be addressed through a number of simplifying approximations to make the problem tractable.

The exact T-matrix for electron-impact excitation-ionization of oriented D_2 can be written as

$$T_{fi} = \langle \Psi_f \mid H - H_0 \mid \Phi_i \rangle, \tag{3}$$

where H is the full Hamiltonian for the system, H_0 is an approximate initial-state Hamiltonian, and the wave functions Ψ_f and Φ_i are eigenfunctions of the two Hamiltonians

$$\begin{aligned} H \mid \Psi_f \rangle &= E \mid \Psi_f \rangle, \\ H_0 \mid \Phi_i \rangle &= E \mid \Phi_i \rangle. \end{aligned} \tag{4}$$

For electron-impact excitation-ionization of D_2 , the full Hamiltonian is given by

$$\mathrm{H} = \mathrm{H}_{\mathrm{target}} + \mathrm{K}_{\mathrm{i}} + \mathrm{V}_{\mathrm{i}} \ , \tag{5}$$

where H_{target} is the Hamiltonian for a neutral target with eigenfunctions Ψ_{target} , K_i is the kinetic energy of the projectile electron i and V_i is the initial state interaction between the projectile and target and given by the expression

$$V_i = -\frac{1}{r_{N1}} - \frac{1}{r_{N2}} + \frac{1}{r_{i1}} + \frac{1}{r_{i2}}. \tag{6}$$

Here $-\frac{1}{r_{Nj}}$ is the interaction of the projectile electron with nucleus *j*, and $\frac{1}{r_{ij}}$ is the interaction of the projectile electron with electron *j*. In the distorted wave approximation, the approximate initial state Hamiltonian is given by

$$H_0 = H_{target} + K_i + U_i \ , \tag{7}$$

where U_i is the an initial-state spherically-symmetric approximation for the projectile target interaction V_i . U_i is given by the expression

$$U_i = U_{ele} + U_{Nuc} \ , \tag{8}$$

with U_{ele} a spherically symmetric approximation for the interaction between the projectile electron and the target electrons, which is obtained from the quantum mechanical charge

density of the target, and the nuclear contribution U_{Nuc} is the interaction between the projectile electron and the two deuterons averaged over all orientations. Averaging the nuclei over all orientations is equivalent to putting the total nuclear charge of 2 on a thin spherical shell whose radius is the distance of the nuclei from the center of mass (CM). The eigenfunctions of the distorted wave Hamiltonian (7) are given by

$$|\Phi_i\rangle = |\Psi_{target}(\mathbf{r}_1,\mathbf{r}_2)\chi_i^+(\vec{k}_i,\mathbf{r_0})\rangle, \tag{9}$$

where $\chi_i^+(\vec{k}_i,\mathbf{r_0})$ is a continuum state distorted wave for wavenumber $\vec{k}_i$ and the + indicates outgoing wave boundary conditions. We initially tried using an accurate numerical wavefunction for $\Psi_{target}(\mathbf{r}_1,\mathbf{r}_2)$ but it quickly became clear that, even with a generous XSEDE grant, it was not practical to use this wavefunction. Consequently, we instead used the following approximation

$$\Psi_{target}(\mathbf{r}_1,\mathbf{r}_2) \approx \Psi_{Dy}^{1s}(\mathbf{r}_1)\Psi_{Dy}^{1s}(\mathbf{r}_2), \tag{10}$$

where Ψ_{Dy}^{1s} is the ground state Dyson wavefunction.

The exact wave functions for each final-state wave function are approximated as a product of wave functions for each of the final three particles and the final state Coulomb interaction between the two continuum electrons

$$\Psi_f(\mathbf{r}_0,\mathbf{r}_1,\mathbf{r}_2) \approx \chi_a^-(\vec{k}_a,\mathbf{r}_0)\chi_b^-(\vec{k}_b,\mathbf{r}_1)\phi_{Ion}(\mathbf{r_2})C_{se}(\mathbf{r_{01}}). \tag{11}$$

Here $\chi_a^-(\vec{k}_a,\mathbf{r}_0)$ is the final-state distorted-wave function for the scattered projectile with wave number $(\vec{k}_a)$, $\chi_b^-(\vec{k}_b,\mathbf{r}_1)$ is the distorted wave for the ejected electron, $\phi_{Ion}(\mathbf{r_2})$ is the Dyson wave function for the excited state of D_2^+, and $C_{se}(\mathbf{r_{01}})$ and is the Coulomb interaction between the scattered projectile and the ejected electron, which is normally called the postcollision interaction (PCI). The final-state distorted waves are calculated similarly to the initial-state distorted waves except that the spherically symmetric potential for the final ion is used. Consequently, the M4DW T matrix is given by

$$T_{fi} = \langle \chi_a^-(\vec{k}_a,\mathbf{r}_0)\chi_b^-(\vec{k}_b,\mathbf{r}_1)\phi_{Ion}(\mathbf{r_2})C_{se}(\mathbf{r_{01}})\ |V_i - U_i|\ \Psi_{Dy}^{1s}(\mathbf{r}_1)\Psi_{Dy}^{1s}(\mathbf{r_2})\chi_i^+(\vec{k}_i,\mathbf{r_0})\rangle. \tag{12}$$

Since there are active particles in this T-matrix, the evaluation requires a full 9-Dimensional integration which we perform numerically [32,33]. In our formalism,

alignment-dependent effects emerge through the dependence of the excitation probabilities on the overlap of the initial-state Dyson wavefunctions Ψ_{Dy}^{1s} with the final-state Dyson ion wavefunction $\phi_{Ion}(\mathbf{r}_2)$.

B. Normalization of experiment to theory

The triple differential cross section (TDCS), which is compared to the experimental results of this paper, is related to the T-matrix T_{fi} through the expression:

$$TDCS(\theta_a,\phi_a,\theta_b,\phi_b,E_b) = \frac{d\sigma^5}{d\Omega_a d\Omega_b dE_b} = \frac{1}{(2\pi)^5}\frac{k_a k_b}{k_i}\left|T_{fi}\right|^2. \qquad (13)$$

We measure over a $10°$ to $50°$ interval for θ_a (average azimuthal angle $\overline{\phi_a} = 0°$) and a $40°$ to $80°$ interval for θ_b (average angle $\overline{\phi_b} = 180°$), accepting electrons through a constant-width circular entrance aperture which is centred on the interaction region. The range $\Delta\phi_a$ of ϕ_a values and the range $\Delta\phi_b$ of ϕ_b values for measured emitted electrons varies with the angles θ_a and θ_b respectively. At $\theta_{a(b)} = 90°$ (outside the capture range of both analyzers), the range of $\phi_{a(b)}$, subtended at the interaction region, is bounded by the values $\pm\Gamma°$, where $\Gamma \cong 2°$ in our experiment. To a good approximation, within the two polar angular acceptance ranges of the electron analyzers, values for $\phi_{a(b)}$ are bounded by the limits $\Gamma_{a(b)}$ where $\Gamma_{a(b)} = \Gamma / \sin\theta_{a(b)}$. Thus $\Delta\phi_{a(b)}$ can be approximated by the expression $\Delta\phi_{a(b)} = 2\Gamma / \sin\theta_{a(b)}$.

To relate calculated TDCS values to our measured (e,2e) event rates we must average them over the range of θ and ϕ values contributing to each experimental data point; we denote the resultant quantity as $TDCS_{av}$. The integration is performed over the range of polar $(\Delta\phi_a, \Delta\phi_b)$ and azimuthal $(\Delta\phi_a, \Delta\phi_b)$ angles over which counts are summed in the analysis of the experimental data. In general we have:

$$TDCS_{av} = \int_{\Delta\theta_a}\int_{\Delta\theta_b}\int_{\Delta\phi_a}\int_{\Delta\phi_b} \frac{d\sigma^5(\theta_a,\phi_a,\theta_a,\phi_b,E_b)}{d\Omega_a d\Omega_b dE_b} d\phi_a d\phi_b d\theta_a \sin\theta_a \, \mathrm{d}\theta_b \sin\theta_b \Big/ \int_{\Delta\Omega_a} d\Omega_a \int_{\Delta\Omega_b} d\Omega_b \tag{14}$$

where $\Delta\Omega_{a(b)}$ represents the acceptance solid angles for the electron analyzers accepting the fast a and slow b scattered electrons respectively. For the present experimental arrangement, as the ranges of $\Delta\phi_a$ and $\Delta\phi_b$ are small, we can approximate the integrand by its value at the coordinate $(\phi_a = 0°,\ \phi_b = 180°)$, namely $d\sigma^5(\theta_a,\phi_a = 0°,\theta_b,\phi_b = 180°,E_b)/d\Omega_a d\Omega_b dE_b$. Substituting for $\Delta\phi_{a(b)}$ and through rearrangement we obtain

$$TDCS_{av} \cong \int_{\Delta\theta_a}\int_{\Delta\theta_b} \frac{d\sigma^5(\theta_a,\phi_a = 0°,\theta_b,\phi_b = 180°,E_b)}{d\Omega_a d\Omega_b dE_b} d\theta_a \sin\theta_a d\theta_b \sin\theta_b \int_{\Delta\phi_a} d\phi_a \int_{\Delta\phi_b} d\phi_b \Big/ \int_{\Delta\Omega_a} d\Omega_a \int_{\Delta\Omega_b} d\Omega_b$$

$$= \frac{1}{\Delta\theta_a \Delta\theta_b} \int_{\Delta\theta_a}\int_{\Delta\theta_b} \frac{d\sigma^5(\theta_a,\phi_a = 0°,\theta_b,\phi_b = 180°,E_b)}{d\Omega_a d\Omega_b dE_b} d\theta_a d\theta_b. \tag{15}$$

To reduce statistical fluctuations between experimental data points, (e,2e) events were summed over the range of polar angles $\Delta\theta_b$ where $40^\circ \le \theta_b \le 80^\circ$ and over the $10°$ range of azimuthal angles $\Delta\theta_a(j^\circ)$, where $j^\circ = 15^\circ + (i-1)\times 10^\circ$, $i = 1-4$ and $i\times 10^\circ \le \theta_a \le (i+1)\times 10^\circ$. The resultant experimental counts (presented in Figs. 5 and 6 of this paper) are then ascribed to the mean angular values j° of the respective angular ranges $\Delta\theta_a(j^\circ)$. To facilitate the comparison of theory with experiment and to reduce computational overheads we make a further approximation in Eq. (15); we replace the integrand by its value at the angular coordinates $\theta_a = j^\circ$:

$$\begin{aligned} TDCS_{av}\left[\theta_a = j°\right] &\cong \frac{1}{\Delta\theta_a \Delta\theta_b} \times \int_{40°}^{80°} \frac{d\sigma^5(\theta_a = j°,\phi_a = 0°,\theta_b,\phi_b = 180°,E_b)}{d\Omega_a d\Omega_b dE_b} d\theta_b \int_{\Delta\theta_a} d\theta_a \\ &= \frac{1}{\Delta\theta_b} \int_{40°}^{80°} \frac{d\sigma^5(\theta_a = j°,\phi_a = 0°,\theta_b,\phi_b = 180°,E_b)}{d\Omega_a d\Omega_b dE_b} d\theta_b \end{aligned} \tag{16}$$

Where $\Delta\theta_b = 40^\circ$.

V. RESULTS

In Figs. 5(a) to 5(d) we present triple-coincidence count rates for transitions to the $2s\sigma_g$ and $2p\pi_u$ and to $2p\sigma_u$ excited states and for selected molecular alignments of the D_2^+ ion as a function of the scattering angle θ_a for 100 eV scattered electrons. For each alignment direction the data comprises events for which deuterons are emitted within a cone of $\pm 15°$, corresponding to 3.3 % of the spherical surface. As all transitions and all alignments were measured simultaneously under identical experimental conditions, their relative strengths are reflected in the respective coincidence count rate scales of the four panels. As mentioned earlier, deuterons emitted over the full 4π solid angle are detected. This enables the dependence of the dissociative ionization rate on all deuterium alignment-directions to be explored. To aid interpretation of the underlying physics, however, ionization rates are presented for five specific high-symmetry alignment-directions of the deuterium internuclear axis with respect to both the momentum direction of the incident electron, and the direction of the momentum transfer $\mathbf{K}$. The alignment directions denoted as D_X, D_Y and D_Z correspond, respectively, to deuterium molecules oriented perpendicular to the primary beam direction and within the x-z scattering plane (D_X alignment), perpendicular to the primary beam and perpendicular to the scattering plane (D_Y alignment) and molecules oriented along the primary beam direction (D_Z alignment). Each lie parallel to one of the cartesian coordinate axes x, y and z (see Fig. 1). Two further alignment directions within the $x-z$ scattering plane are defined. One ($D_{\mathbf{K}}$ alignment) describes an alignment along the direction of momentum transfer $\mathbf{K}$ and the other ($D_{\mathbf{K}\perp}$ alignment) defines an alignment perpendicular to $\mathbf{K}$.

The triple-coincidence count rate is presented as a function of the scattering angle θ_a of the 100 eV scattered electron. Varying θ_a is equivalent to varying the momentum transfer both in magnitude and direction. For example, for transitions to the $2p\sigma_u$ state, varying the value of θ_a from 15° to 45° varies the magnitude of momentum transfer $|\mathbf{K}|$ from 1.2 to 2.6 a.u. and the direction $\theta_{\mathbf{K}}$ of momentum transfer from 37° to 50°. Furthermore, as only around 5% of all measured (e,2e) ionization events are accompanied

by fragmentation of the residual D_2^+ ion, the data are averaged over the slow-electron scattering-angle θ_b and over the electron-energy pass-bands ΔE_a and ΔE_b to reduce the statistical spread of the presented data. In spite of this integration, dramatic alignment-dependent effects remain.

Figure 5(a) shows the measured electron-electron-ion triple-coincidence rate for transitions to the $2s\sigma_g$ and $2p\pi_u$ excited states of the D_2^+ ion as a function of the scattering angle θ_a of the 100 eV scattered electron for the D_X, D_Y and D_Z molecular alignments. As the fragment-deuteron energy-distributions associated with transitions to the individual $2s\sigma_g$ and $2p\pi_u$ states strongly overlap in energy (see [26]), their individual contributions cannot be resolved. To assist the eye by highlighting the dependency of count rate on the alignment and momentum transfer, the data have been fitted with second order polynomials. Immediately evident is the strong alignment dependence of the dissociative ionization rate as reflected by the alignment-dependence of the coincidence count rates. Of the three alignment directions considered, "side-on" collisions of the projectile with the deuterium molecule ejected out of the scattering plane (D_Y alignment) leads to the highest rates of dissociative ionization. "Side-on" collisions of the projectile with the deuterium molecule and with the deuteron ejected in the scattering plane (D_X alignment) exhibits a smaller rate, and "end-on" collisions (D_Z alignment) with the molecule giving rise to smallest rate overall. Given that the present measurements were performed under identical kinematical conditions to our previous study of H_2 and given that the electronic structure (as opposed to the vibrational structure) of deuterium and hydrogen molecules is essentially the same, one would expect that the present results and those published by us previously for H_2 (Fig. 5 of [24]) would be the same. This is indeed the case when one compares the relative transition strengths for the D_Y and D_Z alignments. However, when one compares the relative count rates for all three alignments, D_X (labeled P_X in [24]) is different. Subsequent detailed checking revealed an error in our analysis for the P_X alignment data of H_2, accounting for this discrepancy.

Figure 5(b) shows analogous results for transitions to the $2p\sigma_u$ dissociative state. Comparing to the results in 5(a), a dramatic transition-dependence on the rate of dissociative ionization is seen. In 5(b) "end-on" collisions, which were the least-favored molecular-alignment to lead to dissociative ionization in Fig 5(a), now dominates for transitions to the $2p\sigma_u$ state. Of the "side-on" collisions (D_X and D_Y alignments), deuteron emission in the scattering plane (D_X alignment) is strongly favored relative to emission out of the scattering plane (D_Y alignment). The D_Y alignment now has the lowest cross section, whereas for the $2s\sigma_g$ and $2p\pi_u$ transitions it possessed the largest [Fig. (5a)].

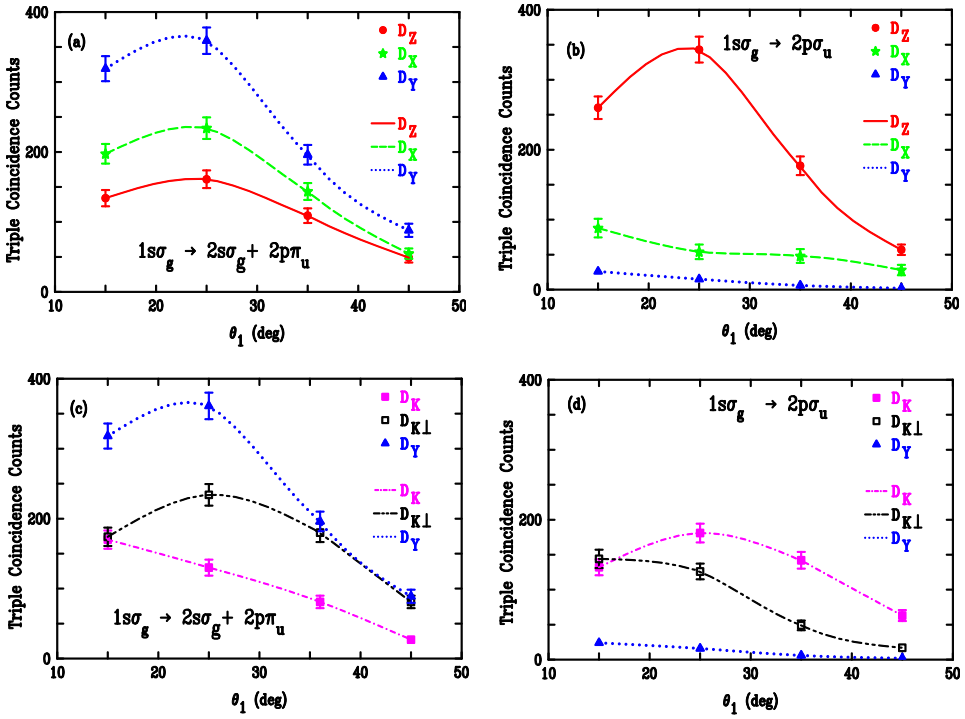

FIG. 5. Triple-coincidence counts for transitions to the $2s\sigma_g$ and $2p\pi_u$ [panels (a) and (c)] and $2p\sigma_u$ states [panels (b) and (d)] of D_2^+ as a function of the fast-electron scattering-angle θ_a. Panels (a) and (b) show experimental results for the three molecular alignments D_X, D_Y and D_Z. Panels (c) and (d) show experimental results for the three molecular alignments $D_{\mathbf{K}}, D_{\mathbf{K}\perp}$ and D_Y. The data has been averaged over the slow-electron scattering angle θ_b and have been fitted with second order polynomials to aid visualization of the trends. As all results were accumulated simultaneously under identical experimental conditions; the relative count rates between data in all four panels therefore reflect the relative strengths of their associated cross sections.

Figures 5(c) and 5(d) show the same D_Y alignment data as in 5(a) and 5(b), but additionally data for the $D_{\mathbf{K}}$ and $D_{\mathbf{K}\perp}$ alignments. These particular alignment directions, which depend on θ_a, are chosen to facilitate a comparison of the present results with findings from photo-ionization studies, where dipole selection rules can account for strong alignment dependence in the angular distributions of photoelectrons. However, the present results occupy a kinematic regime well-removed from the optical limit of high electron-impact energies and negligible values for momentum transfer $\mathbf{K}$. Thus while one might anticipate, *a priori*, that some physical insight into the present observations might be obtained from considering dipole selection rules, a fully quantum mechanical treatment is required for an accurate interpretation of the data.

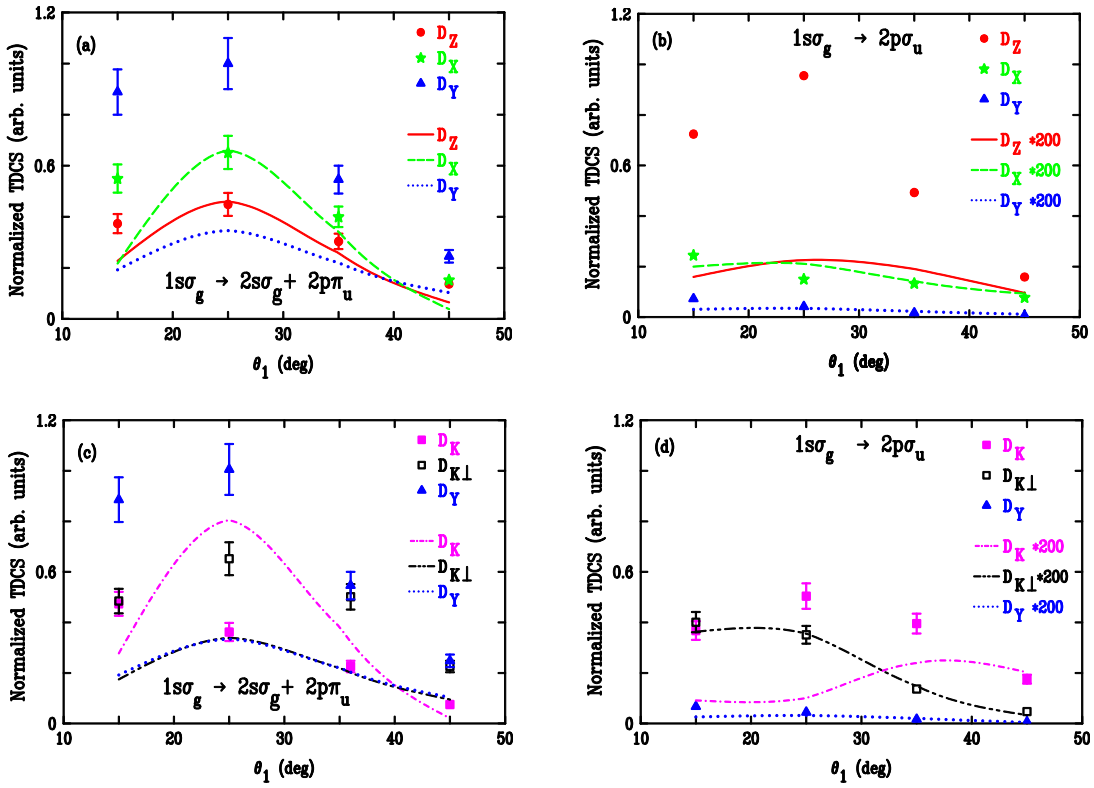

FIG. 6. Same experimental data shown in Fig. 5 compared to M4DW calculations. The experimental results have been normalized to the calculations [averaged according to Eq. (16)] at the scattering angle $\theta_a = 25°$ for the D_X molecular-frame alignment of the $2s\sigma_g$ and $2p\pi_u$ transition.

Figures 6(a) to 6(d) show the same experimental results in Figs. 5(a) to 5(d) but this time compared to the M4DW theory. Normalization of the experimental results to the calculations was achieved at the scattering angle $\theta_a = 25°$ for the $2s\sigma_g$ and $2p\pi_u$ transition and for the D_X molecular-frame alignment [5(a)]. Figure 6(a) shows results for transitions to the $2s\sigma_g$ and $2p\pi_u$ excited states. The M4DW predicts the same order and relative magnitude as experiment for alignment in the scattering plane. However, for the alignment out of the scattering plane D_Y, theory predicts this to be the weakest transition while in contrast experiment finds it to be the strongest. In Fig. 6(c) alignments along the D_Y, $D_{\mathbf{K}}$ and $D_{\mathbf{K}\perp}$ directions are considered. In this case, experiment finds $D_{\mathbf{K}}$ has a similar magnitude to D_Z and $D_{\mathbf{K}\perp}$ has a similar magnitude to D_X, with the $D_{\mathbf{K}\perp}$ alignment preferred over the $D_{\mathbf{K}}$. In contrast, theory predicts that the largest cross section should be found for the momentum transfer direction (as was found in both experiment and theory for direct ionization of the ground state). Furthermore, it predicts almost identical results for the two directions perpendicular to momentum transfer, both in- and out-of the scattering plane, in contrast to the experimental findings.

For the isolated $2p\sigma_u$ transition shown in Figs. 6(b) and 6(d) and using the same normalization as in panel (a) (i.e. at the scattering angle $\theta_a = 25°$ for the $2s\sigma_g$ and $2p\pi_u$ transition and for the D_X molecular-frame alignment) experiment finds a relative cross-section value that is 200 times larger than predicted by theory. Furthermore, experiment shows a much stronger dependence on alignment than theory, although the relative order for the predicted alignment dependencies is the same for both at larger values for θ_a. While experiment finds a very small cross section for D_Y, the theoretical cross section is zero to within numerical error due to the symmetry of the state. The small non-zero value found experimentally is most likely due to the summation of the data over the finite angular cone of $\pm 15°$. Interestingly, both the shape and relative magnitude of the theoretical D_X, $D_{\mathbf{K}\perp}$ and D_Y results agree with the experimental measurements. As a result, theory and experiment are in fairly good agreement for the shape and relative magnitudes for the $2p\sigma_u$

state except for the beam (D_Z) and momentum transfer (D_K) directions and the magnitudes relative to the $2s\sigma_g$ and $2p\pi_u$ states. We have previously found a similar result for electron-impact excitation-ionization of helium where the 4DW results were badly incorrect for the absolute magnitude of the cross section while giving reasonable agreement with the shape of the data [34].

As mentioned above, the experimental results were integrated over an acceptance angle between 40° and 80° for θ_b to improve statistics. Figure 7 shows the theoretical results for θ_b between zero and 90° with vertical lines at 40° and 80°. The theoretical results were integrated between the two vertical lines. This range was picked because it was expected that the cross sections would be largest in this angular range, which is the case for the larger scattered-projectile angles. However, for the smaller values of θ_a, a significant part of the cross section lies outside the angular range. Also note the relative magnitudes of the cross sections for the 3 states. The scale for the $2p\pi_u$ is 40 times smaller than the $2s\sigma_g$, which means that the $2s\sigma_g$ and $2p\pi_u$ results are essentially all $2s\sigma_g$. Also the $2p\sigma_u$ scale is a factor of 400 times smaller than that for the $2s\sigma_g$ state.

VI. CONCLUSIONS

We have presented experimental and M4DW theoretical results for excitation--ionization of molecular D_2. The alignment of the D_2 molecules was inferred by determining the momenta of emitted deuterons for three different excited states of D_2^+ which dissociate immediately following ionization. A significant dependence of the dissociative-ionization cross section on both the molecular alignment and on the symmetry of the excited D_2^+ dissociative states was found in the results of both experiment and calculations. Discrepancies between the two data sets are, however, observed.

For the $2s\sigma_g$ and $2p\pi_u$ state, experiment found the largest cross section for a molecular alignment perpendicular to the scattering plane while theory predicted the largest cross sections for the alignment parallel to the momentum-transfer direction. Theory predicted the smallest cross sections for alignment perpendicular to the scattering plane. There was fairly good agreement between experiment and theory for the alignment

directions parallel and perpendicular to the incident-beam direction. For the $2p\sigma_u$ state, the relative magnitude of the experimental data is a factor of 200 larger than the theoretical prediction. However, there was otherwise reasonable agreement between experiment and theory with respect to the relative magnitude and shape of the cross sections for the different alignment directions. The only significant disagreements were for molecular alignments parallel to the electron-beam axis and parallel to the momentum transfer direction. For the case of alignment perpendicular to the scattering plane, theory predicts a cross section of zero due to the symmetry of the state. This is supported by the measurements.

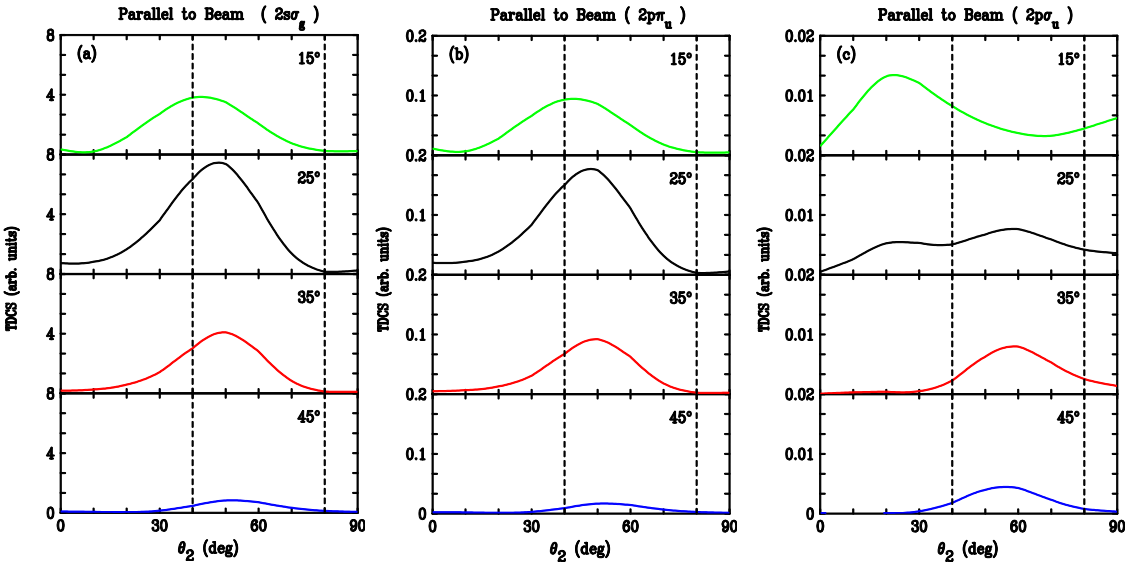

FIG. 7. M4DW theoretical results for the three different excited states as a function of the ejected-electron scattering angle and for the D_Z alignment of the internuclear axis. The angles noted in each panel are the faster (projectile) electron scattering angles. To compare with experiment, the theoretical cross sections were integrated between the two vertical lines.

Although there are some encouraging aspects of the agreement between experiment and theory, there are also significant disagreements. In particular, the theory predicts very small values for the ratio of cross sections for transitions leading to ungerade- relative to those for gerade-states, some 200 times smaller than determined by experiment. Given the clean separation of measured events by appearance energy, and the very low background

at these appearance energies, the authors expect the accuracy of the experimentally determined ratio to be dominated by the statistical error. In addition, theory predicts that the cross sections describing transitions to the $2p\sigma_u$ state are 40 times smaller than those for transitions to the $2s\sigma_g$ states. The remaining disparities between theory and experiment are probably largely due to the rather crude wavefunction used for the initial state of the target. To check the importance of this wavefunction, we will repeat the calculation using a better configuration interaction wavefunction. However, there are approximations in the theory other than the elementary ground state wavefunction that could be important, such as using continuum wavefunctions that are calculated using a scattering potential which has been averaged over all molecular orientations. Although this might logically seem to be more important than the ground state wavefunction approximation, we have previously found that the M4DW gives good agreement with experiment for the case of ionization of aligned H_2 with the ion being left in the ground state [9,10], so we assume that this would also be a good approximation if the ion is left in an excited state.

ACKNOWLEDGMENTS

HC and DM acknowledge support of the US National Science Foundation under grant PHY-1068237 and XSEDE resources ~\cite{Catlett07} provided by the Texas Advanced Computing Center (Grant No.TG-MCA07S029). XSEDE systems are hosted by Indiana University, LONI, NCAR, NCSA, NICS, ORNL, PSC, Purdue University, SDSC, TACC, and UC/ANL. CGN would like to acknowledge the support of the National Natural Science Foundation of China under contract No. 10704046. JL, SB and EW thank Colin Dedman, Stephen Battisson and Ross Tranter for their outstanding technical support at the Australian National University.

[1] V. I. Shematovich, R. E. Johnson, M. Michael, and J. G. Luhmann, J. Geophys. Res. **108**,5087 (2003).

[2] J. Liu, F. Sun, and H. Yu, Current Appl. Phys. **5**, 625 (2005).

[3] I. IPolyi, P. Cicman, S. Denifl, V. Matejcik, P. Mach, J. Urban, P. Scheier, T.D.Mark, and S. Matejvcik, J. Mass Spectrom. 252, 228 (2006).

[4] J. Lower, M. Yamazaki, and M. Takahashi, in {\it Fragmentation Processes}, ed. Colm T. Whelan (Cambridge University Press 2013), pg. 137.

[5] M. Takahashi, N. Watanabe, Y. Khajuria, K. Nakayama, Y. Udagawa, and J. H. D. Eland, J. Electron Spectrosc. Relat. Phenom. **141**, 83 (2004).

[6] M. Takahashi, N. Watanabe, Y. Khajuria, Y. Udagawa, and J. H. D. Eland, Phys.

[7] M. Takahashi, and Y. Udagawa, *Nanoscale Interactions and Their Applications: Essays in Honour of Ian McCarthy* ed F. Wang and M. J. Brunger (Kerala, India: Transworld Research Network) p 157 (2007).

[8] M. Takahashi, Bull. Chem. Soc. Jpn. **82**, 751 (2009).

[9] A. Senftleben, T. Pfl¨uger, X. Ren, O. Al-Hagan, B. Najjari, D. Madison, A. Dorn, and J. Ullrich, J. Phys. B **43**, 081002 (2010).

[10] A. Senftleben, O. Al-Hagan, T. Pfl¨uger, X. Ren, D. Madison, A. Dorn, and J. Ullrich, J. Chem. Phys. **133**, 044302 (2010).

[11] X. Ren, T. Pfl¨uger, S. Xu, J. Colgan, M. S. Pindzola, A. Senftleben, J.Ullrich, andA.Dorn, Phys. Rev. Lett. **109**, 123202 (2012).

[12] X. Ren, A. Senftleben, T. Pfl¨uger, A. Dorn, J. Colgan, M. S. Pindzola, O. Al-Hagan, D. H.Madison, I. Bray, D. V. Fursa, and J. Ullrich, Phys. Rev. A **82**, 032712 (2010).

[13] J. Gao, J. L. Peacher, and D. H. Madison, J. Chem. Phys. **123**, 204302 (2005).

[14] J. Gao, D. H. Madison, and J. L. Peacher, J. Chem. Phys. **123**, 204314 (2005).

[15] J. Gao, D. H. Madison, and J. L. Peacher, J. Phys. B **39**, 1275 (2006).

[16] C. R. Stia, O. A. Fojon, P. F. Weck, J. Hanssen, and R. D. Riverola, J. Phys. B **36**, L257 (2003).

[17] O. Al-Hagan, C. Kaiser, D. Madison, and A. J. Murray, Nat. Phys. **5**, 59 (2009).

[18] M. S. Pindzola, F. Robicheaux, S. D. Loch, J. C. Berengut, T. Topcu, J. Colgan, M. Foster, D. C. Griffin, C. P. Balance, D. R. Schultz, T. Minami, N. R. Badnell, M. C. Witthoeft, D. R. Plante, D. M. Mitnik, J. A. Ludlow, and U. Kleiman, J. Phys. B **40**, R39 (2007).

[19] J. Colgan, M. S. Pindzola, F. Robicheaux, C. Kaiser, A. J. Murray, and D. H. Madison, Phys. Rev. Lett. **101**, 233201 (2008).

[20] J. Colgan, O. Al-Hagan, D. H. Madison, C. Kaiser, A. J. Murray, and M. S. Pindzola, Phys. Rev. A **79**, 052704 (2009).

[21] J. Colgan and M. S. Pindzola, J. Phys.: Conf. Ser. **288**, 012001 (2011).

[22] I. Bray and D. V. Fursa, Phys. Rev. A **54**, 2991 (1996).

[23] A. T. Stelbovics, I. Bray, D. V. Fursa, and K. Bartschat, Phys. Rev. A **71**, 052716 (2005).

[24] S. Bellm, J. Lower, E. Weigold, and D. W. Mueller, Phys. Rev. Lett. **104**, 023202 (2010).

[25] R. N. Zare, Mol. Photochem. **4**, 1 (1972).

[26] T. E. Sharp, At. Data **2**, 119 (1970).

[27] S. Bellm, J. Lower, D. Mueller, and E. Weigold, J. Phys. Conf. Ser. **212**, 012005 (2010).

[28] J. Lower, R. Panajotovic, S. Bellm, and E. Weigold, Rev. Sci. Instrum. **78**, 111301 (2007).

[29] O. Jagutzki, V. Mergel, K. Ullmann-Pfleger, L. Spielberger, U. Spillmann, R. D¨orner, and H. Schmidt-B¨ocking, Nucl. Instrum. Methods Phys. Res., Sect. A **477**, 244 (2002).

[30] J. Ullrich, R. Moshammer, A. Dorn, R. D¨orner, L. P. H. Schmidt, and H. Schmidt-Bocking, Rep. Prog. Phys. **66**, 1463 (2003).

[31] SIMION, ion source software, P.O. Box 2726, Idaho Falls, ID 83404, USA.

[32] A. L. Harris, M. Foster, J. L. Peacher, and D. H. Madison, J. Phys. B **41**, 135203 (2008).

[33] A. L. Harris, J. L. Peacher, D. H. Madison, and J. Colgan, Phys. Rev. A **80**, 062707 (2009).

[34] S.Bellm, J. Lower, E.Weigold, I.Bray,D.V. Fursa,K.Bartschat, A. L. Harris, and D. H. Madison, Phys. Rev. A **78**, 032710 (2008).

[35] C. Catlett et al., in HPC and Grids in Action, edited by Luco Grandinetti (IOS Press, Amsterdam, 2007).

IX. Fully differential cross sections for electron impact excitation-ionization of aligned D_2

E. Ali[1], A. L. Harris[2], J. Lower[3], E. Weigold[3], C.G. Ning[4], and D.H. Madison[1]

[1]Missouri University of Science and Technology, Rolla, MO 65409, USA

[2]Illinois State University, Normal, IL, 61761, USA

[3]The Australian National University, Canberra ACT 0200)

[4]Department of Physics and State Key Laboratory of Low-Dimensional Quantum Physics, Tsinghua University, Beijing 100084, China

We examine Fully Differential Cross Sections (FDCS) for 176 eV electron-impact dissociative excitation-ionization of orientated D_2 for transitions to final ion states $2s\sigma_g$, $2p\sigma_u$, and $2p\pi_u$. In previous work [Phys. Rev. A **88**, 062705 (2013)], we calculated these cross sections using the molecular 4-body distorted wave (M4DW) method with the ground state D_2 wave function being approximated by a product of two Dyson 1s-type orbitals. The theoretical results were compared with experimental measurements for five different orientations of the target molecule (four in the scattering plane and one perpendicular to the scattering plane). For the unresolved $2s\sigma_g + 2p\pi_u$ final states, good agreement with experiment was found for to of the five measured orientations and for the $2p\sigma_u$ final state, good agreement was found for Three of the five orientations. However, theory was a factor of 200 smaller than experiment for the $2p\sigma_u$ state. In this paper, we investigate the importance of the approximation for the molecular ground state wavefunction by repeating the M4DW calculation using a better variational wavefunction for the ground state.

I. INTRODUCTION

One of the fundamental unsolved problems in physics is the few body problem which arises from the fact that the Schrödinger equation can only be solved analytically for two interacting particles. Consequently, for three or more particles, theoretical approximations must be made and the validity of these approximations can only be checked by comparing with experiment. In the last couple of decades, there have been numerous studies of the effective 3-body problem and significant progress has been made in terms of agreement between experiment and theory, especially for ionization of the smaller atoms (see, for example, the convergent close-coupling (CCC) method by Bray and Stelbovics[1], the complex exterior scaling (ECS) technique by Rescigno, et al.[2], or the time-dependent close-coupling method by Colgan, et al.[3]).

For high energy incident electrons, the collision takes place so fast that the interactions between the free particles and the target are not important and plane waves can be used to represent the free particles. In this case, the initial bound state wave function of the target determines the outcome of the collision and the T-matrix becomes the Fourier transform of the target coordinate space wave function which is the momentum space wave function. Consequently, measuring the cross section becomes equivalent to measuring the momentum space wave function [4]. For lower incident-electron energies, one cannot ignore the interactions between the free electrons and the target nor the final state interactions between the projectile and ejected electron. In this case the dynamics become important and measuring these cross sections represents a more sensitive test of the theoretical models. For collisions with molecules, most of the measurements do not determine the orientation of the molecule so theories have to average over all orientations and any averaging procedure can potentially mask important physics so the most sensitive test of theory would be measuring cross sections which determine the orientation of the molecule. The first measurement of this type was performed by Takahashi *et al.* [5] but the statistics were not very good.

One way to determine the alignment of the molecule is to measure one of the fragments of dissociation since the fragments leave the molecule in a straight line along the direction of alignment. The excited states of H_2 will immediately disassociate and the ground state can disassociate. The first experiment with better statistics was measured by

Dorn's group [6],[7] and they looked at ground state dissociation. We have recently reported the first experiment which determined the alignment by looking at dissociation of the excited state [8],[9]. This measurement represents the most stringent test of theory since there are two active electrons (4-body problem). To date, there have been a limited number of studies reported of the 4-body problem for electron-impact excitation-ionization of atoms [10]-[14] and molecules [4],[5],[8],[9]. For excitation-ionization of helium, although there was some qualitative shape agreement between experiment and theory, overall the agreement was not very good [5].

In the last few years, there have been several papers comparing experiment and the M3DW (Molecular 3-body Distorted Wave) for electron-impact ionization molecules for cases where the target orientation is not determined in the experiment[15]-[18]. In the early work, an approximation called the OAMO (orientation averaged molecular orbital) was made [19] which greatly reduced the computer demands and this approximation worked well for ionization of H_2 [20]-[23] but not so well for the larger molecules [6],[7],[21]-[27]. Very recently, the computer codes were parallelized such that proper averages over orientations can be performed and the agreement between experiment and theory was greatly improved for the larger molecules [28].

As mentioned above, the orientation of the molecule can be determined be either looking at dissociation of the ground state or the excited state. For ground state dissociation, there is only one active target electron and the problem can be treated as a 3-body problem. For this case, good agreement between experiment and theory is found for both the M3DW and the TDCC (Time Dependent Close Coupling) approximations[6],[7],[21]-[27]. In the second type of experiment, the residual target electron is excited and the excited state ion will disassociate. This type of experiment requires a 4-body theoretical approach and very recently we compared the results of the M4DW with the Canberra measurements [9] for excitation-ionization of D_2. In this measurement, the $2p\sigma_u$ excited state was energetically resolved while the $2s\sigma_g$ and $2p\pi_u$ states could not be energetically resolved from one another due to their common dissociation limit, which meant that we needed to calculate cross sections for $2s\sigma_g + 2p\pi_u$ to compare with experiment.

The theoretical results were compared with experimental measurements for five different orientations of the target molecule (four in the scattering plane and one perpendicular to the scattering plane). For the unresolved $2s\sigma_g + 2p\pi_u$ final states, good agreement with experiment was found for two of the five measured orientations and for the $2p\sigma_u$ final state, the magnitude of the theory was much smaller than experiment. However, excellent shape agreement was found for three of the five orientations. In the theoretical calculation, the ground state wave function for D_2 was approximated as a product of two 1s-type Dyson orbitals. In this paper, we investigate the importance of the approximation for the molecular ground state wave function by repeating the M4DW calculation using a better variational wave function for the ground state.

II. METHOD OF CALCULATION

In this paper, we have used the molecular four-body distorted wave (M4DW) approach, which is described more fully in Ref. [29]. Since the collision time is much shorter than the vibrational or rotational times, we make the usual assumption of stationary nuclei. For the four-body problem, the T-matrix is a nine dimensional (9D) integral which we evaluate numerically,

$$T_{fi} = \left\langle \psi_f \left| \mathrm{V}_i - U_i \right| \phi_i \right\rangle \tag{1}$$

Here ϕ_i is the initial state wave function which we express as

$$\left| \phi_i \right\rangle = \left| \psi_{\text{target}}(\mathbf{r}_1, \mathbf{r}_2) \chi_i^+(\mathbf{k}_i, \mathbf{r}_0) \right\rangle \tag{2}$$

Here $\chi_i^+(\mathbf{k}_i, \mathbf{r}_0)$ is a continuum-state distorted wave for wave number $\mathbf{k_i}$ and the + indicates outgoing wave boundary conditions. In our previous work, we approximated the ground-state wave function for the target $\psi_{\text{target}}(\mathbf{r}_1, \mathbf{r}_2)$ as a product of two Dyson 1s-type orbitals. In this work, we use the variational wave function of Rosen [30] which contains both s- and p-state contributions. For this wave function, the dissociation energy was within 10% of the experimental value which represents a significant improvement over the product of Dyson orbitals. There are more complicated wavemfunctions for H_2 which give even better energies but we found that, in the evaluation of a 9D integral, the time required to evaluate the ground state wave function was crucial to the feasibility of evaluating the integral. For example, we tried a 50 term and a 30 term HF (Hartree-Fock) ground state

wave function and quickly learned that it was not feasible to use these wavefunctions. The calculations presented here using the Rosen wave function required 2 million SU on the XSEDE cluster (Kraken) while we estimated that the HF wave functions would require several hundred million SU on the same cluster which is obviously not feasible. The Rosen wave function can be expressed as

$$\psi_{\text{target}} = N\left[\phi_{A1}(\mathbf{r}_{A1})\phi_{B2}(\mathbf{r}_{B2}) + \phi_{A2}(\mathbf{r}_{A2})\phi_{B1}(\mathbf{r}_{B1})\right] \tag{3}$$

Where N is the normalization factor, A and B denote the two nuclei for the D_2 molecule, and (r_{A1}, r_{B2}) are the distance of electrons 1 and 2 from the nuclei as shown in Fig. 1.

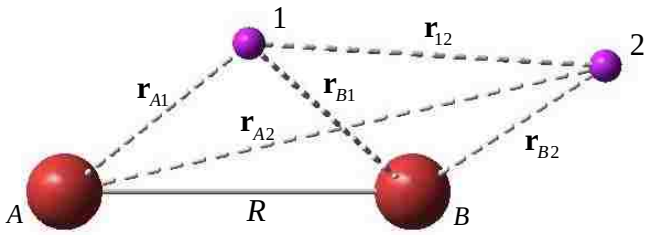

FIG. 1. Coordinates used in the Rosen wave function [30].

The trial wave function ϕ_{A1} is expressed as a linear combination of a 1s and $2p_z$ wave function,

$$\phi_{A1}(\mathbf{r}_{A1}) = N_0\left\{\phi_{1s}(\mathbf{r}_{A1}) + \sigma\,\phi_{2pz}(\mathbf{r}_{A1})\right\} \tag{4}$$

Here σ is a parameter to minimize the energy, N_0 is the normalization factor and we use the values obtained by Rosen[30].

The final state wave function ψ_f in the T-matrix of Eq. (1) is approximated as follows:

$$\left|\psi_f\right\rangle = \left|\chi_a^-(\mathbf{k}_a, \mathbf{r}_0)\chi_b^-(\mathbf{k}_b, \mathbf{r}_1)\ \phi_{ion}(\mathbf{r}_2)C_{a-b}(\mathbf{r}_{01})\right\rangle \tag{5}$$

Here $\chi_a^-(\mathbf{k}_a, \mathbf{r}_0)$ is the final state distorted wave function for scattered projectile with wave number $\mathbf{k}_a$, $\chi_b^-(\mathbf{k}_b, \mathbf{r}_1)$ is the distorted wave function for the ejected electron, the (-) indicates incoming wave boundary conditions, $\phi_{ion}(\mathbf{r}_2)$ is the excited state wave function for the final state ion which is a Dyson wave function, and $C_{a-b}(\mathbf{r}_{01})$ is Coulomb interaction between the two outgoing electrons.

The perturbation in Eq. (1) contains the initial state interaction potential V_i between the projectile electron and target is given by

$$V_i = -\frac{1}{r_{0A}} - \frac{1}{r_{0B}} + \frac{1}{r_{01}} + \frac{1}{r_{02}} \tag{6}$$

Here r_{01}, r_{02} are the distance between the projectile electron and the two bound electrons of the D_2 molecule, and r_{0A} and r_{0B} are the distance between the projectile electron and the two nuclei as shown in Fig. 2.

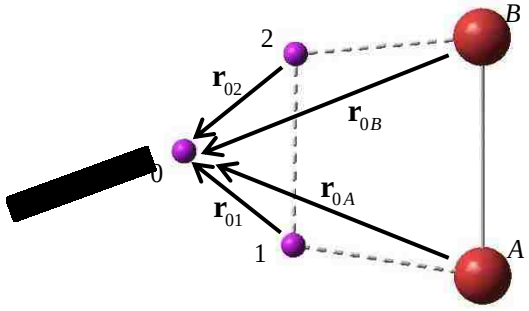

FIG. 2. Coordinates for the initial state interaction potential.

The final term in the perturbation of Eq. (1) is U_i which is an initial state spherically symmetric approximation for V_i.

Combining all our approximations, the M4DW T-matrix [29] can be written as

$$T_{fi} = \left\langle \chi_a^-(\mathbf{k}_a, \mathbf{r}_0)\chi_b^-(\mathbf{k}_b, \mathbf{r}_1)\ \phi_{ion}(\mathbf{r}_2)C_{a-b}(\mathbf{r}_{01}) \middle| V_i - U_i \middle| \psi_{target}(\mathbf{r}_1, \mathbf{r}_2)\chi_i^+(\mathbf{k}_i, \mathbf{r}_0) \right\rangle \tag{7}$$

In terms of computer time, the calculation of the wave functions and Coulomb interactions takes very little time and can basically be ignored compared to the time required for the 9D integral so this is the part of the code we parallelized. The 9D integral is 9-nested do loops and the number of available processors determines which loop we use for parallelization.

III. RESULTS

Simultaneous measurements were performed under identical experimental conditions for three orthogonal molecular orientations described in two different Cartesian coordinate systems (see [9] for details). Figure 3 shows the three different measured orientations for the D_2 molecule in one of the systems – (a) parallel to the incident beam (z-axis); (b) perpendicular to the incident beam and in the scattering plane (x-axis); and (c)

perpendicular to the incident beam and perpendicular to the scattering plane (y-axis). Both final state electrons were detected in the scattering plane (xz-plane) with $\mathbf{k}_a$ (θ_a) being the wave number and scattering angle of the faster final state electron and $\mathbf{k}_b$ (θ_b) being the wave number and scattering angle of the slower final state electron

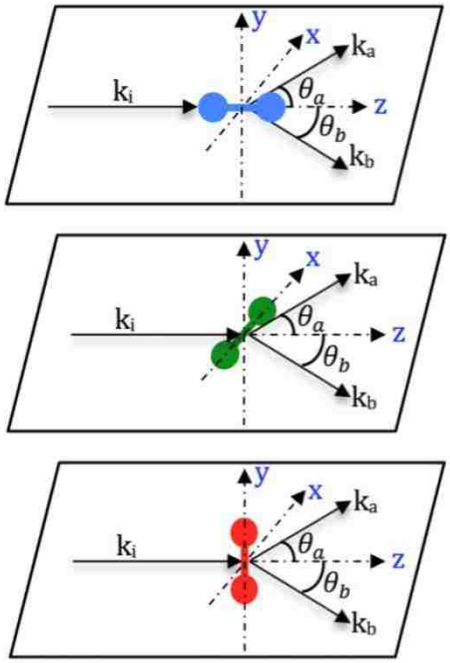

FIG. 3. Three of the measured orientations of the deuterium molecule. The wave number of the incident electron is $\mathbf{k}_i$, $(\mathbf{k}_a, \theta_a)$ are the wave number and scattering angle for the faster final state electron and $(\mathbf{k}_b, \theta_b)$ are the wave number and scattering angle for the slower final state electron.

Figure 4 compares the old and new results for excitation of the $2s\sigma_g$ state. The top half of the figure contains theory and experiment for three different measured orientations for the D_2 molecule: (1) parallel to the incident beam (z-axis labeled D_Z); (2) perpendicular to the incident beam and in the scattering plane (x-axis labeled D_X); and (c) perpendicular to the incident beam and perpendicular to the scattering plane (y-axis labeled D_Y). The bottom half of Fig. 4 contains theory and experiment for a different set of three mutually perpendicular orientations for the D_2 molecule: (1) parallel to the momentum transfer direction (labeled D_K); (2) perpendicular to the momentum transfer direction and in the scattering plane (labeled $D_{K\perp}$); and (c) perpendicular to the scattering plane (y-axis labeled

D_Y). Both final state electrons were detected in the scattering plane (xz-plane) with $\mathbf{k}_a$ (θ_a) being the wave number and scattering angle of the faster final state electron and the ejection angle for the slower final state electron is averaged over an angular range of 40^0 to 80^0.

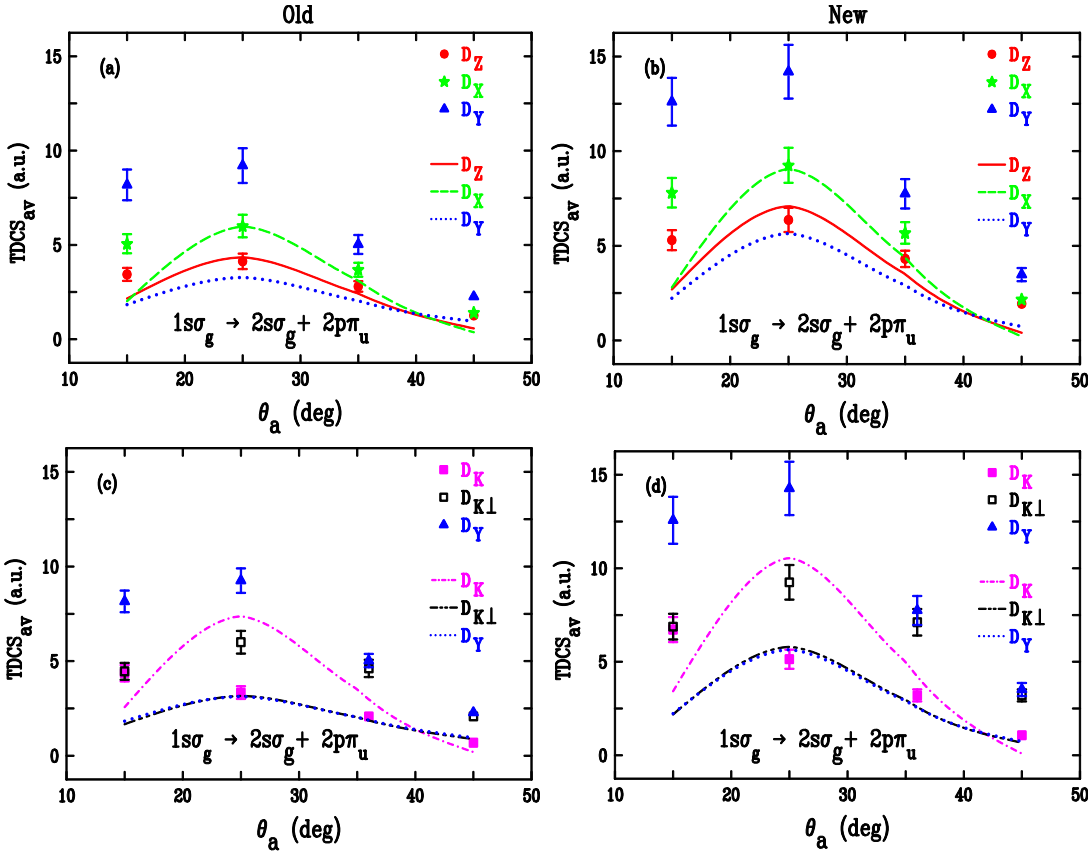

FIG. 4. Triple differential cross sections (TDCS) for electron-impact ionization of aligned molecular D_2. Experimental results are from [9] . The figure contains a comparison of theory and experiment for the old theoretical obtained using a product of Dyson wave functions for the ground state of D_2 and the new results obtained using the Rosen wave function. The different molecular orientations are described in the text. The scattering angle for the faster final state electron is θ_a and the ejection angle for the slower final state electron is averaged over an angular range of 40^0 to 80^0.

The experiments were performed for exciting the unresolved ($2s\sigma_g + 2p\pi_u$) states. However, in Ref. [9], we found that the $2p\pi_u$ state made a negligible contribution and could be ignored. Consequently, since these calculations are very computationally

expensive, we only calculated results for the $2s\sigma_g$ state using the new Rosen wave function. The results are for an incident-electron energy of 178 eV, fast and slow electron energies of 101.5 eV and 37.4 eV respectively, and for varying θ_a from 15^0 to 45^0. The direction of molecular orientation was determined by assuming that the molecular ion fragments leave the collision in the same direction as the molecular orientation [9]. The experimental measurements were performed simultaneously under identical experimental conditions which means that a single normalization will place all the measured data on an absolute scale and we have normalized experiment to theory for excitation of the $2s\sigma_g$ state, $\theta_a = 25^0$, and D_X orientation. The absolute value of the old and new cross sections are different at this point since the new wavefunction gave a somewhat larger cross section for this point. As can be seen from Fig. 4, there is very little difference between the old and new results in terms of agreement between experiment and theory for excitation of the $2s\sigma_g$ state. We attribute the fact that there is little difference between the results of two different ground state wavefunctions to the nearly symmetrical symmetry of the excited state.

It is interesting to note that there is very good agreement between experiment and theory (both shape and relative magnitude) for D_X and D_Z which are both in the scattering plane while the agreement is not good for the other two in-scattering-plane measurements D_K and $D_{K\perp}$. In fact, experiment and theory do not even agree on which cross section is largest for D_K and $D_{K\perp}$. This is quite different from ionization of the ground state of H_2 where both experiment and theory found the largest cross sections for the D_K orientation [6] while here theory still finds the largest cross section for D_K while experiment finds the smallest cross sections for D_K. It is also interesting to note that experiment finds the largest cross sections for the D_Y orientation while theory finds this the smallest cross section (even zero for the $2p\sigma_u$ state see below).

Figure (5) compares experiment with old and new theoretical fully differential cross sections (FDCSs) for electron-impact dissociative excitation-ionization of the $2p\sigma_u$ state for the same orientations shown in Fig. 5. The experimental data have been normalized

for the $2p\sigma_u$ state the same as described above. With this normalization, both the old and new theoretical calculations are a factor of 200 smaller than the experiment (obviously we could have normalized experiment to the theoretical $2p\sigma_u$ state which would have made theory 200 times larger than experiment for the $2s\sigma_g$ state). As can be seen from the figure, the shape agreement between experiment and theory is significantly better for the Rosen ground state wavefunction. Except for the smallest θ_a, the relative magnitudes and shapes of the various theoretical orientations are in good agreement with experiment. For this state, the cross section for the D_Y orientation is zero for both ground states due to the symmetry of the $2p\sigma_u$ state. It seems a bit odd that theory is in much better agreement with experiment for the small $2p\sigma_u$ cross sections than for the dominant $2s\sigma_g$ cross sections.

IV. CONCLUSIONS

In conclusion, we have previously reported a M4DW calculation for electron impact excitation-ionization of molecular D_2 using an elementary product of two Dyson orbitals to approximate the ground state wave function. In comparison with experiment, we found good agreement for approximately 2/3 of the measured cases and poor to bad agreement for the rest. In this paper, we examined the importance of the quality of the ground state wave function by repeating the calculation with a variational wave function containing both s-state and p-state components.

Interestingly, for excitation of the dominant $2s\sigma_g$ state, we found that the results were almost the same using the better wave function. However for exciting the weaker $2p\sigma_u$ final state, the new M4DW results were in good agreement with all the measured data points (shape and relative magnitude) except for a projectile scattering angle of 15^0 (the smallest angle measured). In spite of the improvement brought about by implementation of a superior ground state wave function, the large disparity (around a factor of 200) between the predictions of theory and experiment for the strength of the transition to the $2p\sigma_u$ state relative to that for the combined $2s\sigma_g / 2p\sigma_u$ states remains.\

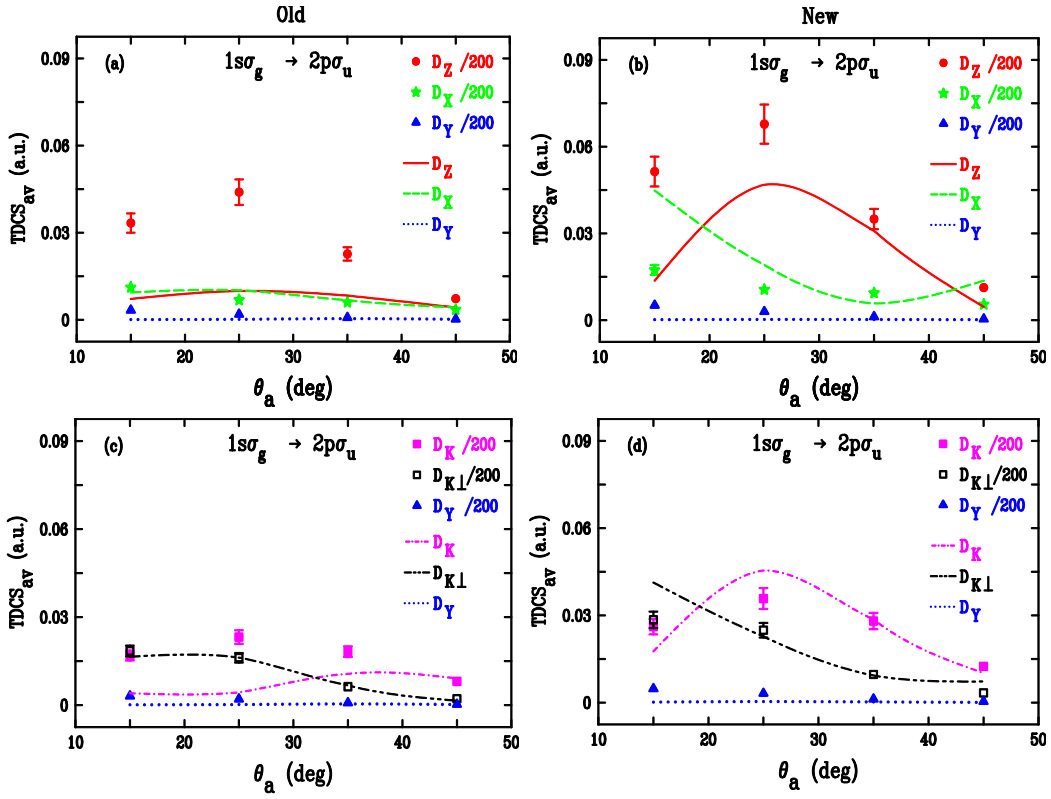

FIG. 5. Triple differential cross sections (TDCS) for electron-impact ionization of aligned molecular D_2. Experimental results are from [9]. The figure contains a comparison of theory and experiment for the old results obtained using a product of Dyson wave functions for the ground state of D_2 and the new results obtained using the Rosen wave function. The different molecular orientations are described in the text. The scattering angle for the faster final state electron is θ_a and the ejection angle for the slower final state electron is averaged over an angular range of 40^0 to 80^0.

ACKNOWLEDGEMENTS

EA and DM acknowledge support of the US National Science Foundation under grant PHY-1068237 and XSEDE resources provided [31] by the Texas Advanced Computing Center (Grant No.TG-MCA07S029).

[1] I. Bray and A. T. Stelbovics, Phys. Rev. A **46**, 6995 (1992).

[2] T. N. Rescigno, M. Baertschy, W. A. Isaacs, and C. W. McCurdy, Science 286, 2474 (1999).

[3] J. Colgan, M.S. Pindzola, F. Robicheaux, J. Phys. B: Atom., Molec. Opt. Phys. **37**, L377 (2004).

[4] E. Weigold and I. E. McCarthy, *Electron Momentum Spectroscopy*, (Kluwer Academic / Plenum Publishers, New York, 1999).

[5] M. Takahashi, N. Watanabe, Y. Khajuria, Y. Udagawa, and J. H. D. Eland, Phys. Rev. Lett. **94**, 213202 (2005).

[6] A. Senftleben, O. Al-Hagan, T. Pflüger, X. Ren, D. Madison, A. Dorn and J. Ullrich, J. Chem. Phys. **133**, 044302 (2010).

[7] X. Ren, T Pflüger, S Xu, A Senftleben, J Colgan, M S Pindzola, A Dorn and J Ullrich, J. Phys.: Conf. Ser. **388**, 052037 (2012).

[8] S. Bellm, J. Lower, E. Weigold, and D. W. Mueller, Phys. Rev. Lett. **104**, 023202 (2010).

[9] J. Lower, E. Ali, S. Bellm, E. Weigold, A. Harris, C. G. Ning, and D. Madison, Phys. Rev. A **88**, 062705 (2013).

[10] G. Sakhelashvili, A. Dorn, C. Höhr, J. Ullrich, A. S. Kheifets, J. Lower, and K. Bartschat, Phys. Rev. Lett. **95**, 033201 (2005).

[11] J. Lower, R. Panajotovic, S. Bellm, and E. Weigold, Phys. Rev. A. **75**, 042704 (2007).

[12] S. Bellm, J. Lower, K. Bartschat, X. Guan, D. Weflen, M. Foster, A.L. Harris, and D.H. Madison, Phys. Rev. A **75**, 042704,(2007).

[13] S. Bellm, J. Lower, E. Weigold, I. Bray, D.V. Fursa,K.Bartschat, A.L. Harris, and D. H. Madison, Phys. Rev. A. **78**, 032710 (2008).

[14] A.L. Harris, B. Milum, and D.H. Madison, Phys. Rev. A **84**, 052718 (2011).

[15] O. Al-Hagan, D. H. Madison, and C. Ning, J. Phys. B. **43**, 035201 (2010).

[16] D. H. Madison and O. Al-Hagan, Journal of Atomic, Molecular, and Optical Physics, **2010** ,367180 (2010).

[17] D. Jones, J. D. Builth-Williams, S. Bellm, L. Chiari, H. Chaluvadi, D. Madison, C. Ning, B. Lohmann, O. Ingólfsson, and M. Brunger, Chem. Phys. Let. **572**, (2013).

[18] J. D. Builth-Williams, S. M. Bellm, L. Chiari, P. A. Thorn, D. B. Jones, H. Chaluvadi, D. H. Madison, C. G. Ning, B. Lohmann, G. da Silva, and M. J. Brunger, J. Chem. Phys. **139**, 034306 (2013).

[19] J.L. Peacher and D.H. Madison, J. Chem. Phys. **123**, 204302 (2005).

[20] O. Al-Hagan, C. Kaiser, D. Madison and A. Murray, Nature Physics **5**,(2009).

[21] J. Colgan, O. Al-Hagan, D.H. Madison, C. Kaiser, A.J. Murray, and M.S. Pindzola, Phys. Rev. A **79**, 052704 (2009).

[22] O. Al-Hagan, A.J. Murray, C. Kaiser, J. Colgan, and D.H. Madison, Phys. Rev A **81**, 030701 (2010).

[23] J. Colgan, M.S. Pindzola, F. Robicheaux, C. Kaiser, A.J. Murray, and D.H. Madison, Phys. Rev. Lett. **101**, 233201 (2008).

[24] A. Senftleben, T Pflüger, X Ren, O Al-Hagan, B Najjari, D Madison, A Dorn and J Ullrich, J. Phys. B: At. Mol. Opt. Phys. **43**, 081002 (2010).

[25] K. Nixon, A. Murray, H. Chaluvadi, S. Amami, D.H. Madison and C. Ning, J. Chem. Phys. **136**, 094302 (2012).

[26] X. Ren, T. Pflüger, A. Senftleben, C. G. Ning, S. Yan, P. Zhang, J. Yang, X. Ma, J. Ullrich, D. H. Madison, and A. Dorn, J. Chem. Phys. **137**, 024301 (2012).

[27] X. Ren, T. Pflüger, S. Xu, J. Colgan, M. S. Pindzola, A. Senftleben, J. Ullrich, and A. Dorn, Phys. Rev. Lett. **109**, 123202 (2012).

[28] H. Chaluvadi, C. G. Ning, and D. Madison, Phys. Rev. A. **89**, 062712 (2014).

[29] A. L. Harris, M. Foster, J. L. Peacher, and D. H. Madison, J. Phys. B **41**, 135203 (2008).

[30] N. Rosen, Phys. Rev. **38**, 2099 (1931).

[31] C. Catlett et al., in HPC and Grids in Action, edited by Luco Grandinetti (IOS Press, Amsterdam, 2007).

X. Experimental and theoretical study of electron-impact ionization plus excitation of aligned H_2.

Esam Ali[1], XueGuang Ren[2,3], Alexander Dorn[2], Chuangang Ning[4] and Don Madison[1]

[1]Missouri University of Science and Technology, Rolla, MO USA

[2]Max-Planck-Institute for Kernphysik, Heidelberg, Germany

[3]Physikalisch-Technische Bundesanstalt, Braunschweig, Germany

[4]Department of Physics and State Key Laboratory of Low-Dimensional Quantum Physics, Tsinghua University, Beijing, China

E-mail: eaagx2@mst.edu

Received 26 January 2015, revised 16 March 2015

Accepted for publication 25 March 2015

Published 17 April 2015

Abstract

We report quadruple differential cross sections for electron-impact ionization of H_2 with simultaneous excitation of the H_2^+ ion which will immediately dissociate. The alignment of the molecule is determined by detecting the emitted proton. The first measurements of this type were recently reported (2013 *Phys. Rev.* A **88**, 062705). Here we report measurements with much better angular resolution using the COLTRIMS method. Experimental results are compared with M4DW (Molecular 4-body Distorted Wave) calculations and reasonably good agreement between experiment and theory is found.

Keywords: ionization excitation, electron impact, differential cross setions, 4 body

(Some figures may appear in colour only in the online journal)

Introduction

Studying ionization cross section of atoms and molecules by electron impact provides important information about the mechanisms contributing to the collision process. The most detailed information for single ionization of atoms is contained in the triply differential cross section (TDCS) which determines the full kinematical information about the collision particles both initially and finally. For ionization of atomic hydrogen and helium, close coupling methods such as the convergent close-coupling (CCC) method [1], the complex exterior scaling (ECS) technique [2], or the time-dependent close coupling (TDCC) method [3, 4] provide essentially exact numerical results for the TDCS. However, equally accurate methods do not exist for larger atoms and molecules. Single ionization of atoms or molecules with the residual ion being left in the ground state can be treated as a 3-body problem and the distorted wave Born approximation (DWBA) or one of its variants typically yields reasonably good agreement with experiment.

For molecular targets, the orientation of the molecule provides a new variable so the TDCS is not a fully differential cross section. Most experimental measurements do not determine the orientation of the molecule so all possible orientations must be averaged in any theoretical calculation. If the orientation is also determined, the cross sections will be quadruple differential cross section (QDCS). TDCS are actually 5-fold differential (4 angles and 1 energy) so the QDCS is 7-fold differential.

The orientation of a molecule such as H_2 can be determined if it dissociates since the fragments will leave in opposite directions along a straight line path parallel to the orientation. Consequently, detecting the proton, for example, will determine the direction of orientation. Both the ground and excited states of H_2^+ will dissociate and the first experiments were performed for dissociation of the ground state of H_2.[5-9] These works revealed that both the TDCC method and the M3DW (Molecular 3-Body Distorted Wave) approximation gave reasonably good agreement with experimental data. The problem with looking at the ground state is that the dissociation probability is very small whereas the excited state ions will immediately dissociate.

From a theoretical viewpoint, the problem of ionizing plus exciting the target is much more difficult to treat since collisions in which two target electrons change state

requires a 4-body treatment. One such problem on the atomic level is electron-impact ionization of helium with simultaneous excitation of the remaining target electron [10, 11]. While agreement between experiment and theory for this case is not good for perturbation approaches [10, 11] good agreement was achieved within a close-coupling approximation [12]. Here we study the four-body problem of electron impact excitation-ionization of the hydrogen molecule. The possible excited states of H_2^+ are $(2s\sigma_g, 2p\sigma_u, 2p\pi_u)$ all of which immediately dissociate and the alignment of the molecule can be determined by detecting one of the fragments.

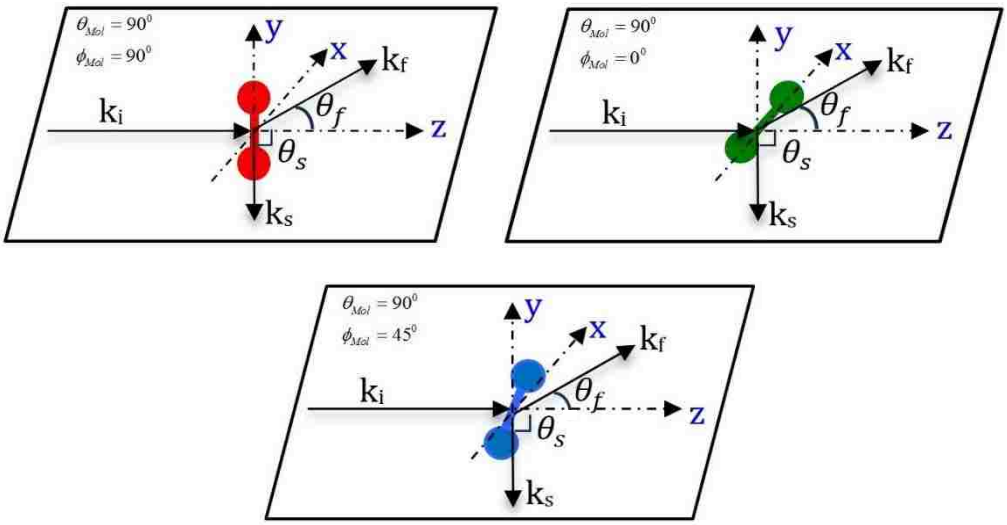

Figure 1. Different molecular alignments. The incident electron momentum is k_i along the z- axis, the scattered and ejected electrons momentum are k_f, k_s respectively, k_f is in the scattering plane (xz) and the ejected electron momentum k_s is in the perpendicular plane (xy).

An experiment of this type was recently performed in Canberra, Australia [13-15]. In that experiment, the energy resolution was good enough to resolve the $2p\sigma_u$ state but not the individual $2s\sigma_g$ and $2p\pi_u$ states. In the Canberra experiment, the experimental angular width was 2 degrees FWHM. However, to have sufficient statistics, the ejected electron detector was integrated over the angular range of 40^0 to 80^0 and the scattered electron was integrated over a 10^0 angular range. Measurements were made for 4 different scattered projectile angles for each molecular orientation (i.e. 4 data points for each

orientation). The experimental results were compared with M4DW (molecular 4-body distorted wave) calculations and reasonably good agreement between experiment and theory was found for the shape of the data and relative magnitudes for different orientations. However, experiment found the magnitude of the $2p\sigma_u$ state relative to the $2s\sigma_g + 2p\pi_u$ to be a factor of 200 larger than theory. The energy of the incident electron was 176 eV for these measurements, the scattered electron energy was 100 eV, and the scattered and ejected electrons were measured in the scattering plane.

Here we compare experiment and theory for a similar QDCS for electron ejection in the perpendicular plane measured using the reaction microscope technique. With this method, we can access almost the full solid angle and we have good statistics for a much better angular resolution for the ejected electron than the Canberra experiment. In this experiment, the ejected electron is integrated over a 12^0 angular range (as opposed to 40^0) and the angular acceptance of the scattered electron is 4^0 (as opposed to 10^0) Whereas the Canberra measurement was for one ejected electron angle, 4 projectile scattering angles and one energy, we have results for 25 ejected electron angles, 2 projectile scattering angles and 3 different energies. Whereas the Canberra measurements had 4 data points for each molecular orientation, here we report 150 measured points for each molecular orientation. Consequently, the present measurement represents a much more stringent test of theory. However, our energy resolution is not as good as Canberra and we cannot distinguish which of the three possible states has been excited so our measurements represent a sum over the three possible excited states $(2s\sigma_g, 2p\sigma_u, 2p\pi_u)$. The experimental measurements were performed for an incident electron energy of 126 eV and ejected electron energies of 4, 10, and 25 eV.

Results are presented for three different alignments of the molecule as shown in Fig. 1. The scattering plane is xz and the orientations of interest are in the xy-plane which is perpendicular to the incident beam direction. Measurements were performed for alignments along the y-axis, x-axis, and 45^o between the x- and y-axes. Here, we present a comparison of theortical M4DW QDCS results with experimental data for electron impact ionization of H_2 with simultaneous excitation of the H_2^+ ion summed over the three possible $(2s\sigma_g, 2p\sigma_u, 2p\pi_u)$ excited states with the ejected electron also being detected

in the perpendicular plane. However the $2s\sigma_g$ state completely dominates theoretically so the other two states can be ignored.

Experiment

The experiment was performed using a dedicated reaction microscope [16]. Details about the molecular frame (e,2e) experiment have been described elsewhere [8]. Briefly, a pulsed electron beam crosses a cold H_2 gas jet. Using uniform electric and magnetic fields, the final state fragments, electrons, and ions are projected (with almost 4π solid angle) onto two position- and time-sensitive multi-hit detectors. From the positions of the hits and the fragment times of flight, the momentum vectors of the detected particles can be calculated. Triple-coincidence detection of both outgoing electrons and the proton was achieved. In the present experiment, H_2 was chosen as a target gas instead of D_2, which was used in previous studies. There, the lower fragment velocity of D^+ give more time for ramping up their electric extraction field. In our experiment, we use constant electric field. The fragment trajectories for both species (H^+ and D^+) are identical and using D_2 is not advantageous.

Theory

The details of the M4DW approach were presented in [14] and [15] so only a brief overview will be presented here. Since the collision time is much shorter than the vibrational or rotational times, we make the usual assumption of stationary nuclei. For the 4-body problem, the T-matrix is a nine dimensional integral which we evaluate numerically. The T-matrix is given by

$$T_{fi} = \left\langle \chi_f^-(\mathbf{k}_f,\mathbf{r}_0)\, \chi_s^-(\mathbf{k}_s,\mathbf{r}_1)\, \phi_{\text{ion}}(\mathbf{r}_2)\, C(\mathbf{r}_{01}) \middle| \mathrm{V_i} - U_i \middle| \psi_{\text{target}}(\mathbf{r}_1,\mathbf{r}_2)\, \chi_i^+(\mathbf{k}_i,\mathbf{r}_0) \right\rangle \quad (1)$$

Here $\chi_i^+(\mathbf{k}_i,\mathbf{r}_0)$ is a continuum initial state distorted wave for wave number $\mathbf{k_i}$ and the + indicates outgoing wave boundary conditions, $\chi_f^-(\mathbf{k}_f,\mathbf{r}_0)[\chi_s^-(\mathbf{k}_s,\mathbf{r}_1)]$ is a continuum distorted wave for the faster (slower) final state electron with wave number $\mathbf{k}_f$ $[\mathbf{k}_s]$ and the minus indicates incoming wave boundary conditions, $\psi_{\text{target}}(\mathbf{r}_1,\mathbf{r}_2)$ is the initial state target wavefunction, $\phi_{\text{ion}}(\mathbf{r}_2)$ is the final state ion wavefunction, $C(\mathbf{r}_{01})$ is the Coulomb interaction between the two final state continuum electrons, $\mathrm{V_i}$ is the initial state

interaction between the projectile electron and the target, and U_i is an initial state spherically symmetric approximation for V_i.

In our previous work, we have used two different approximations for the ground state wavefunction for the target $\psi_{\text{target}}(\mathbf{r}_1, \mathbf{r}_2)$; (1) a product of two Dyson 1s-type orbitals and (2) a variational wavefunction of Rosen [30] which contains both s- and p-state contributions. For this wave function, the dissociation energy was within 10% of the experimental value which represents a significant improvement over the product of Dyson orbitals. There are better wavefunctions for H_2 which give even better energies but we found that, in the evaluation of a 9D integral, the time required to evaluate the ground state wavefunction was crucial to the feasibility of evaluating the integral. For example, we tried a 30 term and a 50 term HF (Hartree-Fock) ground state wavefunction and quickly learned that it was not feasible to use these wavefunctions. The calculations presented here using the Rosen wavefunction required 3 million SU on the NSF XSEDE cluster (Kraken) while we estimated that the HF wavefunctions would require several hundred million SU on the same cluster which is obviously not feasible. The time required to run results for the Dyson wavefunction was essentially the same as the Rosen wavefunction so about 6 million SU were used to obtain the results presented in this paper.

Results

Experimental results were measured for the three orientations shown in Fig. (1), for three different ejected electron energies (4 eV, 10 eV, and 25 eV), and for each energy two different fixed scattering angles for the scattered projectile (18 different cases). (Obviously we do not know which final state electron is the projectile and which one is the ejected electron but we refer to the faster final state electron as the projectile and the slower one as the ejected electron for convenience.) Recall that the experiment represents a sum over the three possible unresolved excited states $(2s\sigma_g, 2p\sigma_u, 2p\pi_u)$ while theory predicts that the only important state is the $2s\sigma_g$ so this is effectively a comparison with excitation of the $2s\sigma_g$ state only. Although the experimental measurements are not absolute, they are 'relatively absolute' which means that the ratio of any two cross sections is absolute. Consequently, only one normalization is required to put the entire data set (18 angular

distributions) on an absolute basis and we have normalized the data to the Rosen calculation. The results of the Dyson wavefunction calculation were uniformly larger than Rosen so we normalized the Dyson results to the Rosen for the case of 10 eV, and $\theta_f = 30^0$ since the shape of the two calculations were almost the same for this case (and this case only!). This normalization was achieved by multiplying all the Dyson results by $\frac{2}{3}$. It seems odd that the two calculations have identical shapes for this case only but we have checked for errors and could not find any.

Figure 2 compares experiment and theory for 4 eV ejected electrons (largest cross section), Fig. 3 for 10 eV ejected electrons (next largest cross sections) and Fig. 4 compares experiment and theory for 25 eV ejected electrons (smallest cross sections). Both the molecular alignment and ejected electrons are in the perpendicular plane (perpendicular to the incident beam and perpendicular to the scattering plane). For the coordinate system we are using, the beam direction is the z-axis, the xz plane is the scattering plane, and the xy plane is the perpendicular plane. The projectile is scattered in the +x-direction so the final-state scattering angle for the faster projectile θ_f is in the (+x,+z) plane. Since the slower electron is in the perpendicular plane, $\theta_s = 90^0$ and the azimuthal angle for the slow electron ϕ_s is measured counterclockwise in the xy plane starting at the x-axis $(\phi_s = 0^0)$, y-axis $(\phi_s = 90^0)$, negative x-axis $(\phi_s = 180^0)$, etc. The cross sections are symmetric about the scattering plane for molecules oriented along the x-axis and y-axis but they are not symmetric for orientation at 45^o in the xy plane. This means that the x-orient and y-orient cross sections should be symmetric about $\phi_s = 180^0$, while the differential cross sections should not be symmetric for orientation at 45^o in the xy plane. This symmetry (and lack thereof) can be seen in both the theoretical and experimental results.

Interestingly a large part of the cross section patterns can be assigned to intuitively accessible mechanisms. Firstly, there is a binary peak in the cross section originating from the direct knock out of the target electron by the projectile. Accordingly it lies in the scattering plane on the opposite side of the z-axis from the scattered projectile (i.e. negative x-axis). The perpendicular plane cuts through this binary lobe such that a maximum can be

found at $\phi_s = 180^0$ for almost all kinematics of the Figs. 2-4. Secondly, in a previous study of (e,2e) on hydrogen leaving the ion in the ground state, cross section peaks were found for electron emission along the direction of the molecular axis [9]. These maxima were prominent for large projectile scattering angle and low energy of the ejected electron. These maxima can be found also in the present data for ionization-excitation. In the figures, vertical lines are drawn at the angles corresponding to the direction of the molecular orientation and significant maxima can be seen for the larger angle $\theta_f = 30^0$ and the lowest energy E_s = 4 eV (Fig. 2). If the ejection energy is increased to 10 eV (Fig. 3), and 25 eV (Fig. 4), these maxima decrease relative to the central binary peak. In these cases there is rather good agreement between experiment and theory. If the scattering angle is decreased to $\theta_f = 20^o$,the peaks essentially disappear in the experimental data. Theory in contrast shows increasing peak magnitude causing strong discrepancy to the experimental data in all top-left panels of Fig. 2. To find an intuitive explanation for this behavior is not straight forward. In the earlier publication [9] for ionization into the H_2^+ ground state, it was argued that the maxima for electron emission along the molecular axis are stronger for larger projectile scattering angle since then the projectile classically undergoes a close collision. For close collisions with classical impact parameters in the order of the H_2 internuclear distance, the target structure and orientation can become relevant. For small scattering angle and, thus, distant collisions the cross section should become less sensitive to the target structure and orientation. In this sense apparently theory overestimates the target wave function anisotropy at large distance.

In the middle row panels the binary peak and molecular axis directions coincide at 180° giving rise to a dominating central maximum. Finally, in the bottom row panels the molecular axis maxima are at ϕ_s =45° and ϕ_s =225°. It is a somewhat surprising finding that the main dynamical features in the QDCS are the same for single ionization (a one electron transition) and the much more involved and complex ionization and excitation reaction (a two electron transition).

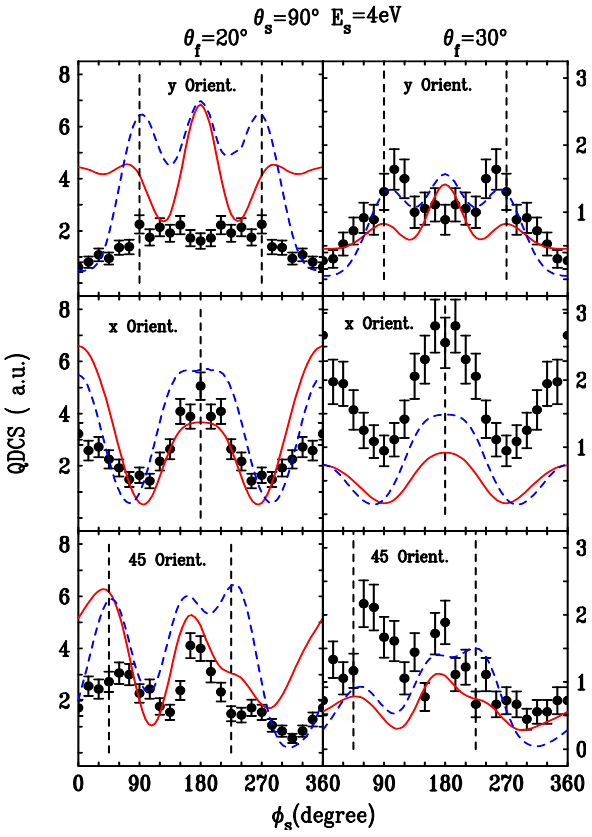

Figure 2. Experimental and Theoretical QDCS for electron-impact ionization of orientated H_2 in the perpendicular plane. The orientation of the molecule is indicated in each part of the figure and the energy of the ejected electrons is 4 eV. The black circles are the present experimental measurements. The M4DW calculations are: solid (red) line results using Rosen [30] ground state wavefunction; and dashed (blue) line results using Dyson ground state wavefunction. Vertical dashed lines indicate the molecular alignment direction.

Overall, the agreement between experiment and the M4DW theory is reasonably good – certainly much better than was found earlier for excitation-ionization of helium [10, 11] and the Canberra measurement of excitation-ionization for D_2. Comparing the two different theoretical calculations, sometimes the Rosen results look better and sometimes the Dyson results look better. Overall the Rosen results are a little better. The more important point is that the theoretical results are quite sensitive to the initial state wavefunction and theory would presumably be in even better agreement with data if a better ground state wavefunction were used. The worst agreement between experiment and theory was found for $\theta_f = 20^0$ and the molecule aligned along the y-axis (which is the

smallest cross section for the three different orientations). There is at least a qualitative agreement between experiment and theory for all the other cases. In most cases, the shape agreement between experiment and theory is quite good even when the relative magnitude is not that good. For example, looking at $(E_s = 4\,\text{eV}, \theta_f = 30^0,\ x-\text{Orient})$, the theory is about a factor of 2 lower than the data but the shape of the theory is in very good agreement with experiment.

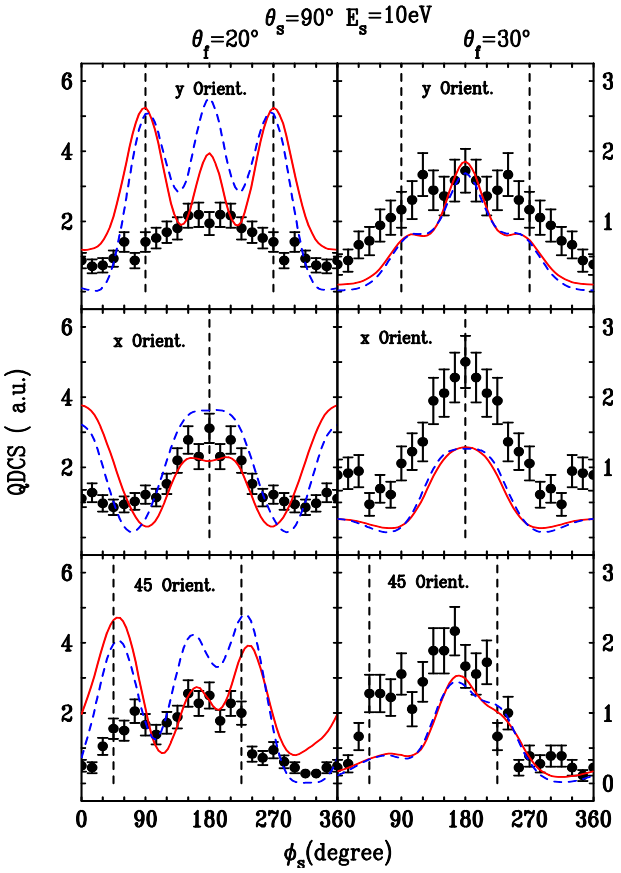

Figure 3. Same as Fig. 2, except that the energy of the ejected electrons is 10 eV.

Conclusion

In conclusion, we present a comparison between experiment and theory for the 4-body QDCS problem of electron-impact ionization of molecular H_2 with simultaneous excitation of the final state ion. Similar measurements have been recently reported by Lower *et al.* [14, 15]. However, in that work the cross sections were integrated over a 40° angular range for the ejected electron and a 10^0 angular range for the scattered electron to achieve

acceptable statistics. Our detector angular resolution is 12° for the ejected electron and 4^0 for the scattered electron, and we access the full angular range in the perpendicular plane. Because of the extremely long data acquisition times, the earlier measurements reported 4 data points per molecular alignment whereas we have measured 150 so the present work represents a much more stringent of theory.

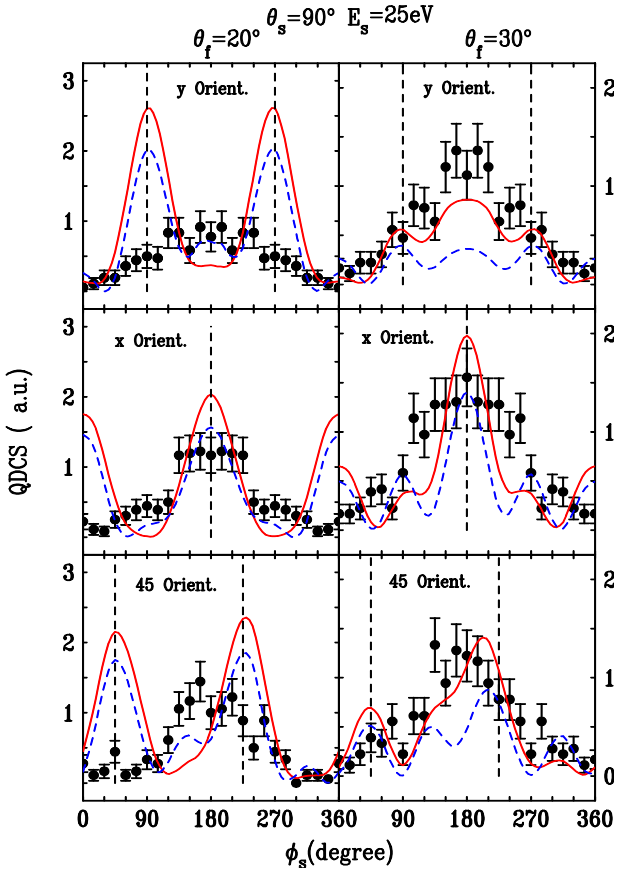

Figure 4. Same as Fig. 2, except that the energy of the ejected electrons is 25 eV.

This is a particularly important 4-body problem since the excited state ion will immediately dissociate and detection of the proton fragment determines the orientation of the molecule at the time of the collision. Over the last 2-3 decades, there have been numerous studies of electron-impact ionization of molecules which do not determine the orientation of the molecule so this possibility is a very recent development. We have measured relatively absolute QDCS which means that one normalization factor places the entire data set on an absolute scale (i.e. one normalization factor for the 18 different panels

in Figs. 2-4). The observed cross section pattern can be understood as originating primarily from binary knock-out of the target electron plus preferential electron emission along the molecular axis.

The experimental results were compared with the results of the M4DW (molecular 4-body distorted wave) calculation and reasonably good agreement with experiment was found – much better than was found for the much smaller data set [14, 15] and very much better than was found for the equivalent atomic scattering problem of electron-impact excitation-ionization of helium [10, 11]. Two different ground state wavefunctions were used in the calculation and a significant wavefunction dependence was found. Since the better wavefunction gave the best agreement with experiment, it was postulated that an even better wavefunction would give improved agreement with experiment. This calculation will have to wait for a new generation of computers (for this calculation we have used 5000 processors at a time whereas a calculation with a much better ground state wavefunction would require at least 500,000 processors to finish in a comparable time).
It is somewhat surprising that the agreement between experiment and theory is as good as it is. The experiment cannot distinguish between different excited states so it represents a sum over the three possible $(2s\sigma_g, 2p\sigma_u, 2p\pi_u)$ excited states of the H_2^+ ion. The theory, on the other hand predicts that the $2s\sigma_g$ totally dominates so that the comparison in figs. 2-4 represents a comparison with this state only. The earlier Canberra measurements had a better energy resolution and they could distinguish the $2p\sigma_u$ state from the unresolved $(2s\sigma_g, 2p\pi_u)$ states and they found the relative magnitude of the $2p\sigma_u$ state to be 200 times larger than theory predicted which means that $2s\sigma_g$ and $2p\sigma_u$ should be of comparable magnitude. Consequently, one would expect the summed cross sections to be substantially different from the cross section for the $2s\sigma_g$ state alone. It would be very interesting to have an independent determination of the relative sizes of these cross sections.

Acknowledgements

E.A. and D.M. acknowledge support of the US National Science Foundation under Grant No. PHY-1068237 and XSEDE resources [18] provided by the Texas Advanced Computing Center (Grant No. TG-MCA07S029). XSEDE systems are hosted by Indiana University, LONI, NCAR, NCSA, NICS, ORNL, PSC, Purdue University, SDSC, TACC, and UC/ANL. C.G.N. would like to acknowledge the support of the National Natural Science Foundation of China under Contract No. 10704046.

References

[1] Bray I and Stelbovics A T 1992 *Phys. Rev.* A **46** 6995

[2] Rescigno T N, Baertschy M, Isaacs W A and McCurdy C W 1999 *Science* **286** 2474

[3] Colgan J, Pindzola M S and Robicheaux F 2004 *J. Phys. B: At. Mol. Opt. Phys*. **37** L377

[4] Colgan J, Pindzola M S, Robicheaux F, Kaiser C, Murray A J and Madison D H 2008 *Phys. Rev. Lett.* **101** 233201

[5] Takahashi M, Watanabe N, Khajuria Y, Udagawa Y and Eland J H D 2005 *Phys. Rev. Lett.* **94** 213202

[6] Takahashi M, Khajuria Y and Udagawa Y 2003 *Phys. Rev*. A **68** 042710

[7] Senftleben A, Pflueger T, Ren X, Al-Hagan O, Najjari B, Madison D, Dorn A and Ullrich J 2010 *J. Phys. B: At. Mol. Opt. Phys*. **43** 081002

[8] Senftleben A, Al-Hagan O, Pflueger T, Ren X, Madison D, Dorn A and Ullrich J 2010 *J. Chem. Phys*. **133** 044302

[9] Ren X, Pflüger T, Xu S, Colgan J, Pindzola M S, Senftleben A, Ullrich J and Dorn A 2012 *Phys. Rev. Lett.* **109** 123202

[10] Bellm S, Lower J, Bartschat K, Guan X, Weflen D, Foster M, Harris A L and Madison D H 2007 *Phys. Rev*. A **75** 042704

[11] Bellm S, Lower J, Weigold E, Bray I, Fursa D V, Bartschat K, Harris A L and Madison D H 2008 *Phys. Rev*. A **78** 032710

[12] Zatsarinny O and Bartschat K 2011 *Phys. Rev. Lett*. **107** 023203

[13] Bellm S, Lower J, Weigold E and Mueller D W 2010 *Phys. Rev. Lett*. **104** 023202

[14] Lower J, Ali E, Bellm S, Weigold E, Harris A, Ning C G and Madison D 2013 *Phys. Rev. A* **88** 062705

[15] Ali E, Harris A, Lower J, Weigold E, Ning C G and Madison D 2014 *Phys. Rev*. A **89** 062713

[16] Dürr M, Dimopoulou C, Najjari B, Dorn A and Ullrich J 2006 *Phys. Rev. Lett*. **96** 243202

[17] Rosen N 1931 *Phys. Rev*. **38** 2099

[18] Catlett C et al *2007 HPC and Grids in Action* ed Luco Grandinetti (Amsterdam: IOS Press)

SECTION
3. CONCLUSION

In conclusion, The M3DW approximation has been applied to electron-impact ionization of the phenol molecule (C_6H_5OH) with coplanar asymmetrical kinematics for an incident energy of 250 eV. The TDCSs were measured for an ejected electron energy of 20 eV, and the experimental measurements cannot distinguish between the highest-occupied orbital (HOMO, 4a‴) and next highest-occupied molecular orbital (NHOMO, 3a″). The OAMO-M3DW calculations predict the same shape as the experimental data for the smallest scattered projectile scattering angle but a totally different shape for a projectile scattering angle of 15^o. Consequently, we need to repeat these calculations with the proper average cross sections. It is important to note that the theoretical calculations do include PCI effects, and they do not provide a big change in the agreement to the experimental measurements.

We compared experimental and theoretical results for electron-impact ionization of the "HOMO" state of Ethane (C_2H_6) in coplanar symmetric geometry with equal energy final state electrons (5 eV, 10 eV, 15 eV, and 20 eV). For the higher energies of 15 and 20 eV, it was shown that the PA calculation shows much better agreement with experiment than the OAMO calculation. For lower energies, the two theories make very different predictions. However, the PA results predict three peaks which is the same as was found in the experimental measurements.

We noted the similarity in the experimental data for ionization of *p*-type orbitals with different molecules that have one large nucleus at the center of mass and surrounded by lighter atoms like (NH_3 and CH_4), and two large nuclei like (N_2 and C_2H_6). For the higher energies, we found that the cross sections are almost the same with a large peak at small ejected electron angles in agreement with our calculations. However, for low energies, the cross sections for ethane (C_2H_6) are more complicated than would be expected for a simple p-type orbital

Studies of the electron-impact ionization of furfural ($C_5H_4O_2$) plays an important role in many fields such as petroleum, pharmaceutical, and agro-chemical industries. We

compared experimental and theoretical results for ionization of the HOMO ($4a''$) and NHOMO ($21a'$) states for coplanar equal energy final state electrons and asymmetric angles. We found that the DWBA calculation adequately reproduces the shape of the experimental measurement in the 35-65^o range. However, the DWBA calculation gives unphysical behavior in the limit of small angular separation between the electrons when the cross section should be zero. The M3DW calculations correctly accounts for this limit. Both the DWBA and M3DW calculations predict decreasing intensity as the electron ejection angle increases in agreement with experimental data. We found that the M3DW-OAMO qualitatively reproduces the shape and magnitude of the FDCS for faster electron scattering angles of $\theta_1 = 5^o$ and $\theta_1 = 10^o$. However, it fails for $\theta_1 = 15^o$. However, the PA calculation provides a much better agreement with experiment than OAMO.

In the medical radiation, the secondary low-energy electrons produced by primary ionizing radiation penetrating biological issue can cause significant damage to DNA. If the electron energy is higher than the ionization threshold for DNA, then the target can be ionized and decompose if the interaction couples to a repulsive dissociative state or by a subsequent rearrangement. Although it is not presently possible to directly examine electron impact ionization of DNA experimentally, it is possible to study DNA analog molecules like tetrahydrofuran (THF, C_4H_8O). We present both theoretical and experimental Fully Differential Cross Sections (FDCS) for 26.5 eV electron impact ionization of the biomolecule tetrahydrofuran for the highest, next highest, and next-next highest occupied molecular orbitals (HOMO, NHOMO, and N-NHOMO). We found the M3DW with exact PCI and WM for PCI approximations are in reasonably good agreement with experiment for binary peaks. However, both experiment and theory do not show the traditional recoil peaks around the momentum transfer. It is interesting to note that the PCI does not play an important role for these kinematical conditions.

For the scattering plane, we have also examined electron-impact ionization of the linear triatomic molecule CO_2 ($1\pi_g$) at an intermediate-energy (250 eV). In this work, we compared experiment with the three center Coulomb continuum (TCC) approximation and the M3DW model. It was found that both calculations showed ~~a~~ double peaks in the region of the binary peak~~s~~, which is expected for a *p* orbital state. These calculations showed a

high amplitude cross section for a small fixed scattered electron angle ($\theta_a = 10^o$). Overall, it was shown that the M3DW has best agreement to the experiment.

In studies of electron-impact ionization dynamics for the H_2O molecule for an incident projectile electron E_0=81 eV. The $1b_1$ and $3a_1$ orbital states experimentally unresolved, so, for that reason, we summed the TDCS for two outermost orbitals of H_2O. The theoretical and experimental results have been calculated for two fixed projectile scattering angles 6 and 10^0 and two fixed ejected electron energies of 5 and 10 eV. For ionization from *p* orbitals, the experimental measurements and PA calculations show a double peak at the binary peak in the scattering plane geometry. However, the OAMO does not predict the structure of binary peak. Overall, The PA results show a better agreement with experiment than the OAMO calculations for three different planes (scattering plane, half, and full perpendicular planes).

Finally we examined the process of (e,2e) for ionization of *para*-benzoquinone ($C_6H_4O_2$). It was not experimentally possible to resolve the four highest occupied molecular orbitals [$4b_{3g}$ (n-), $5b_{2u}$ (n+), $1b_{1g}$ (π), and $2b_{3u}$ (π)]. Both the DWBA and M3DW calculations provided reasonable agreement with experimental data in the binary range. Both experiment and theory find very weak recoil peak intensities which indicates a weakening of the interaction between the projectile and nuclei scattering.

We have also presented results of the M4DW approximation for electron-impact excitation-ionization of a D_2 molecule. The results show that the (e,2e) cross sections depends strongly on the orientation of molecule. The variational ground state of Rosen gave a better agreement with experiment than using the product of two Dyson 1*s*-type orbitals. The important physics point is that the variational method of Rosen used a wavefunction which contains both *s*- and *p*-state contributions. For excitation of the orbital state $2p\sigma_u$, both the experiment and theory predict the cross section is zero if the molecule is perpendicular to the scattering plane.

For excitation-ionization of aligned H_2 by electrons with 126 eV incident energy in the perpendicular plane we found that the cross section for excitation of the orbital state $2s\sigma_g$ totally dominates the other excited states ($2p\sigma_u$ and $2p\pi_u$), although the experiment measurements cannot distinguish between these states. Since these calculations are very

computationally expensive, it would have been very valuable to know this before we started. For molecular alignment along the x- and y- axis, there is symmetry about the scattering plane which is not present for 45^0 case.

APPENDIX A.
NUMEROV METHOD

A. NUMEROV METHOD

In this subroutine, we show how we use the Numerov method to obtain the numerical solution for radial Schrodinger equation:

$$\left(\frac{d^2}{dr^2}-\frac{l(l+1)}{r^2}-U(r)+k^2\right)\chi_\ell(r)=0 \tag{1}$$

$$\frac{d^2\chi_\ell(r)}{dr^2}=\left(\frac{l(l+1)}{r^2}-U(r)+k^2\right)\chi_\ell(r) \tag{2}$$

$$\frac{d^2\chi_\ell(r)}{dr^2}=f(r)\chi_\ell(r) \tag{3}$$

The general form of the equation may be written as:

$$\frac{d^2y}{dx^2}\equiv y''=f(x)\,y \tag{4}$$

We assume that the x-mesh is uniform with step size h. We now make a Taylor expansion for two sample points $y_n(x+h)$ and $y_n(x-h)$ and define $x_{n-1}=(x-h)$ and $x_{n+1}=(x+h)$

$$\begin{aligned} y_{n+1} &= y(x_n)+hy'(x_n)+\frac{h^2}{2!}y''(x_n)+\frac{h^3}{3!}y'''(x_n)+\frac{h^4}{4!}y''''(x_n)+\frac{h^5}{5!}y'''''(x_n)+O(h^6) \\ y_{n-1} &= y(x_n)-hy'(x_n)+\frac{h^2}{2!}y''(x_n)-\frac{h^3}{3!}y'''(x_n)+\frac{h^4}{4!}y''''(x_n)-\frac{h^5}{5!}y'''''(x_n)+O(h^6) \end{aligned} \tag{5}$$

The sum of those two equations gives

$$y_{n-1}+y_{n+1}=2y(x_n)+h^2y''(x_n)+\frac{h^4}{12}y''''(x_n)+O(h^6) \tag{6}$$

We solve this equation for y_n'' and replace it by the expression $y''=f(x)\,y$ which we get from the defining differential equation.

$$\begin{aligned} h^2y_n'' &= y_{n-1}-2y_n+y_{n+1}-\frac{h^4}{12}y''''(x_n)+O(h^6) \\ h^2f_ny_n &= y_{n-1}-2y_n+y_{n+1}-\frac{h^4}{12}y''''(x_n)+O(h^6) \end{aligned} \tag{7}$$

We take the second derivative of our defining differential equation and get

$$y''''=\frac{d^2}{dx^2}[f(x)\,y] \tag{8}$$

Now we replace the second derivative $\frac{d^2}{dx^2}$ with the second order difference quotient and insert this into our equation for $f_n y_n$

1st order difference quotient

$$\frac{\Delta g_n}{\Delta x} = \frac{g_{n+1} - g_n}{h} \tag{9}$$

2nd order difference quotient

$$\begin{aligned} \frac{\Delta^2 g_n}{\Delta^2 x} &= \frac{\frac{g_{n+1} - g_n}{h} - \frac{g_n - g_{n-1}}{h}}{h} \\ &= \frac{g_{n+1} - 2g_n + g_{n-1}}{h^2} \end{aligned} \tag{10}$$

Now use Eq. (8) in Eq. (5)

$$h^2 f_n y_n = y_{n-1} - 2y_n + y_{n+1} - \frac{h^4}{12}\frac{f_{n+1}y_{n+1} - 2f_n y_n + f_{n-1}y_{n-1}}{h^2} + O(h^6) \tag{11}$$

Solve Eq. (9) for y_{n+1}

$$\begin{aligned} h^2 f_n y_n &= y_{n-1}[1 - \frac{h^2}{12} f_{n-1}] - 2y_n[1 - \frac{h^2}{12} f_n] + y_{n+1}[1 - \frac{h^2}{12} f_{n+1}] + O(h^6) \\ y_{n+1}(1 - \frac{h^2}{12} f_{n+1}) &= 2y_n [1 - \frac{h^2}{12} f_n] - y_{n-1}[1 - \frac{h^2}{12} f_{n-1}] + h^2 f_n y_n + O(h^6) \end{aligned} \tag{12}$$

So, let's rewrite the solution of equation (12) as following:

$$y(x+h)\left[1 - \frac{h^2}{12} f(x+h)\right] = 2\left[1 - \frac{h^2}{12} f(x)\right] y(x) - \left[1 - \frac{h^2}{12} f(x-h)\right] y(x-h) + h^2 f(x) y(x) \tag{13}$$

$$T(x+h) = 2T(x) - T(x-h) + h^2 f(x) y(x) \tag{14}$$

where $T = 1 - \frac{h^2}{12} f$.

Two boundary conditions are required to solve a second order differential equation using Eq. (14). The first boundary condition is that the wavefunction must not be infinite for $r = 0$. Since the radial form of the wavefunction is $\frac{\chi_\ell(k,r)}{kr}$, the way to satisfy this requirement is to set $\chi_\ell(k,0) = 0$.

To use Eq. (14) to find a solution of the Schrödinger equation requires two points. If two points are known, then Eq. (14) will give the third point, then the second and third point can be used to find the fourth point and so on. In principle, the second point can be picked randomly. If the second point is picked too large, the numerical solution can quickly become larger than the largest possible number for a particular machine. Consequently, we constantly monitor the size of the numerical solution and rescale it smaller if it becomes too large.

Once we generate the numerical wavefunction, it has to be properly normalized. This is done by using the second boundary condition - namely the scattering theory boundary condition that asymptotically the wave must be a combination of a plane wave and an either outgoing or incoming spherical wave. This boundary condition can be expressed as

$$u_{asym} = F_\ell + T_{LJ}(G_\ell + iF_\ell) \tag{15}$$

where u_{asym} is the desired solution and where G_l, F_l are regular and irregular spherical Basel functions. The numerical solution we have found (χ_ℓ) will be some factor time the desired solution.

$$\chi_\ell = Nu_{asym} = N\left\{F_\ell + T_{LJ}(G_\ell + iF_\ell)\right\} \tag{16}$$

where N the is the desired normalization factor. Take the first derivative of Eq. (16)

$$\frac{d\chi_\ell}{d(kr)} \equiv \chi'_\ell = N\left\{F'_\ell + T_{LJ}(G'_\ell + iF'_\ell)\right\} \tag{17}$$

Now divide Eq. (16) by Eq. (17), we get

$$\frac{F_\ell + T_{LJ}(G_\ell + iF_\ell)}{F'_\ell + T_{LJ}(G'_\ell + iF'_\ell)} = \frac{\chi_\ell}{\chi'_\ell} \tag{18}$$

we can approximate numerically the first directive of u_{asym} using four points of the wave function u_{asym} and Tylor's theorem

$$\chi'_\ell = \frac{8\left[\chi_\ell(3) - \chi_\ell(2)\right] - \left[\chi_\ell(4) - \chi_\ell(1)\right]}{12 * h} \tag{19}$$

And we use the last four points of the wavefunction. Solve Eq. (18) for T_{LJ}

$$T_{LJ} = \frac{\chi_\ell F_\ell' - F_\ell \chi'_\ell}{G_\ell \chi'_\ell - \chi_\ell G_\ell' - i\left(\chi_\ell F_\ell' - F_\ell \chi'_\ell\right)} \tag{20}$$

Use the result T_{LJ} in Eq. (15) to find u_{asym} and then calculate the normalization factor of Eq. (20)

$$N = \frac{\chi_\ell}{u_{asym}} \tag{21}$$

which then can be used to obtain the desired properly normalized wave at all radial points. We can also find the elastic scattering phase shift as follows:

$$\begin{aligned} T_{LJ} &= e^{i\delta_\ell} \ \sin(\delta_\ell) \\ \left|T_{LJ}\right| &= \left|e^{i\delta_\ell} \ \sin(\delta_\ell)\right| = \sin(\delta_\ell) \\ \frac{T_{LJ}}{\left|T_{LJ}\right|} &= \frac{e^{i\delta_\ell} \ \sin(\delta_\ell)}{(\sin(\delta_\ell))} = e^{i\delta_\ell} \end{aligned} \tag{22}$$

Figure A.1 shows the logic used in the Fortran code which calculates the numerical solution of the radial part of the distorted wave function.

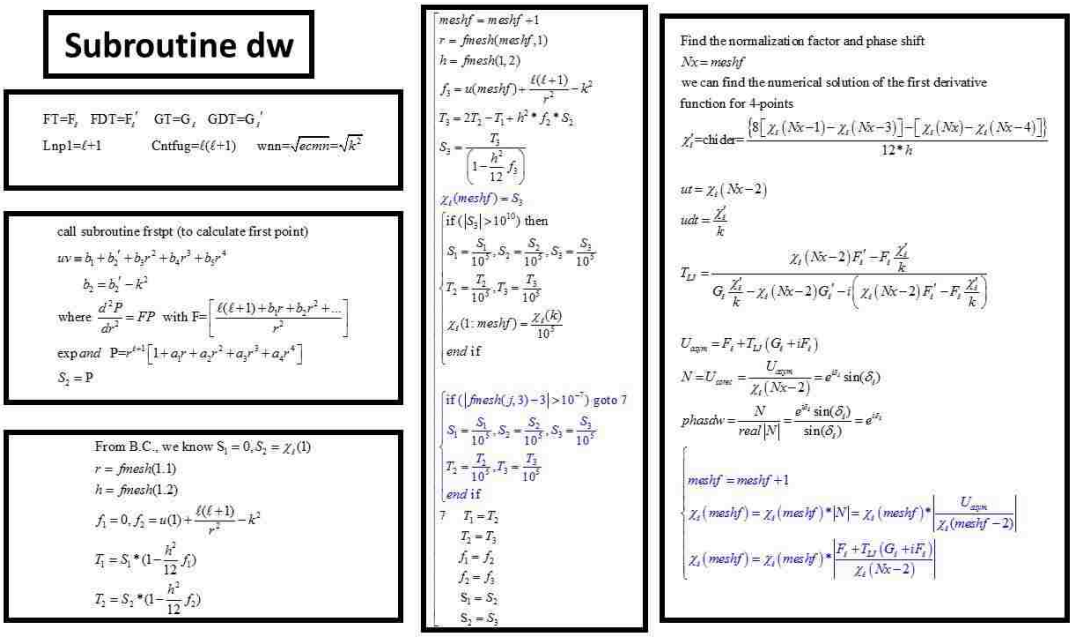

Figure A1. Show the numerical solution for distorted wave of electron

APPENDIX B.

NORMALIZATION OF ROSEN WAVE FUNCTION

B. NORMALIZATION OF ROSEN WAVE FUNCTION

The Rosen wavefunction is expressed as a product of 1s and $2p_z$ wavefunctions. Here we derive the normalization of these wavefunctions.

$$\phi_{1s}(\mathbf{r}_{A1}) = Ae^{-\alpha r_{A1}}$$

$$1 = |A|^2 \, 4\pi \int e^{-2\alpha r_{A1}} r_{A1}^2 dr_{A1} \Rightarrow 1 = |A|^2 \, 4\pi \int e^{-t} \frac{t^2}{4\alpha^2} \frac{dt}{2\alpha}$$

$$1 = |A|^2 \frac{4\pi}{8\alpha^3} \int e^{-t} t^2 dt \;\Rightarrow\; 1 = |A|^2 \frac{\pi}{4\alpha^3} 2!$$

$$A = \sqrt{\frac{\alpha^3}{\pi}}$$

$$\phi_{2p_z}(\mathbf{r}_{A1}) = Ae^{-\alpha r_{A1}} r_{A1} \cos\theta_{A1}$$

$$1 = |A|^2 \, 4\pi \int e^{-2\alpha r_{A1}} r_{A1}^4 dr_{A1} \cos^2\theta_{A1} \, \sin\theta_{A1} \, d\theta_{A1} \, d\phi_{A1}$$

$$1 = |A|^2 \, 2\pi \int e^{-t} \frac{t^4}{16\alpha^4} \frac{dt}{2\alpha} \int \cos^2\theta_{A1} \, \sin\theta_{A1} \, d\theta_{A1}$$

$$1 = |A|^2 \, 2\pi (\frac{2}{3}) \frac{1}{32\alpha^5} \int e^{-t} t^4 dt$$

$$1 = |A|^2 \frac{\pi}{24\alpha^5} 4!$$

$$A = \sqrt{\frac{\alpha^5}{\pi}}$$

The wave functions ϕ_{1s}, ϕ_{2pz} should be orthogonal

$$\phi_{1s}(\mathbf{r}_{A1}) = \sqrt{\frac{\alpha^3}{\pi}} e^{-\alpha r_{A1}}$$

$$\phi_{2p_z}(\mathbf{r}_{A1}) = \sqrt{\frac{\alpha^5}{\pi}} e^{-\alpha r_{A1}} r_{A1} \cos\theta_{A1}$$

$$\int \phi_{1s}(\mathbf{r}_{A1}) \phi_{2p_z}(\mathbf{r}_{A1}) \, \mathrm{d}\tau_{A1} = \sqrt{\frac{\alpha^3}{\pi}} \sqrt{\frac{\alpha^5}{\pi}} \int e^{-2\alpha r_{A1}} r_{A1}^3 dr_{A1} \cos\theta_{A1} \, \sin\theta_{A1} \, d\theta_{A1} \, d\phi_{A1}$$

$$= \sqrt{\frac{\alpha^3}{\pi}} \sqrt{\frac{\alpha^5}{\pi}} 2\pi \int e^{-t} \frac{t^3}{8\alpha^3} \frac{dt}{2\alpha} \left[\int \cos\theta_{A1} \, \sin\theta_{A1} \, d\theta_{A1} \right]$$

$$= \sqrt{\frac{\alpha^3}{\pi}} \sqrt{\frac{\alpha^5}{\pi}} 2\pi \frac{1}{16\alpha^4} \int e^{-t} t^3 dt \left[zero \right]$$

$$\int \phi_{1s}(\mathbf{r}_{A1}) \phi_{2p_z}(\mathbf{r}_{A1}) \, \mathrm{d}\tau_{A1} = zero$$

Let's find the normalization factor N_0 for the linear combination for a single electron

$$\phi_{A1}(\mathbf{r}_{A1}) = N_0\left\{\phi_{1s}(\mathbf{r}_{A1}) + \sigma\,\phi_{2pz}(\mathbf{r}_{A1})\right\}$$

$$1 = |N_0|^2\left[\int \phi_{1s}(\mathbf{r}_{A1})\phi_{1s}(\mathbf{r}_{A1})\,\mathrm{d}\tau_{A1} + \sigma^2\int \phi_{2p_z}(\mathbf{r}_{A1})\phi_{2p_z}(\mathbf{r}_{A1})\,\mathrm{d}\tau_{A1} + 2\sigma\int \phi_{1s}(\mathbf{r}_{A1})\phi_{2p_z}(\mathbf{r}_{A1})\right]$$

$$1 = |N_0|^2\left[1 + \sigma^2(1) + 2\sigma(zero)\right]$$

$$N_0 = \frac{1}{\sqrt{1+\sigma^2}}$$

Now let's find the normalization factor N for the linear combination for two electrons

$$\psi_{\text{target}} = N\left[\phi_{A1}(\mathbf{r}_{A1})\phi_{B2}(\mathbf{r}_{B2}) + \phi_{A2}(\mathbf{r}_{A2})\phi_{B1}(\mathbf{r}_{B1})\right]$$

$$1 = |N|^2\int \psi_{\text{target}}\,d\tau$$

$$1 = |N|^2\int\int\left[\phi_{A1}(\mathbf{r}_{A1})\phi_{B2}(\mathbf{r}_{B2}) + \phi_{A2}(\mathbf{r}_{A2})\phi_{B1}(\mathbf{r}_{B1})\right]\left[\phi_{A1}(\mathbf{r}_{A1})\phi_{B2}(\mathbf{r}_{B2}) + \phi_{A2}(\mathbf{r}_{A2})\phi_{B1}(\mathbf{r}_{B1})\right]d\tau_1 d\tau_2$$

$$1 = |N|^2\int \phi_{A1}(\mathbf{r}_{A1})\phi_{A1}(\mathbf{r}_{A1})d\tau_1\int \phi_{B2}(\mathbf{r}_{B2})\phi_{B2}(\mathbf{r}_{B2})d\tau_2 + 2\int \phi_{A1}(\mathbf{r}_{A1})\phi_{B1}(\mathbf{r}_{B1})d\tau_1\int \phi_{A2}(\mathbf{r}_{A2})\phi_{B2}(\mathbf{r}_{B2})d\tau_2 +$$

$$= \int \phi_{A2}(\mathbf{r}_{A2})\phi_{A2}(\mathbf{r}_{A2})d\tau_2\int \phi_{B1}(\mathbf{r}_{B1})\phi_{B1}(\mathbf{r}_{B1})d\tau_1$$

$$1 = |N|^2\int |\phi_{A1}(\mathbf{r}_{A1})|^2 d\tau_1\int |\phi_{B2}(\mathbf{r}_{B2})|^2\,d\tau_2 + 2\int \phi_{A1}(\mathbf{r}_{A1})\phi_{B1}(\mathbf{r}_{B1})d\tau_1\int \phi_{A2}(\mathbf{r}_{A2})\phi_{B2}(\mathbf{r}_{B2})d\tau_2 +$$

$$\int |\phi_{A2}(\mathbf{r}_{A2})|^2 d\tau_2\int |\phi_{B1}(\mathbf{r}_{B1})|^2\,d\tau_1$$

$$1 = |N|^2\left[1 + 2\int \phi_{A1}(\mathbf{r}_{A1})\phi_{B1}(\mathbf{r}_{B1})d\tau_1\int \phi_{A2}(\mathbf{r}_{A2})\phi_{B2}(\mathbf{r}_{B2})d\tau_2 + 1\right]$$

$$1 = |N|^2\left[2 + 2\int \phi_{A1}(\mathbf{r}_{A1})\phi_{B1}(\mathbf{r}_{B1})d\tau_1\int \phi_{A2}(\mathbf{r}_{A2})\phi_{B2}(\mathbf{r}_{B2})d\tau_2\right]$$

$$1 = |N|^2\left[2 + 2B^2\right]$$

$$N = \frac{1}{\sqrt{2(1+B^2)}}$$

where $B = \int \phi_{A1}(\mathbf{r}_{A1})\phi_{B1}(\mathbf{r}_{B1})d\tau_1\int \phi_{A2}(\mathbf{r}_{A2})\phi_{B2}(\mathbf{r}_{B2})d\tau_2$.

Let's calculate the integration of B

$$\int \left|\phi_{A1}(\mathbf{r}_{A1})\right|^2 d\tau_1 =$$

$$= \int \left| \frac{1}{\sqrt{1+\sigma^2}} \left[\phi_{1s}(\mathbf{r}_{A1}) + \sigma\, \phi_{2pz}(\mathbf{r}_{A1}) \right] \right|^2 d\tau$$

$$= \frac{1}{1+\sigma^2} \left[\int \left|\phi_{1s}(\mathbf{r}_{A1})\right|^2 d\tau_1 + \sigma^2 \int \left|\phi_{2pz}(\mathbf{r}_{A1})\right|^2 d\tau_1 + 2\sigma \int \phi_{1s}(\mathbf{r}_{A1}) \phi_{2pz}(\mathbf{r}_{A1}) d\tau_1 \right]$$

$$\rho = \alpha R_{nuc} = z_{eff} R_{nuc}$$

$$\int \phi_{1s}^{A1} \phi_{1s}^{B1} d\tau_1 = e^{-\rho} \left[\frac{\rho^3}{3} + \rho + 1 \right]$$

$$\int \phi_{1s}^{A1} \phi_{2p}^{B1} d\tau_1 = \frac{1}{2} e^{-\rho} \left[\frac{\rho^3}{3} + \rho^2 + \rho \right]$$

$$\int \phi_{2p}^{A1} \phi_{2p}^{B1} d\tau_1 = e^{-\rho} \left[\frac{\rho^4}{15} + \frac{2\rho^3}{15} - \frac{\rho^2}{5} - \rho - 1 \right]$$

$$B = \int \left|\phi_{A1}(\mathbf{r}_{A1})\right|^2 d\tau_1$$

$$B = \frac{1}{1+\sigma^2} \left[\int \left|\phi_{1s}(\mathbf{r}_{A1})\right|^2 d\tau_1 + \sigma^2 \int \left|\phi_{2pz}(\mathbf{r}_{A1})\right|^2 d\tau_1 + 2\sigma \int \phi_{1s}(\mathbf{r}_{A1}) \phi_{2pz}(\mathbf{r}_{A1}) d\tau_1 \right]$$

$$B = \frac{1}{1+\sigma^2} \left[e^{-\rho} \left(\frac{\rho^2}{3} + \rho + 1 \right) + \sigma^2 e^{-\rho} \left(\frac{\rho^4}{15} + \frac{2\rho^3}{15} - \frac{\rho^2}{5} - \rho - 1 \right) + 2\sigma \frac{e^{-\rho}}{2} \left(\frac{\rho^3}{3} + \rho^2 + \rho \right) \right]$$

$$B = \frac{e^{-\rho}}{1+\sigma^2} \left[\left(\frac{\rho^2}{3} + \rho + 1 \right) + \sigma^2 \left(\frac{\rho^4}{15} + \frac{2\rho^3}{15} - \frac{\rho^2}{5} - \rho - 1 \right) + \sigma \left(\frac{\rho^3}{3} + \rho^2 + \rho \right) \right]$$

$$B^2 = \frac{e^{-2\rho}}{(1+\sigma^2)^2} \left[\left(\frac{\rho^2}{3} + \rho + 1 \right) + \sigma^2 \left(\frac{\rho^4}{15} + \frac{2\rho^3}{15} - \frac{\rho^2}{5} - \rho - 1 \right) + \sigma \left(\frac{\rho^3}{3} + \rho^2 + \rho \right) \right]^2$$

$$B^2 = \int \phi_{A1}(\mathbf{r}_{A1}) \phi_{B1}(\mathbf{r}_{B1}) d\tau_1 \int \phi_{A2}(\mathbf{r}_{A2}) \phi_{B2}(\mathbf{r}_{B2}) d\tau_2$$

$$N = \frac{1}{\sqrt{2(1+B^2)}}$$

$$N = \frac{1}{\sqrt{2\left(1 + \frac{e^{-2\rho}}{(1+\sigma^2)^2} \left[\left(\frac{\rho^2}{3} + \rho + 1 \right) + \sigma^2 \left(\frac{\rho^4}{15} + \frac{2\rho^3}{15} - \frac{\rho^2}{5} - \rho - 1 \right) + \sigma \left(\frac{\rho^3}{3} + \rho^2 + \rho \right) \right]^2 \right)}}$$

$$\psi_{\text{target}} = N \left[\phi_{A1}(\mathbf{r}_{A1}) \phi_{B2}(\mathbf{r}_{B2}) + \phi_{A2}(\mathbf{r}_{A2}) \phi_{B1}(\mathbf{r}_{B1}) \right]$$

Before we normalize the total wave function which contains 6 dimensional integrals, it is convenient to change to the center mass (see Fig. B.1)

$$z_{A1} = z_0 + \frac{R_{nuc}}{2}$$

$$z_{B1} = z_0 - \frac{R_{nuc}}{2}$$

$$\cos\theta_{B1} = \frac{z_B}{r_{B1}}$$

$$R_{cm}^2 = \frac{R_{nuc}^2}{4} + r_{B1}^2 - 2\frac{R_{nuc}}{2} r_{B1}\cos(\pi - \theta_{B1})$$

$$R_{cm}^2 = \frac{R_{nuc}^2}{4} + r_{B1}^2 + R_{nuc} r_{B1}\cos\theta_{B1}$$

$$r_{B1}^2 = R_{cm}^2 - \frac{R_{nuc}^2}{4} - R_{nuc} r_{B1}\cos\theta_{B1}$$

$$r_{B1}^2 = R_{cm}^2 - \frac{R_{nuc}^2}{4} - R_{nuc} r_{B1}\left(\frac{z_{B1}}{r_{B1}}\right)$$

$$r_{B1}^2 = R_{cm}^2 - \frac{R_{nuc}^2}{4} - z_{B1} R_{nuc}$$

$$z_{A1} = z_0 + \frac{R_{nuc}}{2}$$

$$z_{B1} = z_0 - \frac{R_{nuc}}{2}$$

$$\cos\theta_{B1} = \frac{z_B}{r_{B1}}$$

$$R_{cm}^2 = \frac{R_{nuc}^2}{4} + r_{B1}^2 - 2\frac{R_{nuc}}{2} r_{B1}\cos(\pi - \theta_{B1})$$

$$R_{cm}^2 = \frac{R_{nuc}^2}{4} + r_{B1}^2 + R_{nuc} r_{B1}\cos\theta_{B1}$$

$$r_{B1}^2 = R_{cm}^2 - \frac{R_{nuc}^2}{4} - R_{nuc} r_{B1}\cos\theta_{B1}$$

$$r_{B1}^2 = R_{cm}^2 - \frac{R_{nuc}^2}{4} - R_{nuc} r_{B1}\left(\frac{z_{B1}}{r_{B1}}\right)$$

$$r_{B1}^2 = R_{cm}^2 - \frac{R_{nuc}^2}{4} - z_{B1} R_{nuc}$$

$$\cos\theta_{A1} = \frac{z_A}{r_{A1}}$$

$$R_{cm}^2 = \frac{R_{nuc}^2}{4} + r_{A1}^2 - 2\frac{R_{nuc}}{2} r_{A1}\cos\theta_{A1}$$

$$r_{A1}^2 = R_{cm}^2 - \frac{R_{nuc}^2}{4} + R_{nuc} r_{A1}\left(\frac{z_{A1}}{r_{A1}}\right)$$

$$r_{A1}^2 = R_{cm}^2 - \frac{R_{nuc}^2}{4} + z_{A1} R_{nuc}$$

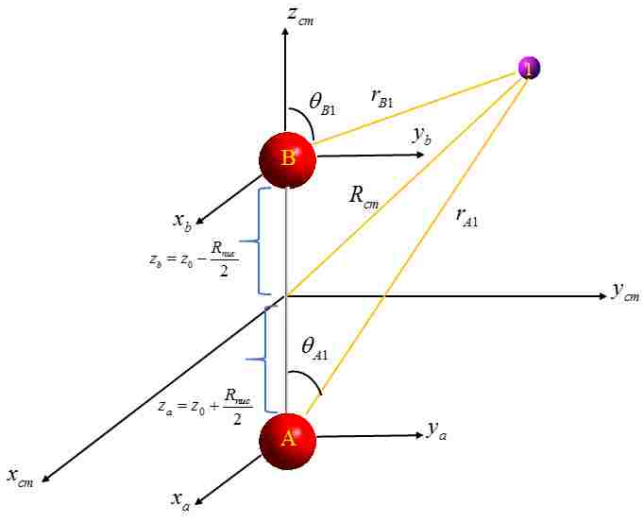

Figure B1. Show the center of mass coordinate for the H_2 molecule

After transforming the total wave function coordinates to the center mass, I have tested all normalization factors by numerical integration, and the results are contained in Table 1.

Table 1. Normalization of wavefunctions used in Rosen calculation.

Wavefunction	**Normalization**
$\phi_{1s}(\mathbf{r}_{A1})$	0.999981404366418
$\phi_{2pz}(\mathbf{r}_{A1})$	0.999993260823854
$\phi_{A1}(\mathbf{r}_{A1}) = N_0\left\{\phi_{1s}(\mathbf{r}_{A1}) + \sigma\,\phi_{2pz}(\mathbf{r}_{A1})\right\}$	0.999988395552230
$\phi_{A1}(\mathbf{r}_{A1})\phi_{B2}(\mathbf{r}_{B2})$	0.99999326082380
$\psi_{\text{target}} = N\left[\phi_{A1}(\mathbf{r}_{A1})\phi_{B2}(\mathbf{r}_{B2}) + \phi_{A2}(\mathbf{r}_{A2})\phi_{B1}(\mathbf{r}_{B1})\right]$	1.00001458752481

BIBLIOGRAPHY

[1] C. Ramsauer, *Ann. Phys., Lpz.* **64** 513 (1921).

[2] O. Al-Hagan, C. Kaiser, D. Madison, and A. J. Murray, *Nat. Phys.* **5**, 59 (2009).

[3] D. H. Madison and O. Al-Hagan, *J. At. Mol. Opt. Phys*. **2010**, 367180 (2010).

[4] S. J. Ward and J. H. Macek, *Phys. Rev. A* **49**, 1049 (1994).

[5] Esam Ali, XueGuang Ren, Alexander Dorn, Chuangang Ning, and Don. Madison, *J. Phys. B* **48**, 115201 (2015).

[6] E. Weigold and I. McCarthy, Electron Momentum Spectroscopy (Kluwer Academic, New York, (1999).

[7] J. Gao, J. L. Peacher, and D. H. Madison, *J. Chem. Phys.* **123**, 204302 (2005).

[8] E. Ali, K. Nixon, A. Murray, C. Ning, J. Colgan, and D. Madison, *Phys. Rev. A* **92**, 042711 (2015).]

[9] B.H. Bransden and C.J. Joachain, Physics of Atoms and Molecules (Prentice Hall, New York, 2003).

[10] N. T. Padial and D. W. Norcross. Phys. Rev. A **29**, 1742 (1984).

[11] N. Rosen, *Phys. Rev*. **38** 2099 (1931).

[12] Ira N. Levine, Quantum Chemistry, (Pearson Education Inc. New Jersey, 2009).

VITA

Esam Abobakr A. Ali was born in Elmarj city, Libya. He graduated from high school in 1997 and obtained his Bachelor degree from Elmarj University, Libya 2001. Then, he received his master degree in Physics from Qaryouins University, Libya 2009. He received a scholarship from the Ministry of High Education and Scientific Research in Libya to complete his PhD program. In May, 2017 he received his PhD in Physics from Missouri University of Science and Technology.

He was the second place winner of the Graduate Student Seminar competition in May 2015. He also was the second place winner of the 23rd Annual Schearer Research Prize competition in December 2016. He had been involved as a teacher in the program of International computer Driving License intended for the employees of the public post office company in Elmarj City in 2007. He had been appointed as a Health institute teacher in the period 2007-2008. He also had been appointed as a teaching assistant at Garyounis University in which he was responsible for the physics lab in 2008-2009.

He has published 10 peer-reviewed articles, and presented his research calculations at 13 national and international conferences. One of his article has been selected for the highlights of the year 2015 in the Journal physics B: At. Mol. Opt. phys.